AD-A057 129 ALUMINUM CO OF AMERICA ALCOA CENTER PA ALCOA LABS F/G 11/6
EFFECT OF MICROSTRUCTURE ON FATIGUE CRACK GROWTH OF 7XXX ALUMIN--ETC(U)
APR 78 T H SANDERS, R R SAWTELL, J T STALEY N00019-76-C-0482

UNCLASSIFIED 56-78-AF8 NL

1 OF 3
AD
A057 129

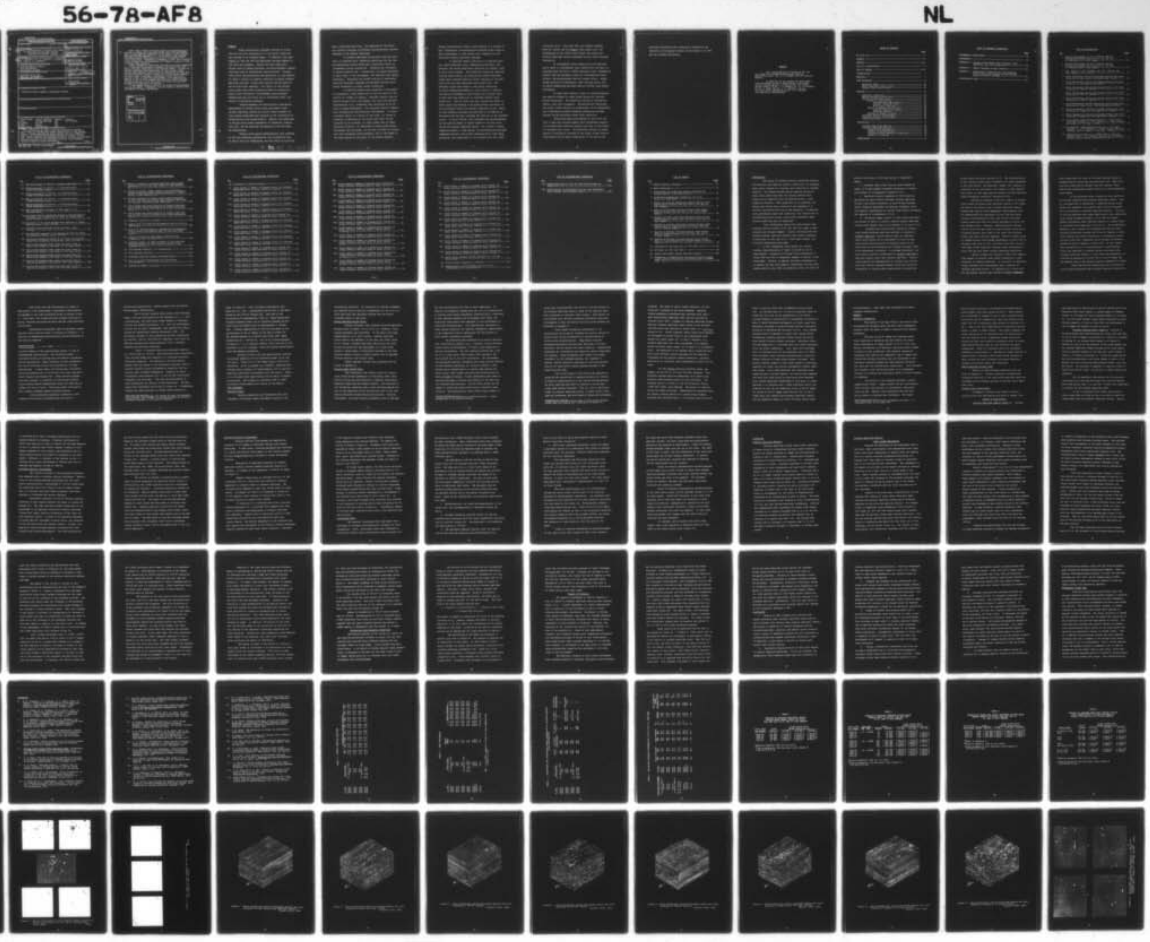

LEVEL II

AD A057129

DDC FILE COPY

AD NO.

Effect of Microstructure on Fatigue Crack Growth of 7000 Aluminum Alloys Under Constant Amplitude and Spectrum Loading

T. H. Sanders, Jr.
R. R. Sawtell
J. T. Staley
Alloy Technology Division
R. J. Bucci
A. B. Thakker
Engineering Properties and Design Division
Alcoa Laboratories

Naval Air Development Center
Contract No. N00019-76-C-0462
For Naval Air Systems Command

Final Report
78 April 14

ALCOA

UNCLASSIFIED

SECURITY CLASSIFICATION OF THIS PAGE (When Data Entered)

REPORT DOCUMENTATION PAGE

READ INSTRUCTIONS BEFORE COMPLETING FORM

1. REPORT NUMBER

2. GOVT ACCESSION NO.

3. RECIPIENT'S CATALOG NUMBER

4. TITLE (and Subtitle)

Effect of Microstructure on Fatigue Crack Growth of 7XXX Aluminum Alloys Under Constant Amplitude and Spectrum Loading.

5. TYPE OF REPORT & PERIOD COVERED

Final rept.

6. PERFORMING ORG. REPORT NUMBER

56-78-AF8

7. AUTHOR(s)

T. H. Sanders, Jr., R. R. Sawtell, J. T. Staley, R. J. Bucci, A. B. Thakker

8. CONTRACT OR GRANT NUMBER(s)

N00019-76-C-0482

9. PERFORMING ORGANIZATION NAME AND ADDRESS

Aluminum Company of America
Alcoa Laboratories
Alcoa Center, PA 15069

10. PROGRAM ELEMENT, PROJECT, TASK AREA & WORK UNIT NUMBERS

11. CONTROLLING OFFICE NAME AND ADDRESS

Department of the Navy
Naval Air Systems Command
Washington, DC 20361

12. REPORT DATE

78-04-14

13. NUMBER OF PAGES

257

14. MONITORING AGENCY NAME & ADDRESS (if different from Controlling Office)

15. SECURITY CLASS. (of this report)

UNCLASSIFIED

15a. DECLASSIFICATION/DOWNGRADING SCHEDULE

16. DISTRIBUTION STATEMENT (of this Report)

APPROVED FOR PUBLIC RELEASE; DISTRIBUTION UNLIMITED.

17. DISTRIBUTION STATEMENT (of the abstract entered in Block 20, if different from Report)

18. SUPPLEMENTARY NOTES

19. KEY WORDS (Continue on reverse side if necessary and identify by block number)

metal fatigue	constant amplitude	toughness	strength
alloy	variable amplitude	7050	heat treatment
aluminum	spectrum	7075	
7XXX	loading	7475	
crack growth	microstructure	7010	

20. ABSTRACT (Continue on reverse side if necessary and identify by block number)

An investigation was made to identify microstructural features which control the fatigue crack growth characteristics of 7XXX aluminum alloys. Constant amplitude and simple overload tests were conducted in humid air on controlled microstructural variations of alloys 7075 and 7050. Results indicated that relative influence of different microstructural features and ranking of the alloys based on fatigue crack propagation resistance depend on loading conditions.

(over)

DD FORM 1 JAN 73 1473 EDITION OF 1 NOV 65 IS OBSOLETE

UNCLASSIFIED

SECURITY CLASSIFICATION OF THIS PAGE (When Data Entered)

017 460

JOB

Higher copper content and overaging modify the strengthening precipitate in a manner which increases fatigue crack growth performance under constant amplitude loading and in load spectra in which constant amplitude conditions dominate (i.e., low overloads or high overloads infrequently spaced between base line cycles of intermediate level stress intensities). Consequently, performance of alloy 7050 is superior to that of alloy 7075, and performance of T7 tempers is superior to that of T6 under these conditions.

20. Coarse, intermetallic constituent particles and $Al_{12}Mg_2Cr$ dispersoids aid in initiating and propagating secondary cracks during high level tensile overloads, particularly in peak strength tempers. If during the overload significant crack advance does not occur by slow, stable tearing, these secondary cracks effectively redistribute and lower crack tip stress intensity, thereby retarding crack growth during subsequent low level cycles. Consequently, performance of alloy 7075 can be superior to that of alloy 7050 and performance of T6 tempers can be superior to that of T7-type tempers when high level tensile overloads are applied and flaw size is well below the critical size which will propagate to failure during the overload.

In more complex spectra, effects of the different microstructural features may compete. Consequently, relative ranking of various alloys and tempers will change with spectrum.

SUMMARY

Eight statistically designed variants of alloys 7050 and 7075 were fabricated to 6.5 mm (0.25") plate and heat treated to an overaged temper. In addition, peak aged tempers of 7050 and 7075 and additional overaged tempers of 7075 were also prepared. Tensile and tear properties, fatigue tests of smooth specimens, and metallographic examinations were used to characterize these materials. Fatigue crack growth characteristics were determined in high humidity air under a variety of loading conditions including constant amplitude; periodic, single peak tensile overload spectra; and an eight-level spectrum. The results of the fatigue crack growth tests were interpreted based on theoretical plastic zone interaction, fractography, metallographic examinations near the crack tip of interrupted tests, and results of statistical analysis.

Limited agreement was found between experimental measurements of fatigue crack growth performance under variable amplitude loading and current theory because the crack growth mechanisms were governed by the interaction of microstructure with stress history. However, the importance on fatigue crack growth retardation of theoretical plastic zone size, and the magnitude and spacing of the overloads was demonstrated.

Fatigue crack growth characteristics were affected by the fine hardening precipitates, the intermediate size $Al_{12}Mg_2Cr$ and Al_3Zr dispersoids, and the coarse Al_7Cu_2Fe and

Mg_2Si constituent particles. The magnitude of the effect and relative influence of different microstructural features depended on the loading conditions.

In constant amplitude and periodic overload tests with 1.4 overload ratio, hardening precipitate was the only microstructural feature which had a significant effect at intermediate stress intensities. Overaging and increasing Cu content modified the η' precipitate, increased resistance to water vapor in the environment, and improved crack growth resistance. Increasing the volume fraction of constituent particles decreased toughness and decreased fatigue crack growth resistance at higher stress intensities.

In spectrum loading tests producing a high degree of retardation, crack growth rate is the net result of the effects of a number of factors. Important factors such as applied stress levels, environment, and crack and specimen configuration (e.g., thickness) were controlled to be constant in these experiments. The following factors, however, were influenced by microstructural differences: (1) state of plastic strain in vicinity of the crack, (2) levels of effective ΔK operating at the crack front after the application of an overload, (3) crack growth rate at these effective ΔK levels, (4) magnitude of crack growth during and between the overloads, (5) the rate of delay of retardation with increasing crack extension, and (6) the shape of the crack contour at any point in the loading sequence.

Because microstructure affects these factors in a variety of ways, differences in microstructure produced either large or small differences in crack growth rate, depending on the particular loading conditions employed.

In spectrum loading tests with 1.8 overload ratio and 1:8000 occurrence ratio, hardening precipitates, dispersoids, and coarse constituent particles all played a role at short crack lengths. The constituent particles separated from the matrix during the overload and induced secondary cracks which reduced effective stress intensity at the main crack front and thus decreased crack growth rate. The secondary cracks were longer in the alloys containing $Al_{12}Mg_2Cr$ dispersoids because of their effect on lowering the energy to propagate a crack during the overload (UPE), so they were more beneficial in retarding fatigue crack growth rate. High Cu level also had a beneficial effect on crack growth rate because it provided greater resistance to the environment during the constant amplitude cycles. Aging to peak strength increased the magnitude of retardation by decreasing UPE and thus increased the severity of the secondary cracks. In alloy 7075-T6, this advantage was counterbalanced by the negative effect of faster growth of the main crack during the constant amplitude cycles. As a result of these competing effects, a wide variety of microstructures provided comparable fatigue crack growth characteristics under these particular test conditions of 1.8 overload ratio and 1:8000

occurrence ratio. Peak aged 7050 (the highest strength material tested) had the highest crack growth rate; the disadvantage of the faster crack growth rate during the constant amplitude cycles outweighed the gain from increased retardation.

At intermediate crack lengths with this spectrum, and at short to intermediate crack lengths with the same 1.8 overload ratio but with a 1:4000 occurrence ratio, retardation effects from the secondary cracks far outweighed the other factors, and microstructure had the largest effect. Higher volume fraction of constituents, peak strength aging, and $Al_{12}Mg_2Cr$ dispersoids provided superior fatigue crack growth performance.

At long crack lengths in both 1.8 overload spectra, the negative effects of crack growth during the overload became significant. The beneficial effects of retardation, however, were still paramount. Microstructures containing the higher volume fraction of constituents, Al_3Zr dispersoids, and a moderately overaged hardening precipitate provided optimum fatigue resistance under these conditions.

Differences among performances of alloy 7075 and 7050 in peak and overaged tempers were considerably smaller in the eight-level spectrum loading tests than in the single 1.8 overload ratio tests. The beneficial effects of higher degree of retardation provided by the higher volume fraction constituents and $Al_{12}Mg_2Cr$ dispersoids in 7075 and by the

peak aged precipitate were essentially balanced by the beneficial environmental effects of the higher Cu in 7050 and the overaged precipitate.

PREFACE

This investigation was conducted for the U.S. Naval Air Systems Command under Contract N00019-76-C-0482. Mr. E. S. Balmuth was the contract monitor.

In addition to the authors of this report, other personnel at Alcoa Laboratories contributed to this investigation. In particular, the experimental efforts of Mr. D. A. Mauney, Dr. W. G. Truckner, Mr. D. J. Lege, and Mr. P. H. Jacobus, and the critique of the manuscript by Mr. J. G. Kaufman are gratefully acknowledged.

TABLE OF CONTENTS

TABLE OF CONTENTS (CONTINUED)

LIST OF LLUSTRATIONS

LIST OF ILLUSTRATIONS (CONTINUED)

LIST OF ILLUSTRATIONS (CONTINUED)

LIST OF ILLUSTRATIONS (CONTINUED)

LIST OF ILLUSTRATIONS (CONTINUED)

LIST OF ILLUSTRATIONS (CONTINUED)

LIST OF ILLUSTRATIONS (CONTINUED)

LIST OF ILLUSTRATIONS (CONTINUED)

LIST OF ILLUSTRATIONS (CONTINUED)

LIST OF ILLUSTRATIONS (CONTINUED)

LIST OF TABLES

INTRODUCTION

The design of reliable aircraft structures requires the provision that material flaws or cracks will not propagate under cyclic loading to a critical size resulting in unstable fracture. The damage-tolerant design approach strives to limit crack growth such that the largest possible flaw missed at one inspection will be detected within a later inspection interval. When inspection is not possible, the design must insure that a crack will not propagate to a critical size during the life of the structure. To optimize alloy performance under such conditions, the interactions of microstructure with fatigue crack growth resistance under various conditions must be understood.

This investigation deals with high-strength 7XXX aluminum aircraft alloys of the 7X75 and 7050 types in peak strength and overaged tempers. Several investigations have studied constant amplitude fatigue crack growth resistance of materials of this type [1-5]. From these studies, the following observations were made:

1. In the intermediate crack growth rate regime (usually characterized by a linear log da/dN vs log ΔK relationship), resistance to fatigue crack propagation of alloys 7050 and 7X75 in comparable tempers is similar in dry environment. However, in ambient and moist atmospheres or in aqueous and salt environments, intermediate fatigue crack growth rates of alloy 7050 are generally slower (by about 50

percent) than those of 7X75-type alloys of comparable temper.

2. Overaging 7XXX alloys from the peak strength T6 temper to T7-type tempers increases resistance to fatigue crack growth in the presence of moisture [1,2].

3. Improving fracture toughness of 7X75 alloys by decreasing Fe and Si levels increases constant amplitude fatigue crack growth resistance at high ΔK where maximum stress intensity approaches the material toughness, while only marginal improvements in fatigue crack growth resistance are apparent at intermediate ΔK [1,2].

4. Increasing copper content in 7XXX alloys from about one percent to about 2.3 percent reduces constant amplitude fatigue crack growth rates in the presence of moisture [1,2].

Although most metallurgical studies on fatigue crack growth processes have been confined to analysis of constant amplitude, tension-tension data, an important factor which should not be overlooked in rating fatigue crack growth characteristics of aluminum alloys is the interaction of microstructure with loading variables likely to be encountered in service. In airframe structures, the load history typically encountered is variable amplitude or spectrum loading rather than constant amplitude. Several investigators have demonstrated for variable load history that high tensile overloads produce significant delays or retardation in fatigue crack growth during low magnitude

stress cycles following overload [6,7]. The characteristics of this fatigue crack growth retardation are highly dependent on the load history. The magnitude, number, and frequency of occurrence of the overload(s) with respect to more numerous load cycles at lower amplitude are perhaps the most important loading parameters affecting retardation [6-8].

Ranking of aluminum alloys with respect to fatigue crack growth resistance under spectrum loading is not always the same as the ranking under constant amplitude loading. Limited test results from independent investigations [4,8-11] demonstrated that specimens of alloy 7050 had longer fatigue crack propagation lives under flight simulation loading conditions than did similar specimens of alloy 7075 and related alloys. Moreover, improved spectrum fatigue life of alloy 7050 was noted at yield strength levels up to 15 percent greater than those of the other 7XXX aircraft alloys with which 7050 was compared. However, another study [5] showed fatigue crack growth performance of alloy 7050 to be poorer than that of 7075, but better than that of alloy 7049 under flight simulation loading, while performance of alloy 7050 was best under constant amplitude conditions.

Chanani showed that ranking of 7XXX alloy tempers with respect to fatigue crack growth retardation is also sensitive to loading conditions. In his tests, he applied a single overload cycle superimposed upon a sequence of constant amplitude cycles. In laboratory air, alloy 7075-T73 had greater ability than 7075-T6 to retard subsequent

crack growth when the ratio of the peak overload stress to maximum baseline stress was less than about two. When this ratio was significantly greater than two, however, alloy 7075-T6 had considerably greater ability to retard subsequent crack growth.

In the foregoing cases, ranking of alloy could not be reliably predicted from constant amplitude results. That is, the magnitude of differences in spectrum fatigue crack growth life appeared to be greater than could be accounted for by differences in constant amplitude behavior. Moreover, it was also apparent that widely used plastic zone interaction crack growth retardation models [12-15] may not always predict performance under spectrum loading in a manner which is consistent with experience [8,10,16,17]. As an additional example of this, Chanani [16] demonstrated that the yield strength differential between the T8 and T3 tempers of alloy 2024 produced far greater difference in retardation characteristics than did a comparable yield strength differential between T6 and T73 tempers of alloy 7075. He also showed that susceptibility of a microstructure to environmental attack was important in ranking fatigue resistance under variable amplitude loading. In salt water the degradation of retardation capability of alloy 7075 in the T6 temper was far greater than in the stress-corrosion resistant T73 temper.

These observations demonstrated that controlling crack growth mechanisms under variable amplitude loading are

dependent on the interaction of microstructure with load history and environment. The generally superior performance of alloy 7050 under spectrum loading conditions was hypothesized to be due to an enhancement of the fatigue crack growth retardation effect caused by differences in microstructure between 7050 and the other alloys. The original object of this investigation was to determine the effect on retardation characteristics of 7075 and 7050 caused by differences in microstructure. After this work was started, however, additional data indicated that yield strength, alloy microstructure, and loading variables interact in a complex manner. Consequently, the additional object of this investigation became to explain these interactions.

MATERIAL

Alloys 7050 and 7075 are high-strength precipitation-hardening aluminum alloys containing three types of second-phase particles which influence static properties such as strength and toughness: (a) large ($\sim$1 to 30 μm), brittle constituent particles formed during solidification by the combination of the impurity elements Fe and Si with Al and the solute elements; (b) smaller (0.02 to 0.3 μm) dispersoid particles formed by solid state precipitation of Cr or Zr at temperatures above about 425°C; (c) fine (0.002 to 0.01 μm) precipitates containing Zn, Mg, and Cu formed during quenching or aging. Relative to alloy 7075, 7050 contains a lower volume fraction of Al_7Cu_2Fe and Mg_2Si constituent particles because of restricted Fe and Si contents; a lower volume

fraction of smaller, coherent dispersoids because Zr is used as the recrystallization suppressing element instead of Cr; and a different composition and higher volume fraction of η', Mg(Zn,Cu,Al), precipitate because of the higher Cu content.

To evaluate the relative importance of these three differences on fatigue crack growth characteristics under spectrum loading conditions, a statistically designed experiment was employed. The eight alloys (Table 1) had the same Zn and Mg contents with variation in Si, Fe, Cu, Cr, and Zr, and provided a full factorial experiment of the effect of high and low levels of Mg_2Si and Al_7Cu_2Fe constituents, $Al_{12}Mg_2Cr$ vs $ZrAl_3$ dispersoids, and high Cu and low Cu variants of η' precipitate. The Zn contents averaged near the maximum for alloy 7075 and near the nominal for alloy 7050. The Mg contents were within the allowable range for both alloys. For descriptive purposes, the alloys were labeled and coded as given in Table 1. The composition of one of the alloys falls within the limits for the European alloy 7010.

All of the alloys were fabricated from laboratory-cast ingot to 6.5 mm (0.25") plate in a T7-type* (overaged) temper. The target yield strength was 450 MPa (66 ksi). This is near nominal for 7050-T73651 plate up to 50 mm (2") thick. In addition, a portion of the alloy 7050 plate was aged to a T6-type (peak strength) temper, and portions of the 7075 plate were aged to T6, T76, and T73-type tempers.

*See Table 2 for heat treatment practices.

The chemical composition and type of certain second-phase particles in the alloys aged to the T7 temper were determined by the complimentary techniques of electron microprobe analyses and Guinier-deWolff X-ray diffraction. Table 3 is a compilation of the phases identified and their relative amounts. The microprobe results were qualitatively similar for all of the alloys and can be summarized by the results for 7475 and 7075 (Figures 1 and 2). Figures 1 and 2 are the characteristic X-ray images of the particular elements that were found to be present from the remelt spectrochemical analyses.

The phases that could be directly identified by microprobe contained copper and iron in one instance and magnesium and silicon in the other. By applying the Guinier-deWolff results, these phases were identified as Al_7Cu_2Fe and Mg_2Si. The smaller $Al_{12}Mg_2Cr$ and $ZrAl_3$ dispersoids are generally below the resolution of the microprobe; consequently, characteristic X-ray images appear as random distribution of intensity (Figure 3). Only in the case of 7075 was there sufficient accumulation of CrK_α intensity to suggest the presence of a dispersoid (Figure 3a).

Three dimensional optical micrographs were prepared to illustrate the morphology of the grain structure and the relative size and distribution of the insoluble phases (Al_7Cu_2Fe and Mg_2Si), Figures 4 through 11. The photomicrographs have been grouped to illustrate the effect of iron and silicon on the structures.

Constituent size and distribution are shown in more detail in the as-polished, longitudinal cross-section micrographs of the eight structures given in Figures 12 and 13. Once again, the alloys have been grouped according to purity. The dark particles are Mg_2Si and the light particles are Al_7Cu_2Fe.

Longitudinal micrographs taken of specimens etched with hot nitric acid are shown in Figures 14 through 17. In addition to homogeneously precipitating and participating in the reaction sequence:

$$\text{Supersaturated solid solution} \longrightarrow \text{G.P. Zones} \longrightarrow \eta' \longrightarrow \eta,$$

a certain amount of the supersaturated solute is lost to heterogeneous precipitation. The metastable phase, η', nucleates directly on dislocations and subgrain boundaries, and the equilibrium η phase nucleates on grain boundaries. The nitric acid etch reveals the distribution of these precipitates. In many cases, the dislocations introduced during stretching prior to artificial aging have been decorated (Figures 14b through 17b). These photomicrographs have been grouped to illustrate the differences between alloys having similar compositions except for additions of either 0.1% Zr or 0.2% Cr. The alloys which contained Zr had a greater tendency toward recrystallization.

X-ray diffraction employing transmission Laue geometry with pinhole collimation was also used to

characterize substructure. Results agreed with the optical metallographic observations.

The structure variants which affect yield strength, namely, size and distribution of the hardening G.P., η', and η precipitates, and those which affect degree of recrystallization and subgrain structure, i.e., size and distribution of Al_3Zr and $Al_{12}Mg_2Cr$ dispersoids, were observed and characterized by transmission electron microscopy (TEM). The structural extremes in this program can be best represented by 7075-T76, 7475-T7, and 7050-T7; therefore, thin foils for TEM were prepared from these materials using a standard dimpling and polishing technique.

Figure 18 contains electron micrographs comparing (a) 7075-T6 and (b) 7475-T7. Both structures were unrecrystallized and TEM showed the presence of a recovered structure containing subgrains. The majority of the dislocations present were the result of the stretching treatment given to minimize residual stress introduced by quenching from the solution heat treatment temperature. Numerous $Al_{12}Mg_2Cr$ dispersoids (approximately 0.15 m) can be seen distributed throughout the structure. The size and distribution of these dispersoids are similar in both materials.* The most significant difference can be seen in Figure 18. A comparison between the same structures at higher magnifications is

*The size and distribution are similar because the patented Alcoa process (USP 3791880) for modifying these particles to increase toughness in 7475 was not employed.

shown in Figure 19. Fine, uniformly distributed, near spherical G.P. and η' precipitates can be seen in the background of the 7075-T6 (Figure 19a). The size of the precipitates is approximately 0.005 μm. Aging beyond peak strength produced larger rod or elliptical-shaped precipitates having an aspect ratio of approximately 3 (Figure 19b). A better appreciation of the size and shape of the precipitates in the T7 temper can be seen in Figure 20. The photomicrograph is a central dark field (CDF) image produced by an η' reflection. One of the crystallographic variants of η' is in contrast (white), while the rest of the structure is out of contrast. Note the copious precipitation along the subgrain boundaries.

Figures 21 and 22 are high magnification electron micrographs comparing the two dispersoid types, Al_3Zr and $Al_{12}Mg_2Cr$. Figure 21 is a CDF image using a (100) Al_3Zr reflection. Al_3Zr is present as a coherent, spherical precipitate with a diameter of approximately 0.05 μm and has a cube/cube orientation relationship with the matrix. Figure 22 is a bright field image showing the $Al_{12}Mg_2Cr$ (E-phase) precipitates. The E-phase is incoherent with no fixed orientation relationship with respect to the matrix.

TEST PROCEDURE

Monotonic Tests

Tensile properties were determined using full thickness, 51 mm gauge length specimens oriented in the

longitudinal direction. An indication of fracture toughness was obtained using triplicate longitudinal 6.4 mm (0.25 in.) thick Kahn-type tear specimens removed from the center thickness region of the plate.

Smooth Specimen Fatigue Tests

Axially stressed, fully reversed tension-compression fatigue tests of smooth, 5.8 mm (0.23 in.) diameter, longitudinal specimens were performed. In the short life range (approximately 10 to 5×10^3 cycles), constant amplitude strain control was employed. In the long life range (5×10^4 to 10^7 cycles), constant amplitude load control was used. Failure criterion was the development of a crack large enough to cause either a significant decrease in the load carrying capacity during a strain control test or specimen fracture during a load control test.

Smooth specimen fatigue test procedures are detailed in Appendix B.

Fatigue Crack Growth Tests

That occasional high tensile loads will retard crack growth during subsequent or intervening lower level tensile cycling has been observed in numerous experiments employing simplified and complex spectra. The magnitude of the retardation resulting from a given overload depends not only on the magnitude of the overload but also on the load history both prior to and following the overload. Material, environment, and other physical parameters such as specimen

and flaw configuration are also of major importance. To simplify the problem of identifying the role of microstructure on fatigue crack growth retardation characteristics, conditions of test specimen geometry and environment were fixed, and simplified load spectra were employed to rate performance of controlled microstuctures. This approach was considered to offer greater potential for improved fundamental understanding of the respective roles of metallurgy and load history on crack growth retardation processes.

All materials were subjected to as nearly identical test conditions as possible (e.g., identical fatigue precrack stress levels and procedures) to insure valid comparison of material performance. The test specimen selected was a 100 mm (4 in.) wide center crack tension (CCT) specimen, and crack growth was in the L-T* orientation. The environment was maintained constant throughout this study and was selected as high humidity laboratory air (relative humidity >90%), thereby being representative of typical applications for these alloys. Crack growth was monitored electronically by crack propagation gauges. Visual measurements were made on selected specimens to permit verification of the data that was obtained electronically. The raw crack length and the number of cycles data were fitted using a piecewise cubic function. The equations for crack length versus number of

*Stress direction parallel to rolling direction. Crack propagation in the width direction.

cycles were differentiated, and ratios of the derivatives of the constant amplitude tests to those of the spectrum tests were calculated at identical crack lengths. More details on crack growth test and data processing procedures along with a discussion on data variability utilizing these methods are described in Appendix A.

Crack growth information established in the investigation was primarily intended for relative ranking of fatigue crack growth performance and characteristics of various alloy microstructures. Experimental and data processing procedures utilized were developed to be cost effective, and yet satisfy the basic objective. Computerized techniques for interpreting and reporting results simplified the analysis. These procedures were judged to be highly successful for the intended purpose, ref. Appendix A. However, caution should be exercized in utilizing reported results for quantitative design purposes because of the simplifications made.

The initial phase of this effort was employed to establish the sensitivity of spectrum selection on ranking retardation characteristics of the various microstructures. The basic spectrum type used is referred to as periodic, single peak tensile overload.* That is, after a particular number of constant amplitude cycles, a single tensile overload was introduced, and this block of cycles was continually

*Nomenclature and definitions used in describing periodic, single peak overloading are illustrated in Figure 23.

repeated. The range of cyclic stress intensity, ΔK, progressively increased as the crack advanced. Spectrum loading parameters considered were overload ratio (OLR = peak load/constant amplitude load) and the overload occurrence ratio (OCR = 1/number of constant amplitude cycles). Baseline constant amplitude stress cycles in the periodic overload tests were selected at stress ratio, $R = \sigma_{min}/\sigma_{max}$, values of 1/3. Stress intensity factor levels were selected to correspond to growth rates in the intermediate crack growth rate range (about 10^{-6} to 5×10^{-4} cm/cycle) in a constant amplitude test. This corresponds to an applied stress intensity factor range, ΔK, of about 6 to 16 MPa$\sqrt{m}$ at R=1/3. The magnitude of the maximum cyclic stress was well below yield strength levels developed for the materials considered and the applied loading conditions, including application of overloads, were predominantly elastic for all tests.

For the initial spectrum screening tests, two tempers (T7 and T6) of 7075 and 7050 were selected. This procedure allowed spectrum comparisons to be made at two distinct yield strength levels for both materials. Two overload ratios, 1.4 and 1.8, and two occurrence ratios, 1:4000 and 1:8000, were examined. The choice of overload ratios was rather arbitrary. Representative exceedence data for typical loading spectra of a ground attack fighter aircraft wing indicated that a 1.8 overload occurred on the

order of once for every 1000 intermediate stress cycles [18]. An overload ratio of 1.8 with an occurrence ratio of 1:4000 was the first of the combinations to be tested. Fracture mechanics calculations at intermediate ΔK levels of about 10 MPa$\sqrt{m}$ indicated overlapping of plastic zones from sequential overloads to permit maximum overload interaction according to Hertzberg and coworkers [19-21]. This loading sequence would be expected to retard crack growth during intermediate constant amplitude cycles during the entire crack growth interval between overloads. Additional tests were performed with 1.4 overload ratio and 1:4000 occurrence ratio for direct comparison. Also, tests were performed with 1.8 overload ratio and an occurrence ratio of 1:8000. This occurrence ratio isolated overload plastic zones by a greater interval of crack growth between overloads. This greater interval tended to allow crack growth to eventually approach its normal rate during intermediate constant amplitude cycles. After these materials were evaluated using simple periodic overload spectra, the results were compared with data from tests using an eight-level block spectrum. From related experience established to this point, a simple spectrum (1.8 overload ratio, 1:8000 occurrence ratio) was selected to test the six remaining alloys in the T7 temper. All alloys in the T7 temper plus 7050 and 7075 in the T6 temper were also tested using constant amplitude loading, and the remaining tempers of alloy 7075 were tested using

selected spectra. Some tests were interrupted for metallographic examinations.

RESULTS

Monotonic Properties

The results of the tear tests in the form of tear strength/yield strength ratios and unit crack propagation energies (UPE) are shown in Table 4 along with the tensile properties.

The data in the T7 temper were analyzed using Yates algorithm to determine the main effects and first order interactions of copper content (2.2% vs 1.5%), dispersoid (Zr-bearing vs Cr-bearing), and alloy purity (higher vs lower) on tear properties. Then multiple regression techniques were used on the combined T7 and T6 temper data. Interactions between variables were not considered in the regression analysis because the Yates analysis indicated that they were not statistically significant.* Yield strength was included in the statistical model as an independent variable to eliminate the confounding effect of yield strength on toughness.

The results of the analyses indicated a strong compositional effect. Copper content did not significantly affect (either statistically or practically) tear/yield ratio and UPE. However, both dispersoid type and alloy purity greatly influenced tear resistance. The higher

*All statistical significance statements are based on a confidence level of at least 95%.

purity alloys containing Zr dispersoid developed significantly higher tear/yield ratios and UPE's. These effects are illustrated in Figures 24 and 25 where predicted tear/yield ratio and UP, respectively, have been plotted in bar graph form for a normalized yield strength of 448 MPa (65.0 ksi). Each of the four combinations of dispersoid type and purity is shown in these figures. The higher toughness for alloys containing Zr is consistent with the observations that the coherent Al_3Zr dispersoids formed during preheating are much less effective nucleating sites for microvoids during fracture than are the incoherent $Al_{12}Mg_2Cr$ dispersoids. Effect of increasing purity on increasing toughness is attributed to a decrease in volume fraction of large Al_7Cu_2Fe, and Mg_2Si constituents which fracture at small strains and thus circumvent the energy absorbing process of microvoid growth and coalescence.

Smooth Specimen Fatigue Tests

Results of these constant amplitude tests are given in Appendix B. Fatigue resistance increased with increasing ductility in the high strain amplitude tests and increased with increasing strength in the low strain amplitude tests.

Fatigue Crack Growth Tests

A summary of fatigue crack growth lives for various alloys and load spectra are given in Tables 5-10.

Effect of Load History

Constant Amplitude Loading (Table 5). Constant

amplitude data for 7075-T6 and T7 and for 7050-T6 and T7 are plotted as half crack length, a, versus number of elapsed cycles, N, in Figure 26, and as average da/dN vs a in Figure 27. For all crack lengths, crack growth resistance of alloy 7050 was superior to that of alloy 7075, and performance of the T7 temper was superior to that of the T6.

Periodic Overload Tests (Table 6). Results of periodic single peak overload tests for alloys 7075 and 7050 in the T6 and T7 tempers are plotted as a versus N in Figures 28 through 31, as average da/dN versus a in Figures 32 through 35, and as RR (the quotient of the crack growth rate for constant amplitude loading divided by the crack growth rate for spectrum loading at the same half crack length, a) versus a in Figures 36 through 39. Curves for da/dN and RR were not plotted below a half crack length of about 1.2 cm because the curve fitting process produced higher error near the origin. As discussed in Appendix A, replicate tests of 7075-T6 and 7050-T7 (OLR = 1.8 and OCR = 1:4000) showed good agreement.

For all materials, the results for the spectrum consisting of an overload 40% higher than the base applied every 4000 cycles (OLR = 1.4 and OCR = 1:4000) were comparable to results for the constant amplitude tests.

In the 1.8 overload ratio tests, crack growth rates ranged from as little as two to as much as about 140 times slower than for constant amplitude loading. Ranking

of materials in these spectra depended on occurrence ratio. With the 1:4000 occurrence ratio, alloy type had little effect, while lives of specimens in the T6 tempers were significantly longer than those in the T7 tempers. With the 1:8000 occurrence ratio, however, lives of alloy 7075 were significantly longer than lives of alloy 7050; moreover, lives of specimens in T7 tempers were longer than lives of those in T6 tempers.

Multi-Level Spectrum (Table 7). Results for the eight-level block loading sequence are given in Figures 40 and 41, respectively, as crack length vs number of elapsed load blocks and as crack growth per block, da/db vs crack length. Details of the eight-level loading sequence are described in Appendix A. Observed crack growth lives under the eight-level spectrum were estimated to be between one and two orders of magnitude longer than lives estimated by linear damage prediction (i.e., assuming no load interaction) from constant amplitude results. Thus, significant retardation was present in these tests.

Relative effect of alloy and temper on fatigue crack growth life under the eight-level spectrum was less significant than observed in constant amplitude and periodic single peak overload tests. Alloys 7075-T7 and 7050-T7 had equal lives. They were about 20% longer than life of 7050-T6 and about 40% longer than life of 7075-T6.

Effect of Composition Variants

Constant Amplitude Loading (Table 8). The constant amplitude results for the eight microstructural variants of alloys 7075 and 7050 in the T7-type temper are plotted as crack length vs number of elapsed cycles and as crack growth rate vs crack length in Figures 42a-b and 43a-b, respectively. Increasing Cu content and increasing purity increased lives and decreased crack growth rates. The Cu content had the largest effect, and purity had a smaller effect. No effect of dispersoid content was detected.

Spectrum Loading (Table 9). The spectrum consisting of an overload 80% above the base applied once every 8000 cycles (1.8 overload ratio and 1:8000 occurrence ratio) was selected to evaluate the eight microstructural variants because it was judged to be the most sensitive to microstructure. Test results are plotted as a vs N in Figure 44, as da/dN vs a in Figure 45, and as RR vs a in Figure 46.

At short crack lengths (a=1.2 cm), all alloys exhibited the same degree of retardation within a factor of about 2.5. At longer crack lengths, however, this factor increased to about 20.

For the 1.8 overload with occurrence ratio 1:8000, the general shape of the log RR vs a curves can be classified according to composition as follows:

Variants	Alloy Type from Table 1
Hi Purity, Hi Cu	7050 and Hi Cu 7475
Hi Purity, Lo Cu	Hi Purity 7010 and 7475
Lo Purity, Cr	7075 and Hi Cu 7075
Lo Purity, Zr	7010 and Lo Purity 7050

With exception of the pair of high purity, low Cu alloys, alloy pairs having log RR vs a curves of comparable shape exhibited similar degrees of retardation. Average difference in magnitude of RR for the high purity, low Cu alloy pair, however, was about three times larger than the average difference in RR for the other pairs.

Effects of Degree of Aging

Some effects of degree of aging were obtained from screening tests of 7075 and 7050 in T6 and T7 tempers (Table 6). Supplementary information was obtained from two additional overaged tempers of 7075 tested with 1.4 and 1.8 overload ratios and 1:4000 occurrence ratios (Table 10).

Results for the four tempers of 7075 are plotted as a vs N for the 1.4 and 1.8 overload ratios in Figures 47 and 48 and as da/dN vs a in Figures 49 and 50. Similar plots for 7050-T6 and T7 are presented in Figures 51 through 54.

The results are complex. Regardless of crack length, crack propagation performance of alloy 7075 in the

1.4 overload ratio tests increased progressively with increasing degree of overaging. Likewise, performance of 7050-T7 was superior to that of 7050-T6 for the same spectrum. In the 1.8 overload ratio tests, however, ranking of 7075 tempers depended on crack length, and performance did not change monotonically with degree of overaging at any crack length. Moreover, in contrast to the ranking in the 1.4 overload ratio tests, performance of 7050-T6 with the 1.8 overload was superior to that of 7050-T7.

Low-Power Optical Fractography

The fracture surfaces of the precracked specimens were examined using a low-power optical microscope. Observations of the surface markings correlated with the crack growth characteristics. Fractographs of 7075-T7 tested under all conditions and of all alloys in the T7 temper tested with 1.8 overload ratio and 1:8000 occurrence ratio were prepared to illustrate the salient features.

Macroscopic features of 7075-T7 fracture surfaces subjected to each loading sequence are shown in Figures 55a through 55e. The light and dark streaks discernible in the macrograph of the specimen tested with constant amplitude (Figure 55a) result from the interaction of the crack tip with different grains. In each of the specimens subjected to single periodic overloads (Figures 55b-d), the locations of the overload cycles are clearly visible. Further, the spacing of these overload markings correlates well with fatigue crack growth measurements. The overload markings

are more closely spaced and the crack fronts are more bell shaped on the specimens tested using an overload ratio of 1.8. At longer crack lengths and higher stress intensity factors, dark bands are noted which formed from local tearing during the overload cycle. Periodic markings were not visible on the specimen tested using the eight-level spectrum (Figure 55e). However, a greater amount of fretting was noted (black spots) on this fracture. The minimum stress of the eight-level test (2MPa) was significantly lower than minimum stress of all constant amplitude and periodic single peak overload tests (18.3 MPa).

The effects of changes in microstructure on macroscopic fracture appearance for materials tested using 1.8 overload ratio and 1:8000 occurrence ratio are illustrated in Figures 56a through h. Overload markings are visible on all fractures. Spacing between these marks is small when crack growth rate was high, and spacing is large when crack growth rate was low. The shape of the overload markings depends on crack length and also seems to correlate with growth rate. Samples exhibiting relatively slow growth rates are characterized by bell-shaped crack fronts, while the crack fronts of high growth rate samples tend to be more nearly linear. The dark bands marking the overloads become more prominent with increasing crack length (increasing stress intensity factor) and are decidedly wider in the low purity materials.

Scanning Electron Fractography

Scanning electron fractography was employed extensively in an attempt to determine fatigue crack growth mechanisms. In some cases, fractured specimens were sectioned at a plane inclined 45° with respect to the fracture surface and were metallographically polished to reveal sub-surface features.

Examination of specimens subjected to constant amplitude loading revealed commonly observed fracture topography. An example of the appearance of 7050-T7 is shown in Figure 57.

Samples tested using an overload ratio of 1:4 and occurrence ratio of 1:4000 were very similar in fracture appearance to samples tested in constant amplitude. The overload cycles appeared to have very little effect on crack growth. An example for 7050-T7 is presented in Figure 58. In 7075 samples, small amounts of tearing were noted in the overload vicinity at longer crack lengths.

In contrast to 1.4 overload ratio tests, fracture surface appearance of 1.8 overload ratio samples were drastically different from appearances of constant amplitude test specimens. Samples with an occurrence ratio of 1:4000 showed deep fissures at the overloads which were very closely spaced. The general appearance of the fractures was more regular and reminiscent of the fracture surface topography normally observed at much lower stress intensity. Sections

of the fracture surfaces also revealed large secondary cracks emanating from overload markings. An example for 7075-T6 is shown in Figure 59. Secondary cracks were also observed at longer crack lengths on the low purity materials tested with an occurrence ratio of 1:8000. These cracks were, again, associated with overload cycles. Examples of the fracture appearance and secondary cracks are shown in Figure 60 for 7075-T7.

At longer crack lengths, the high purity materials tested in overaged tempers using an overload ratio of 1.8 and an occurrence ratio of 1:8000 did not exhibit the features described above. Large fissures and numerous secondary cracks were not observed. Rather, the overloads produced stretched zones followed by changes in fracture topography which always decayed before the next overload cycle. Large changes in fracture surface topography as a consequence of the overload cycle were noted in 7475 (Figure 61). In contrast, very slight changes after overloads were observed in the fractures of the high purity alloy containing the Cu level of 7050 but with Cr (Figure 62). Intermediate amounts of fracture mode transition were noted in the remaining high purity alloys.

Interrupted Tests

Two separate interrupted test experiments were performed to elucidate microstructural influences on crack retardation. First, interrupted tests were conducted on 7075-T6 and 7050-T7 using the periodic single overload (1.8

overload ratio and 1:4000 occurrence ratio) which produced the most retardation. Then, interrupted tests were conducted on higher and lower purity versions of the high copper alloys containing Cr utilizing the spectrum used to evaluate the eight microstructural variants (1.8 overload ratio, 1:8000 occurence ratio).

Two specimens of 7075-T6 and two of 7050-T7 were tested using the 1.8 overload ratio and 1:4000 occurrence ratio. The tests were run to a half crack length of approximately 2.25 cm (shortly before the growth rate of 7075-T6 began to increase sharply and after the degree of retardation of 7050-T7 stabilized). One test on each alloy was interrupted immediately following the overload and one after an additional 2000 cycles. The specimens were examined on planes parallel to the rolled surface both near the specimen surface and at the quarter thickness (t/4) plane. Based on the examinations, the following observations were made:

1. Macroscopically, the crack was perpendicular to the stress axis, but microscopically it deviated (Figures 63a and b).

2. Periodic branching occurred (Figure 64) and the branches were associated with the large intermetallic particles such as Al_7Cu_2Fe (Figure 65). The magnitude of the branching was much greater in 7075-T6.

3. The specimens examined directly after the application of the overload exhibited localized deformation in

front of the crack tip which was directed toward the intermetallic particles (Figure 66).

4. This large, localized deformation region was absent in specimens tested for an additional 2000 cycles of constant amplitude after the overload. Multiple cracks were observed, but one eventually dominated.

Four specimens from the alloys containing high copper and chromium were chosen for the interrupted tests using the 1.8 overload ratio and 1:8000 occurrence ratio. Two test specimens were prepared from each purity variant to observe the effect of microstructure on the crack growth behavior at short and long crack lengths. The crack growth experiments were interrupted at approximately 1.75 and 2.75 cm crack lengths.

The crack growth panels were cut longitudinally through the center notch, and one half of the crack was prepared for metallographic examination. The specimens were polished into the direction of the crack growth by sectioning from the origin to the crack tip. Metallographic examinations were made along the way. Since the Al_7Cu_2Fe and Mg_2Si constituents can readily be seen in the as-polished condition, and etching tended to stain the polished surface, all photomicrographs presented are in the as-polished condition. The direction of crack growth is into the plane of the paper.

Figure 67 contains representative photomicrographs of the lower purity alloy variant at short crack lengths.

All along the crack front numerous secondary cracks were observed. Further, the major crack path was significantly altered by the presence of constituents. Figure 68 contains photomicrographs taken near the tip of the crack. The width of the crack is small, and the interaction of the crack with constituents can be more clearly identified. In general, the matrix-constituent interface was observed to separate, and the constituents did not fracture.

Figure 69 contains representative photomicrographs of the higher purity alloy variant at short crack lengths. These micrographs illustrate the direct contrast between the purity levels and crack front geometry. Few secondary cracks are present, and when they did occur constituent particles were generally present.

Figure 70 contains representative photomicrographs of the lower purity alloy from the specimen tested to a 2.75 cm crack length. Significant diversion of the crack front occurred, and in each case where the elevation in crack height was different, segregation of constituent was also present. This correlation indicates a causal relationship between constituent and crack tip geometry. In some cases, these micrographs also suggest that the matrix-particle interface has been separated.

In contrast, and as noted at the short crack length, very little deviation is observed along the crack front in the higher purity alloy (Figure 71).

DISCUSSION

Constant Amplitude Behavior

Constant amplitude fatigue crack growth resistance of these alloys at intermediate and high stress intensity factors are ranked according to temper and microstructure in Figures 72 and 73, respectively. Factors which increase resistance to stress-corrosion cracking, i.e., overaging and increasing Cu content, increased resistance to fatigue crack propagation at both intermediate and high stress intensity factors (ΔK=9 and 16 MPa$\sqrt{m}$, respectively). Overaging from a T6 to a T7 temper reduced crack growth rates by a factor of about 2-1/2 while increasing copper content from 1.6 to 2.3% reduced crack growth rate by about 35%. Increasing toughness by increasing purity (lowering Fe and Si) provided a 20% reduction in growth rate at the high ΔK, but had little effect at intermediate ΔK. The effect of dispersoid was considered to be insignificant at both ΔK levels. The above results are consistent with findings of other investigations [1-5,22], but also provide additional information. Previous work demonstrated that resistance to fatigue crack growth increased as Cu content increased from 1% to 2.3%, but did not determine whether the benefit was possible with an increase to an amount less than 2.3%. The current work reveals that an increase in Cu content from 1.6 to 2.3% provides a definite increase in resistance to fatigue crack growth.

Variable Amplitude Behavior

Crack Growth Retardation

Although not detectable by the techniques used in this work, other investigators have demonstrated that crack growth rate either immediately or shortly after the application of a tensile overload progressively decreases to a minimum rate, then tends to increase to what it would have been if no overload had been introduced. This phenomenon is attributed to the effect of the tensile overload on reducing effective ΔK to a lower level in a region ahead of the crack. When a second overload is introduced while the crack is still under the influence of the preceding overload, the amount of retardation may be greater than if the second overload were introduced after the crack has grown out of this influence.

Results of this and other investigations [5,8-10] indicate that ranking of crack growth resistance under constant and variable amplitude loading may be different depending on the alloy and spectrum selected. For example, Figure 74 summarizes crack propagation lives obtained in this study for 7075 and 7050 alloys tested under constant amplitude and periodic single peak overload conditions. For the 40% overload applied once every 4000 cycles, the relative amount of retardation was small over the total life of the specimens, and the actual lives, e.g., the ranking of alloy performance, were essentially unchanged from the constant

amplitude results. When the magnitude of the overload ratio was increased to 1.8, however, crack growth retardation and hence, life increased significantly. Ranking of alloy performance did not conform with constant amplitude rating, and also depended on the overload occurrence ratio. The reversals in rating of alloy performance illustrated by the above example suggest competing crack growth processes which are dependent upon alloy and load history.

Several investigators [7,12,19-21,23] have demonstrated a degree of success in relating plastic zone dimensions to overload induced crack growth retarding. Most notably, there appears to be general agreement that the distance of crack travel affected by a prior overload is dependent upon the size of the plastic zone created by the maximum tensile stress of the overload. A basic hypothesis of these investigations is that crack growth is retarded when the crack tip plus plastic zone corresponding to peak stresses of baseline cycles is embedded within the larger monotonic plastic zone developed at peak tensile stress of the previous overload. In some materials, maximum retardation (the slowest rate of crack growth) does not occur immediately after the overload, but occurs only after the crack has progressed a short distance from the point of the overload [19-21].

Trebules has hypothesized [20] that the distance of crack extension required to produce the maximum retardation

is related to dimensions of the reversed plastic zone developed upon unloading from the peak overload stress. The reversed plastic zone corresponds to the region adjacent to the crack tip which undergoes intensive tension-to-compression plastic deformation during each load-unload excursion [24]. The reversed plastic zone is always embedded with a larger zone of tensile plastic deformation created at peak cyclic stress and which undergoes monotonic plastic deformation upon tension loading, but experiences only elastic deformation upon unloading.

With this experience in mind, Figures 75 and 76 were plotted to obtain a relative estimate of the size of the crack growth increment between periodic single overload cycles (da/dB) with respect to estimated monotonic and reversed plastic zone sizes developed during the overload cycle. Plastic zone size estimates were made following assumptions of Irwin [25] for the tensile plastic zone and Rice [26] for the reversed plastic zone. Figure 75 shows for the 1.4 overload ratio, 1:4000 occurrence ratio that the increment of crack extension per block, da/dB, for each material always exceeded the estimated monotonic plastic zone size corresponding to the maximum peak stress of the overload. That is, the crack always grew out of the plastic zone of the previous overload prior to the application of the next overload.

For the same occurrence ratio but with overload ratio of 1.8, the increment of crack growth between overload

cycles was far less than the estimated monotonic plastic zone size, and was also less than the estimated reversed plastic zone size for the majority of the test in all materials. A similar plot for the 1.8 overload ratio and occurrence ratio of 1:8000 is shown in Figure 76. Crack extension per block for alloy 7050-T6, which had the shortest life for this loading sequence, always exceeded the estimated monotonic plastic zone size. On the other hand, alloy 7075-T7 which had the longest life under this loading sequence grew the smallest fraction of the estimated monotonic plastic zone size per block.

Computations for the eight-level block spectrum (described in Appendix A) were made for the same alloys. These computations indicated that crack extension for all four alloys was always embedded within the estimated reversed plastic zone associated with the peak overload cycles which occurred once every 2000 cycles.

Effects of Microstructure

Current crack growth prediction models based on fracture mechanics do not consider microstructure-loading interactions. Material differences in these models are basically accounted for by constant amplitude crack growth rate information and tensile and fracture toughness properties. Several models [12-14,27-29] relate retardation to a system of residual forces derived from plastic deformations created by the overload. In general, these models assume that

effective ΔK decreases with increasing magnitude of plastic deformation introduced by the overload with respect to the plastic deformations introduced during the baseline cycles at lower magnitude stress. Local crack tip plastic deformations are generally treated by considering a symbolic plastic zone size which is proportional to the square of the quotient of applied stress intensity divided by yield strength. Thus, these models, in general, predict that degree of retardation increases with decreasing yield strength.

To demonstrate that plastic zone interaction models alone cannot completely explain our results, the computer program, EFFGRO, based on the Vroman retardation model [14], was used to predict the a vs N curves for 7075-T7 and 7050-T7 in the 1.8 overload ratio, 1:8000 occurrence ratio tests. Results of the EFFGRO analysis underestimated life; in some cases, predicted life was over 50 times shorter than observed. Moreover, 7050-T7-type alloys were predicted to be superior to 7075-T7-type alloys in this spectrum when, in fact, life of 7075-T7-type alloys was superior by factors of two or more. Similarly, for the same overload ratio but with occurrence ratio of 1:4000, the same model would predict longer lives for 7050 and 7075 alloys in the T7 temper, when, in fact, lives were significantly greater for the same alloys in T6 tempers. The EFFGRO predictions are summarized in more detail in Appendix C.

The differences in degree of retardation exhibited by these examples cannot be completely explained by current

fracture mechanics based retardation models since they all neglect microstructural effects. The observations in this investigation, however, reveal that microstructure, particularly coarse, intermetallic constituent particles, plays a major role in retardation under our test conditions. The constituents near the crack tip separated from the matrix when the overload was applied, and introduced secondary cracks into the matrix. These secondary cracks absorbed some of the elastic strain energy during the subsequent constant amplitude cycles, thus lowering the effective ΔK at the front of the main crack. With a lower effective ΔK, the crack advanced at a lower rate during the following constant amplitude cycles.

The variety of shapes of the log RR vs a curves in this investigation is attributed to the competing effects of many factors. The simplest case is the spectrum consisting of 1.4 overload ratio and 1:4000 occurrence ratio. The magnitude of the overloads was so low and their occurrence so infrequent that the crack growth increment during intermittent cycles affected by the overload was negligible compared with the crack growth occurring between overloads. Hence, the overloads acted as isolated events, and retardation was insignificant over the life of the specimen. This is consistent with the relative crack growth to plastic zone size comparison of Figure 76.

When the overload ratio was 1.8 or higher, however, the overloads no longer acted as isolated events. The

crack tip region affected by the overload was such that occurrence ratio, level of effective ΔK, and crack growth rate at particular levels of effective ΔK produced a wide range of results because of the relative interaction between overloads.

The shapes of the log RR vs a curves in this investigation can be explained with the help of the schematic diagram in Figure 77. Region A represents the case where insufficient cycles occur between overloads for the crack to grow out of the influence of the preceding overload. The affected crack length under the influence of the preceding overload increases with increasing crack length because of the increase in stress intensity factor. When this increase in the region of influence is accompanied by an increase in crack growth rate that is insufficient to allow the crack to grow out of the influence of the preceding overload, the crack may remain in region A for the entire test. An example of this phenomenon is 7050-T7 tested with 1.8 overload ratio and 1:4000 occurrence ratio (Figures 39 and 75).

With a higher occurrence ratio of 1:8000, 7050-T7 (and the other high purity, high Cu alloy in the T7 temper) exhibited log RR vs a curves which started out in Region A and then advanced to Region B. As shown in Figure 76, the latter behavior can be explained by considering that, when the crack reached a sufficient length, it was able to grow out of the influence of the preceding overload before the next one was applied. In contrast, the 7050-T6 tested with

the 1:8000 occurrence ratio began in Region B as suggested by Figure 76. This behavior is attributed to the faster crack growth rate of 7050-T6 relative to 7050-T7 during the constant amplitude cycles. Note that the only test conditions in which the retardation of 7050-T7 exceeded that of 7050-T6 was with 1.8 overload ratio, 1:8000 occurrence ratio, and short crack lengths (low nominal ΔK where particle cracking would be minimal).

The behavior of the high purity alloys containing the lower level of Cu was more complex and correlated with relative strength and toughness. The alloy containing Zr (lower strength, high toughness) appeared to be coming out of Region A and progressing into Region B as the test began. Plastic zone estimates for this alloy indicated that the increment of crack extension between applied overloads approximately equaled the overload plastic zone size at short crack lengths. At long crack lengths, the crack growth increment per block more than doubled the overload plastic zone size. On the other hand, the alloy containing Cr (higher strength, lower toughness) appeared to stay in Region A for the entire test. The crack growth increment per block for this alloy never exceeded one-half the computed overload plastic zone size at any crack length. Retardation life analysis of all alloys based on consideration of yield strength and energy to propagate a crack in a tear test will be discussed in a later section of this report.

Behavior of the lower purity alloys was different. Degree of retardation of 7075-T6 and 7075-T7 tested with the 1.8 overload ratio and both 1:4000 and 1:8000 occurrence ratios initially increased with increasing crack length (Region C). At longer crack lengths, the degree of retardation either increased at a lower rate, decreased slightly, or decreased sharply (Region D). The initial increase in RR is attributed to the progressively large influence of constituent particles on the crack path. In these materials, the crack front was decidedly nonplanar. Instead of advancing on a plane perpendicular to the applied stress, the crack both through and along the thickness was diverted by being attracted to regions of concentrations of coarse constituent particles. This crack deviation would reduce the rate of macroscopic crack growth measured by the crack propagation gauge. In addition, the portion of the crack near the surfaces began to lag the portion of the crack in the interior of the specimen of materials exhibiting the crack deviation. Because the crack propagation gauge measured crack length at the surfaces, the crack front curvature would accentuate the degree of retardation.

The change in slope of the log RR vs a curves at long crack length is attributed to an acceleration of crack growth during the tensile overload. This effect is most noticeable on the lowest toughness material (7075-T6) tested with 1.8 overload ratio and 1:4000 occurrence ratio (Figure

75). With this high frequency of occurrence, the acceleration from the overload would begin to progressively offset the retardation occurring during the constant amplitude cycles. The low purity alloys which contained Zr never entered Region D. The higher toughness of these alloys relative to their counterparts which contained Cr probably limited rapid growth during the overloads at the long crack lengths.

The insensitivity of 7075-T7 to occurrence ratio is attributed to the low crack growth rate during the constant amplitude cycles. Even with 1:8000 occurrence ratio, the crack could not grow out of the influence of an overload before the next one was applied (Figure 76).

Degree of retardation of 7075-T7 never exceeded that of 7075-T6. Extrapolations of the 1.8 overload ratio, 1:8000 occurrence ratio tests to very short cracks, however, suggests that the lower strength material may exhibit a higher degree of retardation when the nominal ΔK is lower.

Correlation with Monotonic Properties

Qualitative analysis of the log RR vs a curves for the eight microstructural variants of alloys 7075 and 7050 revealed that features which affected toughness had the strongest effect on curve shape. Yield strength also had a large effect. In an effort to further quantify these observations, an analysis of the data for the eight alloys in the T7 temper tested using the 1.8 overload ratio and 1:8000 occurrence ratio was performed.

The effects of yield strength and unit propagation energy on cyclic retardation life were analyzed empirically using multiple regression techniques. Retardation life (L_R) is defined as number of cycles to grow the crack from 1.2 to 3.0 cm during spectrum testing minus number of cycles to grow the crack the same distance during constant amplitude testing. Initially, a model using linear, squared, and interaction terms was explored. Based on statistical analysis of the regression coefficients, the model was revised to include only UPE, YS^2 and UPE·YS terms. The final form of the least squares solution was:

$$L_R = 3.9581\text{x}10^5 + \{-4.9617\text{x}10^3(\text{UPE}-75)\} + \{-2.5494\text{x}10^2(\text{YS}-445)(\text{YS}-445)\} + \{-7.11582\text{x}10^2(\text{UPE}-75)(\text{YS}-445)\}.$$

This model is capable of accounting for 96.9% of the observed variation in L_R. However, because this model is strictly empirical, it is only useful for illustration of the trends observed in this work. It should not be used for prediction and may not be appropriate for other materials or spectra.

The predictions of the model are presented in contour plot form in Figure 78. Two regions of behavior can be identified in this figure. At UPE's above 75 KJ/m^2, which includes all higher purity materials, increasing yield strength decreased retardation life. Below this value (lower purity material), increasing yield strength increased retardation life. Yield strength had a greater effect at higher UPE's. Decreasing UPE increased life regardless of

yield, but the effect was much stronger at higher strengths and approached 0 at 435 MPa. Although not included in the statistical analysis, the results for the T6 tempers of 7075 and 7050 are consistent with the trends described above. Retardation life of 7050-T7 was much longer than that of 7050-T6 (higher purity) and retardation lives of 7075-T6 and T7 (lower purity) were about equal.

Degree of Overaging

The superior performance of 7XXX-T7 compared to that of 7XXX-T6 in constant amplitude tests has been observed before [1,2]. A recent experiment [1] clearly demonstrated that at least part of the difference is due to a micro-structure-environment interaction. Resistance to fatigue crack growth of underaged, peak aged, and overaged specimens of alloy 7050 progressively increased with degree of aging, regardless of yield strength or toughness. Moreover, the magnitude of the increase was greater in high humidity air than in low humidity air. Based on this experimental evidence, the increased fatigue crack propagation performance with decreasing strength of alloys in this investigation, when tested either under constant amplitude or 1.4 overload ratio loading, is attributed to the same effect of increased aging progressively improving the resistance to the water vapor in the environment.

The monotonic increase in crack growth performance with increasing degree of overaging (decreasing yield strength)

was not generally observed in the tests with the higher overloads. Evidence of a nonmonotonic effect of yield strength on crack growth performance in a flight simulation spectrum loading test has been reported previously [10]. In the referenced investigation, crack propagation life of 7050 heat treated in a variety of ways (strength was modified by decreasing quench rate and by overaging) initially increased with decreasing strength, but then decreased at intermediate strength levels before it began to increase again (Figure 79). Similar analysis for alloy 7075 tested with 1.8 overload ratio and 1:4000 occurrence ratio suggested that this behavior could be reproduced under certain simple spectrum conditions (Figure 80). For short cracks, life decreased with decreasing yield strength before it began to increase with more drastic degrees of overaging. For longer cracks, the limited data suggest that the behavior was similar to that of 7050 in the flight simulation spectrum.

These results can be explained with the help of the diagram in Figure 81. In Region I, crack growth rate is dominated by effects of environment, so performance ranking is the same as in constant amplitude tests. When the overload is low, the crack is short, or the applied stress is low (low nominal stress intensity), even peak aged material will remain in this region. With higher stress intensity spectrum tests, however, constituent particles begin either to fracture or to separate from the matrix during the overload cycle. This produces a decrease in crack growth rate

during the lower amplitude cycles because the secondary cracks reduce effective ΔK at the main crack front as discussed previously. Severity of these secondary cracks during the overload decreases as strength increases because UPE decreases. Consequently, effective ΔK decreases, degree of retardation increases, and fatigue crack propagation life begins to increase with increasing yield strength (Region II). With spectrum tests at even higher stress intensities, the crack can advance appreciably during the overload in low toughness material. Consequently, life will again begin to decrease with increasing yield strength (Region III) because of the concomitant decrease in UPE.

CONCLUSIONS

1. Ranking of 7XXX aluminum alloy fatigue crack growth resistance under variable amplitude loading may be quite different than ranking under constant amplitude loading. The ranking is sensitive to loading parameters such as overload magnitudes, spacings, and nominal stress intensity levels. Alloys of comparable strength but with variations in microstructures may possess significant differences (order of magnitude in some cases) in ability to retard crack growth under certain spectra.

2. Retardation characteristics of 7XXX alloys depend on several competing mechanisms. In any one instance, the mechanism(s) which dominate depend upon the interaction of

loading conditions and microstructure. Different mechanisms may also dominate different stages of a test (i.e., short crack vs long crack) depending on the relative stress intensity factor levels applied.

3. Strength and toughness do not consistently correlate with fatigue crack growth resistance because retardation characteristics depend on the particular microstructure-load-environment interaction mechanism which dominates. The ability to rank materials and/or predict fatigue crack growth lives under variable amplitude loading based on these properties will continue to be limited unless the dominant retardation mechanism is known for the particular application.

4. Higher Cu content and overaging modify the η' precipitate and decrease crack growth rate at least in part by increasing resistance to water vapor in the environment. This attribute is most useful in constant amplitude loading and in spectrum loading with either low level overloads, high level overloads infrequently spaced, or low nominal stress intensities. Consequently, performance of alloy 7050 is superior to that of alloys 7075, 7475, and 7010, and performance of T7 tempers is superior to that of T6 under these conditions.

5. Coarse, intermetallic constituent particles and $Al_{12}Mg_2Cr$ dispersoids aid in initiating and propagating secondary cracks during high level tensile overloads. These secondary cracks lower effective stress intensity at the

main crack front and thereby retard its growth during subsequent low level cycles. Alloy 7075 with a higher volume of constituent particles than alloy 7050 and containing $Al_{12}Mg_2Cr$ dispersoids has superior crack growth characteristics under simple spectrum loading with high nominal stress intensities when high level tensile overloads are frequently applied.

6. Overaging progressively decreases strength and increases toughness as well as increasing resistance to environmental factors. The increased toughness has both positive and negative effects in spectrum loading. It decreases the severity of the secondary cracks during high level overloads, and thus has a negative effect on retardation during subsequent low level cycles. It decreases the growth of the main crack during the overloads, however, and thus has a positive effect. The controlling mechanism depends on the alloy composition and spectrum selected. As a generality, peak strength (T6) aging should provide superior performance in simple spectrum loading where the ratio of the tensile overloads to the base is high and stress intensity is moderate. Overaged T7 tempers should provide superior performance where the stress intensity is high and tensile overloads are frequent.

7. In simple spectra with low nominal stress intensities and in complex spectra, effects of the differences

in microstructure between alloys 7075 and 7050 and between peak strength and overaged precipitates compete. Consequently, differences among variants of alloys 7075 and 7050 and among T6, T76, T736, and T73 tempers may be either insignificant or large, so relative ranking of alloy and temper differs from spectrum to spectrum.

RECOMMENDED FUTURE WORK

From this investigation and previous work, the constant amplitude fatigue crack growth response to variation in 7XXX aluminum alloy microstructure has been reasonably well characterized in the intermediate and high crack growth rate regions. This characterization, however, is rather limited at low rates of crack growth which approach an apparent fatigue threshold. The latter limitation is caused by the scarcity of data in the low growth rate region due to the relatively long time and high expense of testing. Previous work has indicated that certain aspects of aluminum alloy microstructure which control in one crack growth rate region do not necessarily control in another region. That is, a specific microstructural feature may exert dominant influence only over a segment of the fatigue crack growth (log da/dN vs log ΔK) relationship. Since, in many applications, the greatest portion of component life is spent in propagation of very small flaws at slow rates, future work should consider characterization of effects of microstructure in the low crack growth rate region. This characterization

is particularly pertinent to consideration of crack growth delay effects attributed to reduction in effective stress intensity factor at the crack tip by a previous overload.

Present crack growth models do not address effects of microstructure-load-environment interactions. Trends observed in data suggest limitations in models which utilize constant amplitude data for a material(s) data base and predict retardation based solely on plastic zone or yield strength consideration. Work is needed to appropriately introduce aspects of alloy microstructure into these models. For example, the excellent correlation of retardation life with yield strength and UPE (toughness) for a particular load spectra and environment suggests that, within a limited range of alloy compositions and fabrication practices, microstructure can be characterized by monotonic properties to a degree sufficient to be used in quantitative life predictions.

Additional work is needed, however, to verify that monotonic properties adequately correlate with microstructural features which control retardation mechanisms which operate during the component lifetime. Having the ability to incorporate microstructure into flaw growth prediction methodology would simplify and improve cost effectiveness of alloy selection because fewer verification tests would be needed. In addition, alloy and temper could be designed to have optimum fatigue performance for applications where either improvements in performance or savings

in weight could justify the development and production of such specialty materials.

It was demonstrated in this work that the specific microstructural features of 7XXX aluminum alloys which control the magnitude of crack growth retardation are dependent on the type of retardation mechanism operating at the crack tip. For example, when retardation mechanisms are dominated by ductility of material at the crack tip or by factors which increase resistance to environmental attack, specific microstructural features which control crack growth delay differ from those microstructural features which control crack growth retardation by secondary cracking and crack front bifurcation mechanisms. Thus, the understanding gained from this investigation may be utilized to optimize 7XXX aluminum alloy microstructure to provide maximum crack growth retardation if the overriding crack growth retardation mechanism is known. The controlling crack growth mechanisms, however, are influenced by the load history, e.g., magnitude and sequence of the overloads. A missing link to this alloy optimization process is the ability to reliably predict the governing crack growth mechanism(s) that will be operating for a particular application and loading sequence. Additional work is needed to relate component usage, e.g., stress history, environment, and flaw distributions (size) to dominant crack growth mechanisms. Development and use of certain forms of standardized reference load spectra for

rating alloy performance could be useful for this purpose. Fractographic examinations of fractures from these tests will also help.

The work of this investigation was restricted to a particular alloy system and environment. Extending this investigation to alternate alloy systems and environments is believed to be important. In particular, work on 2024-type alloys and the new powder metallurgy Al-Zn-Mg-Cu-Co alloys is recommended.

REFERENCES

1. W. G. Truckner, J. T. Staley, R. J. Bucci, and A. B. Thakker, "Effects of Microstructure on Fatigue Crack Growth of High-Strength Aluminum Alloys." USAF Technical Report AFML-TR-76-169, October 1976.

2. J. T. Staley, W. G. Truckner, R. J. Bucci, and A. B. Thakker, "Improving Fatigue Resistance of Aluminum Aircraft Alloys," WESTEC 77 Paper No. 3, American Society of Metals, Metals Park, Ohio, 1977.

3. D. J. Brownhill, R. E. Davies, G. E. Nordmark, and B. M. Ponchel, "Exploratory Development for Design Data on Structural Aluminum Alloys in Representative Aircraft Environments," USAF Technical Report AFML-TR-77-102, 1977.

4. R. L. Jones and T. E. Coyle, "The Mechanical, Stress-Corrosion, Fracture Mechanics, and Fatigue Properties of 7050, 7475, and Ti-8 Mo-8 V-2 Fe-3 Al Plate and Sheet Alloys," General Dynamics Fort Worth Division Report FGT-5791, 1976.

5. E. A. Lauchner, "Alloy Selection for a Military Fighter Aircraft," Northrup Corporation Aircraft Division, Report NOR-75-147, October 1975.

6. Fatigue Crack Growth Under Spectrum Loads, Proceedings of Symposium presented at 78th Annual Meeting of American Society for Testing and Materials, ASTM STP 595, 1976.

7. H. A. Wood, "The Use of Fracture Mechanics Principles in the Design and Analysis of Damage Tolerant Aircraft Structures," AGARDograph No. 176, November 1973.

8. R. J. Bucci, "Spectrum Loading - A Useful Tool to Screen Effects of Microstructure on Fatigue Crack Growth Resistance," ASTM STP 631, 1977, pp 388-401.

9. K. O. Sippel and D. Weisgerber, "Crack Propagation in Flight by Flight Tests on Different Materials," presented at the 1975 International Conference on Aeronautical Fatigue, Lausanne, 5 June 1977.

10. L. Schra and H. P. VanLeeuwen, "Heat Treatment Studies of Aluminum Alloy Type 7050 Forgings," Interim Report No. 2, NLR-TR-76008C, National Aerospace Lab, NLR the Netherlands, 1976.

11. Private Communication, McDonnell Douglas Corporation, on Data of Spectrum Fatigue Testing of 7075-T7351 and 7050-T73651 Plate, March 1975.

12. O. E. Wheeler, "Crack Growth Under Spectrum Loading," Journal of Basic Engineering Transactions, ASME, March 1972, pp 181-186.

13. J. Willenborg, R. M. Engle, and H. A. Wood, "A Crack Growth Retardation Model Using an Effective Stress Concept," USAF Technical Report TM-71-1-FBR, January 1971.

14. G. Vroman, "Analytical Prediction of Crack Growth Retardation Using a Critical Stress Intensity Concept," North American Rockwell, Los Angeles Division, Technical Report TFR 71-701, 1971.

15. H. A. Wood, J. P. Gallagher, R. M. Engle, and J. M. Potter, "Current Practice on Estimating Crack Growth Damage Accumulation with Specific Application to Structural Safety, Durability and Reliability," USAF Technical Report, AFFDL-TR-75-32, January 1976.

16. G. R. Chanani, "Fundamental Investigation of Fatigue Crack Growth Retardation in Aluminum Alloys," USAF Technical Report AFML-TR-76-156, September 1976.

17. W. S. Johnson and J. W. Hagemeyer, "Yield Strength Considerations for Selecting Material Subjected to Spectrum Loads," International Journal of Fracture Mechanics, May 1977.

18. J. C. Ekvall, Correspondence, 1976 August 18 to ASTM E09.05 Task Group Development of Reference Test Spectra.

19. E. F. J. von Euw, R. W. Hertzberg, and R. Roberts, "Delay Effects in Fatigue Crack Propagation," ASTM STP513, 1972, p 230.

20. V. W. Trebules, R. Roberts, and R. W. Hertzberg, "Effect of Multiple Overloads on Fatigue Crack Propagation in 2024-T3 Aluminum Alloy," ASTM STP536, 1973, pp 115-146.

21. W. J. Mills, "Load Interaction Effects on Fatigue Crack Growth in 2024-T3 Aluminum and A514 Steel Alloys, Ph.D. Dissertation, Lehigh University, November 1975.

22. R. E. Jones and K. A. Fudge, "Engineering Design Data for Aluminum Alloy 7050-T73651 Plate," USAF Technical Report AFML-TR-73-269, November 1973.

23. J. Lankford, D. L. Davidson, and T. S. Cook, "Fatigue Crack Tip Plasticity," Presented at ASTM E-9 Syposium on Cyclic Stress-Strain and Plastic Deformation Aspects of Fatigue Crack Growth, May 1976.

24. P. C. Paris, "The Fracture Mechanics Approach to Fatigue," in Fatigue--An Interdisciplinary Approach, Syracuse University Press, 1964.

25. G. R. Irwin, "Plastic Zone Near a Crack and Fracture Toughness," Proceedings of Seventh Sagamore Ordnance Materials Research Conference, Syracuse University Research Institute, August 1960.

26. J. R. Rice, "The Mechanics of Crack Tip Deformation," ASTM STP415, 1967.

27. W. Elber, "The Significance of Fatigue Crack Closure," ASTM STP486, 1971, pp 230-242.

28. P. D. Bell and A. Wolfman, "Mathematical Modeling of Crack Growth Interaction Effects," ASTM STP595, 1976, pp 306-317.

29. H. D. Dill and C. R. Saff, "Spectrum Crack Growth Prediction Method Based on Crack Surface Displacement and Contact Analysis," ASTM STP595, 1976, pp 306-317.

30. R. P. Wei, "Some Aspects of Environment Enhanced Fatigue-Crack Growth," Engineering Fracture Mechanics, Vol 1, No. 4, April 1970, p 633.

31. J. Schijue, "Fatigue Damage Accumulation and Incompatible Crack Front Orientation," Engineering Fracture Mechanics, Vol 6, 1976, pp 245-252.

32. T. T. Shih and R. P. Wei, "Effect of Specimen Thickness on Delay in Fatigue Crack Growth, Journal of Testing and Evaluation, 1974.

33. ASTM Method E399-74, "Standard Test Method for Plain Strain Fracture Toughness of Metallic Materials, 1977 Annual Book of ASTM Standards, Part 10, pp 505-524.

TABLE 1. REMELT CHEMICAL ANALYSES

S. No.	Alloy Type	Composition (weight percent)							
		Si	Fe	Cu	Zr	Cr	Mg	Zn	Ti
454542	Hi purity 7010	0.06	0.10	1.56	0.12	0.00	2.19	6.20	0.02
454547	7010	0.19	0.27	1.55	0.12	0.00	2.22	5.96	0.03
454545	7475	0.06	0.11	1.46	0.00	0.21	2.09	5.90	0.02
454549	7075	0.23	0.28	1.51	0.00	0.23	2.26	6.34	0.02
454543	7050	0.07	0.11	2.10	0.13	0.00	2.16	6.16	0.02
454548	Lo purity 7050	0.19	0.28	2.16	0.11	0.01	2.18	5.83	0.02
454546	Hi Cu 7475	0.06	0.11	2.27	0.00	0.21	2.08	5.90	0.02
454551	Hi Cu 7075	0.23	0.28	2.29	0.00	0.20	2.23	6.13	0.02

TABLE 2. HEAT TREATMENTS

S. No.	Alloy Type	Temper Type	Aging Practice
454542	Hi purity 7010	T7	24 hr 121°C+37 hr 163°C
454547	7010	T7	24 hr 121°C+24 hr 163°C
454545	7475	T7	24 hr 121°C+21 hr 163°C
454549	7075	T7	24 hr 121°C+12 hr 163°C
454543	7050	T7	24 hr 121°C+40 hr 163°C
454548	Lo purity 7050	T7	24 hr 121°C+32 hr 163°C
454546	Hi Cu 7475	T7	24 hr 121°C+18 hr 163°C
454551	Hi Cu 7075	T7	24 hr 121°C+24 hr 163°C
454550	7075	T6	24 hr 121°C
438642-1	7075	T76	24 hr 121°C+6 hr 163°C
438642-2	7075	T73	24 hr 121°C+24 hr 163°C
454544	7050	T6	100 hr 121°C

SHT - 2 hr 488°C, quench in water at room temperature, stretch 1-1/2%.

TABLE 3. CONSTITUENT AND DISPERSOID PHASES IDENTIFIED BY GUINIER-deWOLFF X-RAY DIFFRACTION

S. No.	Alloy Type	Mg_2Si	Al_7Cu_2Fe β(Al-Cu-Fe)	$Al_{12}Mg_2Cr$ E	Al_2CuMg S	$(Fe,Cu)Al_6$ α(Al-Cu-Fe)
454542	Hi purity 7010	sml	sml	--	--	--
454547	7010	med	med	--	--	--
454545	7475	sml	sml	med	poss.trace	poss.trace
454549	7075	med	med	med	poss.trace	trace
454543	7050	sml	sml	--	--	--
454548	Lo purity 7050	med	med	--	poss.trace	--
454546	Hi Cu 7475	sml	sml	med	--	--
454551	Hi Cu 7075	med	med	med	poss.trace	--

TABLE 4. LONGITUDINAL MECHANICAL PROPERTIES OF 6.4 mm (0.25 in.) 7XXX PLATE

Alloy Type and Temper	S. No.	Tensile Strength, MPa	Tensile Strength, ksi	Yield Strength, MPa	Yield Strength, ksi	El., %	TrS/YS	Unit Propagation Energy in.lb/in.^{2}	Unit Propagation Energy KJ/M^2
Hi purity 7010-T7	454542	517	75.0	454	65.9	13	1.45	595	105
7010-T7	454547	490	71.1	435	63.1	11.5	1.28	380	66.5
7475-T7	454545	505	73.2	441	64.0	13	1.38	510	89.5
7075-T7	454549	505	73.2	454	65.8	11	1.16	280	49.0
7050-T7	454543	511	74.1	440	63.8	14	1.46	645	115
Lo purity 7050-T7	454548	496	71.9	435	63.1	12	1.29	385	67.5
Hi Cu 7475-T7	454546	532	77.1	470	68.1	12	1.32	450	79.0
Hi Cu 7075-T7	454551	505	73.3	446	64.7	11.5	1.19	270	47.5
7075-T6	454550	558	81.0	530	76.9	9.5	1.02	200	35.0
7075-T76	438642-1	546	79.2	507	73.6	11	1.16	280	49.0
7075-T73	438642-2	484	70.2	417	60.5	12	1.24	260	46.0
7050-T6	454544	612	88.7	570	82.7	12	1.19	545	95.5

TABLE 5

RESULTS OF CONSTANT AMPLITUDE LOADING FATIGUE CRACK GROWTH TESTS[+] OF ALLOY 7050 AND 7075 IN T6- AND T7-TYPE TEMPERS

Alloy Type and Temper	Life* (Cycles)	Crack Growth Rate da/dN (cm/cycle) at 1.5 cm	2.2 cm	3.0 cm
7050-T6	56 000	2.45×10^{-5}	4.75×10^{-5}	1.05×10^{-4}
7050-T7	136 000	1.12×10^{-5}	2.00×10^{-5}	4.70×10^{-5}
7075-T6	36 000	4.00×10^{-5}	8.20×10^{-5}	1.90×10^{-4}
7075-T7	92 000	1.53×10^{-5}	3.30×10^{-5}	6.70×10^{-5}

[+]Relative humidity >90% for all tests.

*Crack propagation life from half crack length of 1.02 cm to 3.3 cm.

TABLE 6

RESULTS OF PERIODIC OVERLOAD FATIGUE CRACK GROWTH TESTS+ OF ALLOYS 7050 AND 7075 IN T6- AND T7-TYPE TEMPERS

Alloy Type and Temper	Spectrum		Life*		Crack Growth Rate da/dN (cm/cycle) at		
	OLR	OCR	Blocks	Cycles	1.5 cm	2.2 cm	3.0 cm
7050-T6	1.4	1:4000	19	76 000	2.00×10^{-5}	4.60×10^{-5}	---
7050-T7			38	152 000	1.15×10^{-5}	2.05×10^{-5}	5.00×10^{-5}
7075-T6			9	36 000	4.50×10^{-5}	7.20×10^{-5}	1.45×10^{-4}
7075-T7			23	92 000	1.65×10^{-5}	3.50×10^{-5}	6.90×10^{-5}
7050-T6	1.8	1:4000	484	1 936 500	7.00×10^{-7}	1.70×10^{-6}	2.90×10^{-6}
7050-T7			210	840 200	2.17×10^{-6}	2.28×10^{-6}	4.30×10^{-6}
7075-T6			485	1 940 500	8.10×10^{-7}	1.00×10^{-6}	---
7075-T7			279	1 116 300	1.50×10^{-6}	2.25×10^{-6}	4.00×10^{-6}
7050-T6	1.8	1:8000	14	112 000	1.40×10^{-5}	3.20×10^{-5}	6.20×10^{-5}
7050-T7			62	496 100	1.95×10^{-6}	1.05×10^{-5}	2.20×10^{-5}
7075-T6			100	800 100	5.00×10^{-6}	2.50×10^{-6}	2.00×10^{-6}
7075-T7			128	1 024 100	2.12×10^{-6}	2.40×10^{-6}	3.00×10^{-6}

+Relative humidity >90% for all tests.

*Crack propagation life from half crack length of 1.02 cm to 3.3 cm.

TABLE 7

RESULTS OF EIGHT LEVEL BLOCK SPECTRUM* FATIGUE CRACK GROWTH TESTS** OF ALLOYS 7050 AND 7075 IN T6- AND T7-TYPE TEMPERS

Alloy Type and Temper	Life+		Crack Growth Rate da/dN (cm/cycle) at		
	Blocks	Cycles	1.5cm	2.2 cm	3.0 cm
7050-T6	1458	2 916 000	5.50×10^{-7}	9.00×10^{-7}	1.45×10^{-6}
7050-T7	1802	3 604 000	4.40×10^{-7}	7.20×10^{-6}	1.40×10^{-6}
7075-T6	1143	2 286 000	6.20×10^{-7}	1.45×10^{-7}	3.50×10^{-6}
7075-T7	1789	3 578 000	2.30×10^{-7}	7.40×10^{-7}	1.70×10^{-6}

*Refer to Appendix A.

**Relative humidity >90% for all tests.

+Crack propagation life from half crack length of 1.02 cm to 3.3 cm.

TABLE 8

RESULTS OF CONSTANT AMPLITUDE LOADING FATIGUE CRACK GROWTH TESTS[+] OF EIGHT VARIANTS OF ALLOYS 7050 AND 7075 IN T7-TYPE TEMPERS

Alloy Type	Life,* Cycles	Crack Growth Rate da/dN (cm/cycle) at 1.5 cm	2.2 cm	3.0 cm
Hi Purity 7010	96 000	1.52×10^{-5}	3.10×10^{-5}	7.40×10^{-5}
7010	84 000	1.92×10^{-5}	3.48×10^{-5}	7.50×10^{-5}
7475	104 000	1.58×10^{-5}	2.60×10^{-5}	6.00×10^{-5}
7075	92 000	1.53×10^{-5}	3.30×10^{-5}	6.70×10^{-5}
7050	136 000	1.12×10^{-5}	2.00×10^{-5}	4.70×10^{-5}
Low Purity 7050	124 000	1.27×10^{-5}	2.40×10^{-5}	6.15×10^{-5}
Hi Cu 7475	108 000	1.15×10^{-5}	2.45×10^{-5}	5.00×10^{-5}
Hi Cu 7075	108 000	1.38×10^{-5}	2.60×10^{-5}	6.35×10^{-5}

[+]Relative humidity >90% for all tests.

*Crack propagation life from half crack length of 1.02 cm to 3.3 cm.

TABLE 9

RESULTS OF PERIODIC OVERLOAD FATIGUE CRACK GROWTH TESTS[+] OF EIGHT VARIANTS OF ALLOY 7050 AND 7075 IN T7-TYPE TEMPERS

Alloy Type	Spectrum OLR	Spectrum OCR	Life* Blocks	Life* Cycles	Crack Growth Rate da/dN (cm/cycle) at 1.5 cm	Crack Growth Rate da/dN (cm/cycle) at 2.2 cm	Crack Growth Rate da/dN (cm/cycle) at 3.0 cm
Hi Purity 7010	1.8	1:8000	22	176 000	8.00×10^{-6}	2.15×10^{-5}	4.00×10^{-5}
7010			63	504 100	3.60×10^{-6}	5.81×10^{-6}	5.20×10^{-6}
7475	1.8	1:8000	83	664 100	2.75×10^{-6}	4.60×10^{-6}	9.00×10^{-6}
7075			128	1 024 100	2.12×10^{-6}	2.40×10^{-6}	3.00×10^{-6}
7050	1.8	1:8000	62	496 100	1.95×10^{-6}	1.05×10^{-5}	2.20×10^{-5}
Low Purity 7050			79	632 100	2.60×10^{-6}	5.80×10^{-6}	4.50×10^{-6}
Hi Cu 7475	1.8	1:8000	38	304 000	4.30×10^{-6}	1.40×10^{-5}	3.60×10^{-5}
Hi Cu 7075			95	760 100	2.95×10^{-6}	3.40×10^{-6}	4.10×10^{-6}

[+]Relative humidity >90% for all tests.

*Crack propagation life from half crack length of 1.02 cm to 3.3 cm.

TABLE 10

RESULTS OF PERIODIC OVERLOAD FATIGUE CRACK GROWTH TESTS+ ON PEAK STRENGTH AND OVERAGED TEMPERS OF ALLOY 7075

Temper Type	Spectrum OLR	Spectrum OCR	Life* Blocks	Life* Cycles	Crack Growth Rate da/dN (cm/cycle) at 1.5 cm	Crack Growth Rate da/dN (cm/cycle) at 2.2 cm	Crack Growth Rate da/dN (cm/cycle) at 3.0 cm
T6	1.4	1:4000	9	36 000	4.50×10^{-5}	7.20×10^{-5}	1.50×10^{-4}
T76			16	84 000	2.00×10^{-5}	5.30×10^{-5}	8.80×10^{-5}
T7			23	92 000	1.65×10^{-5}	3.50×10^{-5}	6.90×10^{-5}
T73			28	112 000	1.35×10^{-5}	2.54×10^{-5}	5.80×10^{-5}
T6	1.8	1:4000	485	1 940 500	8.10×10^{-7}	9.00×10^{-7}	---
T76			451	1 804 500	9.00×10^{-7}	1.40×10^{-6}	3.30×10^{-6}
T7			279	1 116 300	1.50×10^{-6}	2.25×10^{-6}	4.00×10^{-6}
T73			348	1 392 300	1.15×10^{-6}	1.90×10^{-6}	3.00×10^{-6}

+Relative humidity >90% for all tests.

*Crack propagation life from half crack length of 1.02 cm to 3.3 cm.

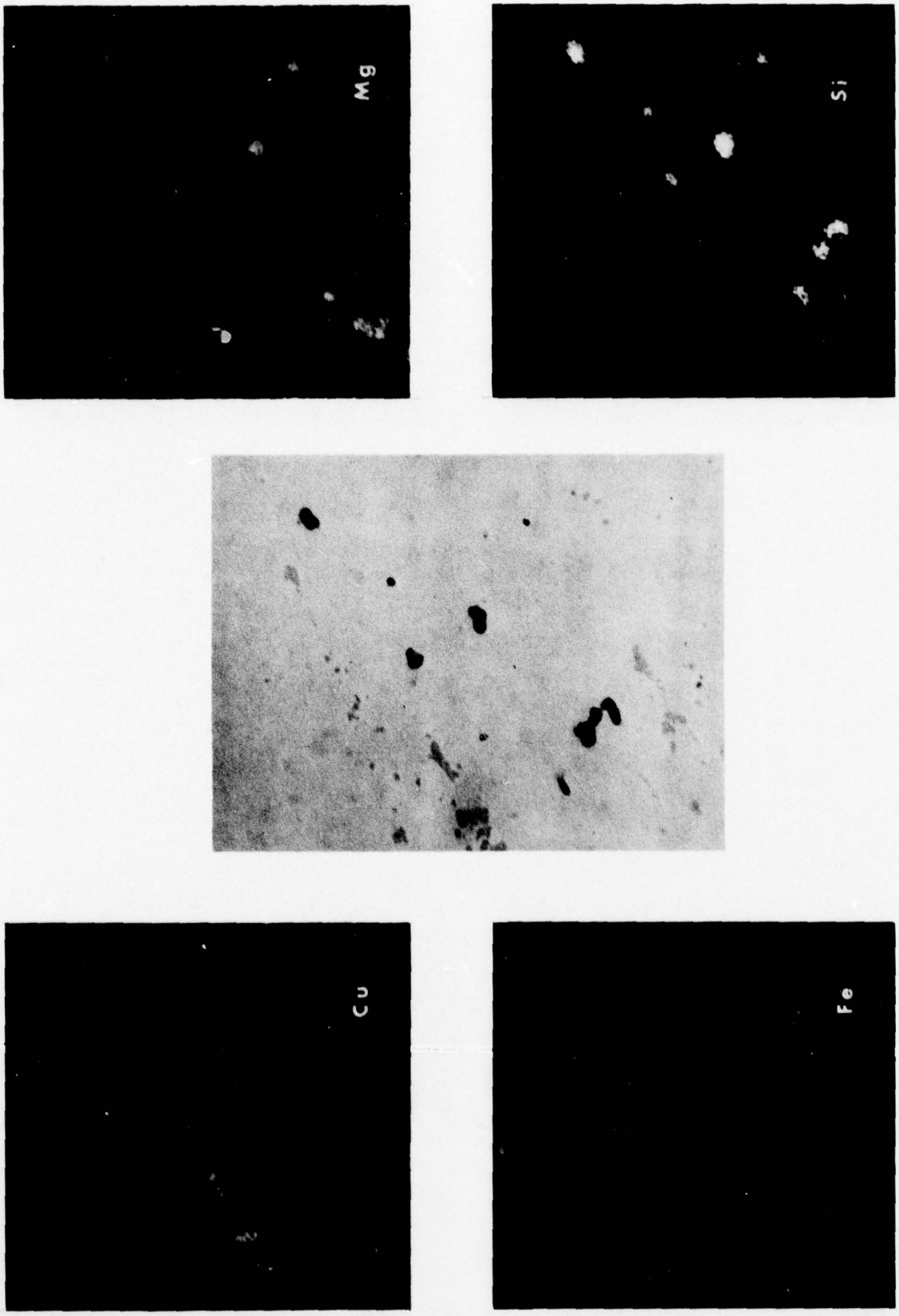

Figure 1 - Optical micrographs of 7475 (454545) showing undissolved phases along with Cu, Fe, Mg, and Si characteristic X-ray images (500X)

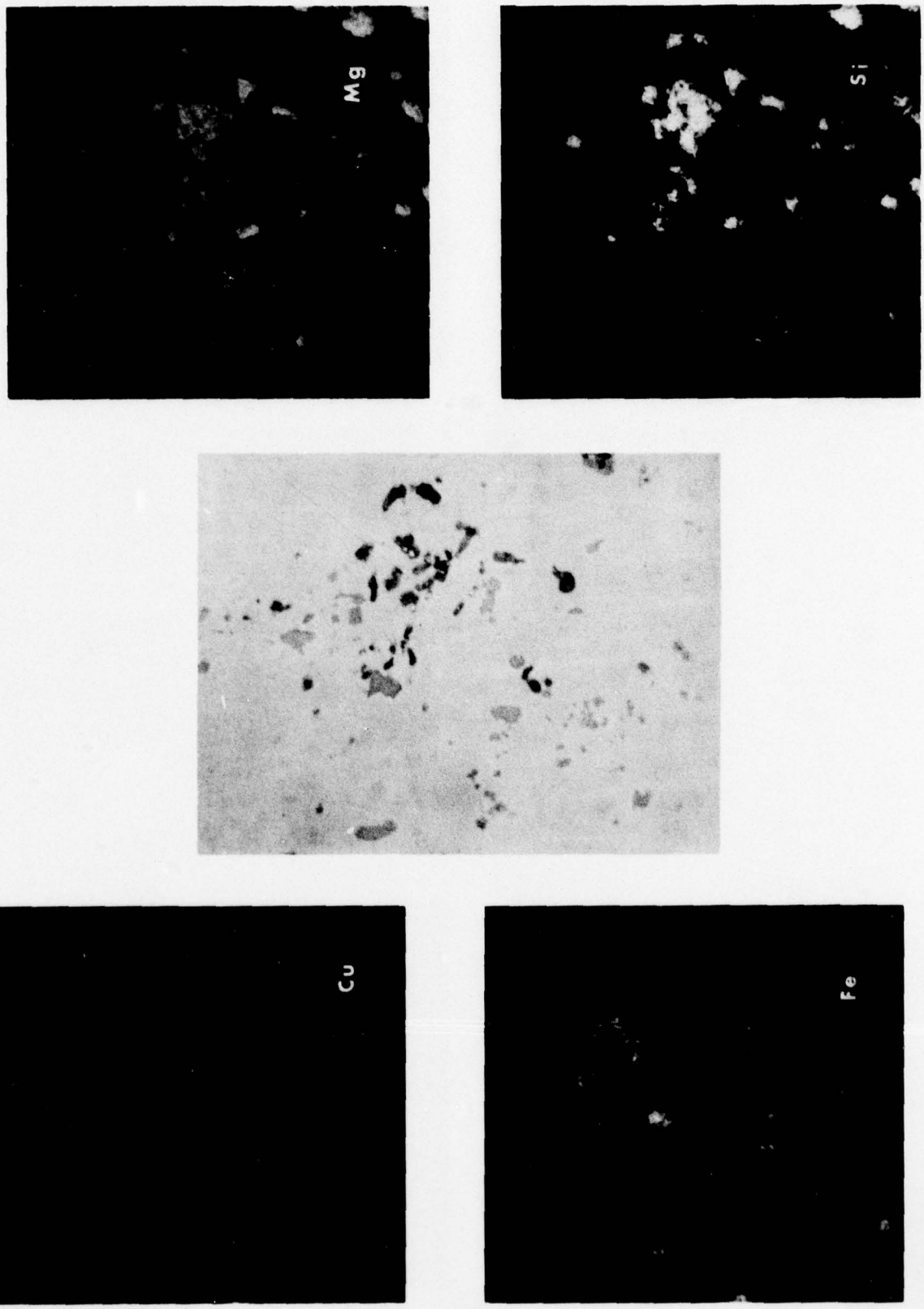

Figure 2 - Optical micrographs of 7075 (454549) showing undissolved phases along with Cu, Fe, Mg, and Si characteristic X-ray images. (500X)

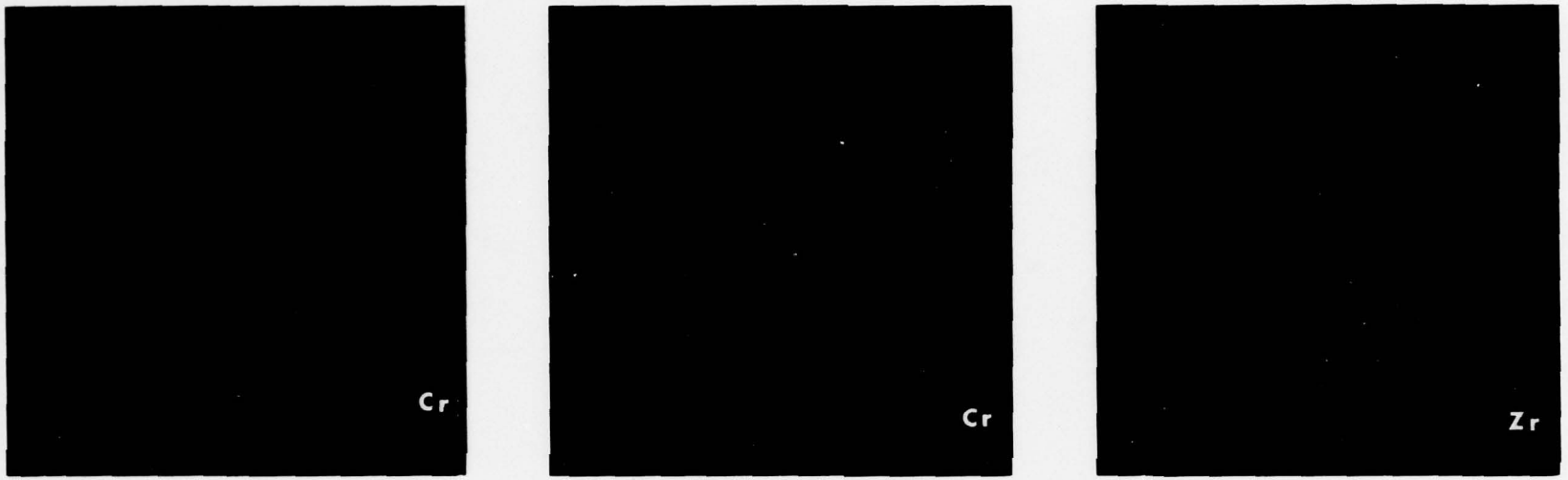

Figure 3 - CrK_{α} images of 7075 (454549) and 7475 (454545) and ZrK_{α} image of 7050 (454543). (500X)

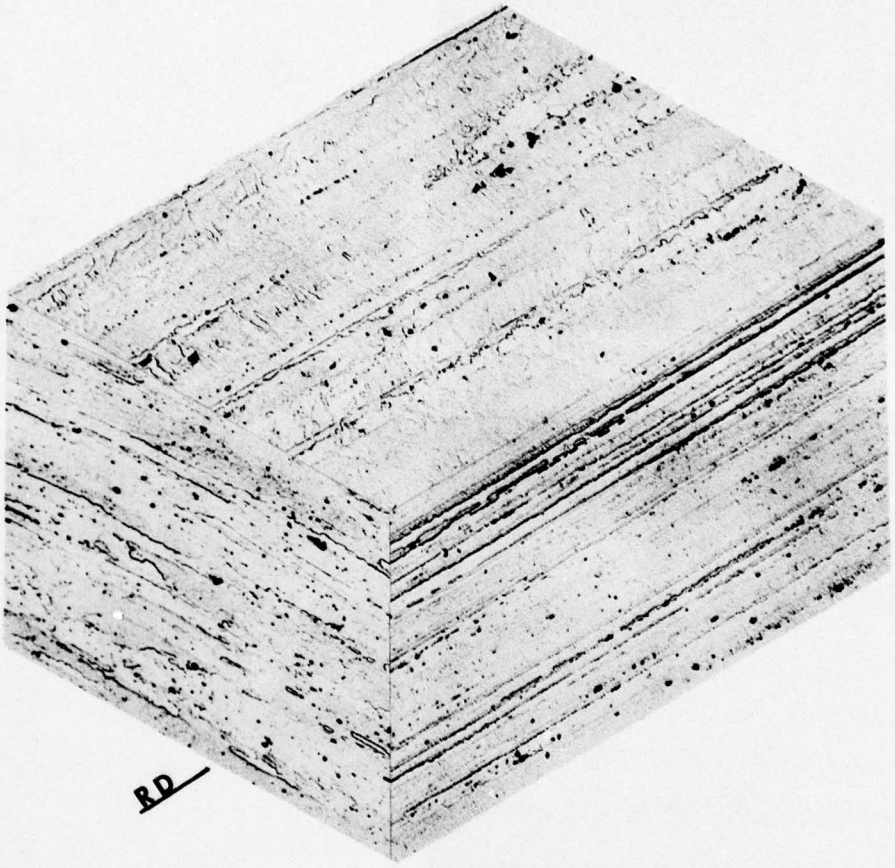

Figure 4 - Three deimensional optical micrograph showing the grain structure of High Purity Alloy 7010-Type (454542). (Keller's Etch, 100X)

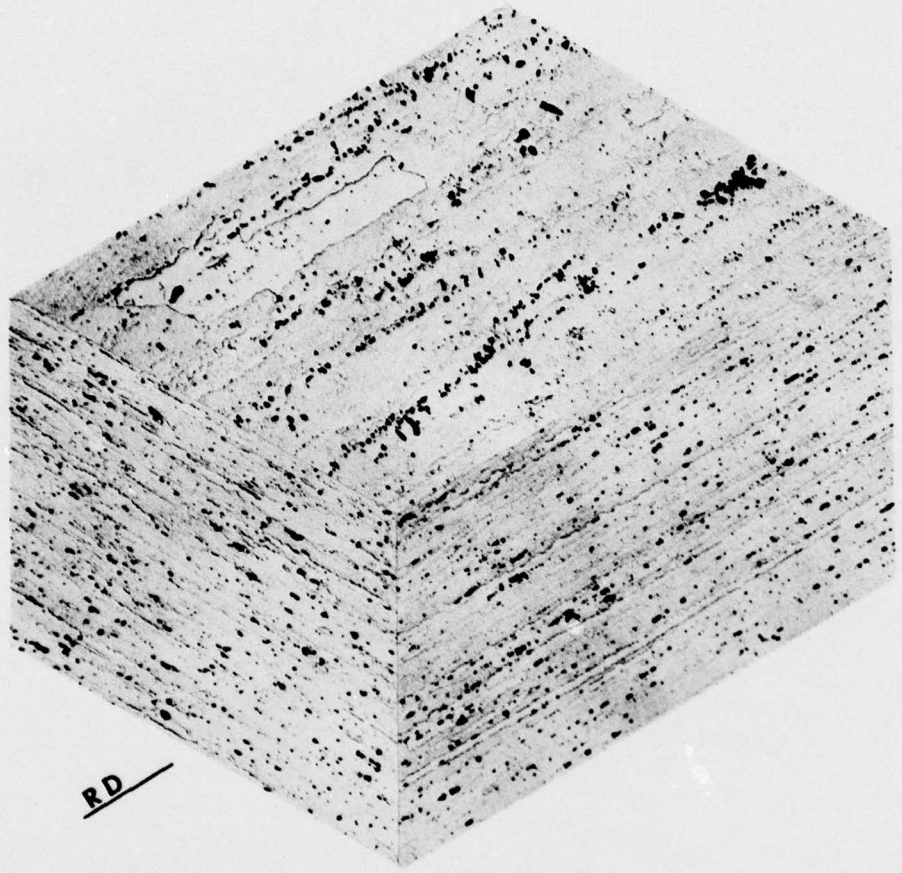

Figure 5 - Three dimensional optical micrograph showing the grain structure of Alloy 7010-Type (454547).
(Keller's Etch, 100X)

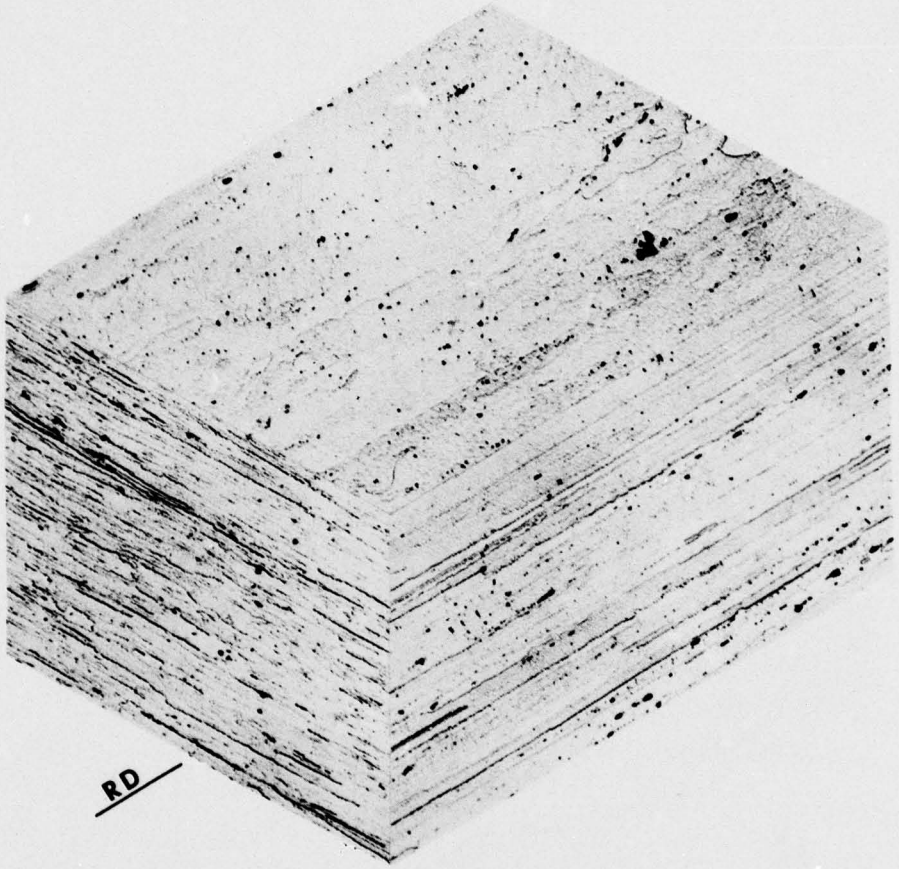

Figure 6 - Three dimensional optical micrograph showing the grain structure of 7475-T7 (454545).
(Keller's Etch, 100X)

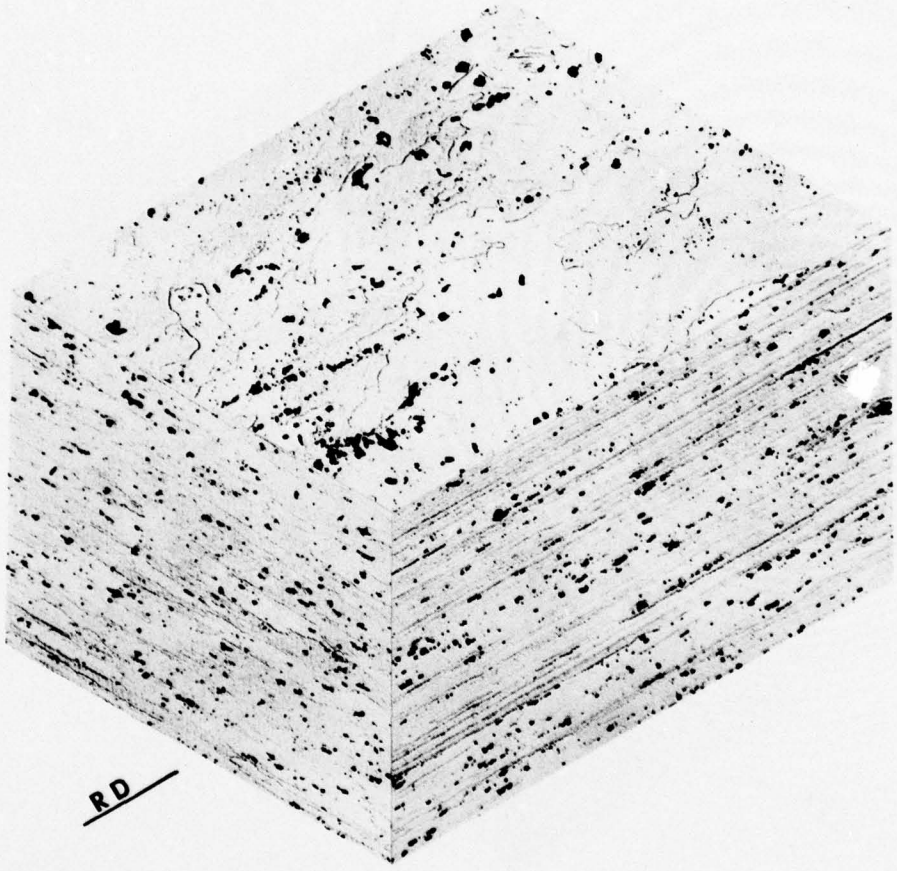

Figure 7 - Three dimensional optical micrograph showing the grain structure of 7075-T7 (454549).
(Keller's Etch, 100X)

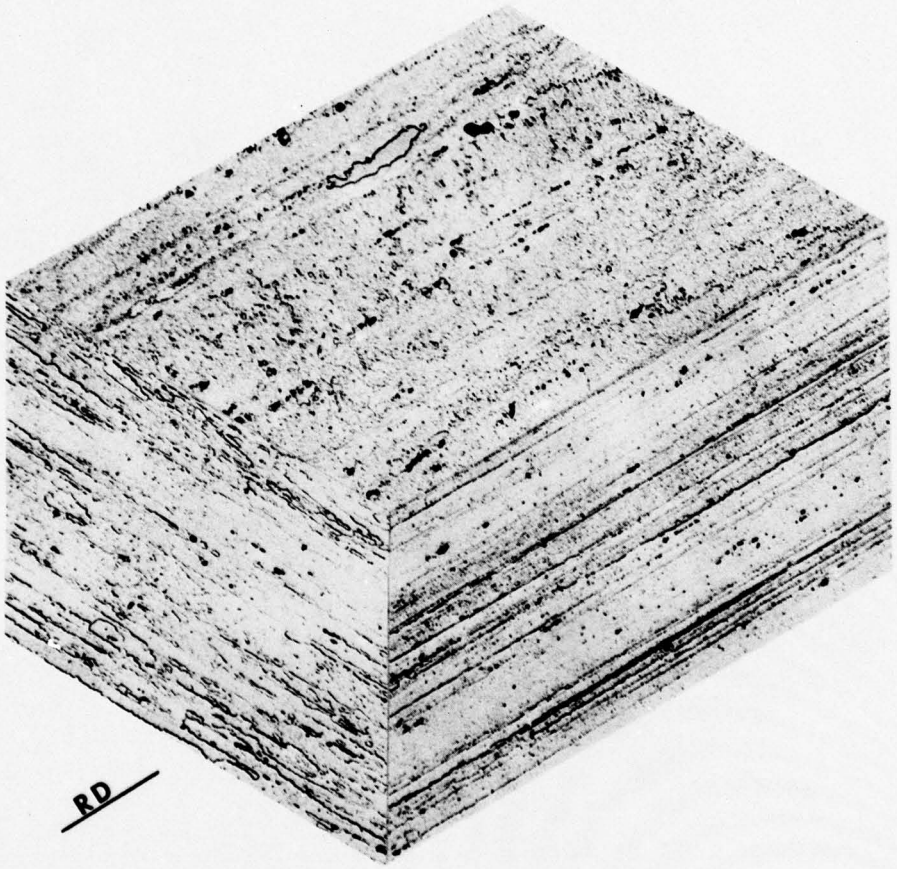

Figure 8 - Three dimensional optical micrograph showing the grain structure of 7050-T7 (454543).
(Keller's Etch, 100X)

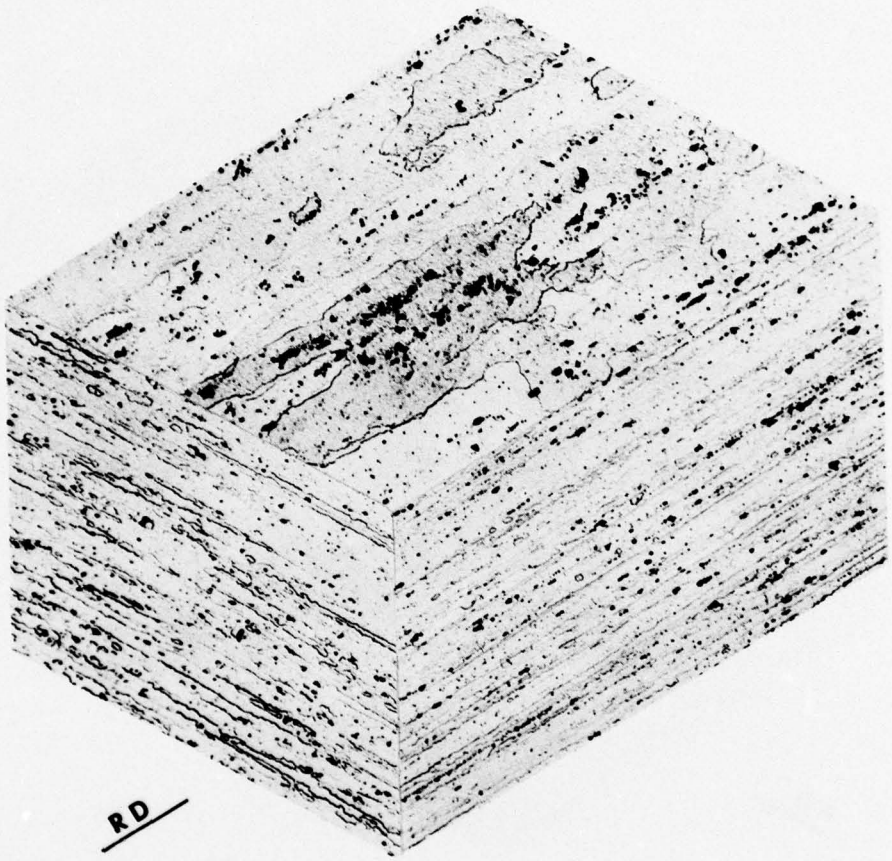

Figure 9 - Three dimensional optical micrograph showing the grain structure of Lower Purity 7050-Type (454548). (Keller's Etch, 100X)

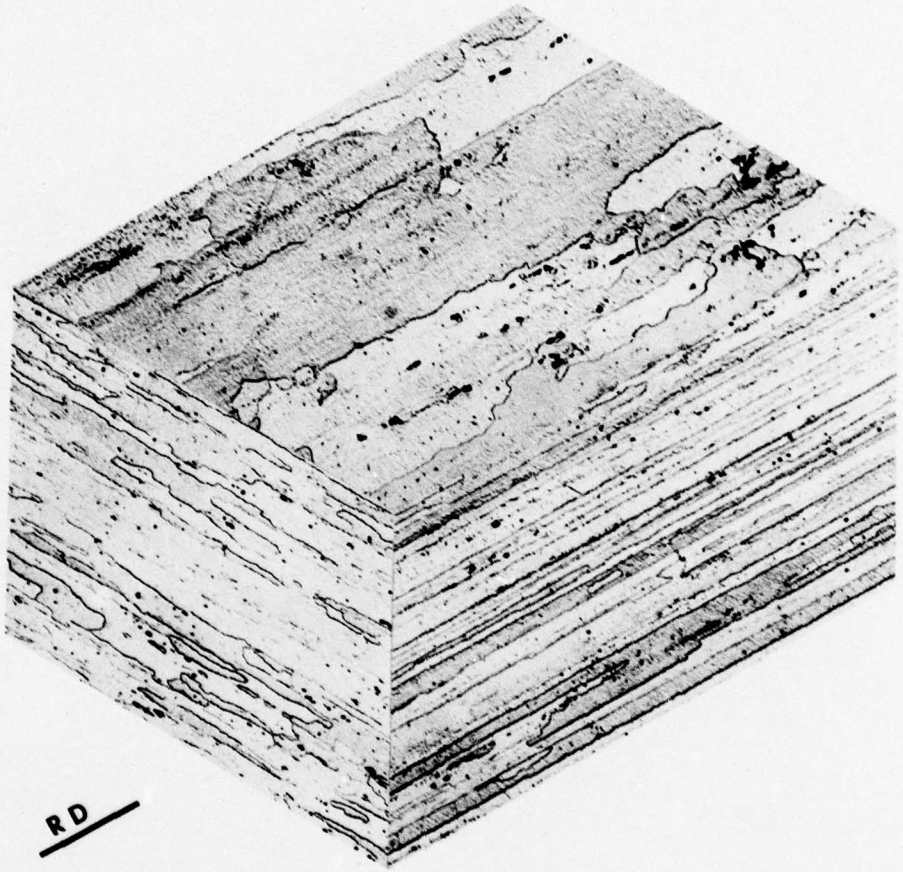

Figure 10 - Three deimensional optical micrograph showing the grain structure of Higher Cu 7475-Type (454546).
(Keller's Etch, 100X)

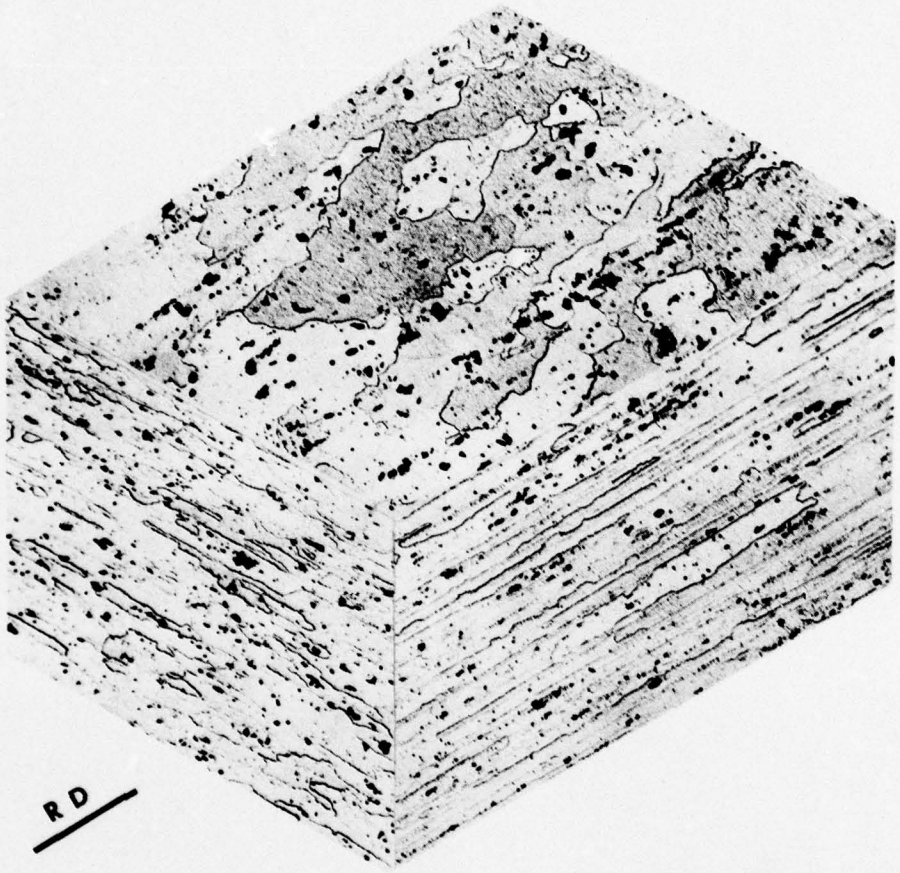

Figure 11 - Three dimensional optical micrograph showing the grain structure of Higher Cu 7075-Type (454551).
(Keller's Etch, 100X)

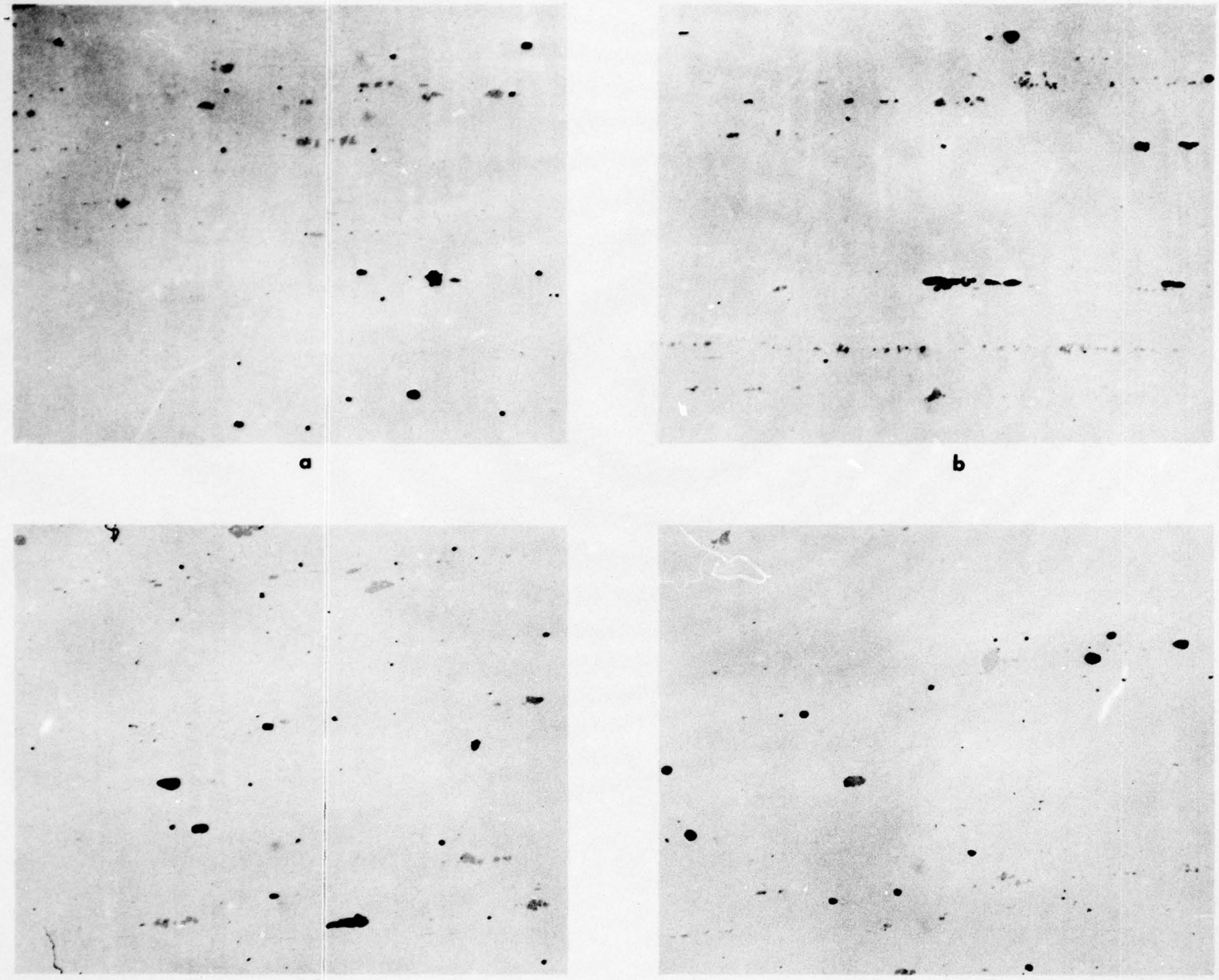

Figure 12 - As-polished, longitudinal section of a. High Purity 7010-Type (454542), b. 7475 (454545), c. 7050 (454543) and d. Higher Cu 7475-Type (454546). (500X)

AD-A057 129 ALUMINUM CO OF AMERICA ALCOA CENTER PA ALCOA LABS F/G 11/6
EFFECT OF MICROSTRUCTURE ON FATIGUE CRACK GROWTH OF 7XXX ALUMIN--ETC(U)
APR 78 T H SANDERS, R R SAWTELL, J T STALEY N00019-76-C-0482

UNCLASSIFIED 56-78-AF8 NL

2 OF 3
AD
A057 129

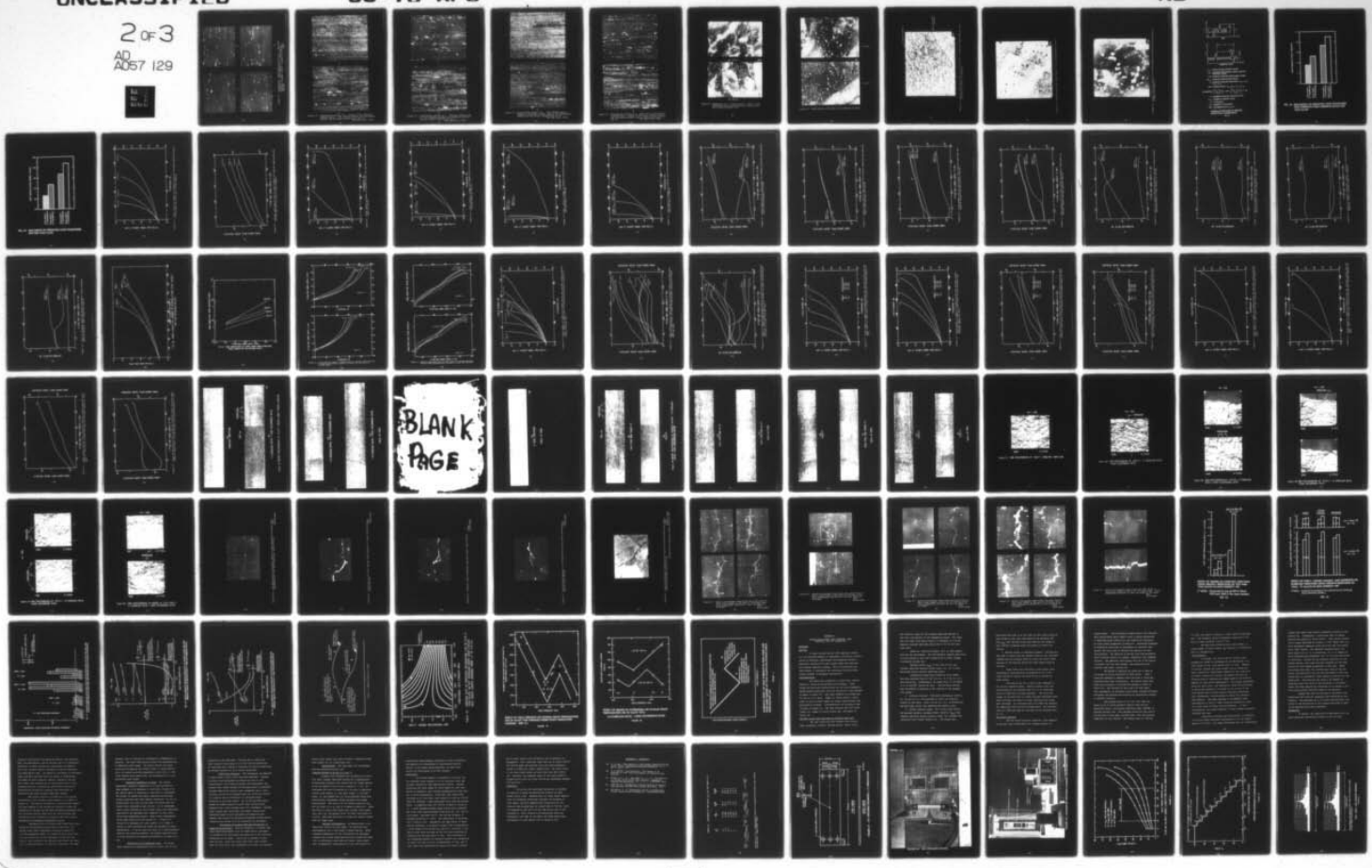

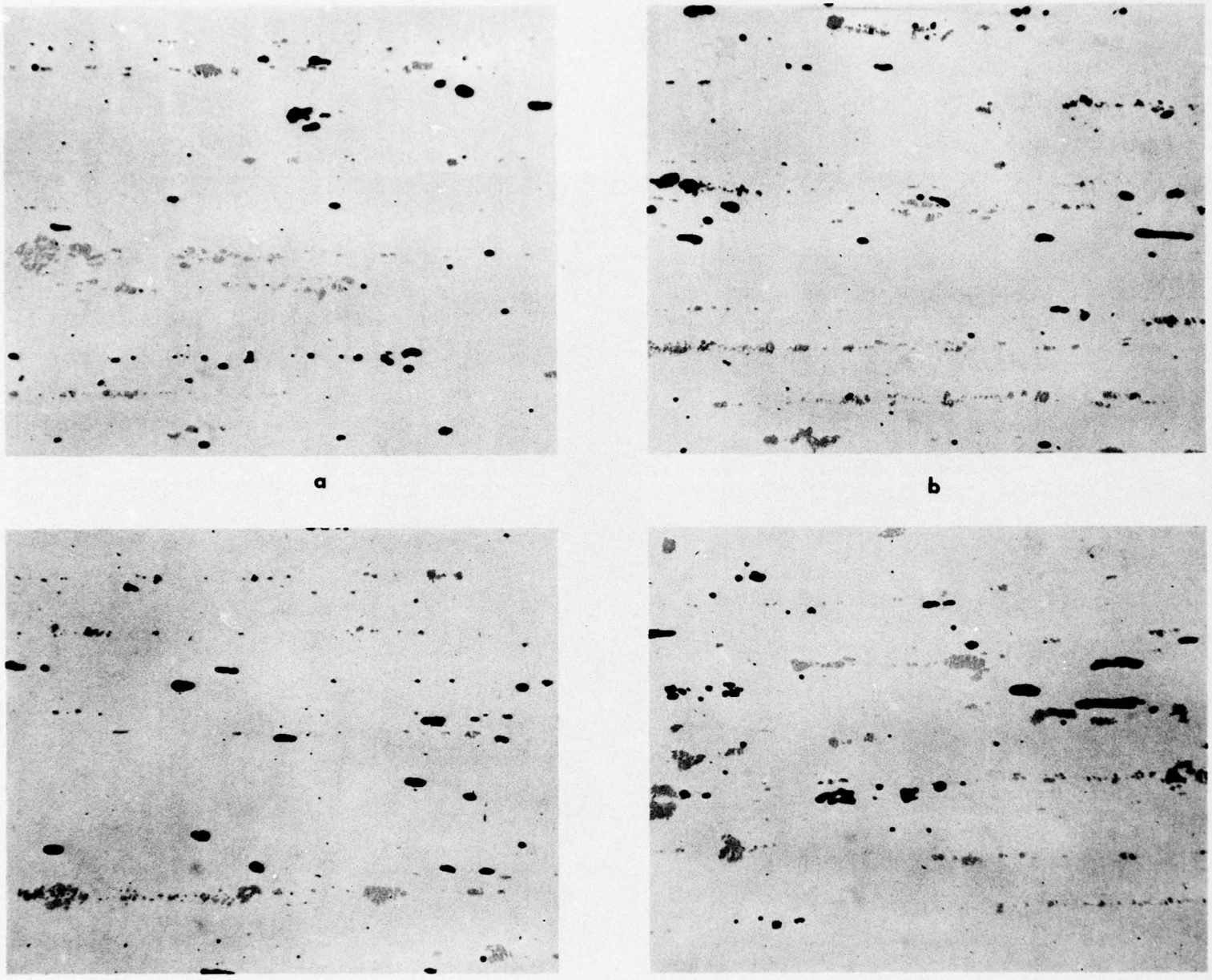

Figure 13 - As-polished, longitudinal section of a. 7010-Type (454547), b. 7075 (454549), c. Lower Purity 7050-Type (454548), and d. Higher Cu 7075-Type (454551). (500X)

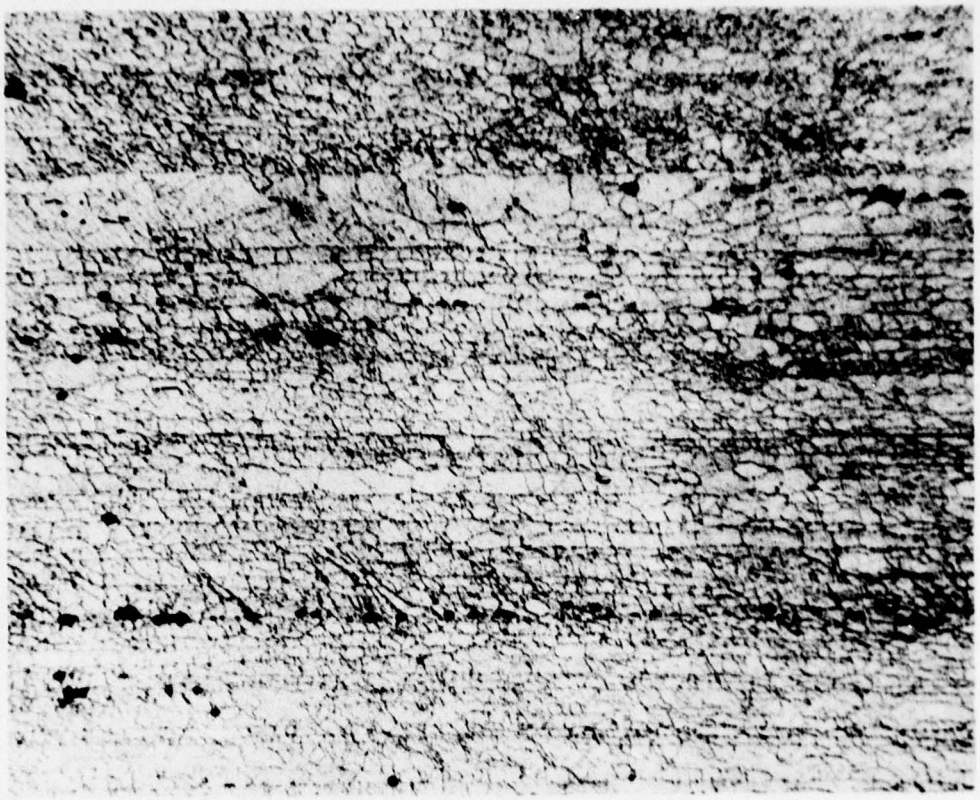

a

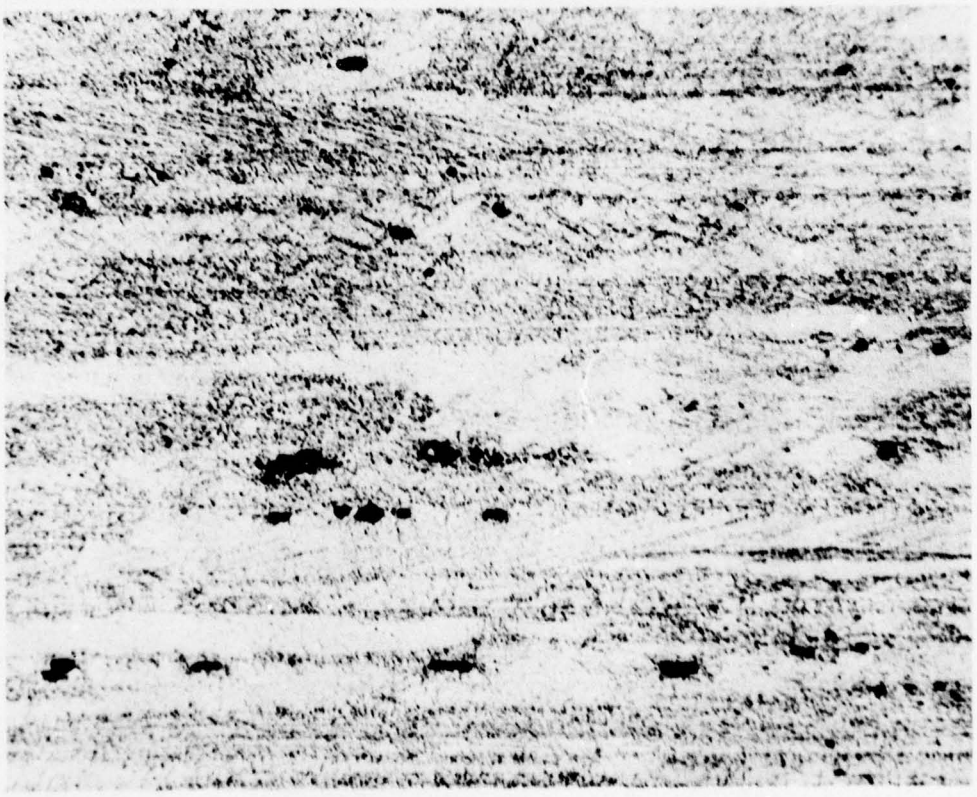

b

Figure 14 - Longitudinal section of a. Higher Purity 7010-Type (454542) and b. 7475 (454545) showing the differences between similar alloys containing Zr and Cr.
(Hot HNO_3 Etch, 500X)

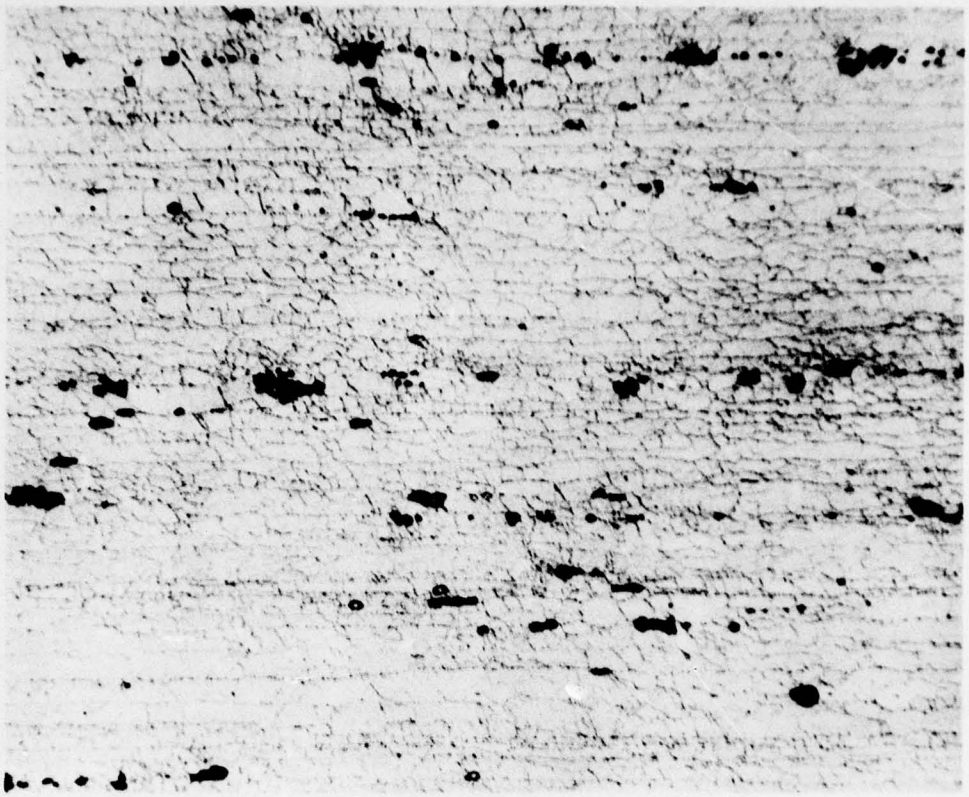

a

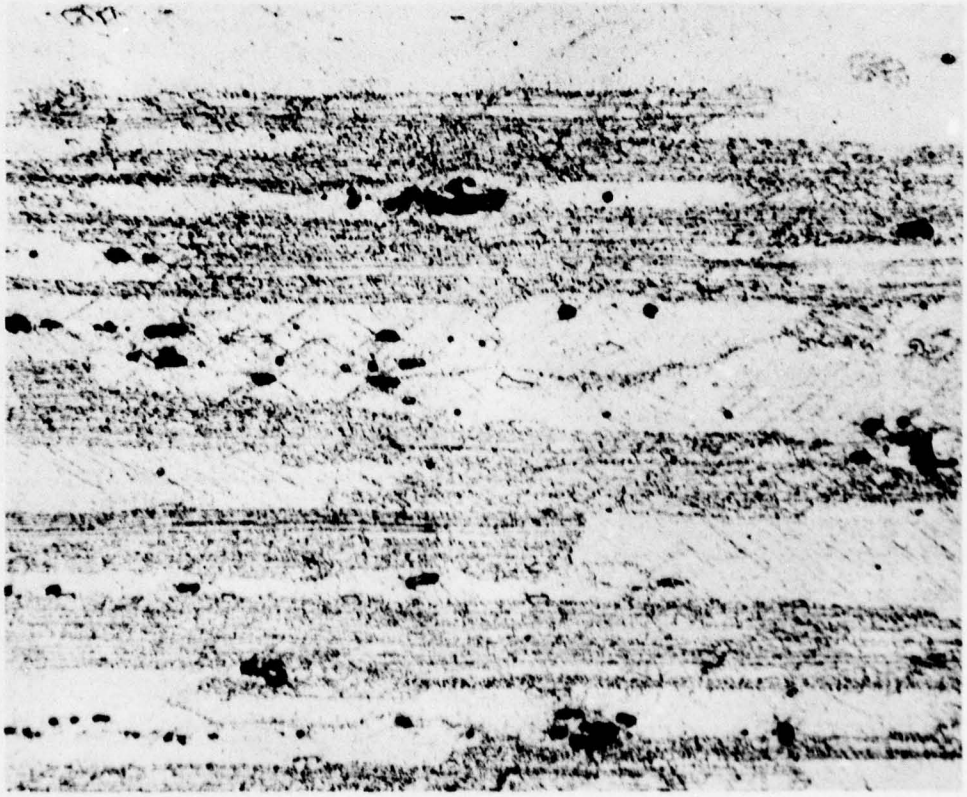

b

Figure 15 - Longitudinal section of a. 7010-Type (454547) and b. 7075 (454549) showing the differences between similar alloys containing Zr or Cr.
(Hot HNO_3 Etch, 500X)

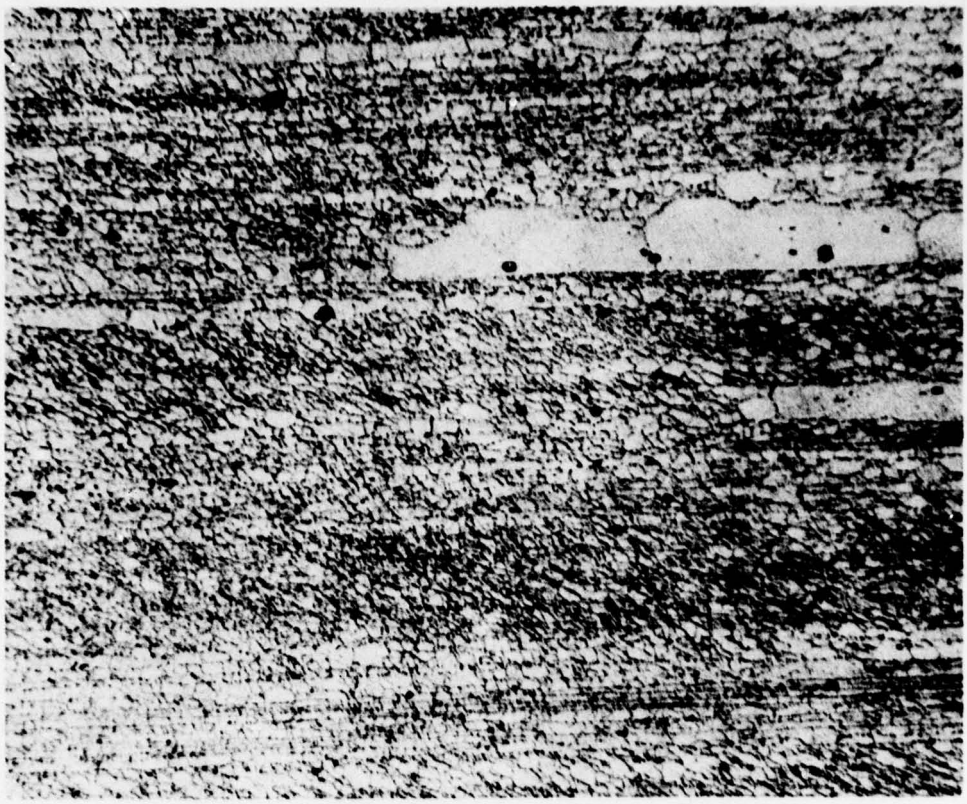

a

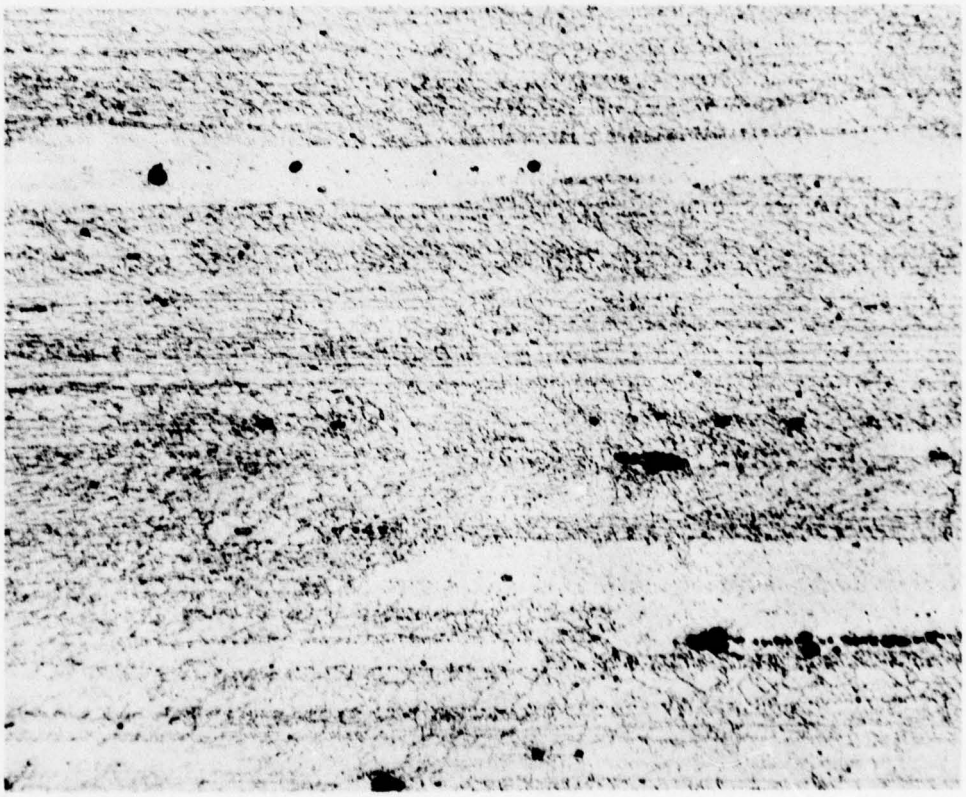

b

Figure 16 - Longitudinal section of a. 7050 (454543) and b. Higher Cu 7475-Type (454546) showing the differences between similar alloys containing Zr or Cr.
(Hot HNO_3 Etch, 500X)

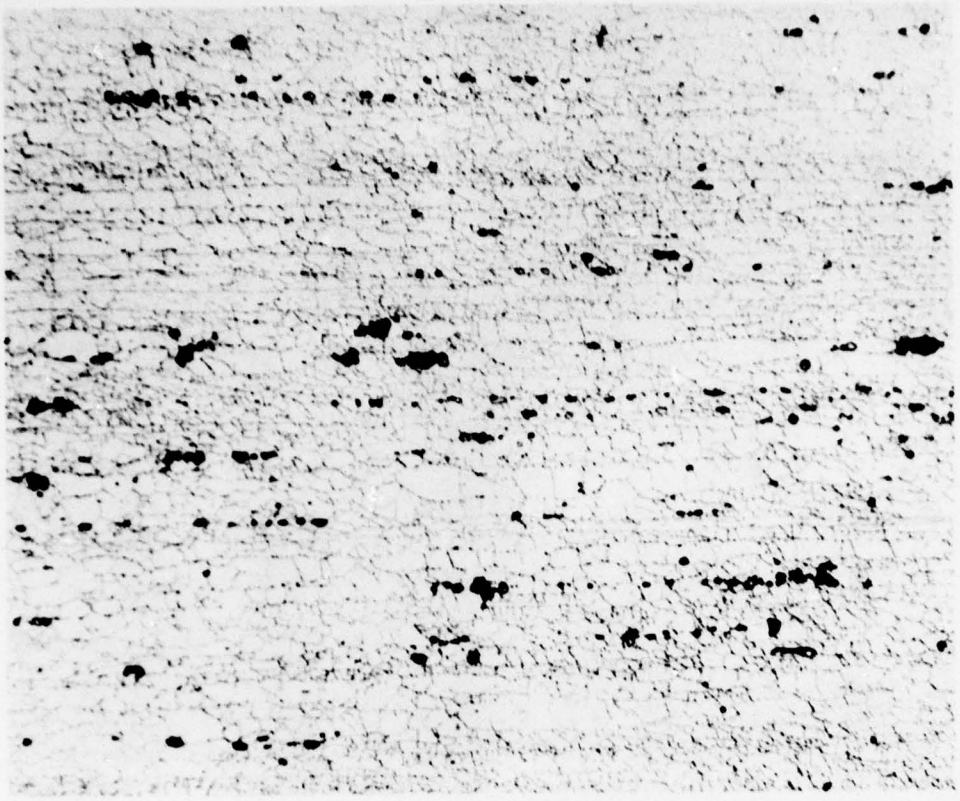

a

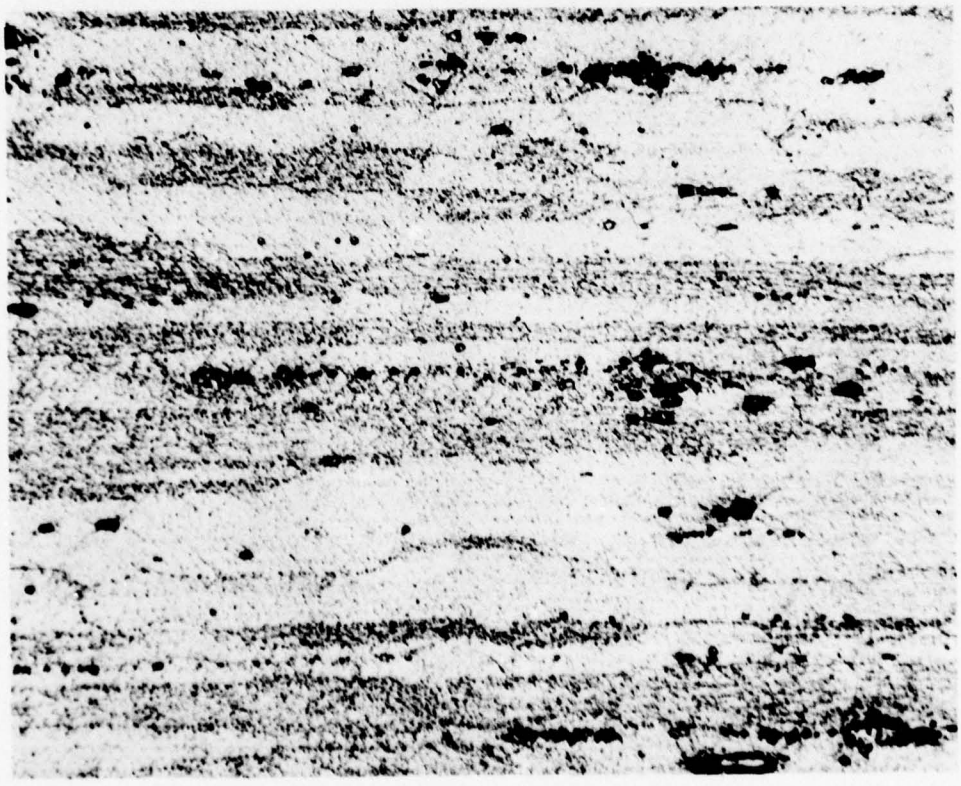

b

Figure 17 - Longitudinal section of a. Lower Purity 7050-Type-T7 (454548) and b. Higher Cu 7075-Type (454551) showing the differences between similar alloys containing Zr and Cr. (Hot HNO_3 Etch, 500X)

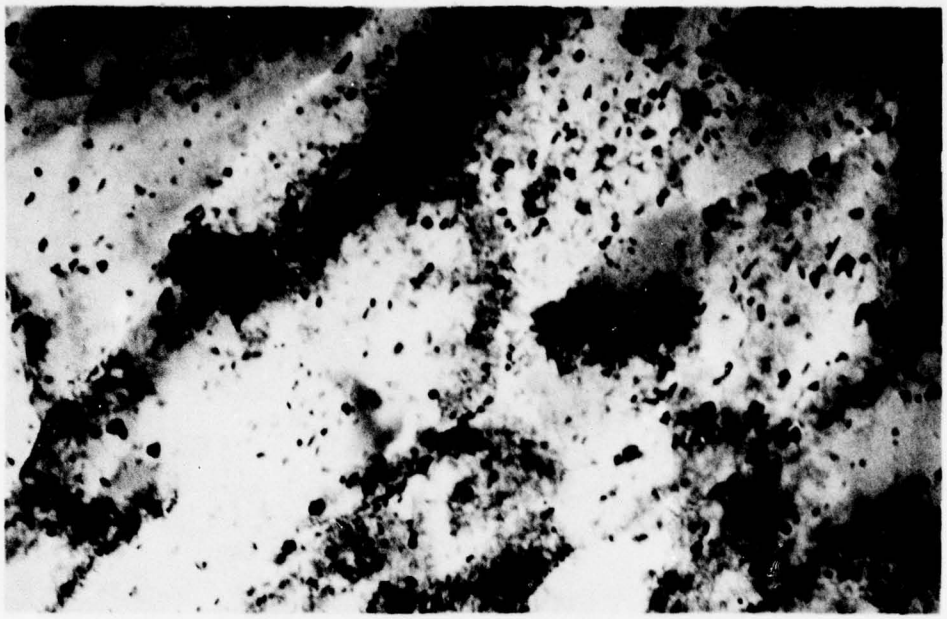

(a) 7075-T6 .5μm

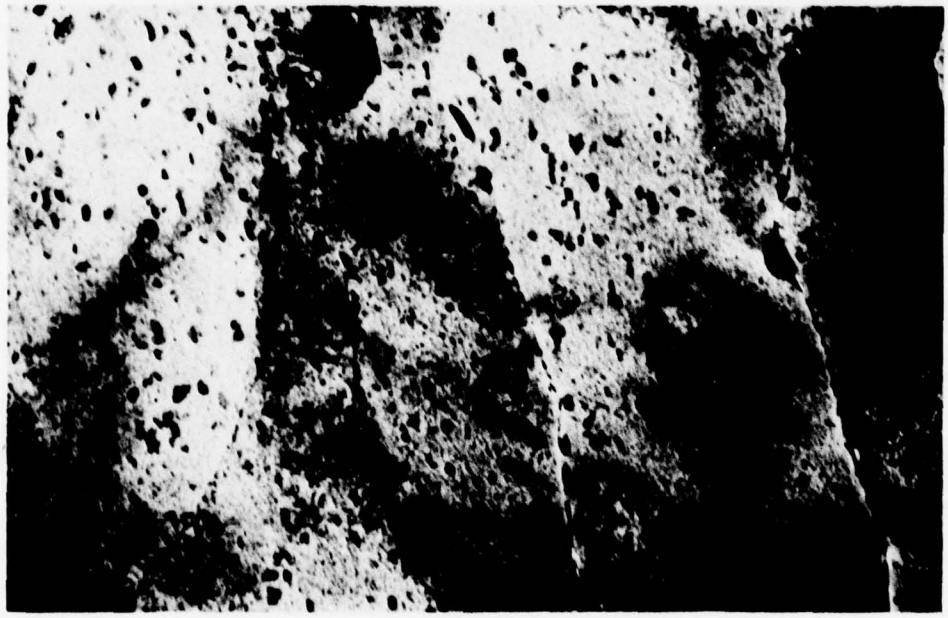

(b) 7475-T7

Figure 18 - Comparison of a. 7075-T6 and b. 7475-T7. Both structures were unrecrystallized, containing a high volume fraction of E.

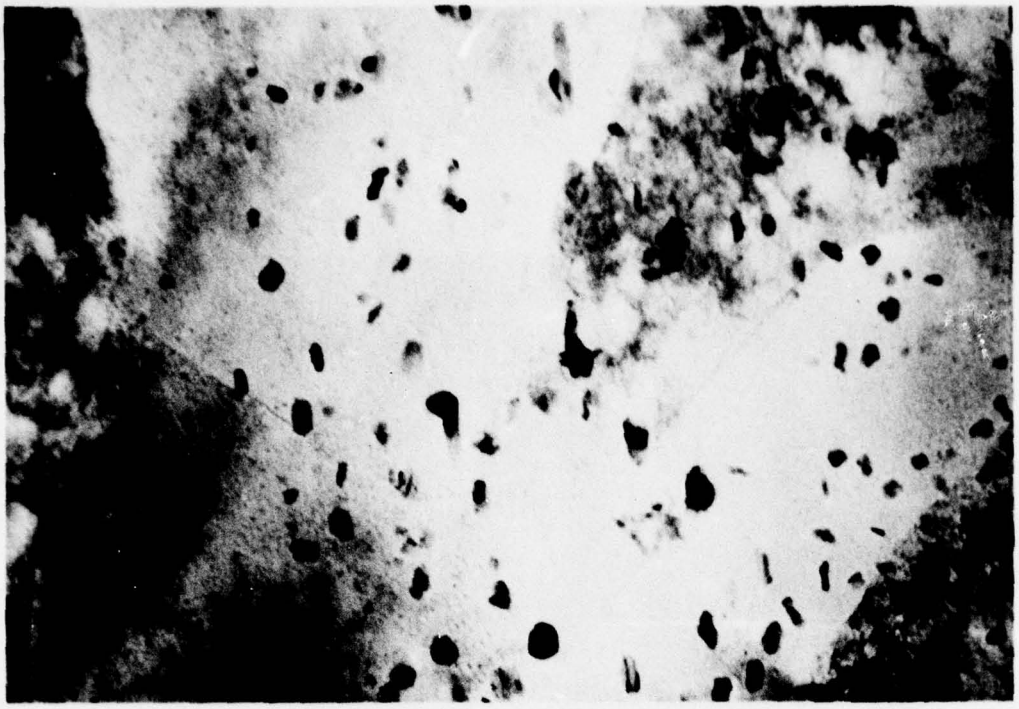

7075-T6

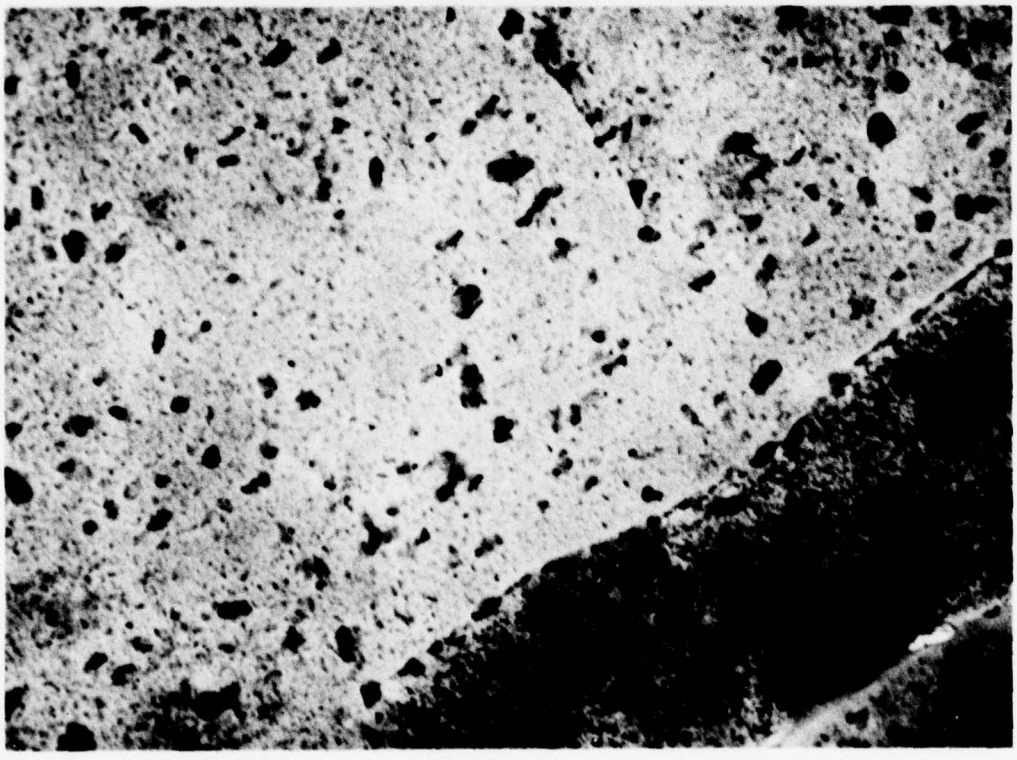

7075-T7

Figure 19 - Distribution of GP and η' as a function of aging.

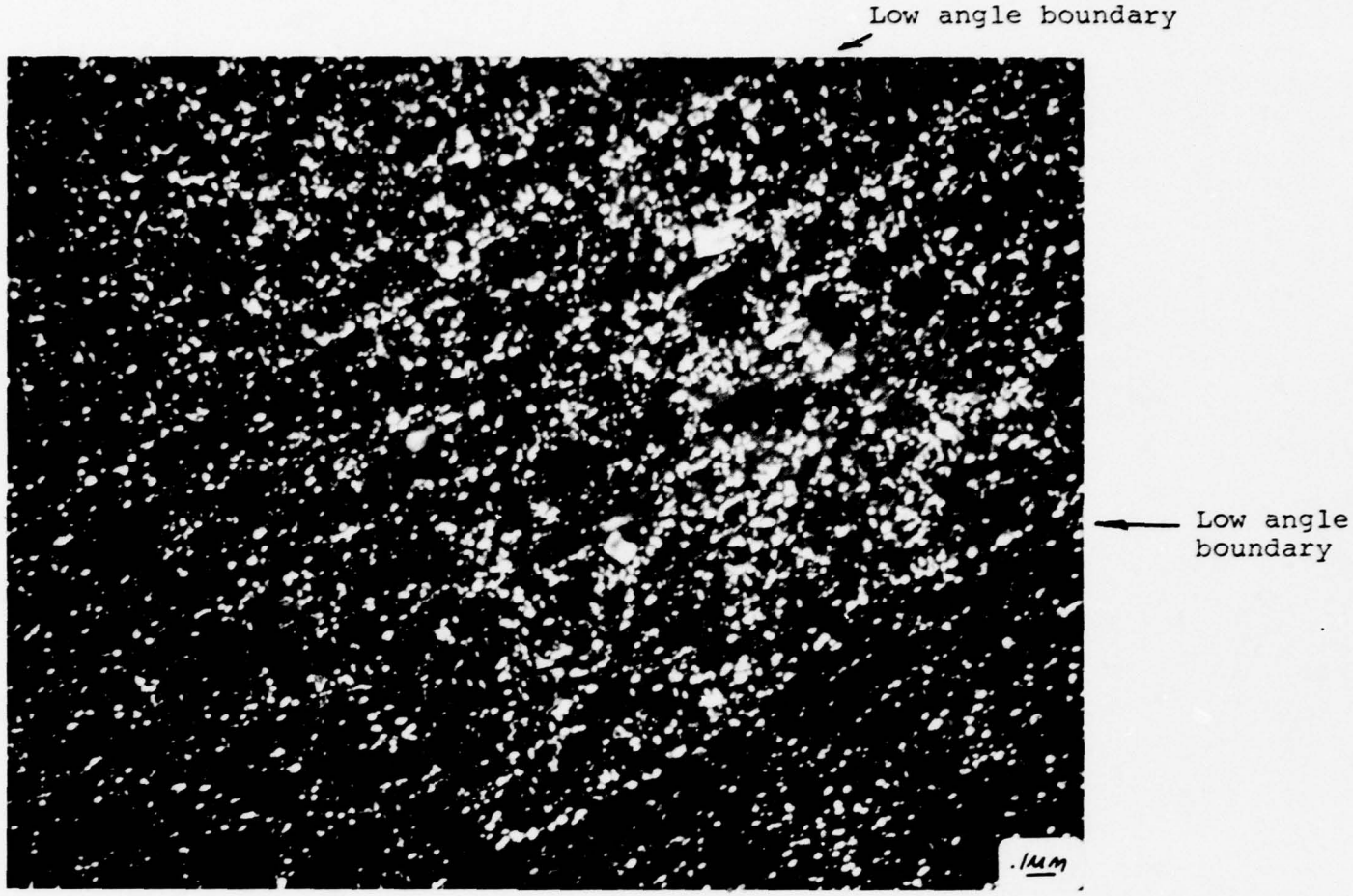

Figure 20 - Central Dark Field (CDF) of η′ in 7075-T7. Localized precipitation along low angle boundaries is apparent.

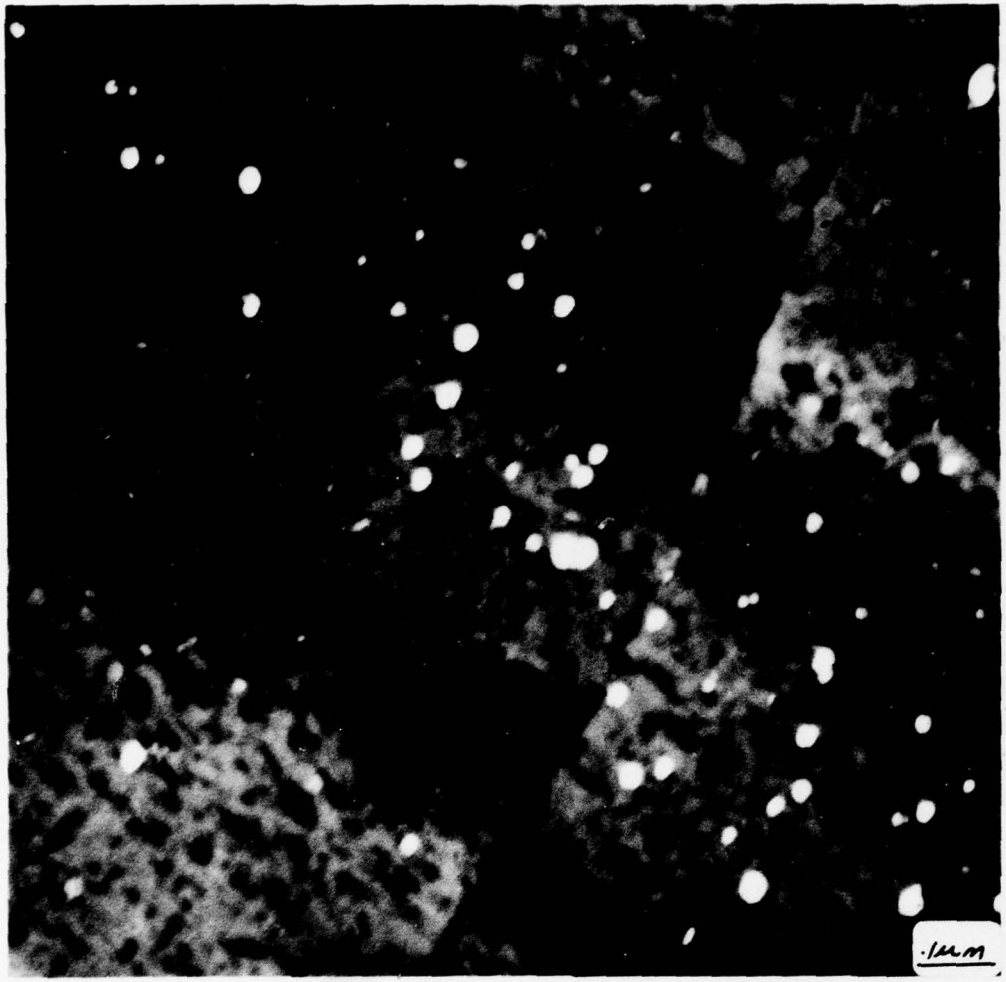

Figure 21 - Central Dark Field (CDF) Image of Al_3Zr Precipitates in 7050.

Figure 22 - Bright field micrograph of 7075-T6 showing the size and distribution of E-phase ($Al_{12}Mg_2Cr$).

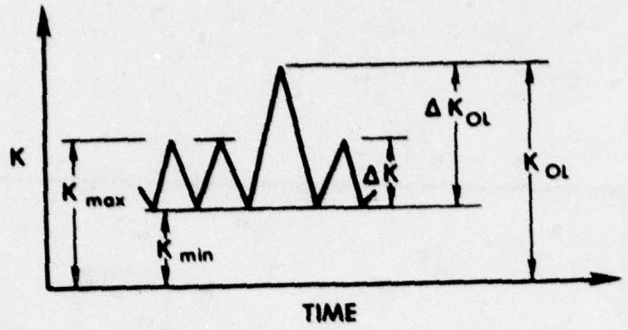

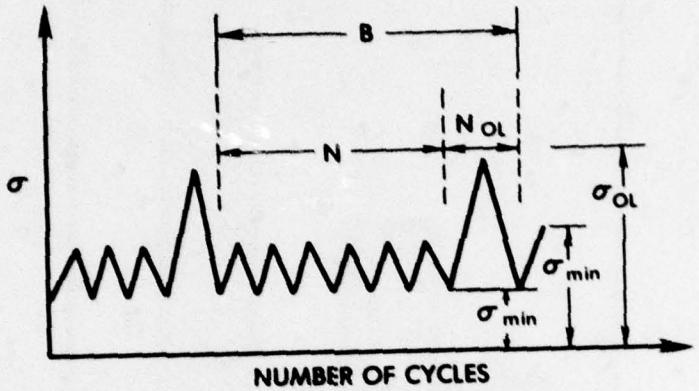

K_{OL} = OVERLOAD STRESS-INTENSITY FACTOR

K_{max} = MAXIMUM STRESS-INTENSITY DURING CONSTANT-AMPLITUDE CYCLING

ΔK = CONSTANT-AMPLITUDE STRESS-INTENSITY RANGE

ΔK_{OL} = OVERLOAD STRESS-INTENSITY RANGE

R = CONSTANT-AMPLITUDE STRESS RATIO = $\sigma_{max} / \sigma_{min}$ = K_{max} / K_{min}

OLR = OVERLOAD RATIO = $\sigma_{OL} / \sigma_{max} = K_{OL} / K_{max}$

$$\% \text{ OVERLOAD} = \left(\frac{\sigma_{OL} - \sigma_{max}}{\sigma_{max}}\right) \times 100 = \left(\frac{K_{OL} - K_{max}}{K_{max}}\right) \times 100$$

N = NUMBER OF CONSTANT- AMPLITUDE CYCLES

N_{OL} = NUMBER OF OVERLOAD CYCLES

B = CYCLIC BLOCK

N_B = NUMBER OF CYCLIC BLOCKS

OCR = OCCURRENCE RATIO = N_{OL} / N

NOMENCLATURE USED IN PERIODIC SINGLE PEAK OVERLOADING

FIG. 23

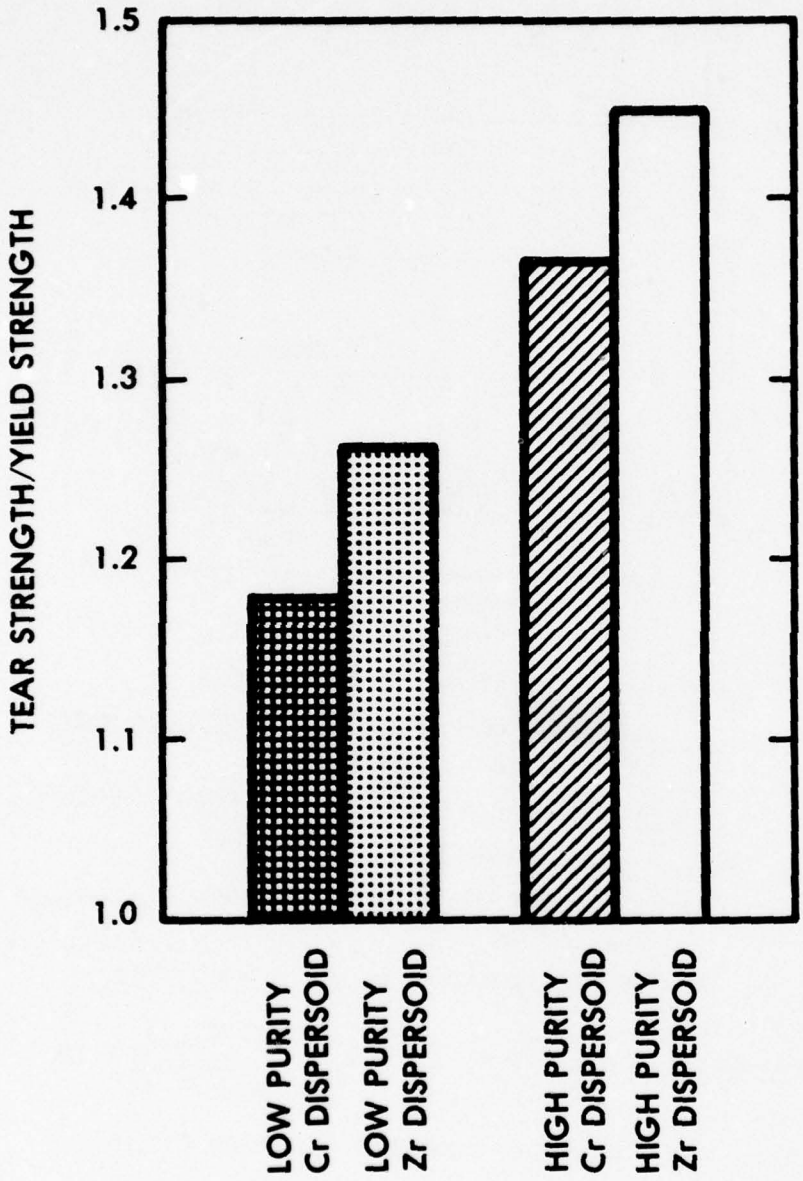

FIG. 24 BAR GRAPH OF PREDICTED LONG-TRANSVERSE TEAR STRENGTH/YIELD STRENGTH RATIO FOR 7XXX PLATE

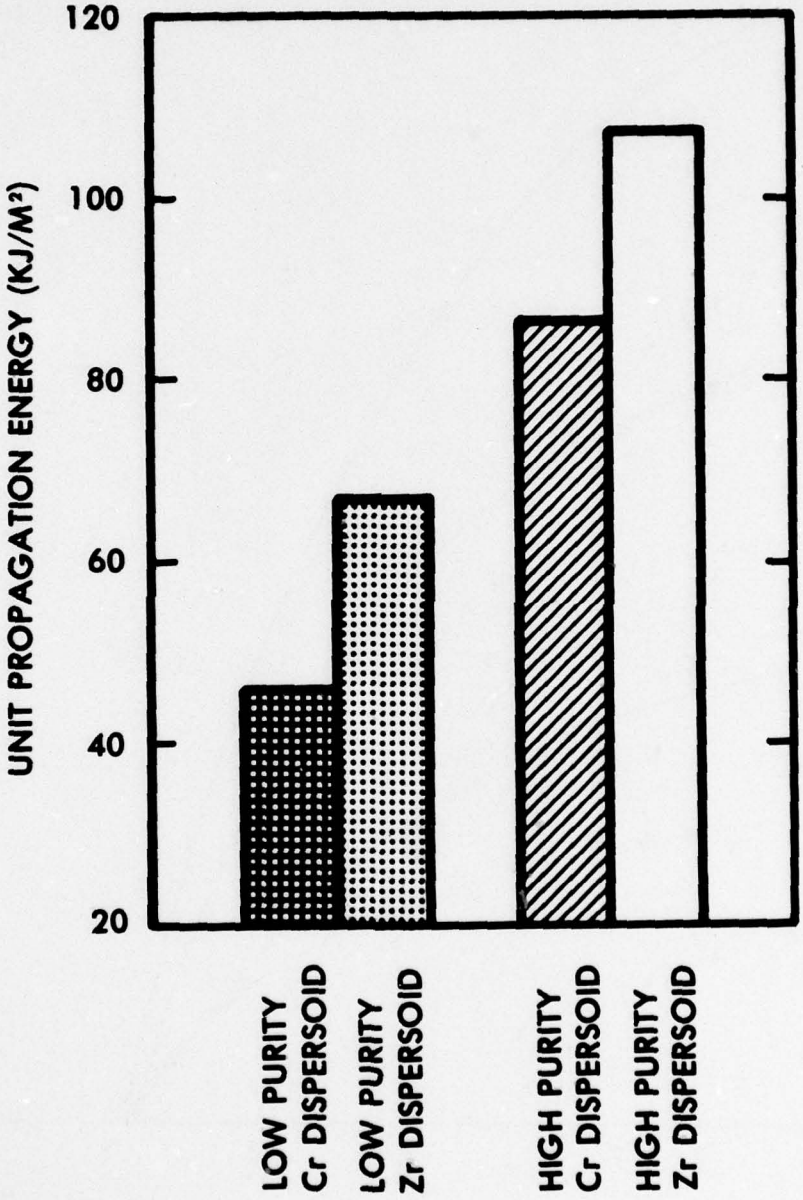

FIG. 25 BAR GRAPH OF PREDICTED LONG-TRANSVERSE UPE FOR 7XXX PLATE

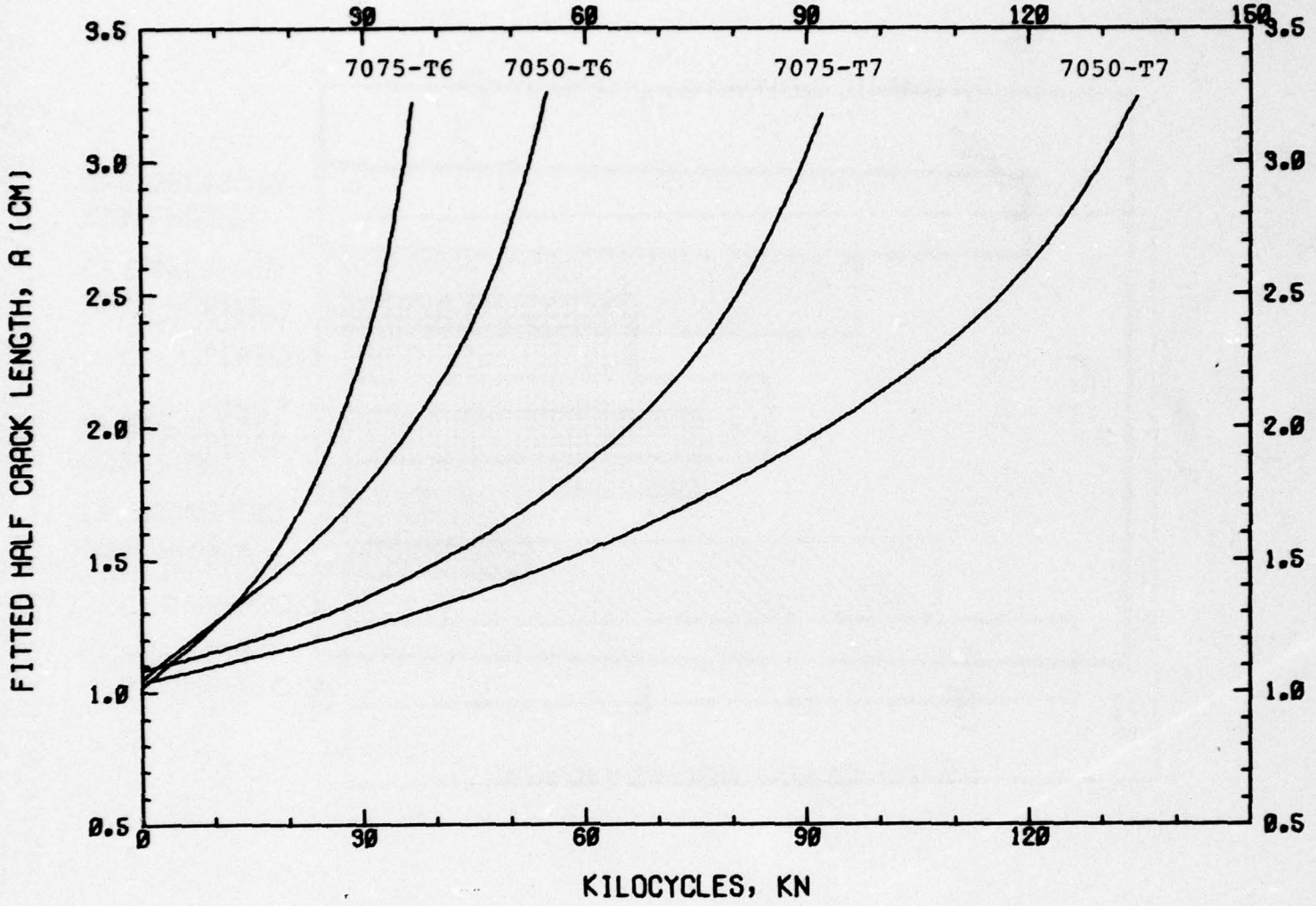

Figure 26 - Crack length vs number of elapsed cycles for constant amplitude tests of 7075 and 7050 in T6 and T7-type tempers.

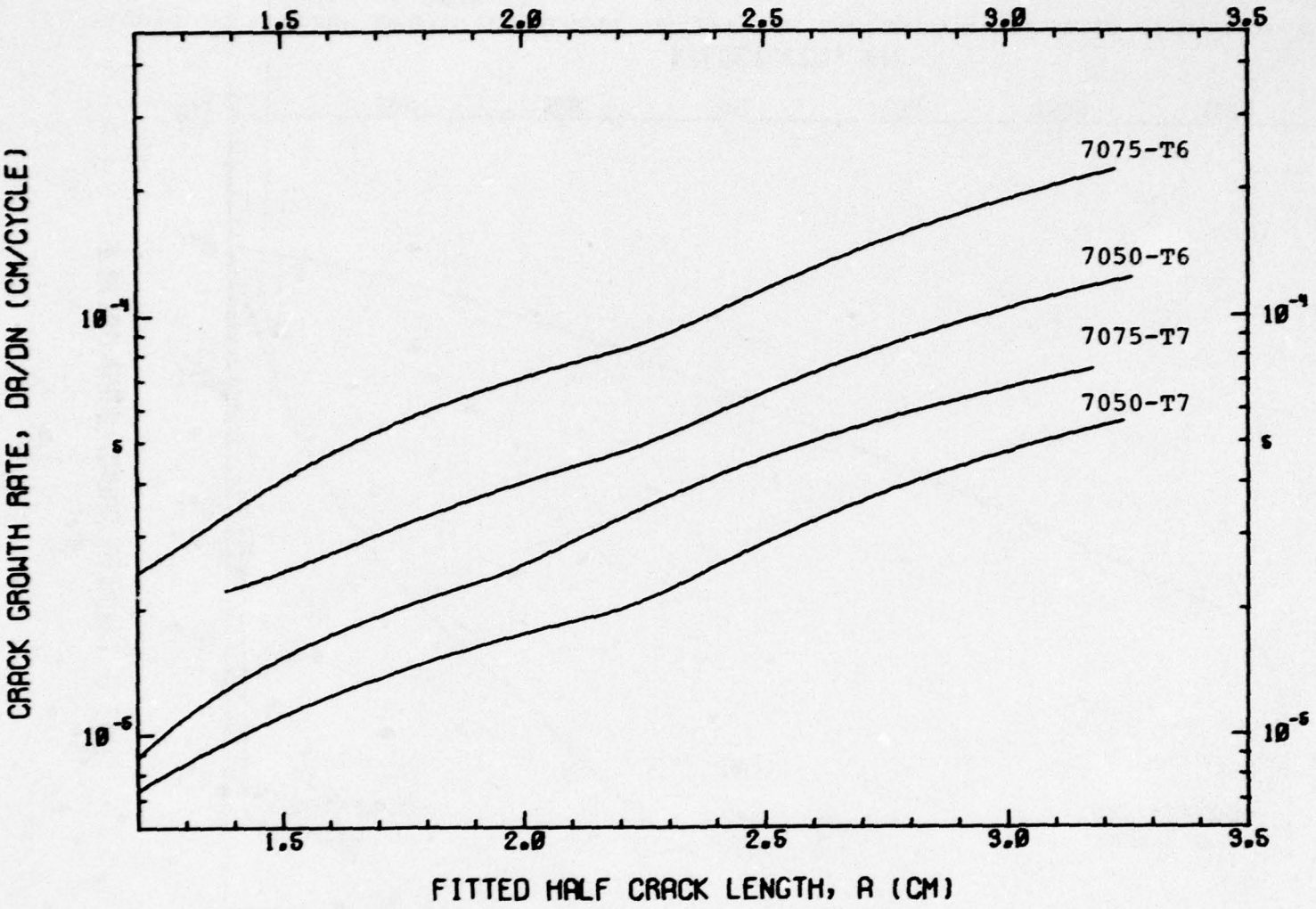

Figure 27 - Fatigue crack growth rate vs crack length for constant amplitued tests of 7075 and 7050 in T6 and T7-type tempers.

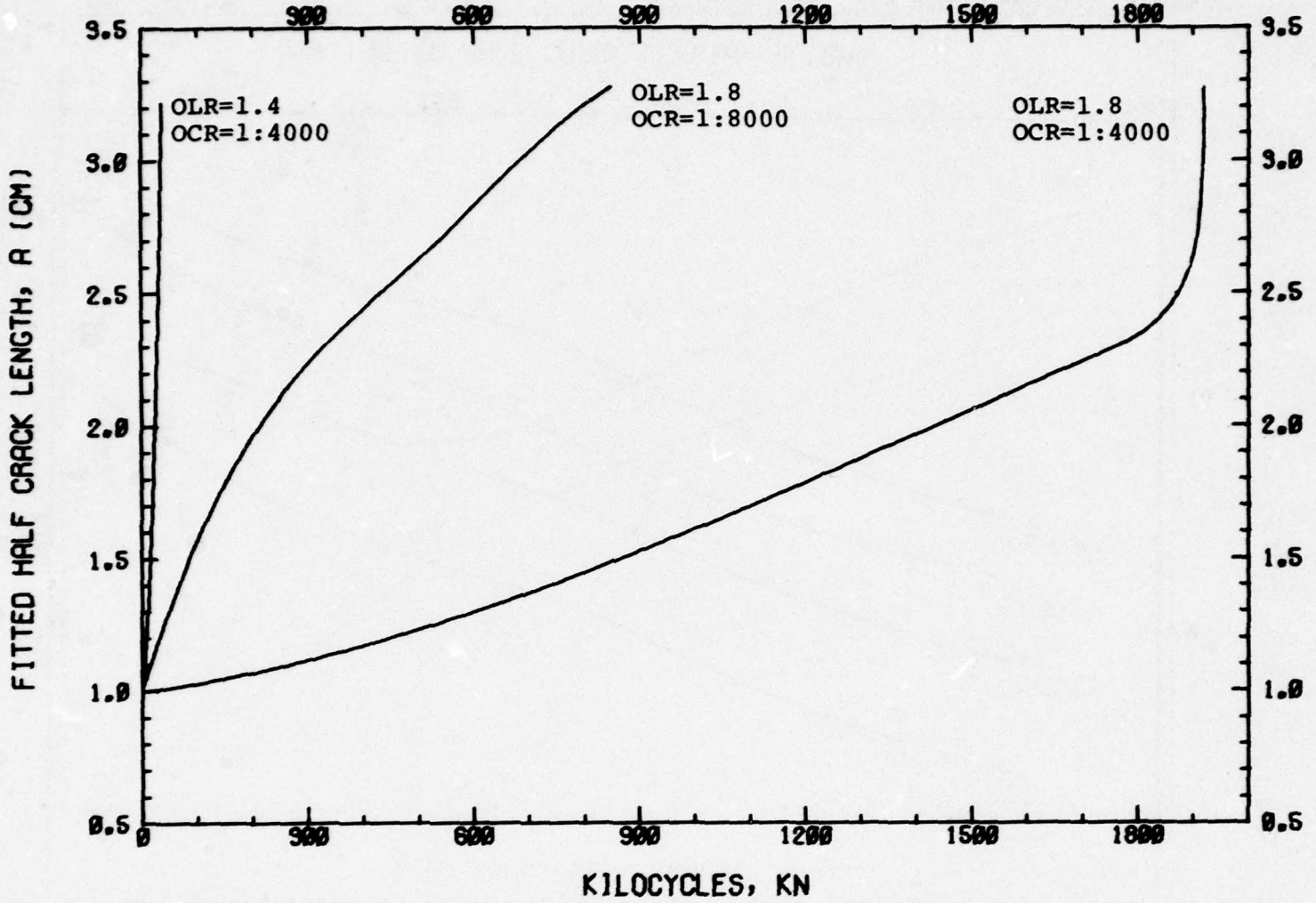

Figure 28 - Crack length vs number of elapsed cycles for periodic single overload tests of 7075-T6.

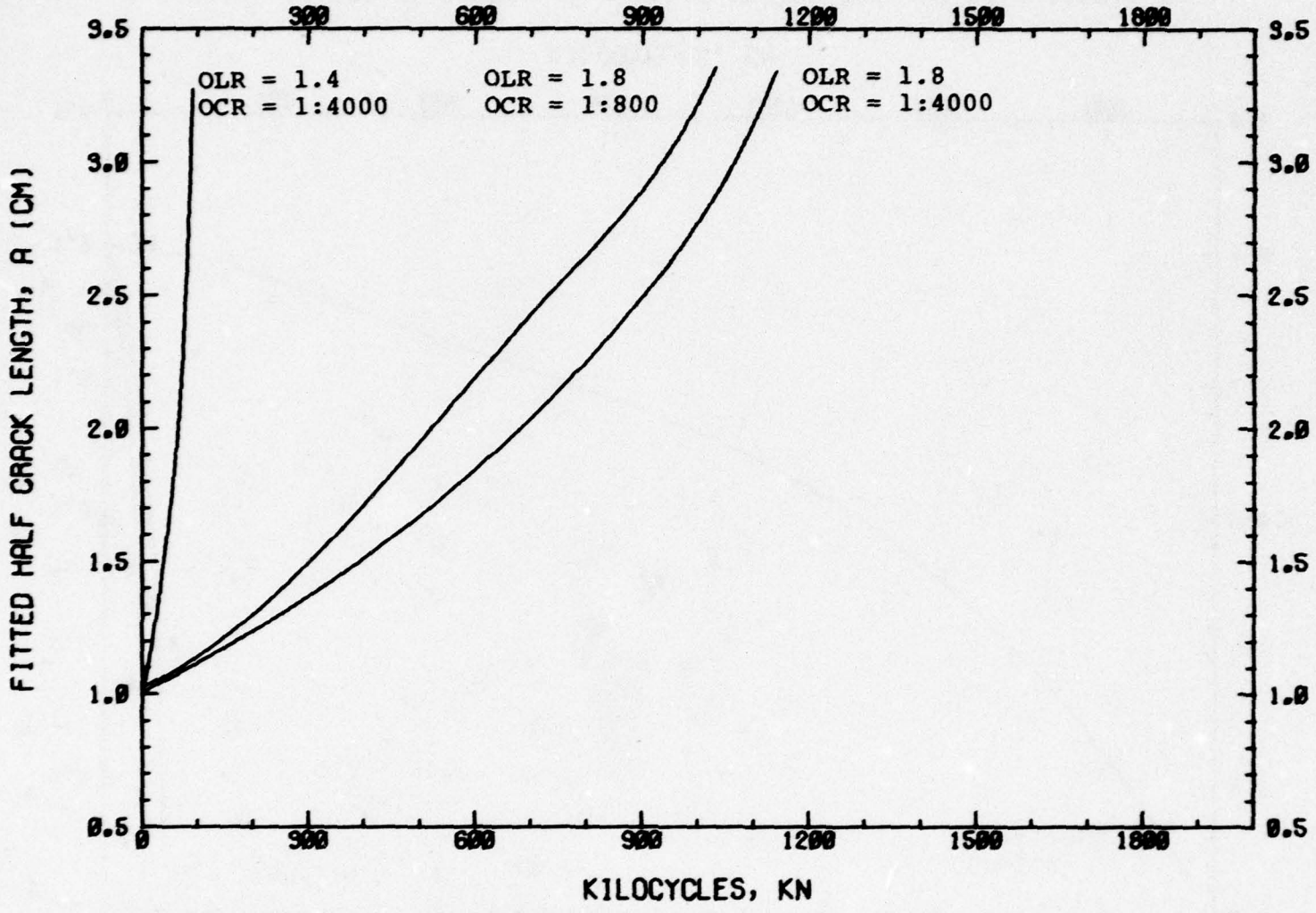

Figure 29 - Crack length vs number of elapsed cycles for periodic single overload tests of 7075-T7.

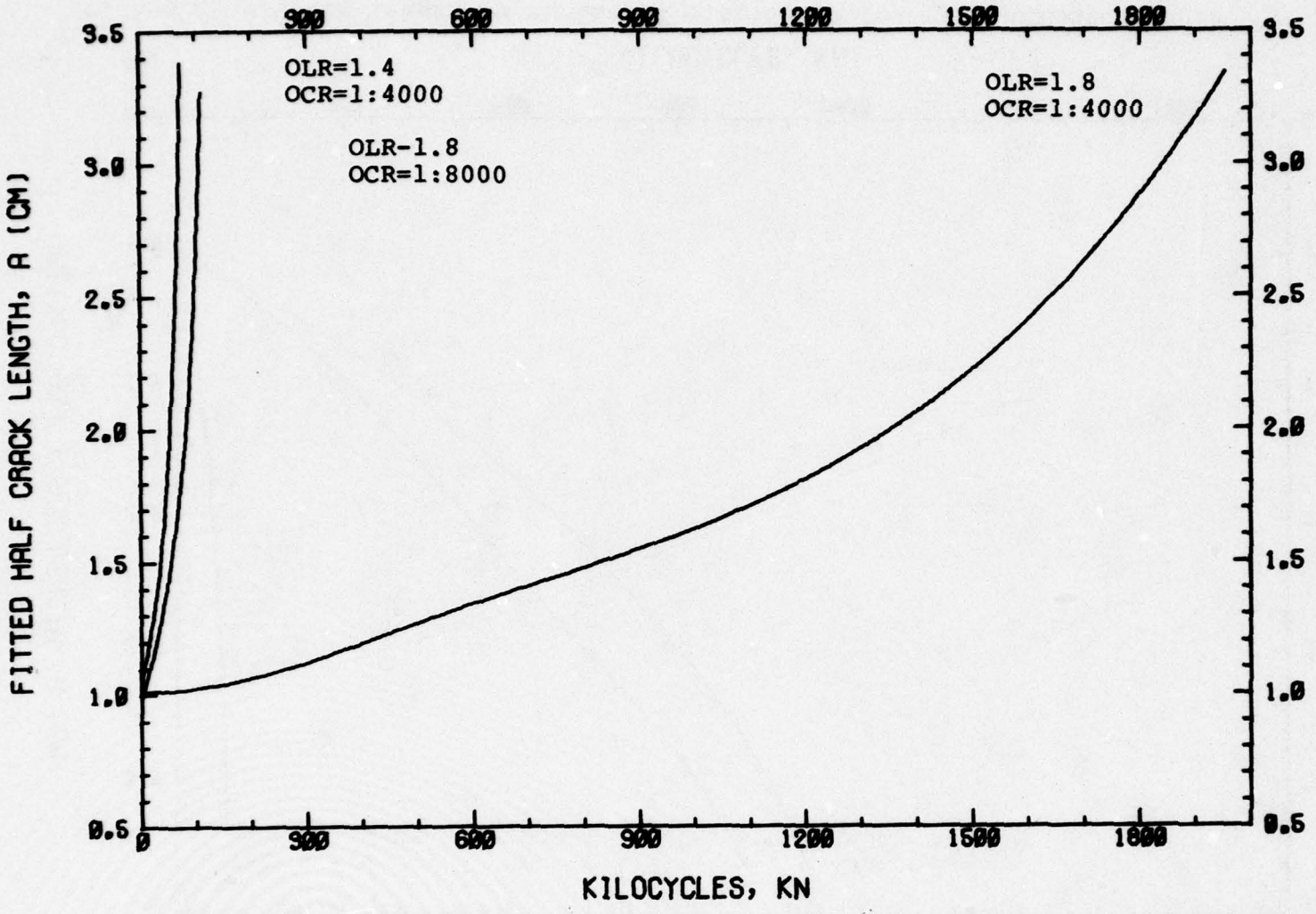

Figure 30 - Crack length vs number of elapsed cycles for periodic single overload tests of 7050-T6.

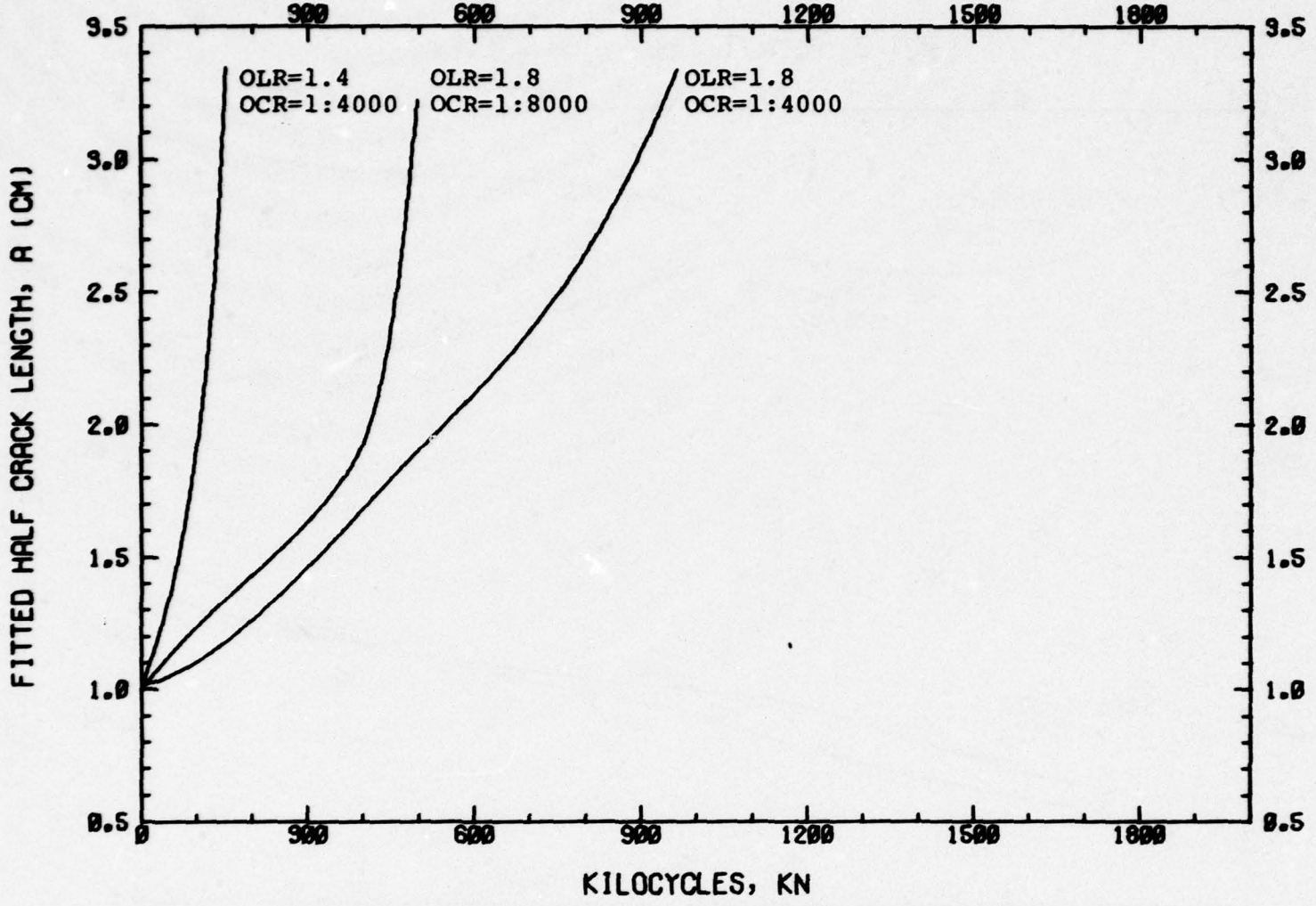

Figure 31 - Crack length vs number of elapsed cycles for periodic single overload tests of 7050-T7.

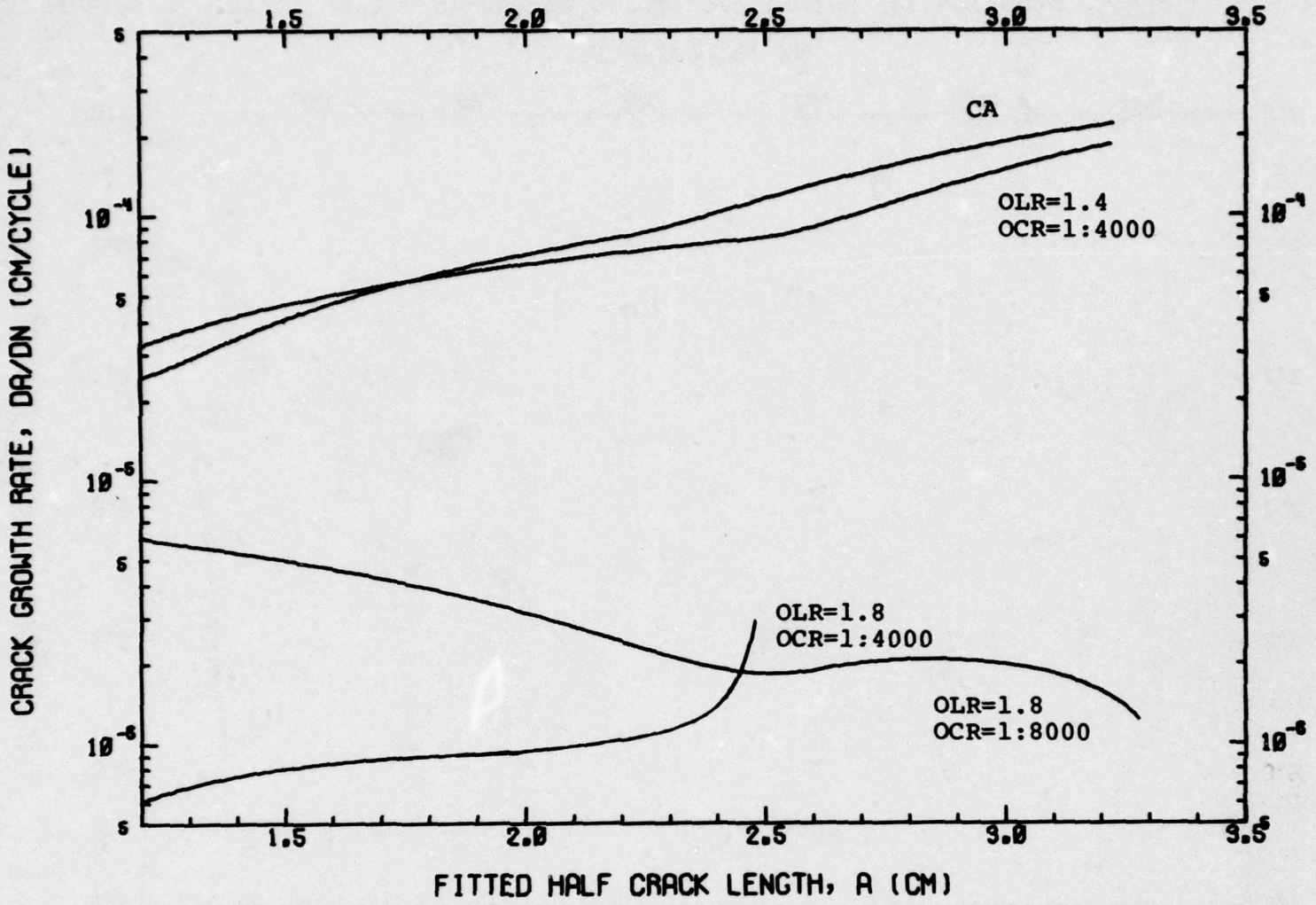

Figure 32 - Crack growth rate vs crack length for constant amplitude and periodic single overload tests of 7075-T6.

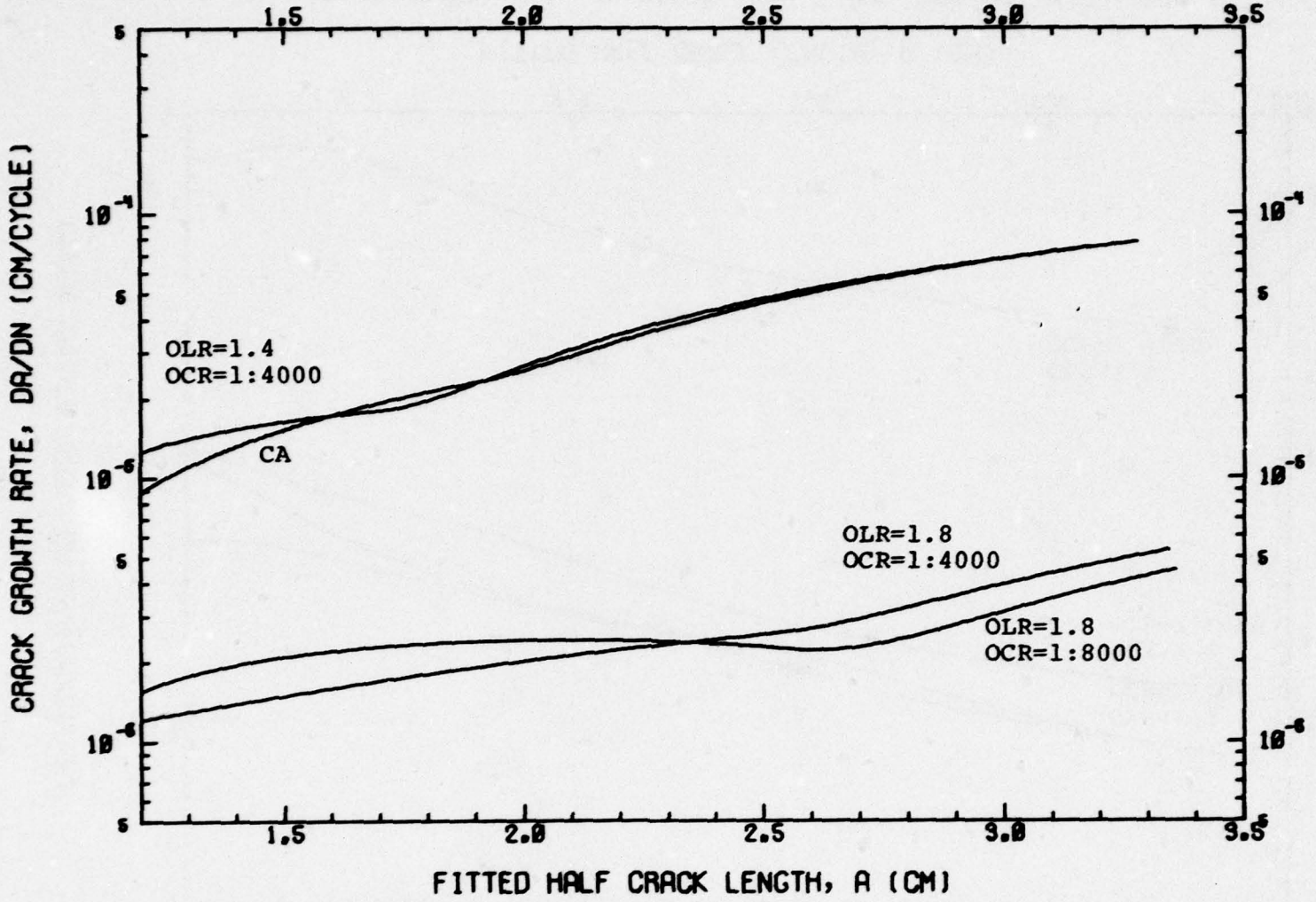

Figure 33 - Crack growth rate vs crack length for constant amplitude and periodic single overload tests of 7075-T7.

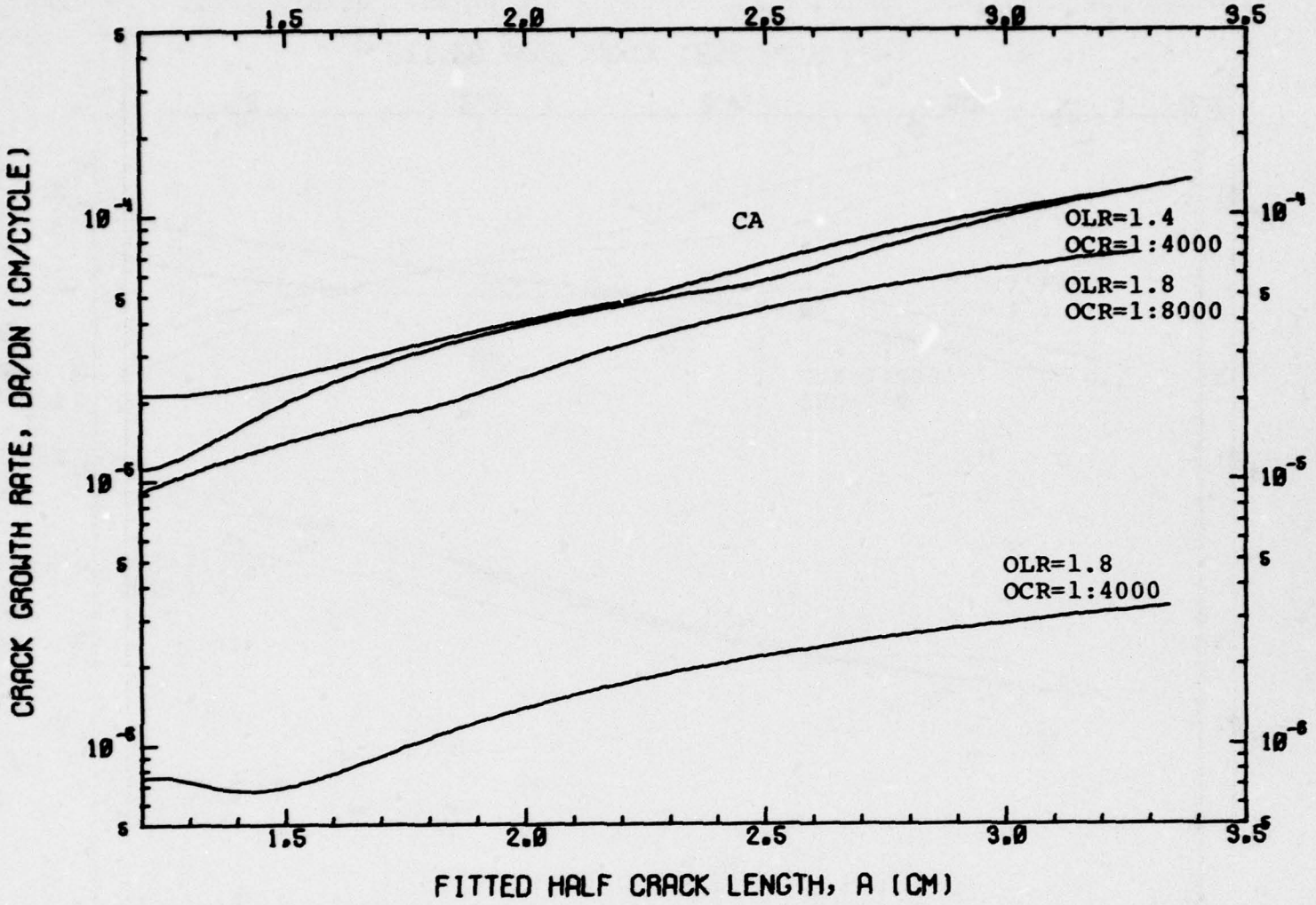

Figure 34 - Crack growth rate vs crack length for constant amplitude and periodic single overload tests of 7050-T6.

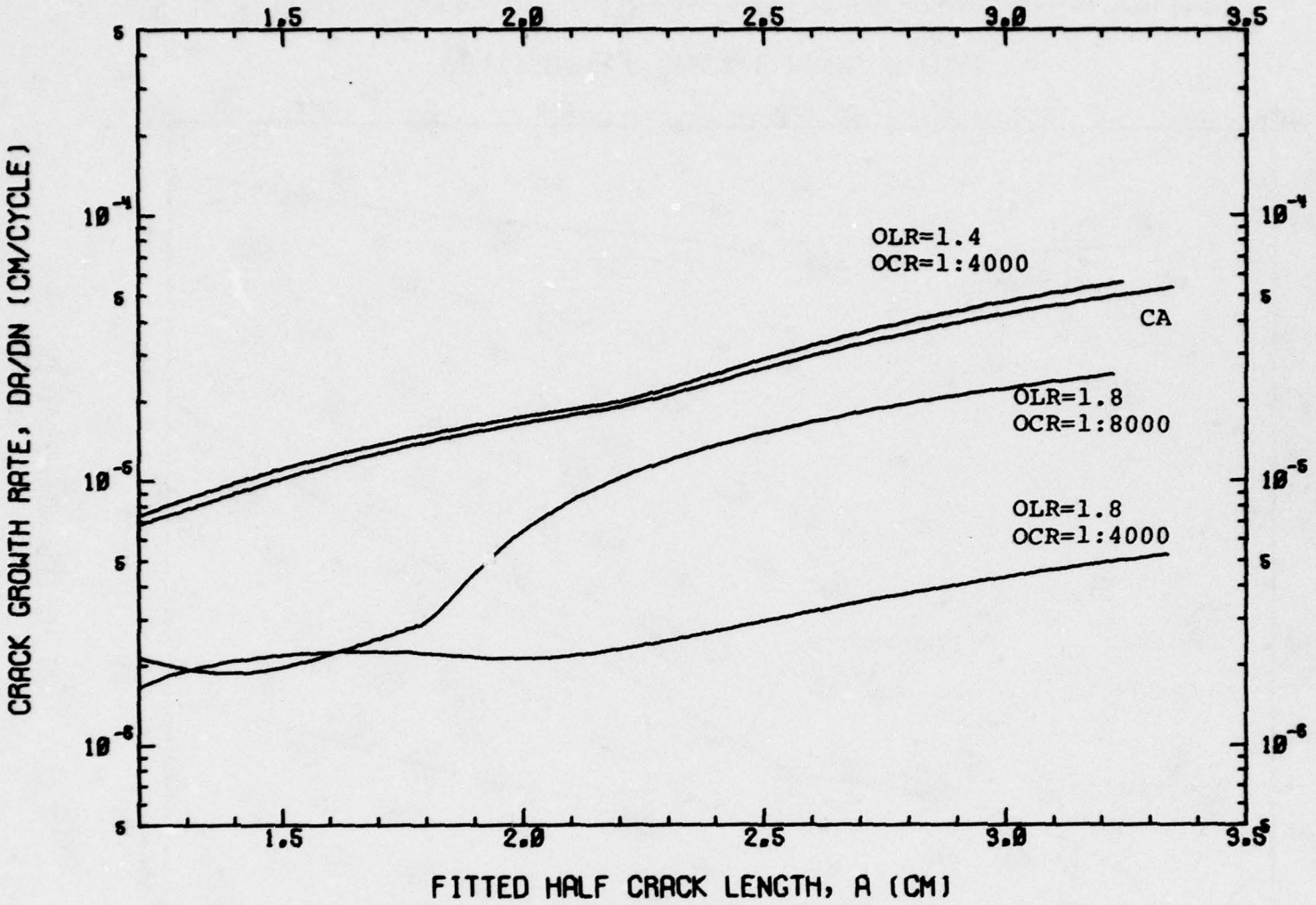

Figure 35 - Crack growth rate vs crack length for constant amplitude and periodic single overload tests of 7050-T7.

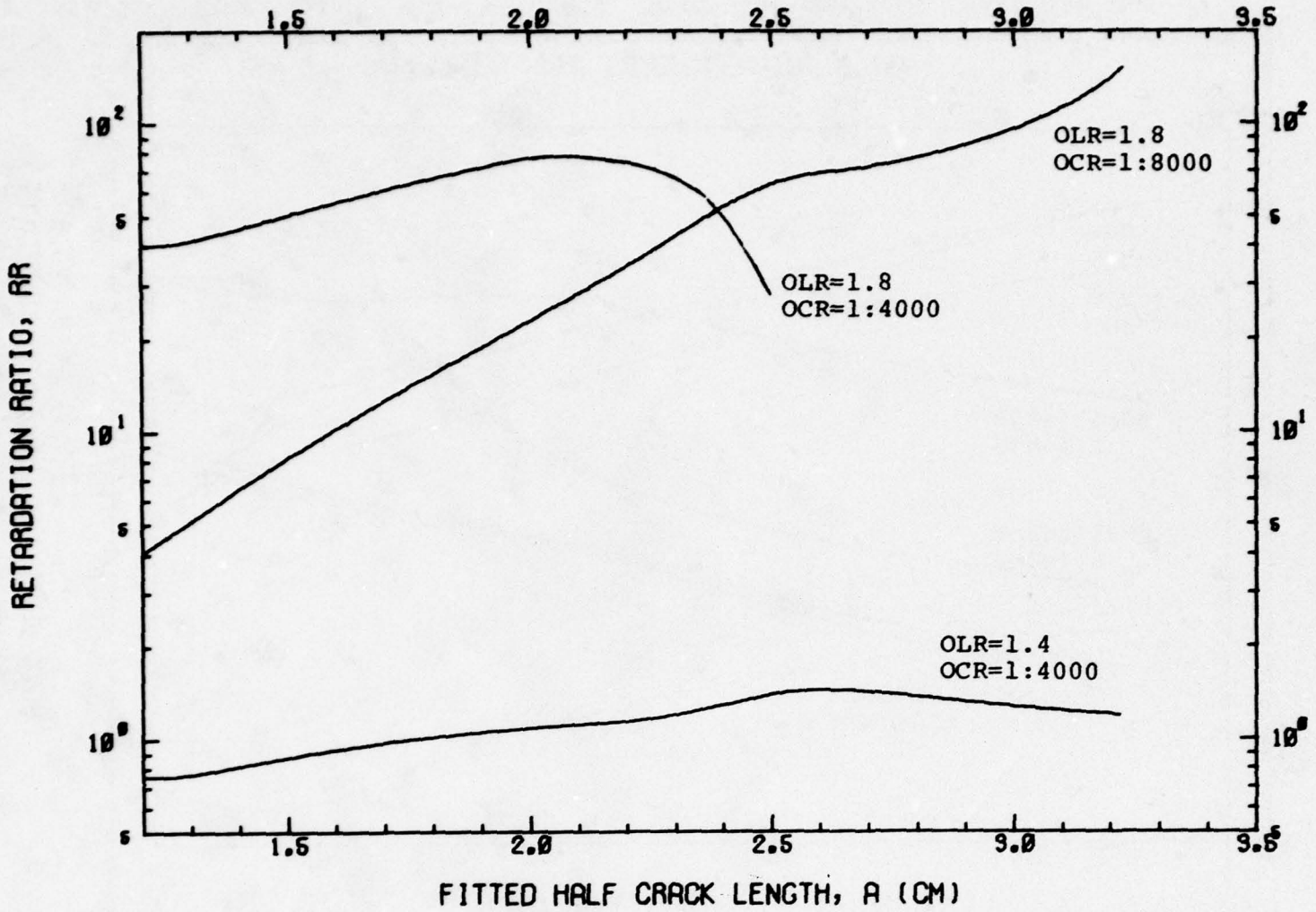

Figure 36 - Ratio of constant amplitude, da/dN, to periodic single overload spectrum, da/dN, vs crack length for 7075-T6.

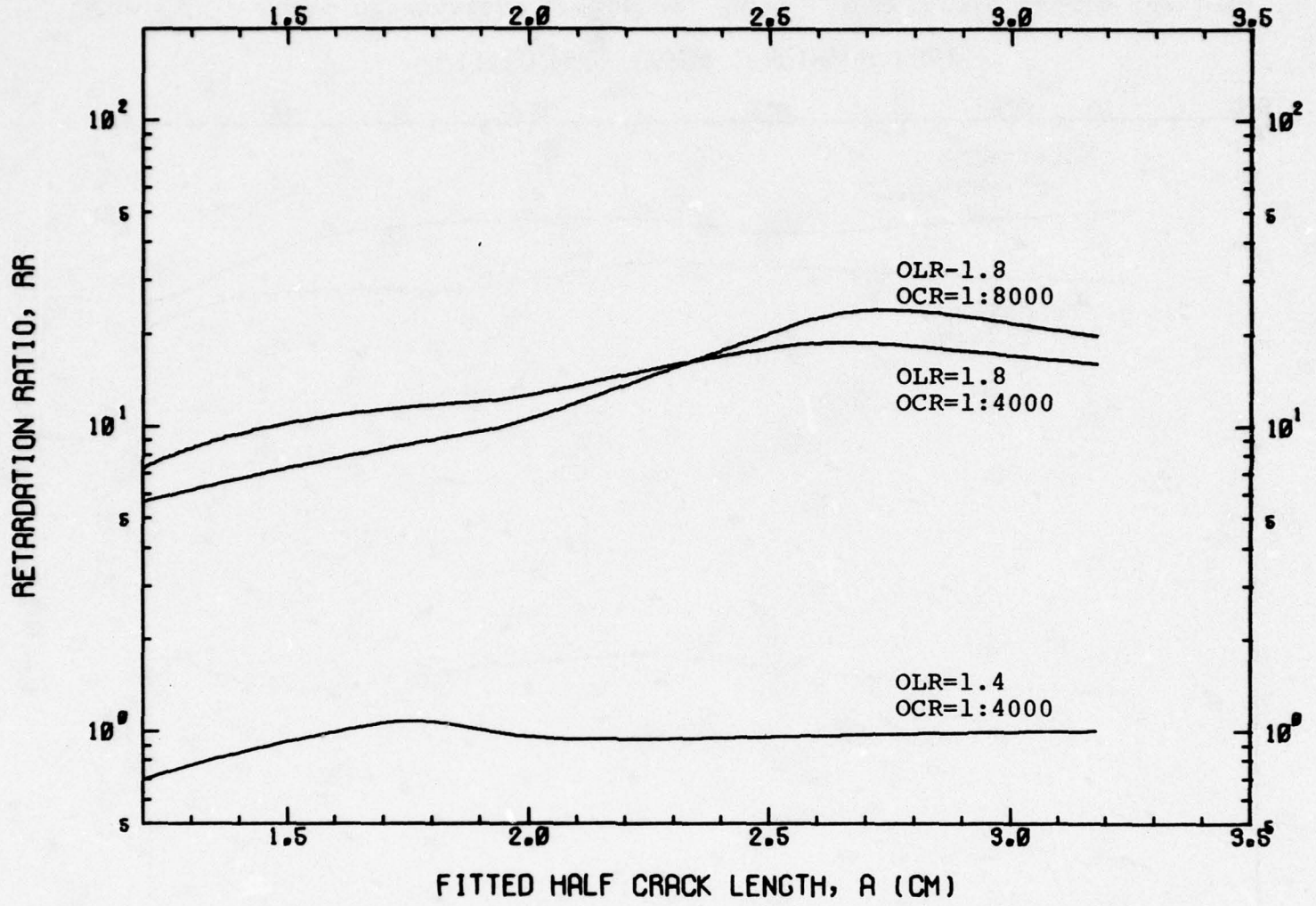

Figure 37 - Ratio of constant amplitude, da/dN, to periodic single overload spectrum, da/dN, vs crack length for 7075-T7.

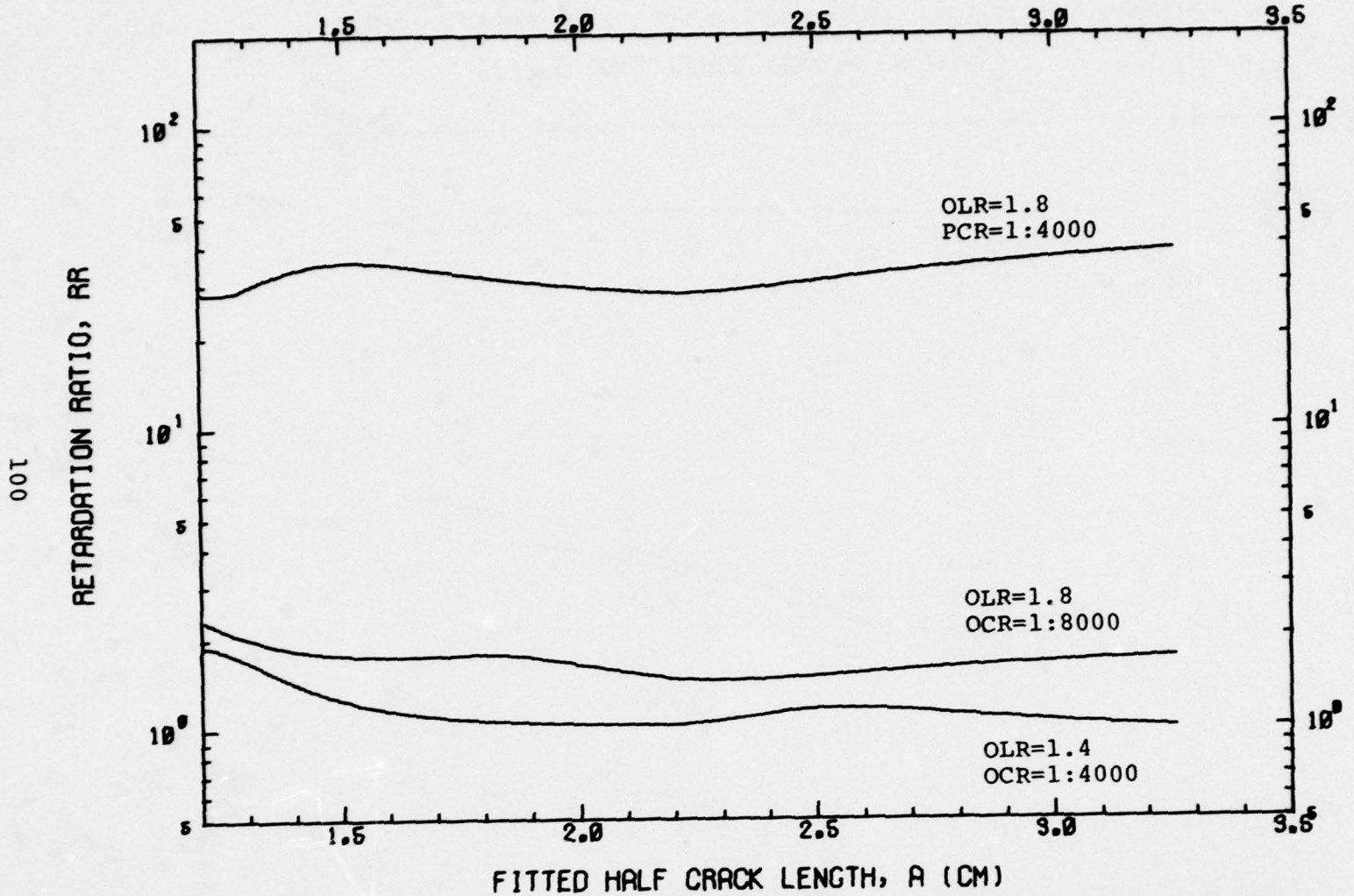

Figure 38 - Ratio of constant amplitude, da/dN, to periodic single overload spectrum, da/dN, vs crack length for 7050-T6.

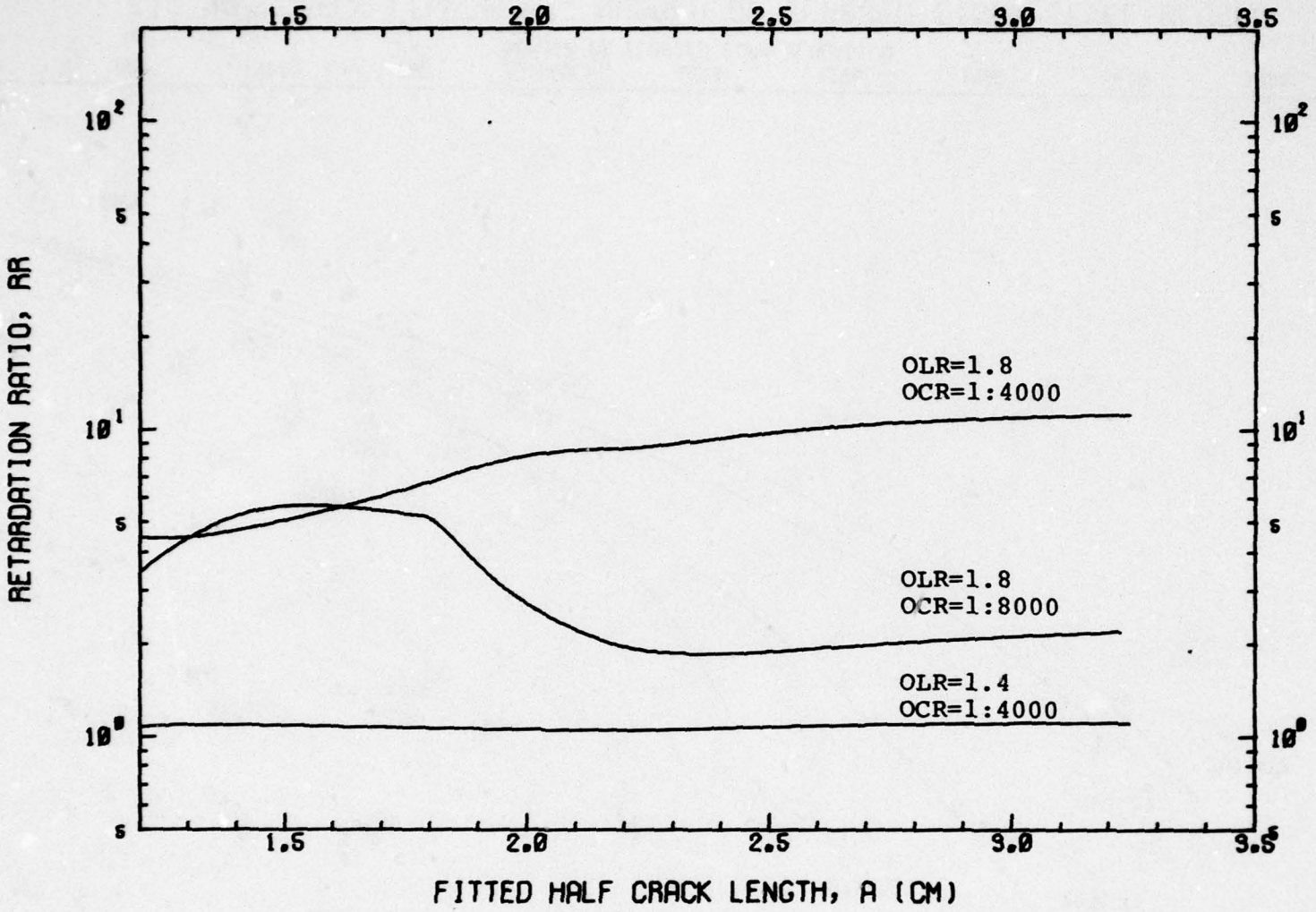

Figure 39 - Ratio of constant amplitude, da/dN, to periodic single overload spectrum, da/dN, vs crack length for 7050-T7.

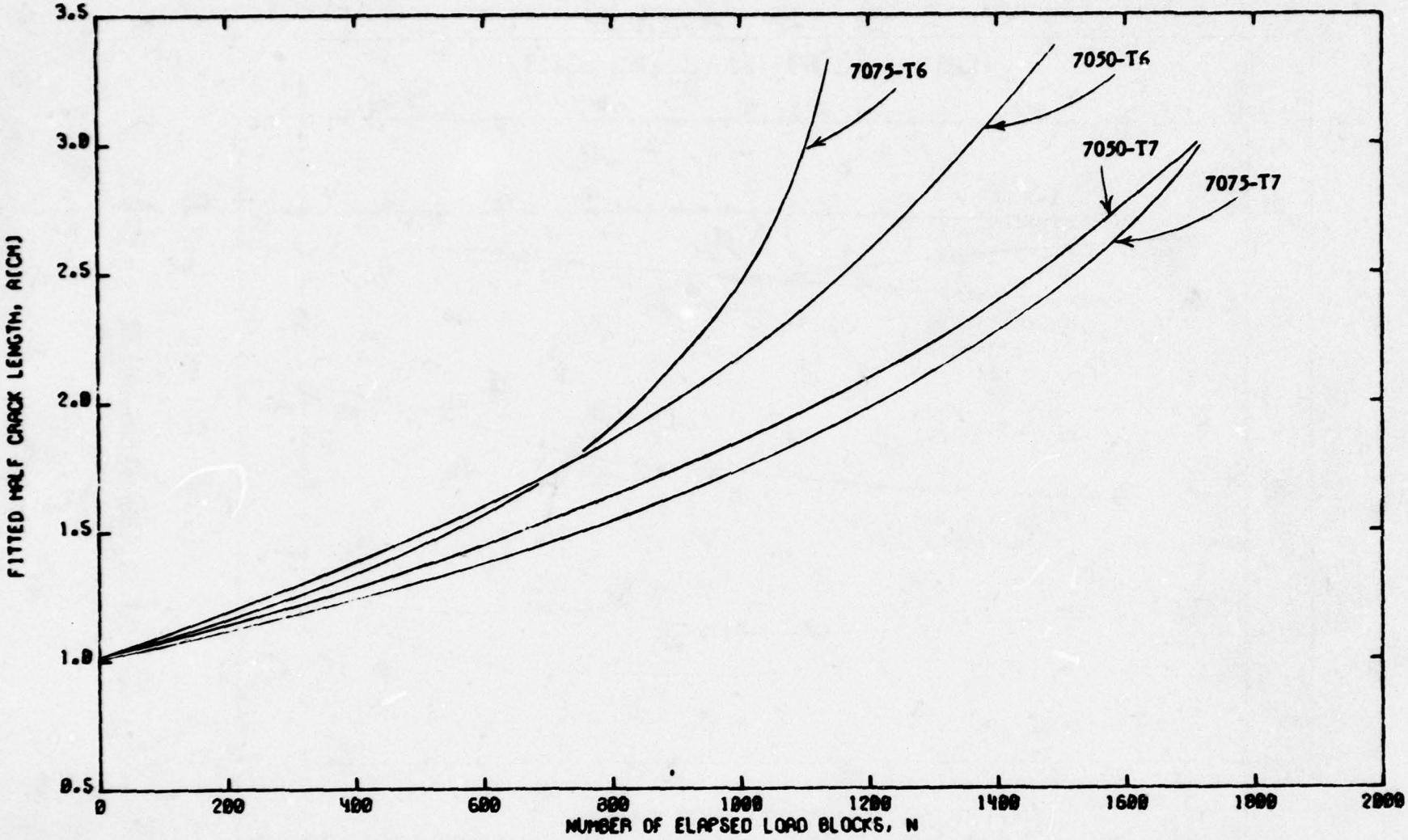

FIG 40 CRACK LENGTH VS. NUMBER OF ELAPSED EIGHT LEVEL BLOCKS FOR 7XXX ALUMINUM ALLOYS

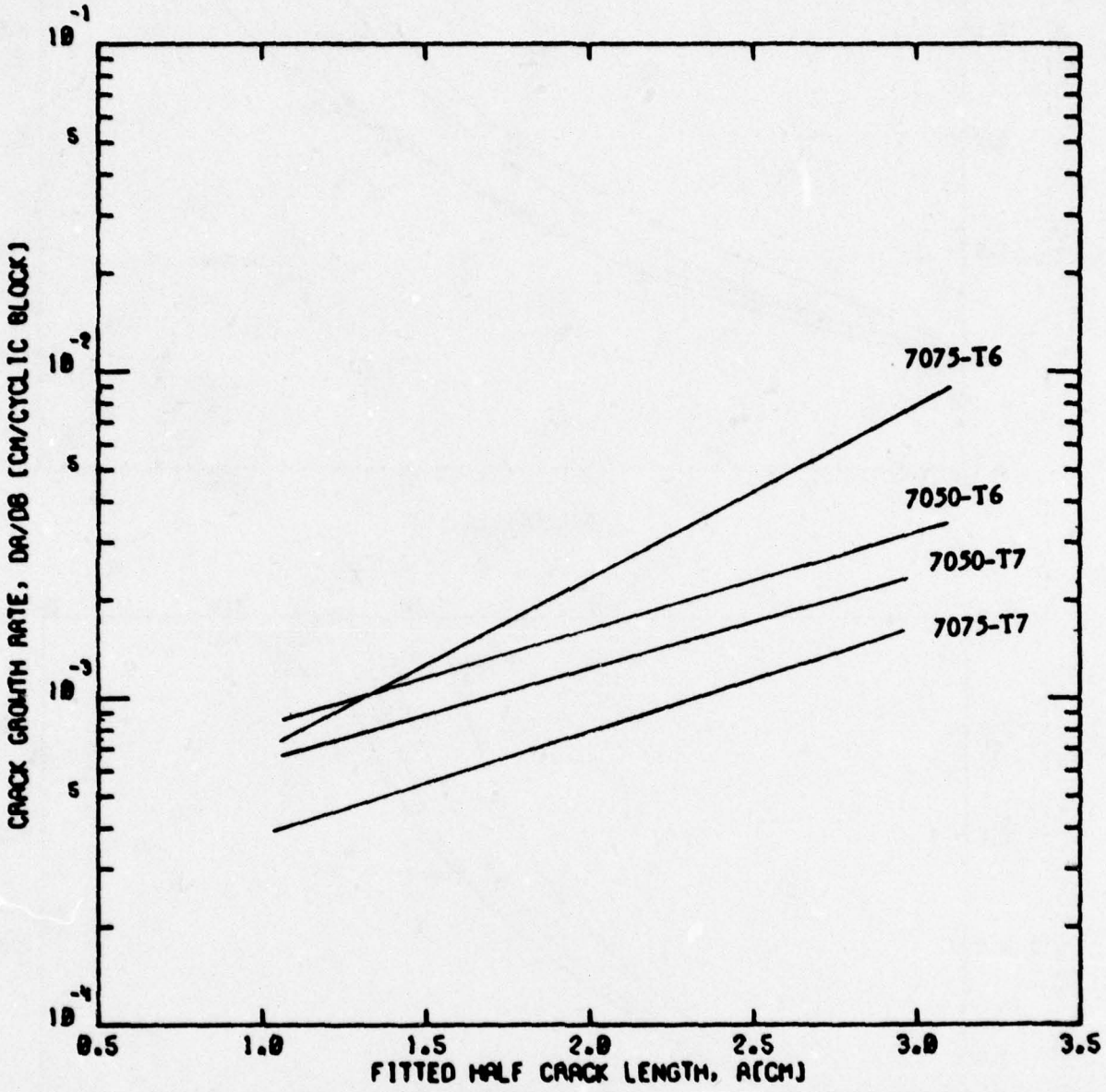

FIG 41 CRACK GROWTH RATES VS. CRACK LENGTH UNDER EIGHT LEVEL BLOCK LOADING FOR 7XXX ALUMINUM ALLOYS

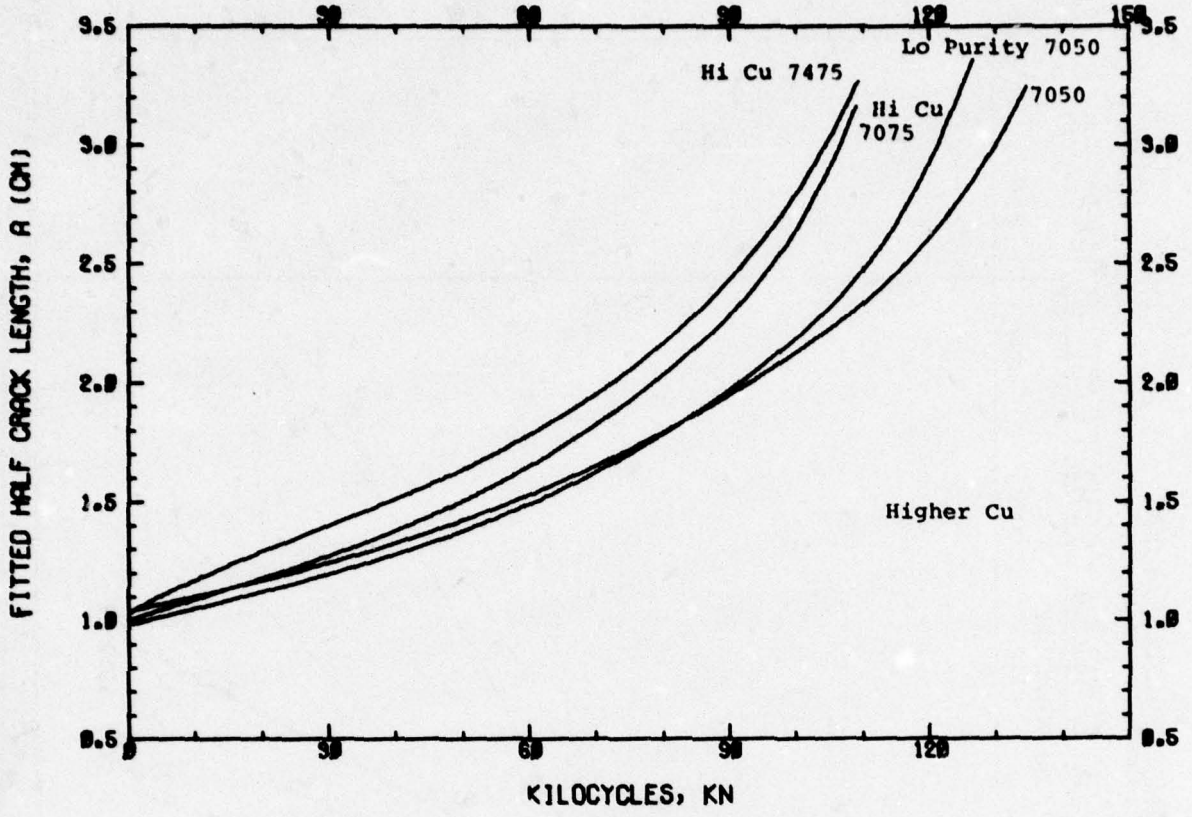

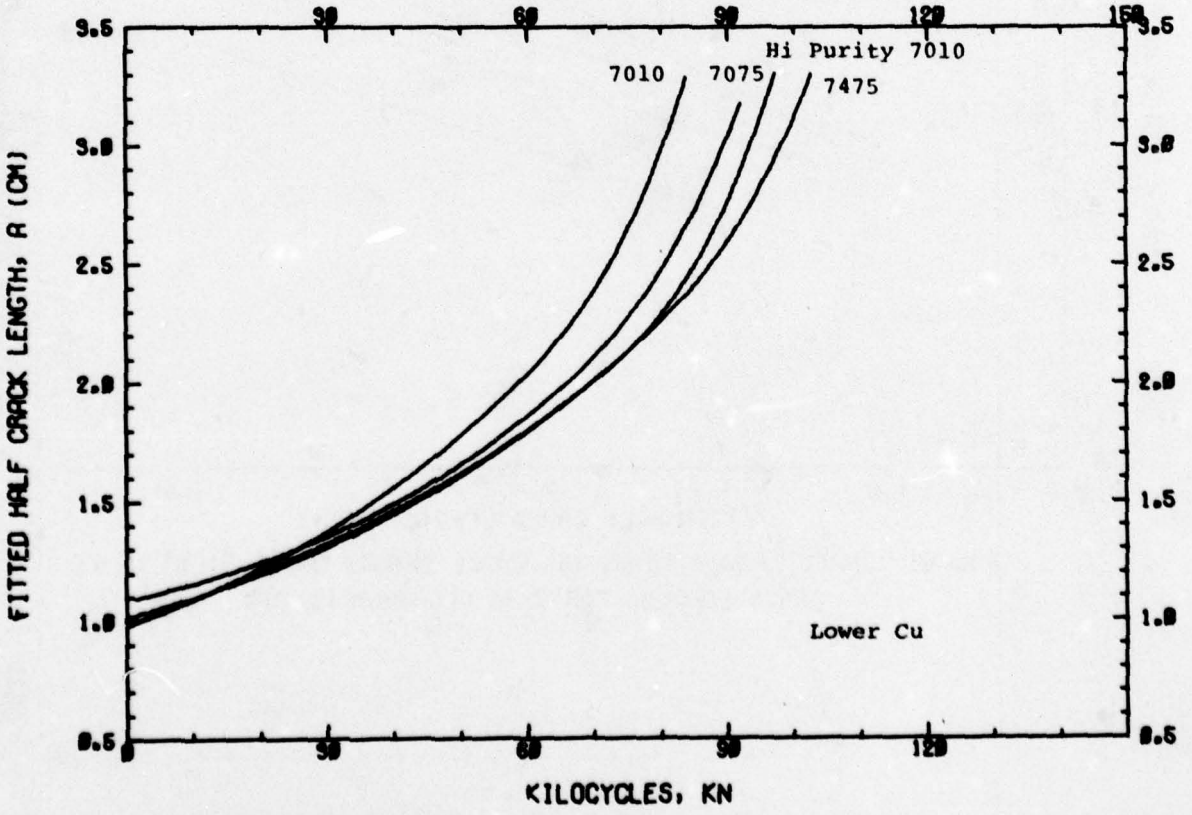

Figure 42 - Crack length vs number of elapsed cycles for constant amplitude tests of eight microstructural variants of alloys 7075 and 7050 in a T7-type temper.

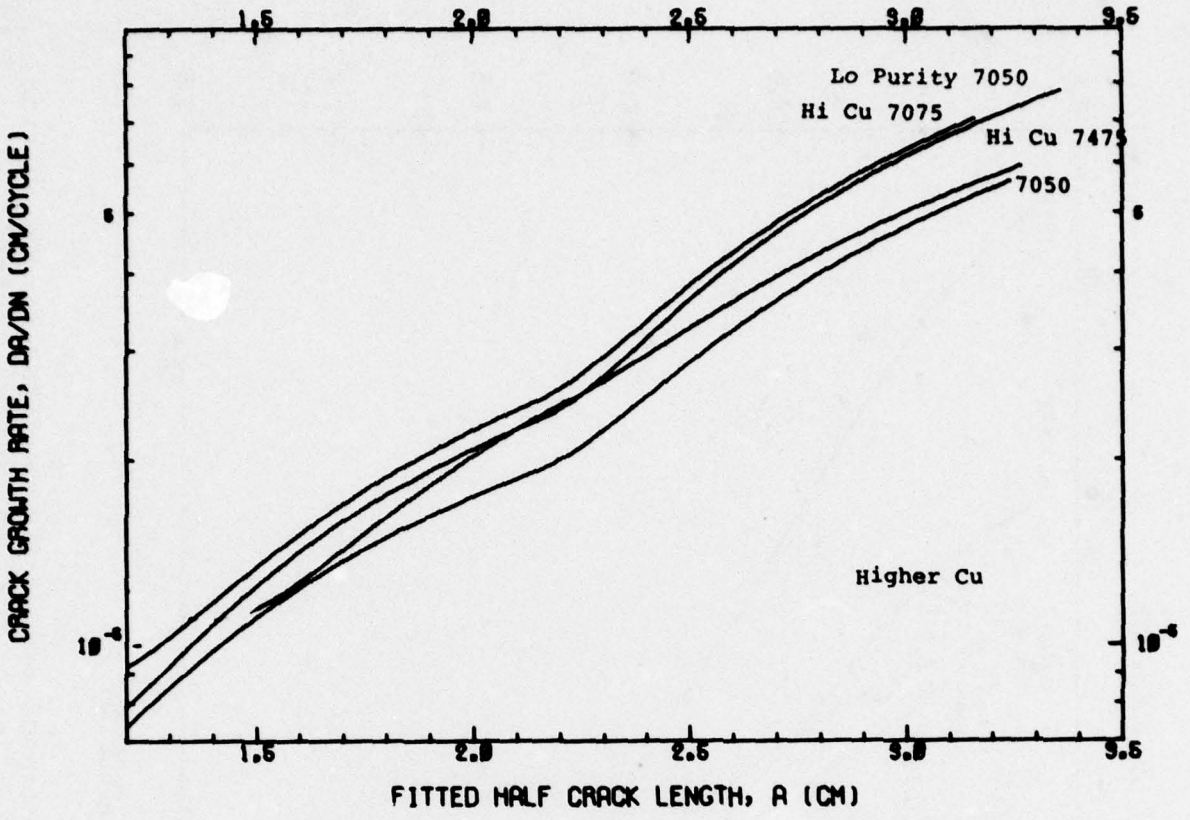

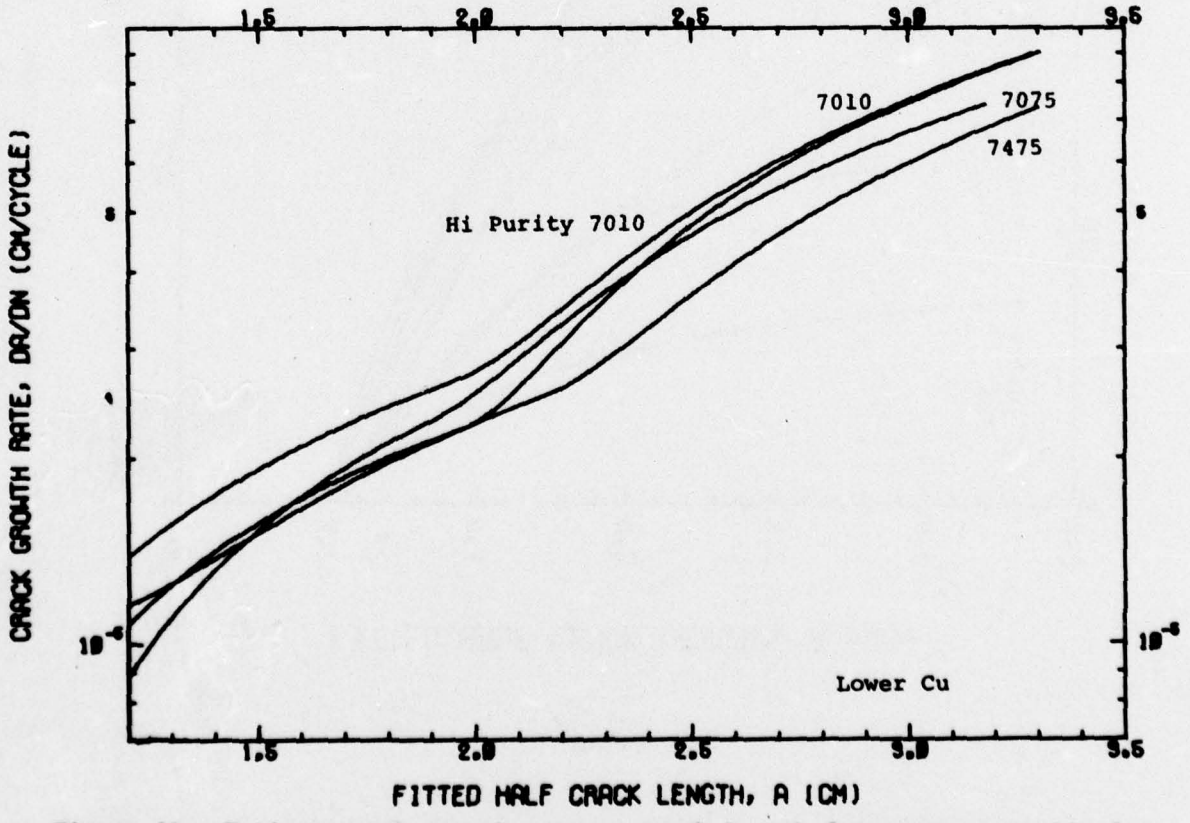

Figure 43 - Fatigue crack growth rate vs crack length for constant amplitude tests of eight microstructural variants of alloys 7075 and 7050.

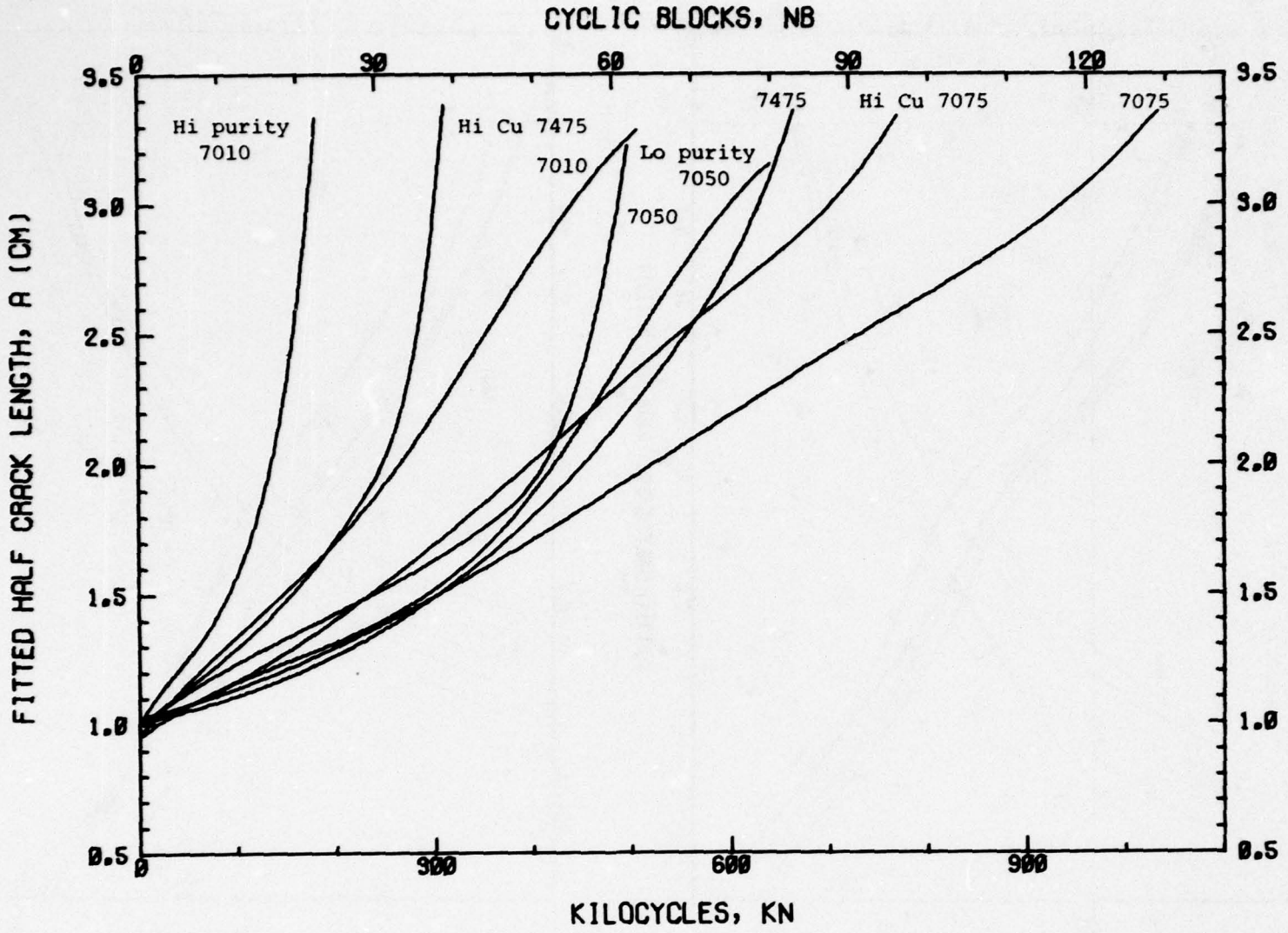

Figure 44 - Crack length vs number of elapsed cycles for periodic single overload tests (OLR=1.8, OCR=1:8000) of eight microstructural variants of alloys 7075 and 7050.

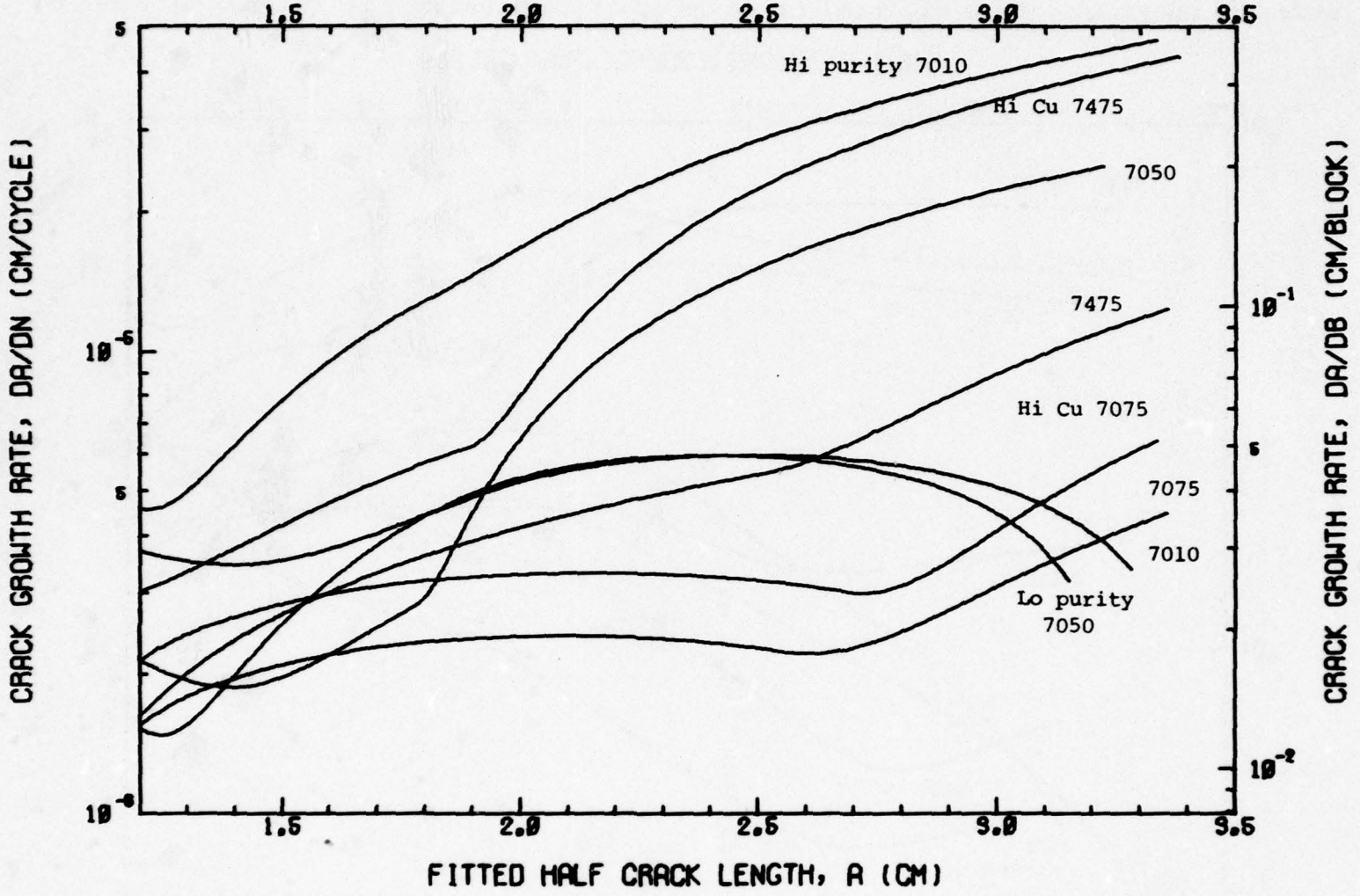

Figure 45 - Crack growth rate vs crack length for periodic single overload tests (OLR=1.8, OCR=1:8000) of eight microstructural variants of alloys 7075 and 7050.

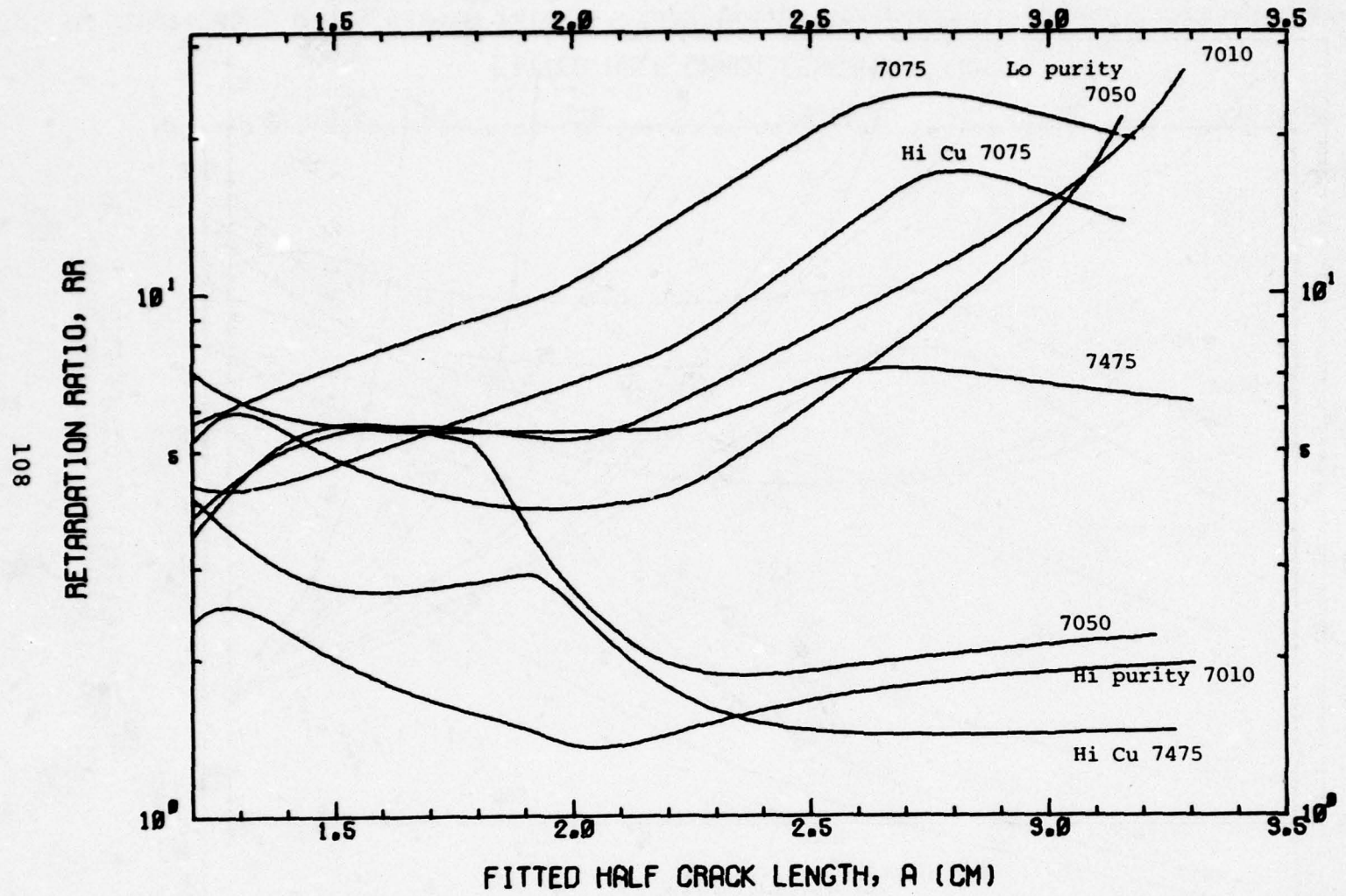

Figure 46 - Ratio of constant amplitude, da/dN, to periodic single overload spectrum (OLR=1.8, OCR=1:8000), da/dN, vs crack length for eight microstructural variants of alloys 7075 and 7050.

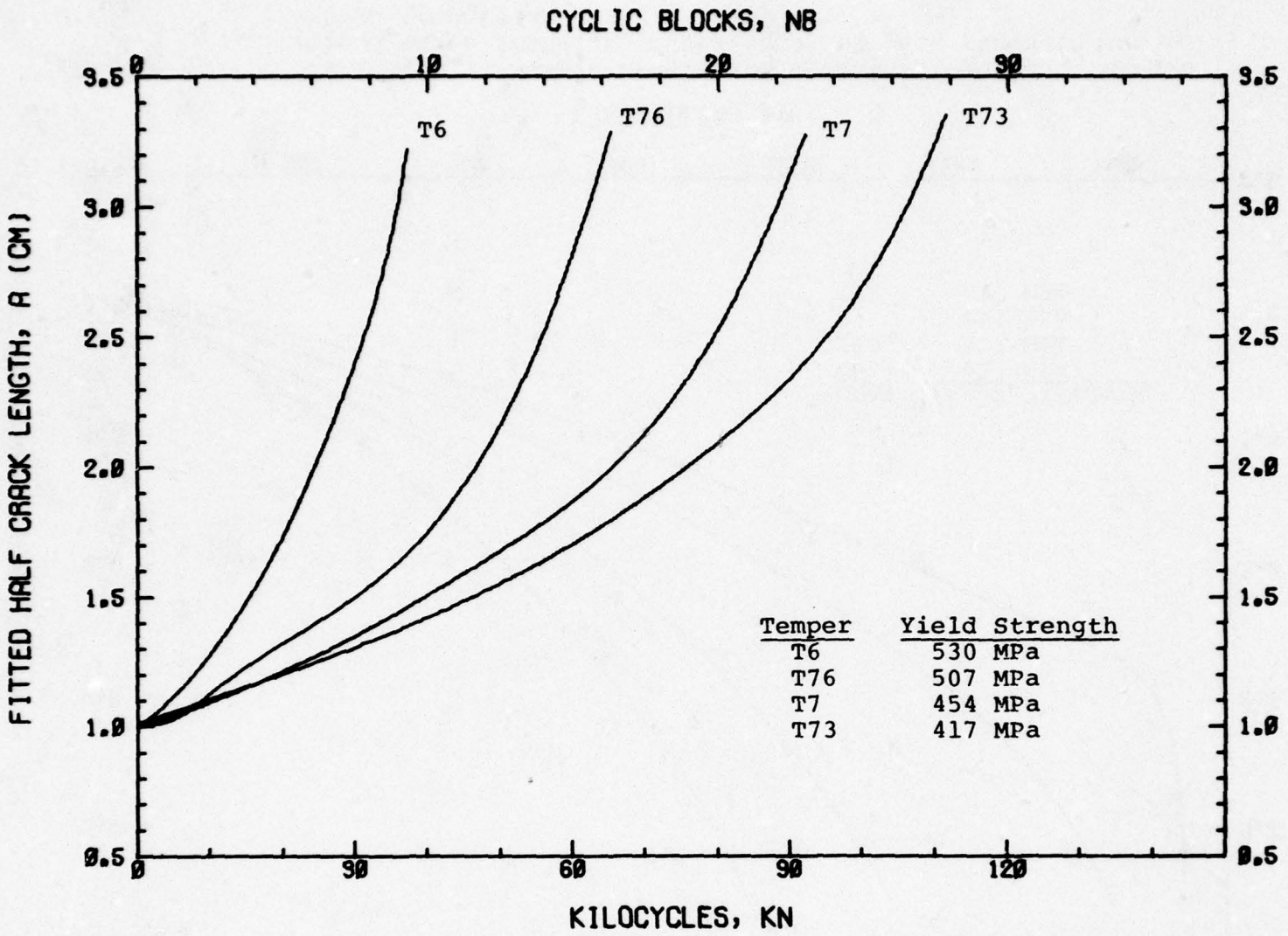

Figure 47 - Crack length vs number of elapsed cycles for periodic single overload tests (OLR=1.4, OCR=1:4000) of peak strength and overaged tempers of 7075.

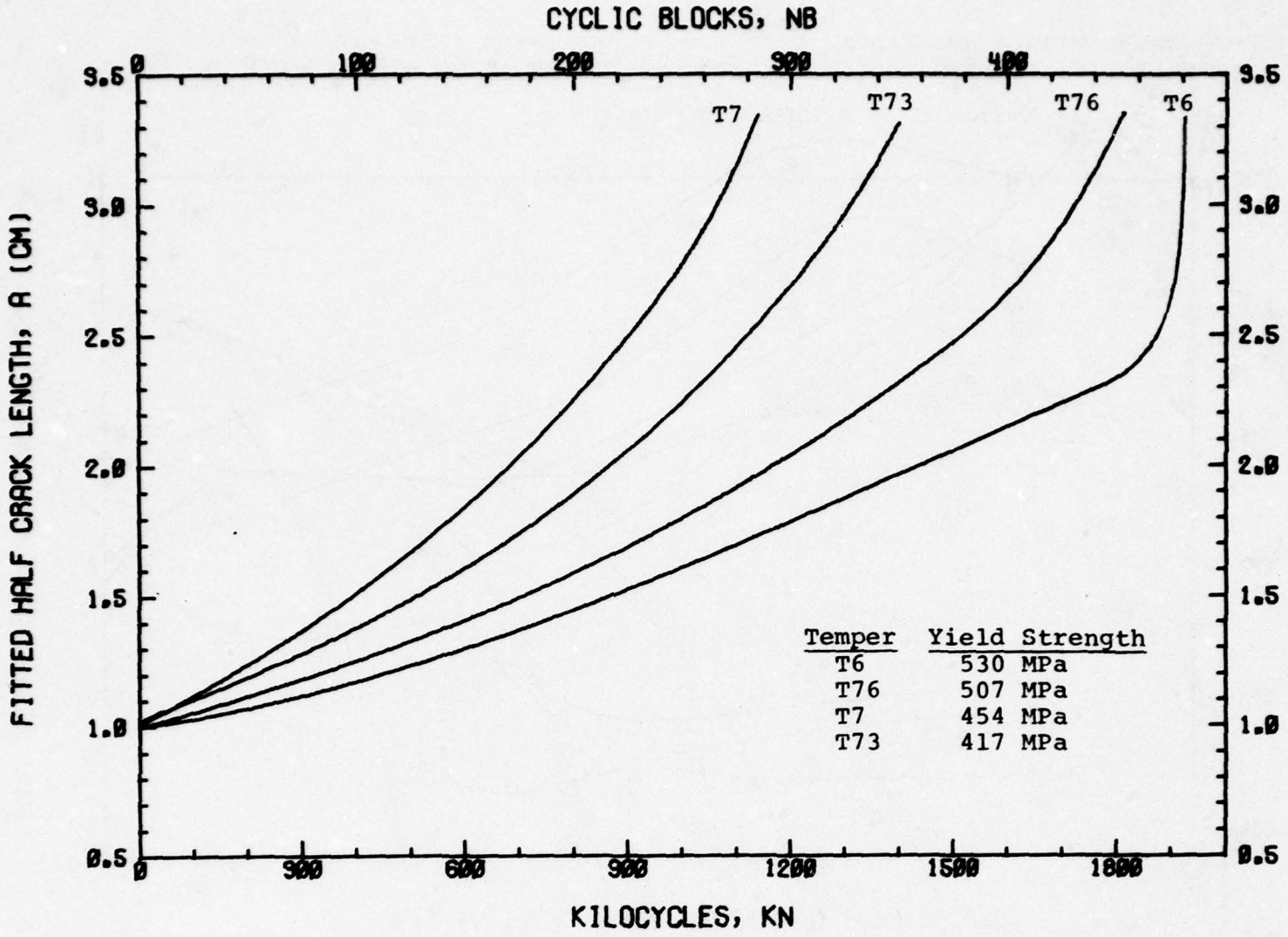

Figure 48 - Crack length vs number of elapsed cycles for periodic single overload tests (OLR=1.8, OCR=1:4000) of peak strength and overaged tempers of 7075.

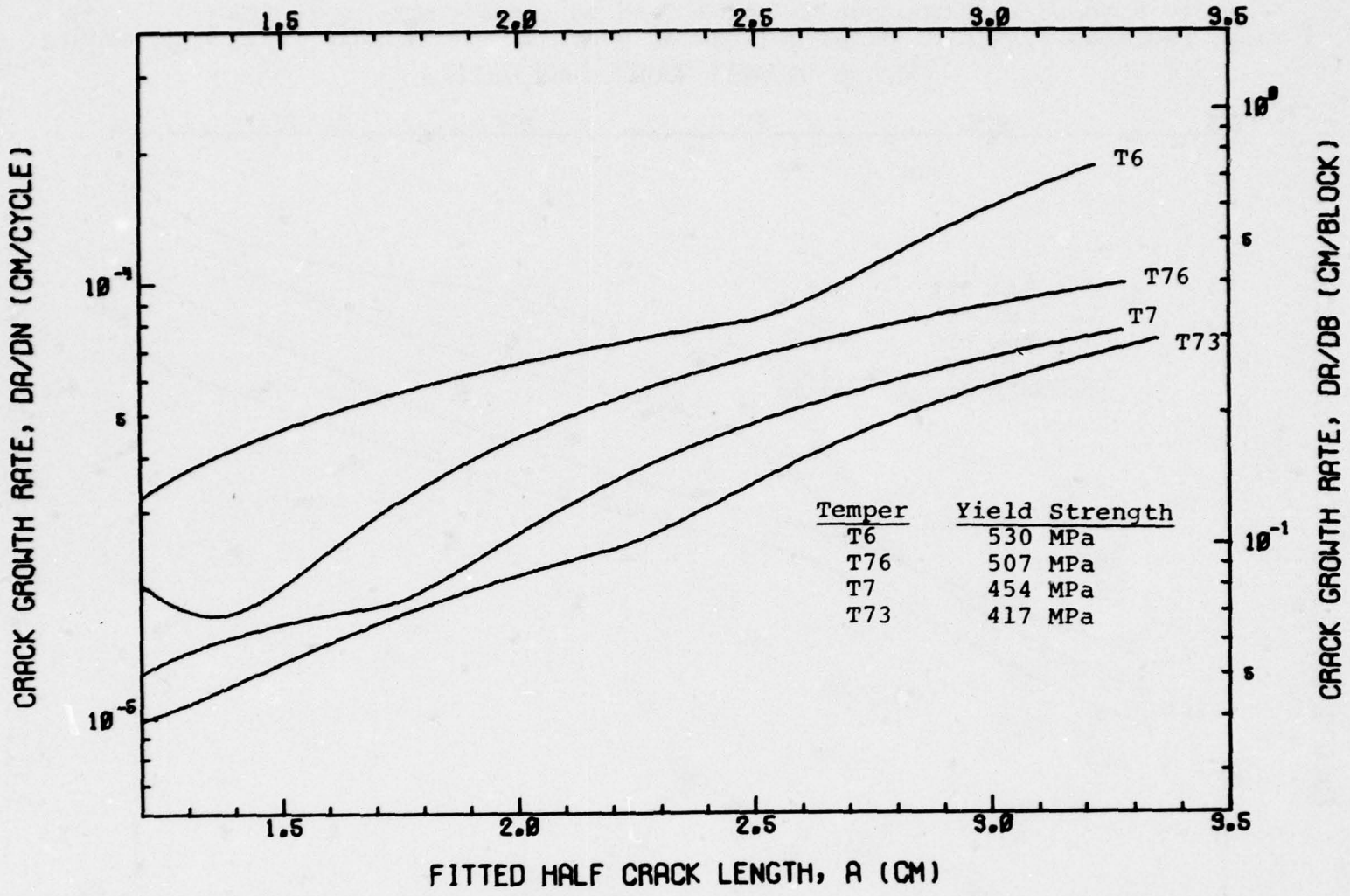

Figure 49 - Crack growth rate vs crack length for periodic single overload tests (OLR=1.4, OCR=1:4000) of peak strength and overaged tempers of 7075.

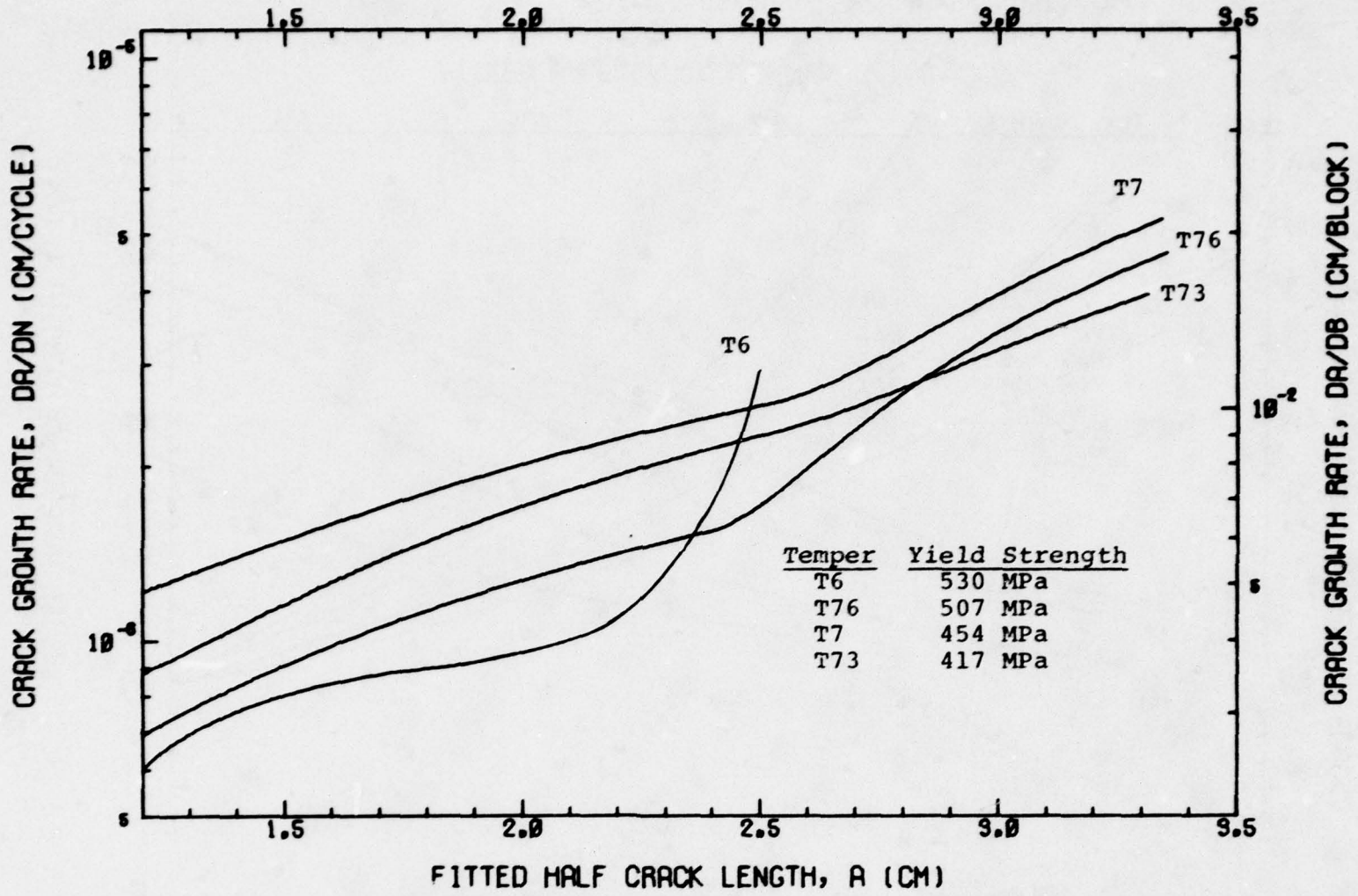

Figure 50 - Crack growth rate vs crack length for periodic single overload tests (OLR=1.8, OCR=1:4000) of peak strength and overaged tempers of 7075.

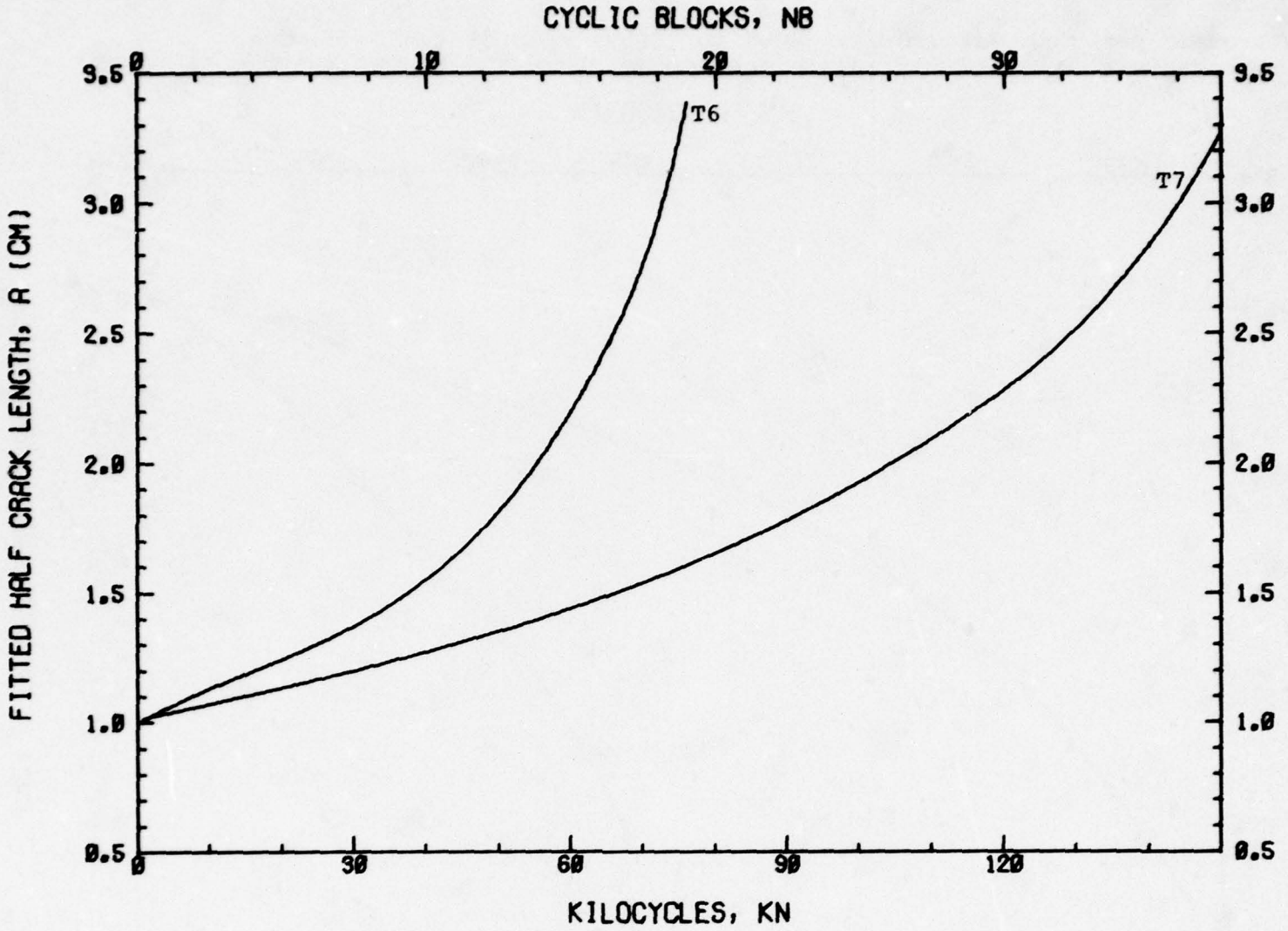

Figure 51 - Crack length vs number of elapsed cycles for periodic single overload tests (OLR=1.4, OCR=1:4000) of peak strength and overaged tempers of 7050.

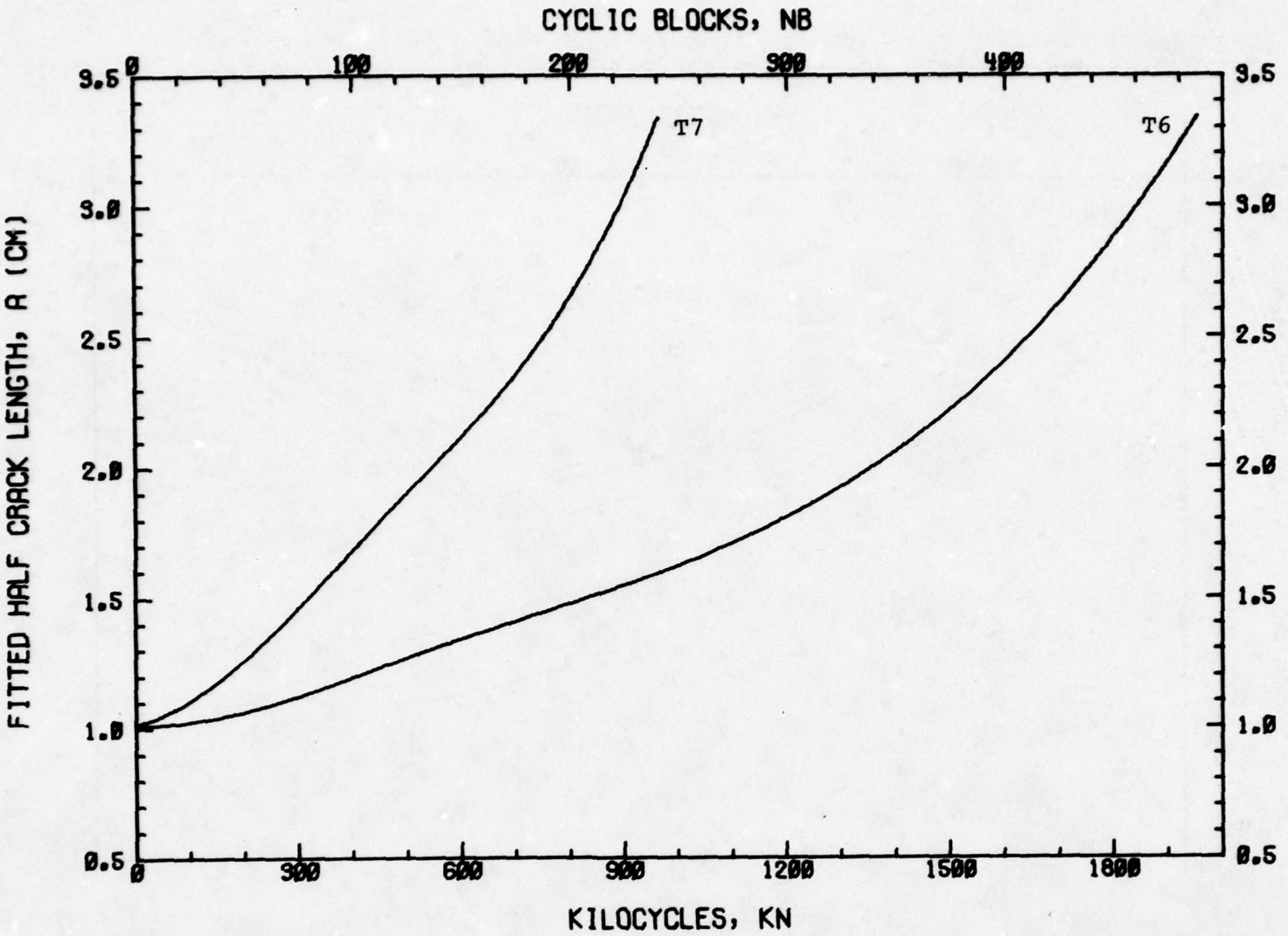

Figure 52 - Crack length vs number of elapsed cycles for periodic single overload tests (OLR=1.8, OCR=1:4000) of peak strength and overaged tempers of 7050.

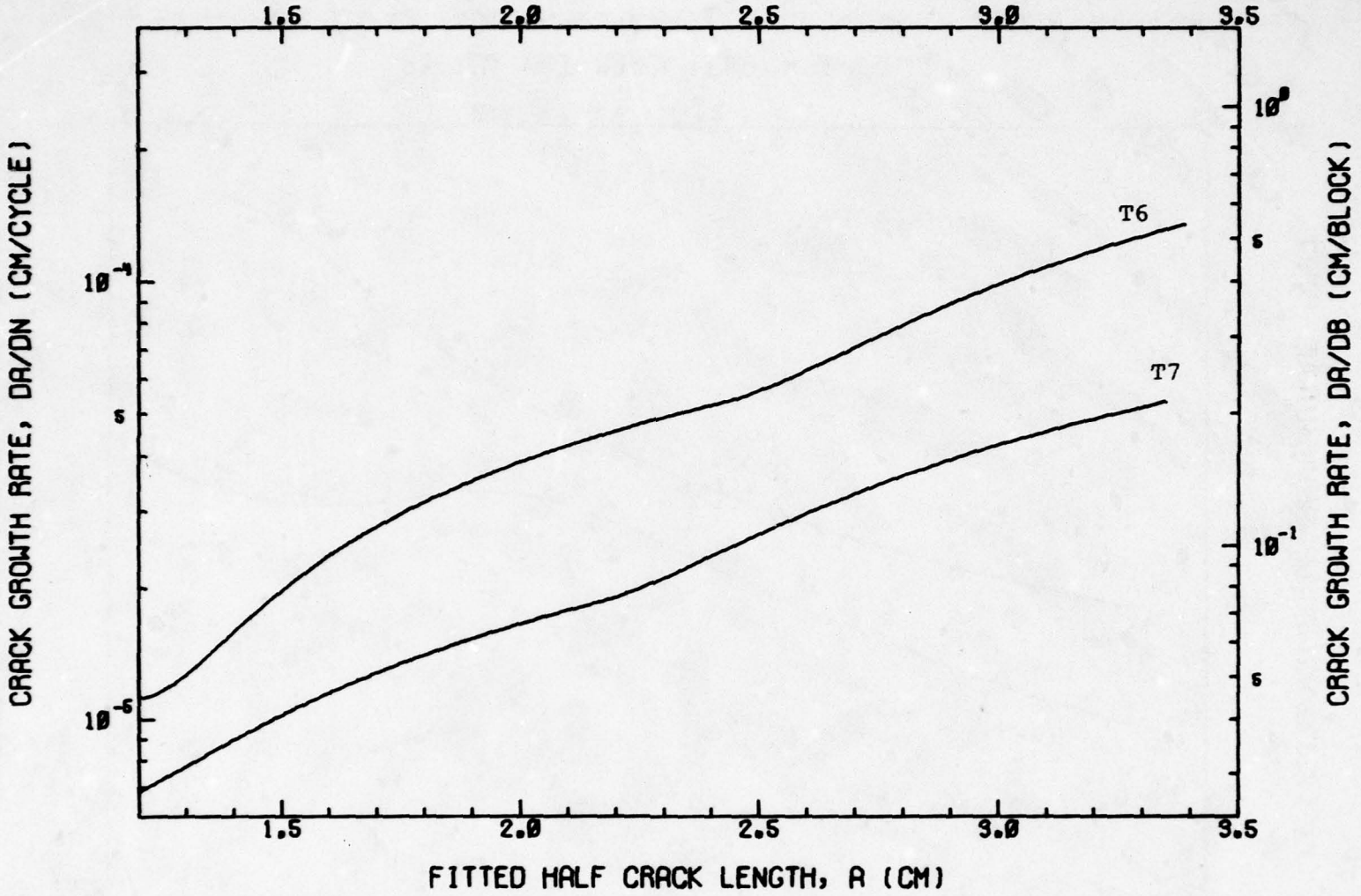

Figure 53 - Crack growth rate vs crack length for periodic single overload tests (OLR=1.4, OCR=1:4000) of peak strength and overaged tempers of alloy 7050.

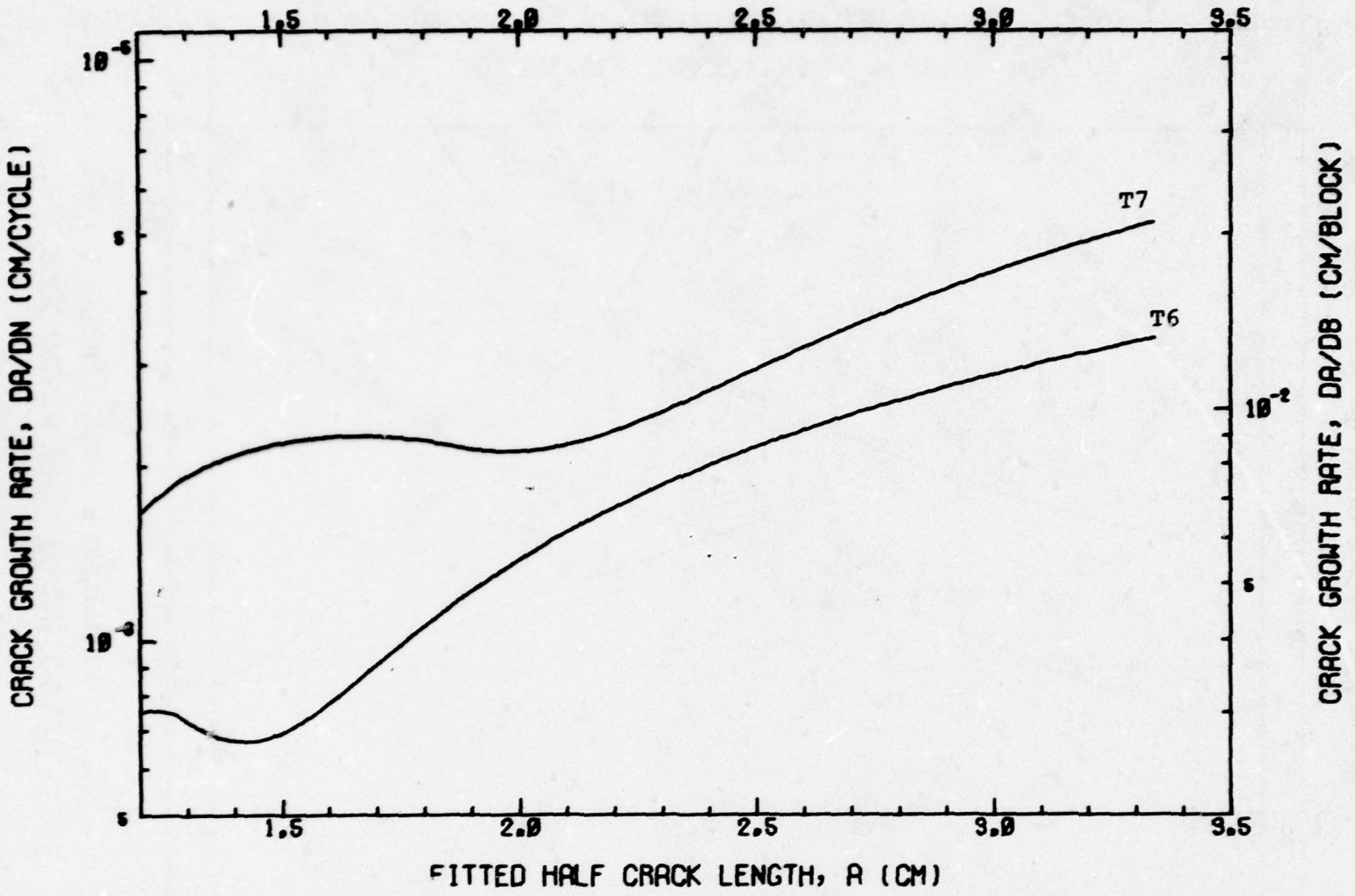

Figure 54 - Crack growth rate vs crack length for periodic single overload tests (OLR=1.8, OCR=1:4000) of peak strength and overaged tempers of 7050.

(a)
CONSTANT AMPLITUDE

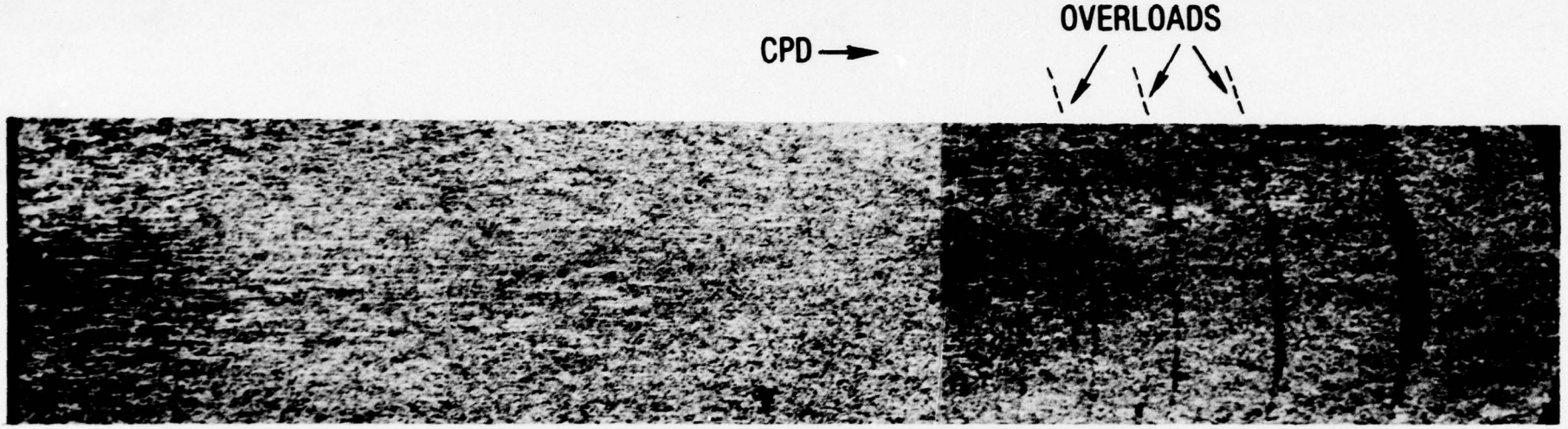

8X

(b)
1.4 OVERLOAD RATIO, 1:4000 OCCURRENCE RATIO

Figure 55 MACRO FRACTOGRAPHS OF 7075-T7 TESTED USING VARIOUS SPECTRA

(c)
1.8 OVERLOAD RATIO 1:8000 OCCURRENCE RATIO

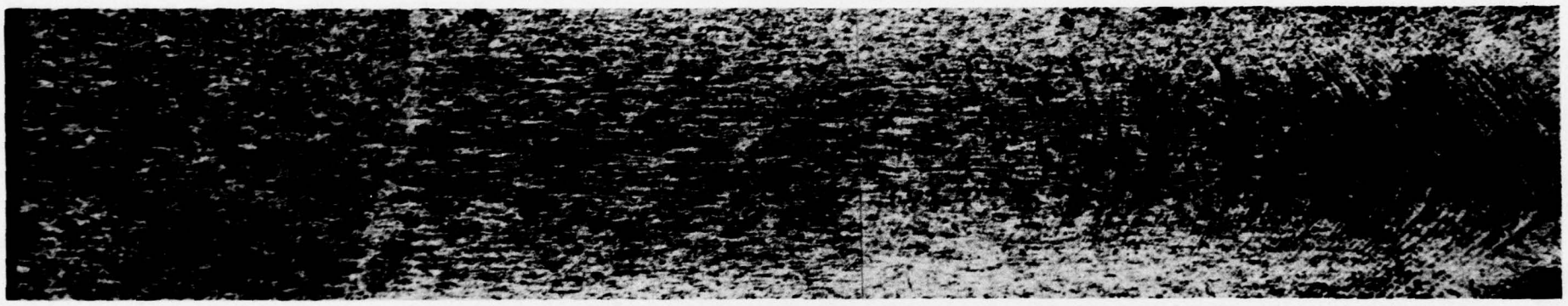

(d)
1.8 OVERLOAD RATIO 1:4000 OCCURRENCE RATIO

Figure 55 CONT.

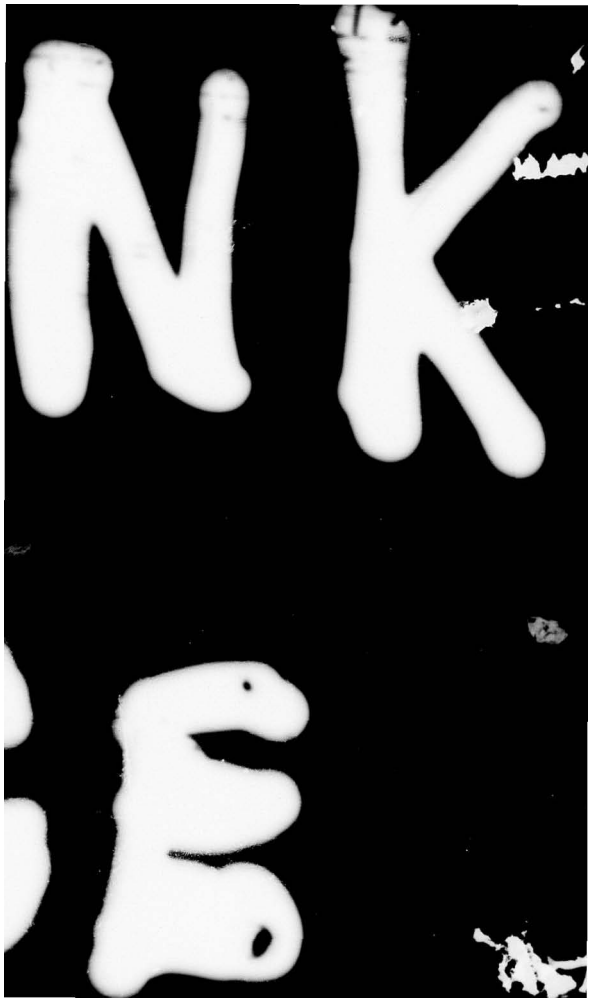

8X

(e)
8 LEVEL SPECTRUM

Figure 55 CONT.

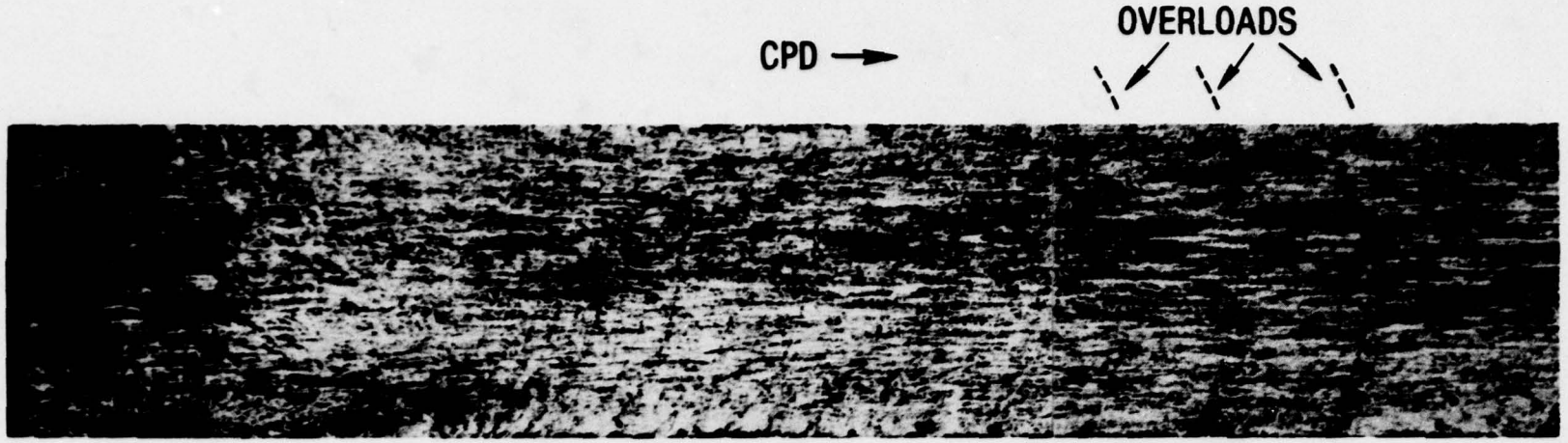

(a)
7010 TYPE HIGH PURITY-T7

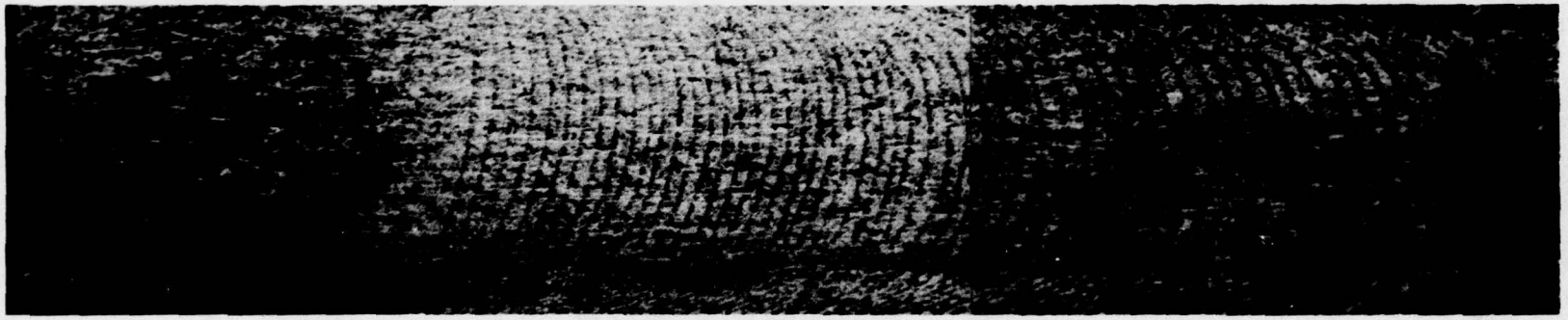

(b)
7010-T7

Figure 56 MACRO FRACTOGRAPHS OF VARIOUS ALLOYS, 1.8 OVERLOAD RATIO 1:8000 OCCURRENCE RATIO

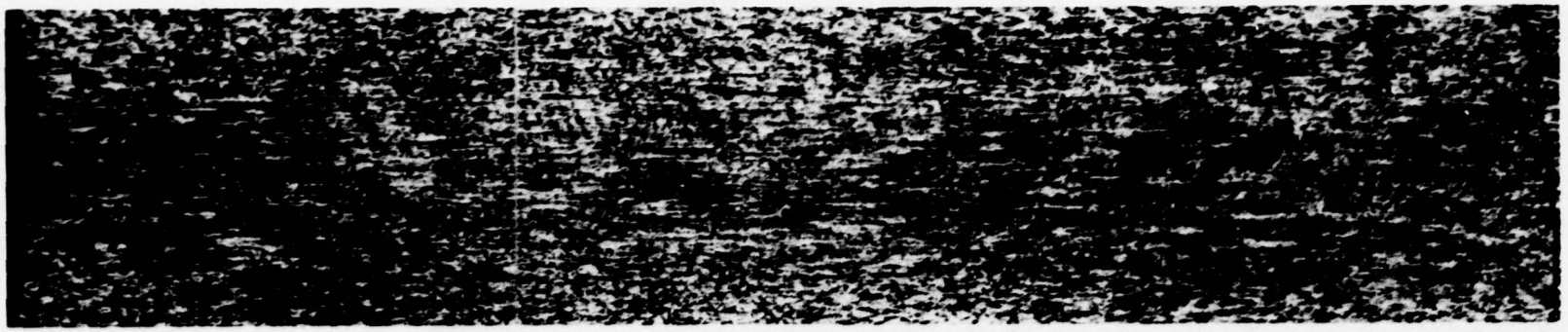

(g)
7475 TYPE HIGH Cu-T7

(h)
7075 TYPE HIGH Cu-T7

Figure 56 CONT.

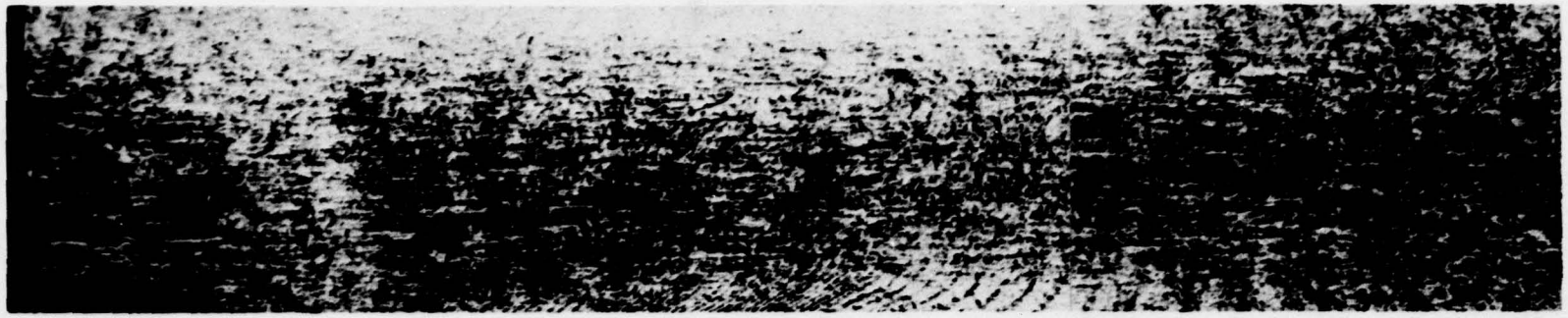

(e)
7050-T7

(f)
7050 TYPE LOW PURITY-T7

Figure 56 CONT.

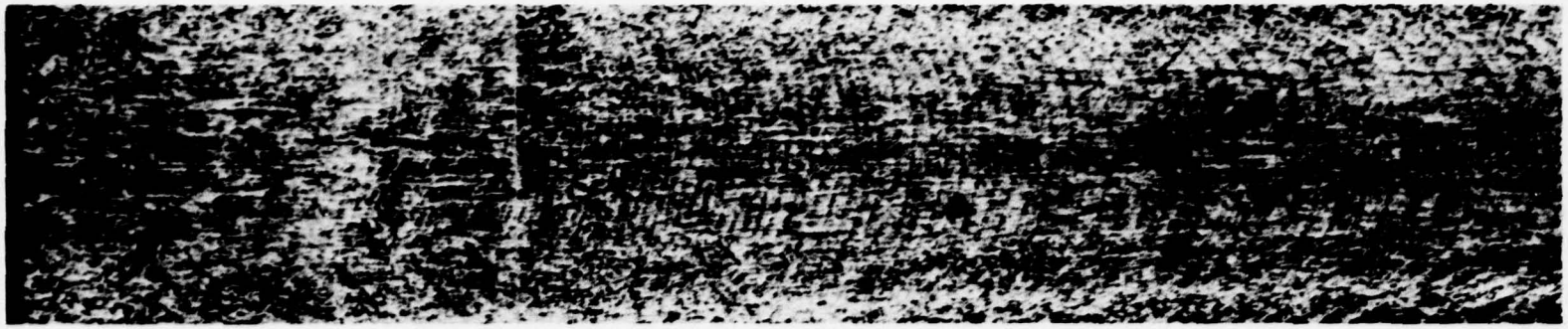

(c)
7475-T7

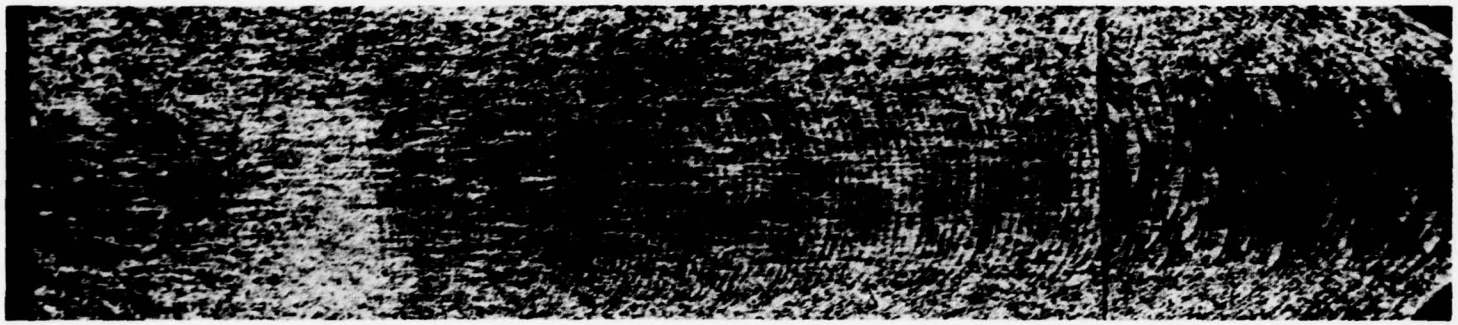

(d)
7075-T7

Figure 56 CONT.

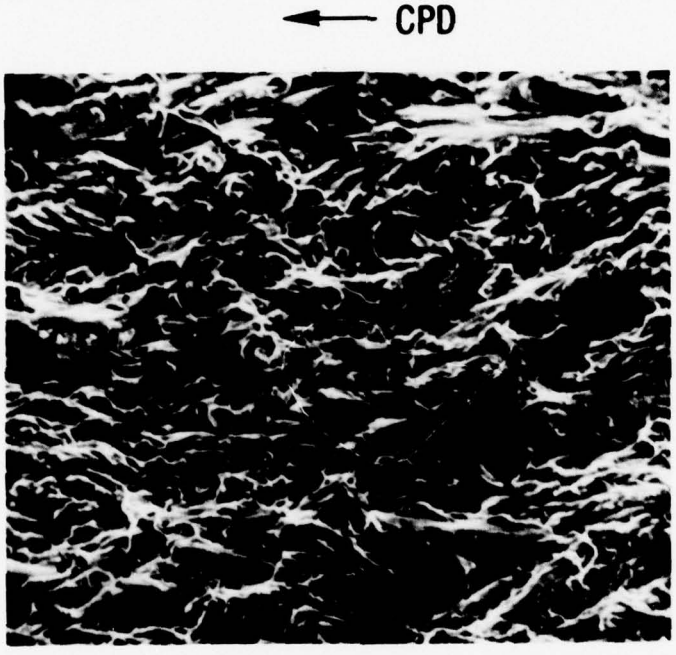

Figure 57 SEM FRACTOGRAPH OF 7050-T7, CONSTANT AMPLITUDE

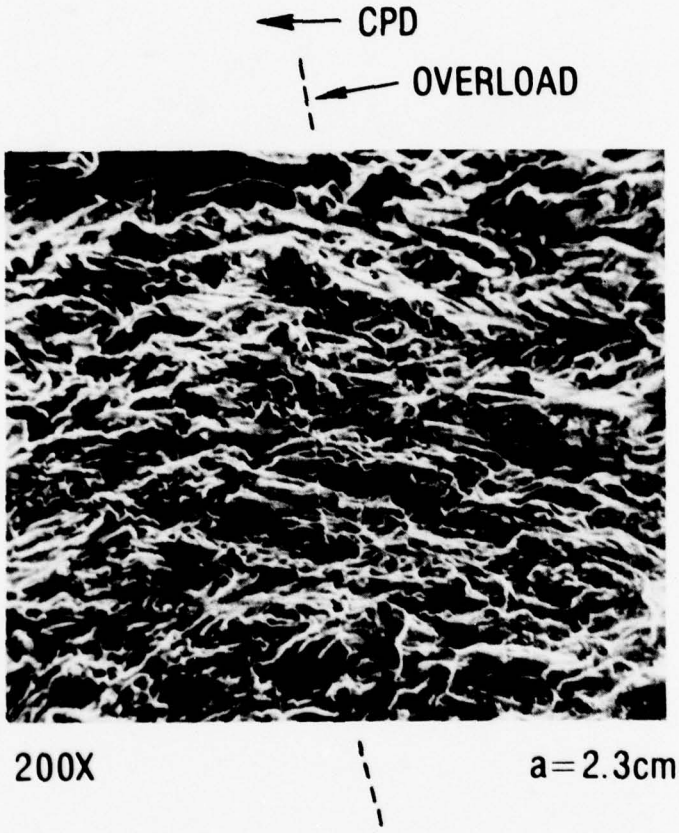

Figure 58 SEM FRACTOGRAPH OF 7050-T7, 1.4 OVERLOAD RATIO 1:4000 OCCURRENCE RATIO

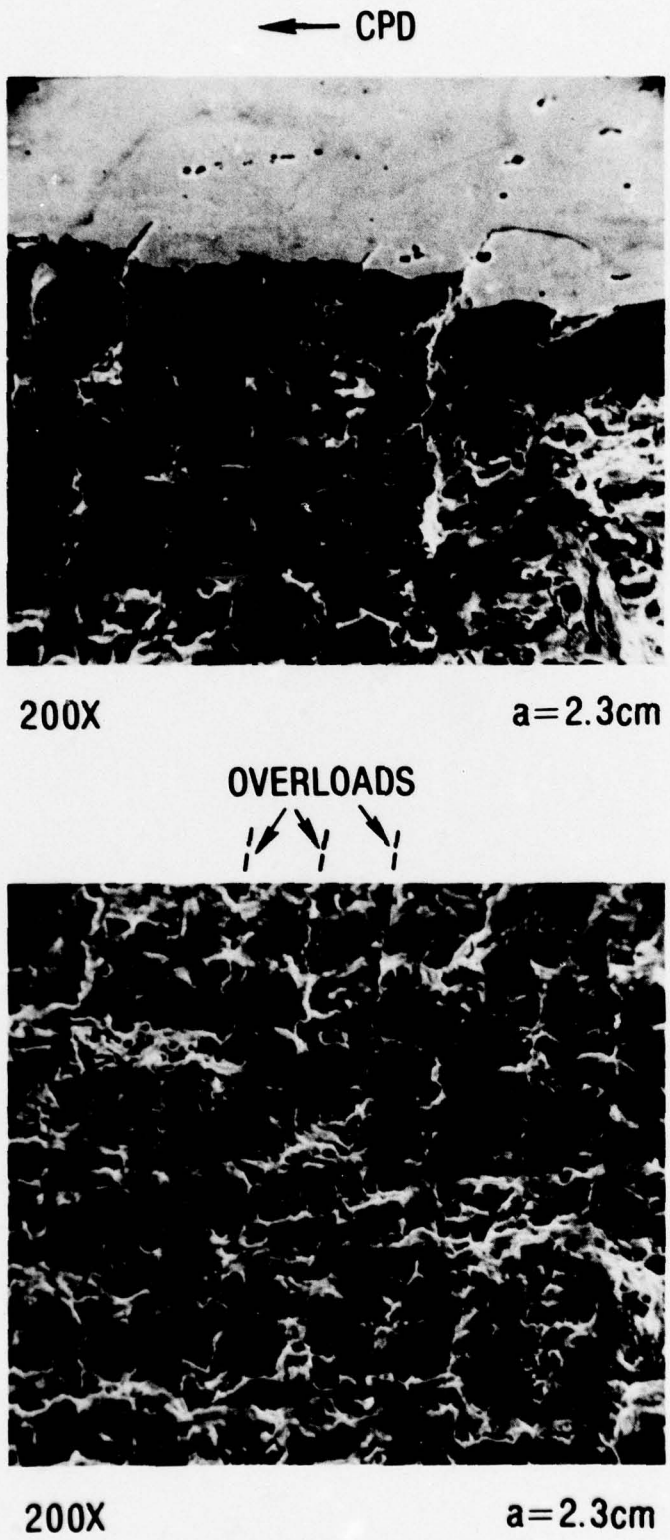

Figure 59 SEM FRACTOGRAPHS OF 7075-T6, 1.8 OVERLOAD RATIO 1:4000 OCCURRENCE RATIO

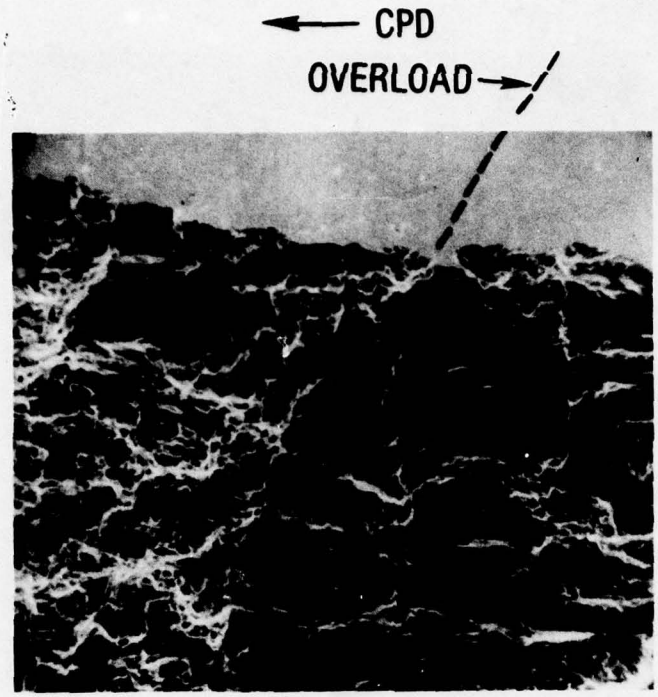

100X a=2.5

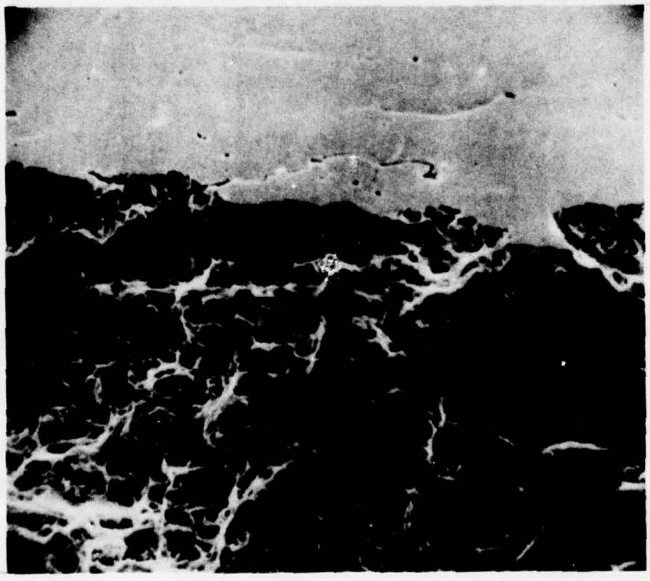

200X a=2.5cm

Figure 60 SEM FRACTOGRAPHS OF 7075-T7, 1.8 OVERLOAD RATIO, 1:8000 OCCURRENCE RATIO

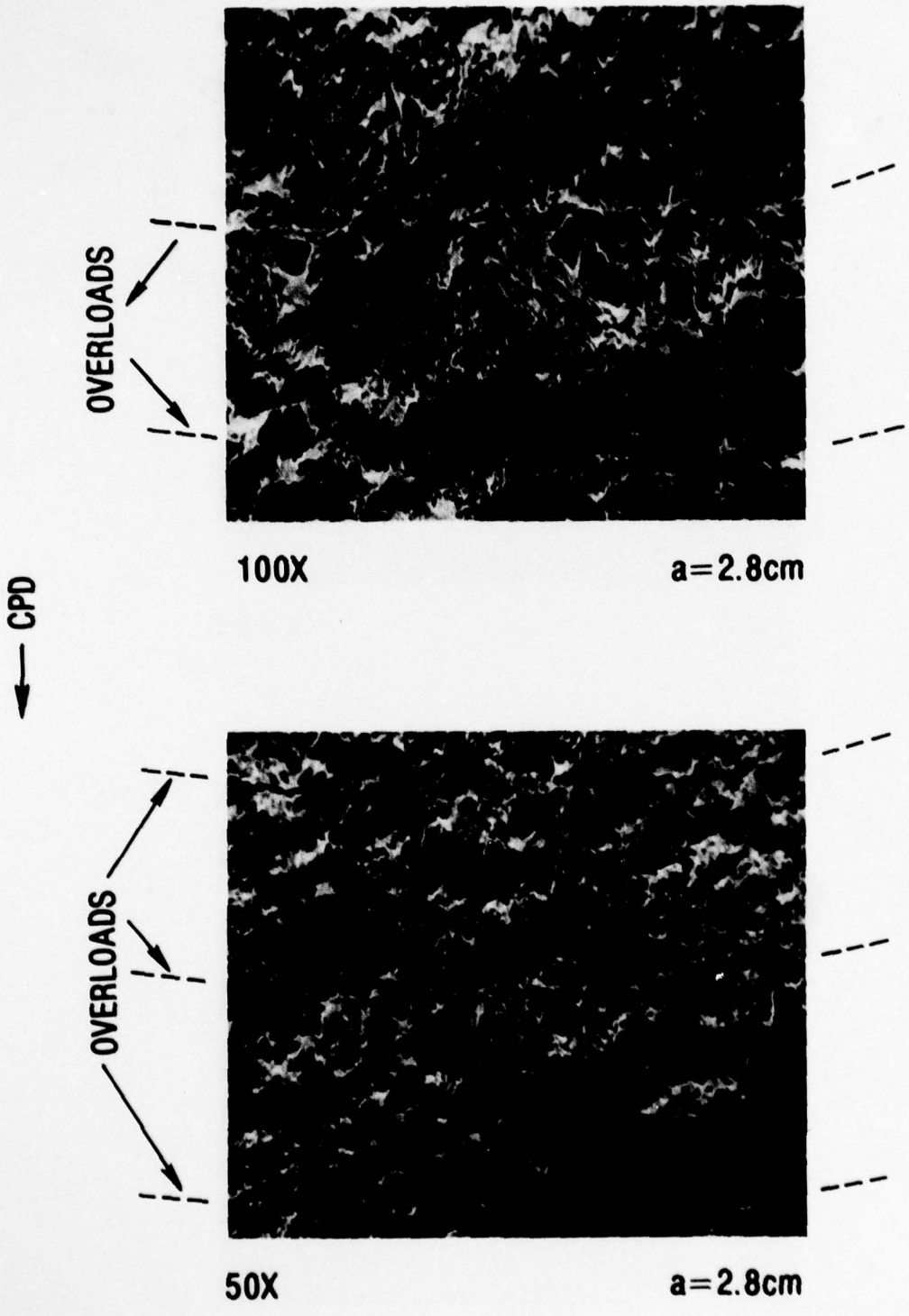

Figure 61 SEM FRACTOGRAPHS OF 7475-T7, 1.8 OVERLOAD RATIO, 1:8000 OCCURRENCE RATIO

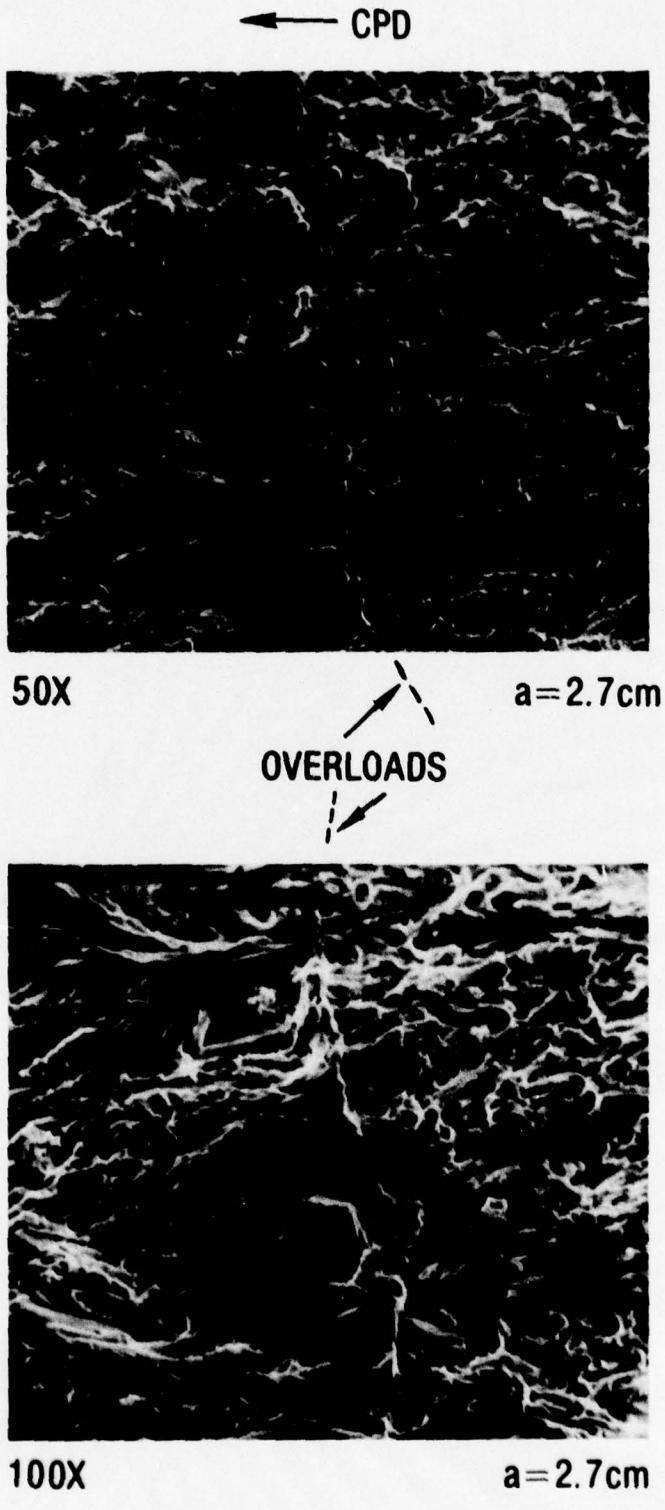

Figure 62 SEM FRACTOGRAPHS OF HIGHER Cu 7475 TYPE-T7, 1.8 OVERLOAD RATIO, 1:8000 OCCURRENCE RATIO

Figure 63a - Low Magnification Photograph Showing a Macroscopically Straight Crack Propagating 90° from the Stress Axis, Alloy 7075-T6
100X
As-Polished

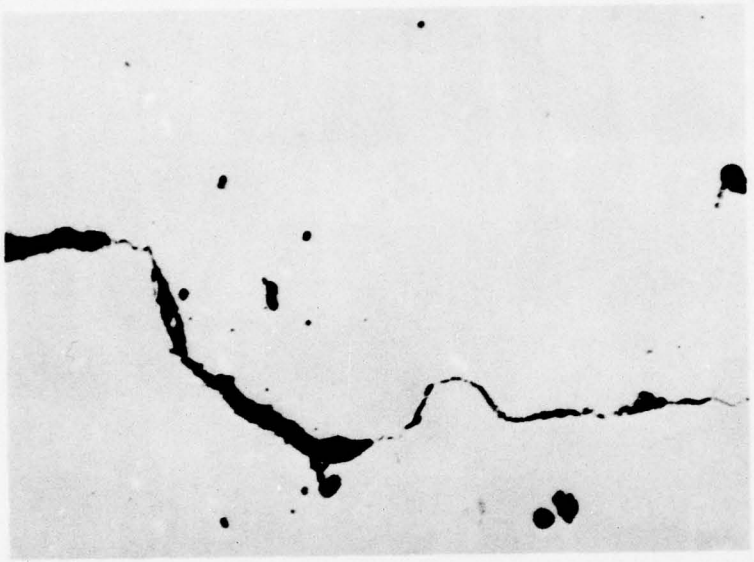

Figure 63b - Deviation of the Crack Becomes More Apparent at Higher Magnifications,
Alloy 7075-T6.
500X
As-Polished

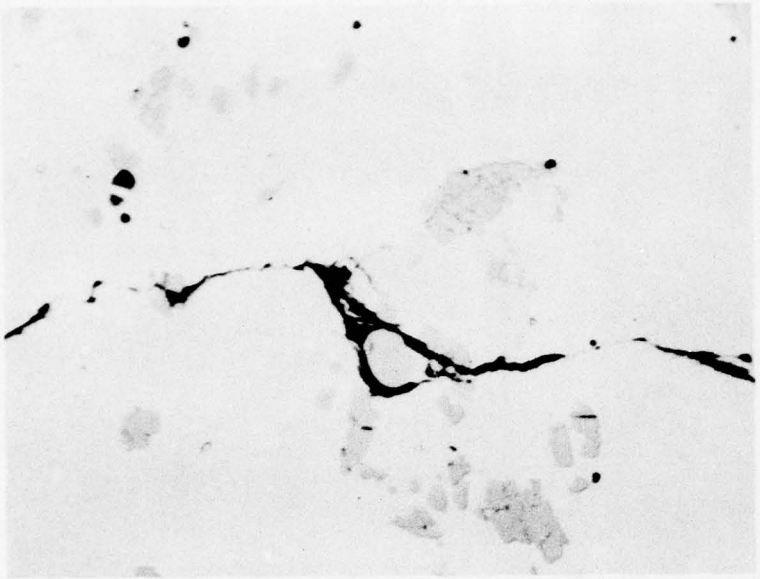

Figure 64 - Periodic crack branching along the crack, alloy 7075-T6.

1000X
As-Polished

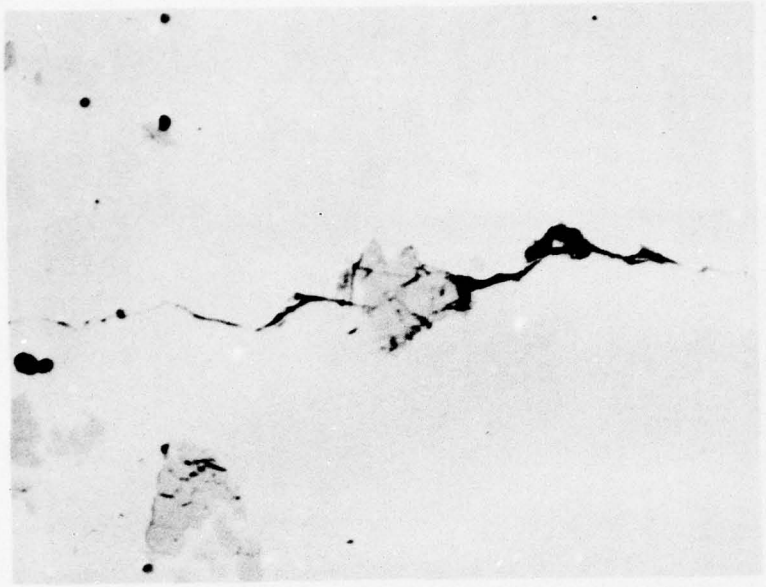

Figure 65 - The Branching Appeared to be Associated with the Large Intermetallic Phases, Alloy 7075-T6. 1000X As-Polished

Figure 66 - Localized Deformation Ahead of the Crack Tip Directed Toward the Intermetallic Particles, Alloy 7075-T6. 1000X
Keller's Etch
Differential Interference Phase Contrast (DIC)

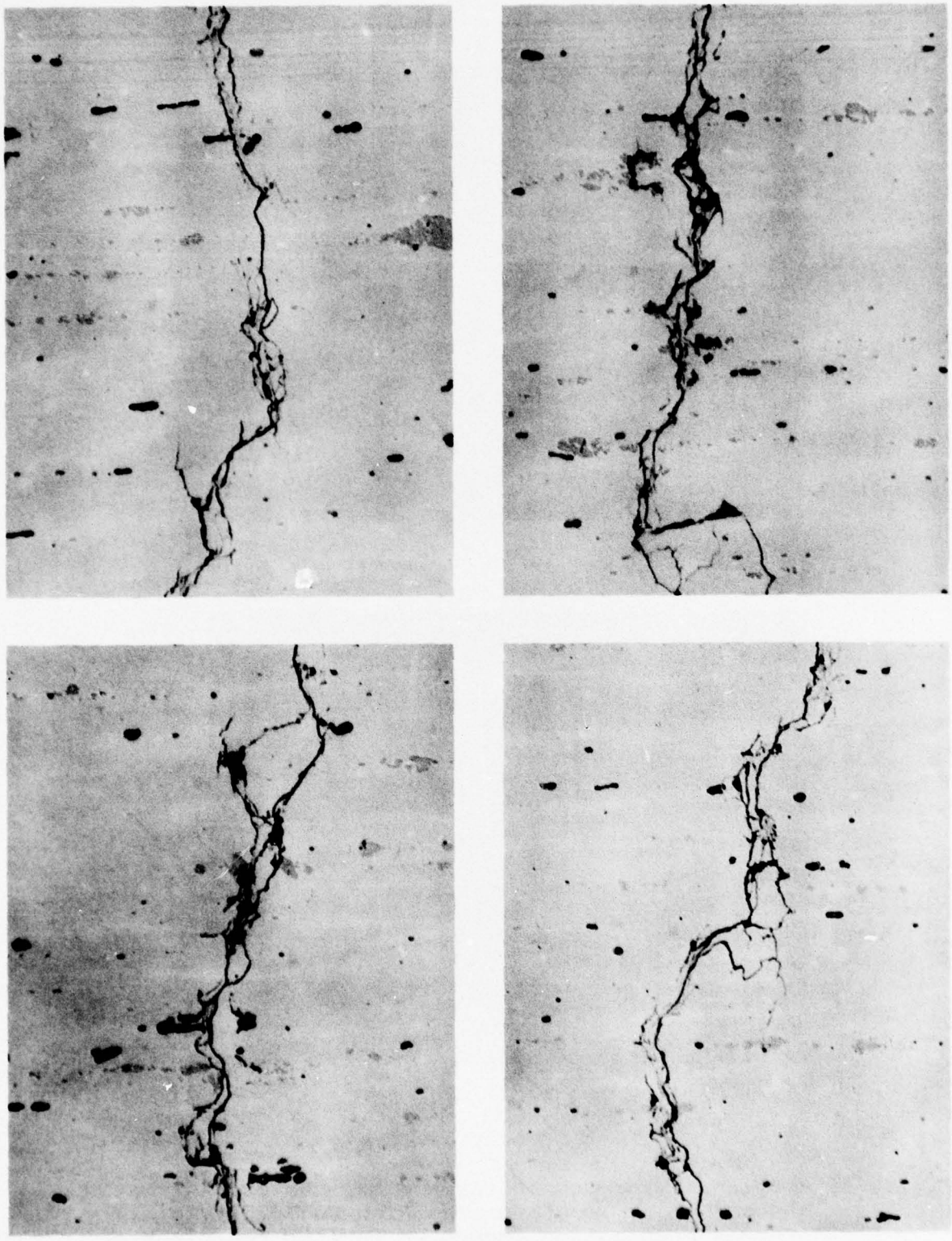

Figure 67 - Optical micrographs taken along the crack front at short crack length in the High Cu 7075-type alloy. Crack propagation direction is into the plane of the paper.
500X
As-Polished

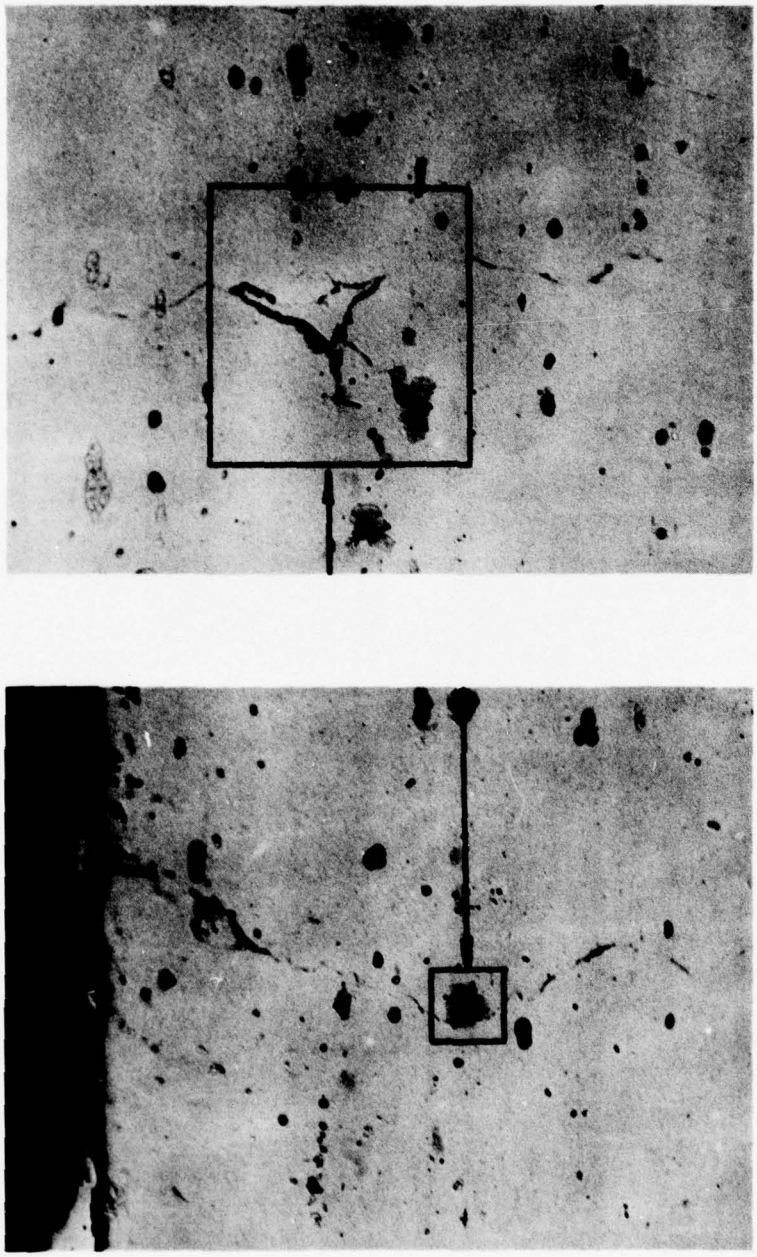

Figure 68 - Optical micrographs taken along the crack front at short crack length in the High Cu 7075-type alloy. Crack propagation direction is into the plane of the paper. 500X As-Polished

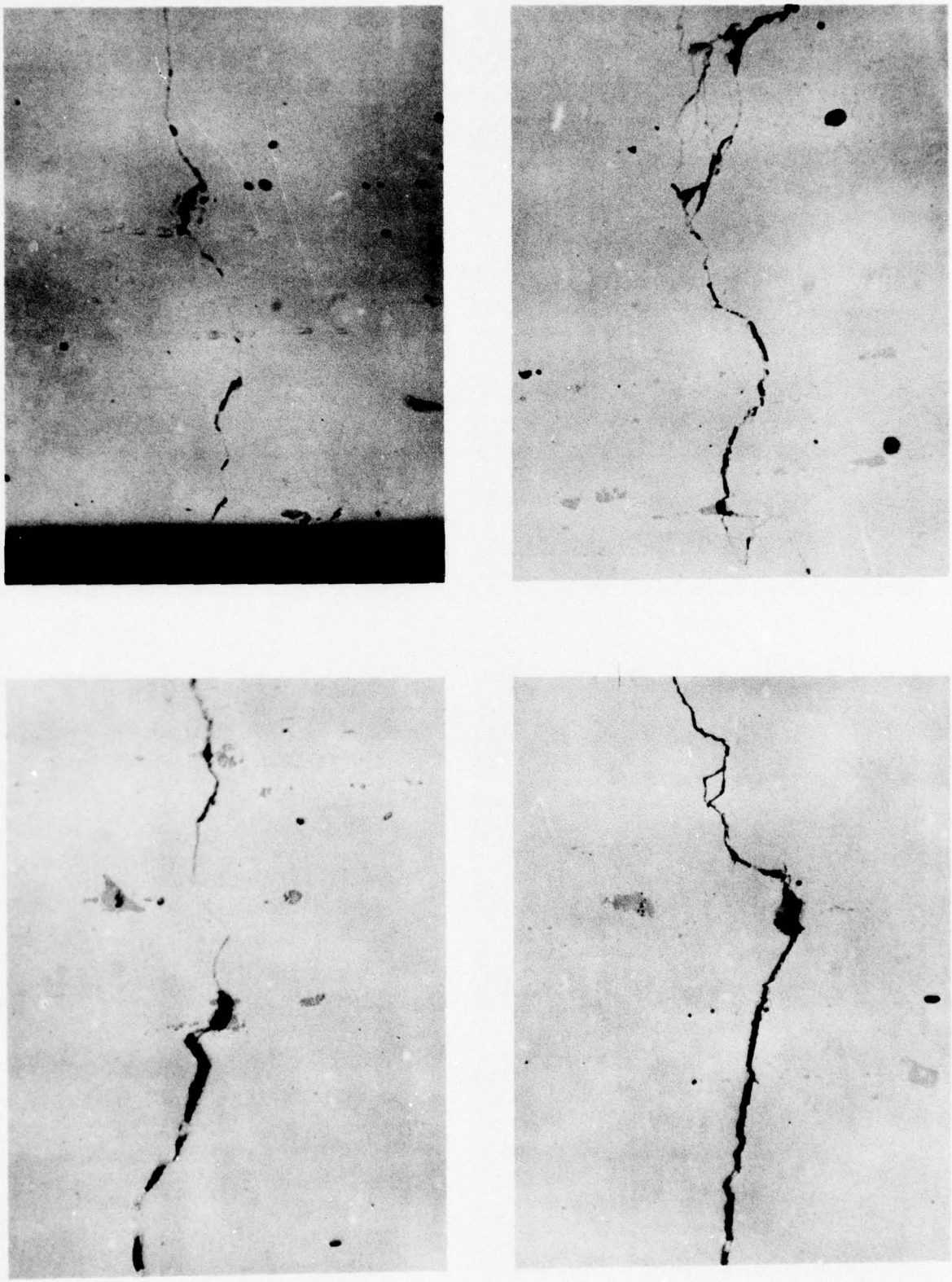

Figure 69 - Optical micrographs taken along the crack front at short crack length in the High Cu 7475-type alloy. Crack propagation direction is into the plane of the paper.
500X
As-Polished

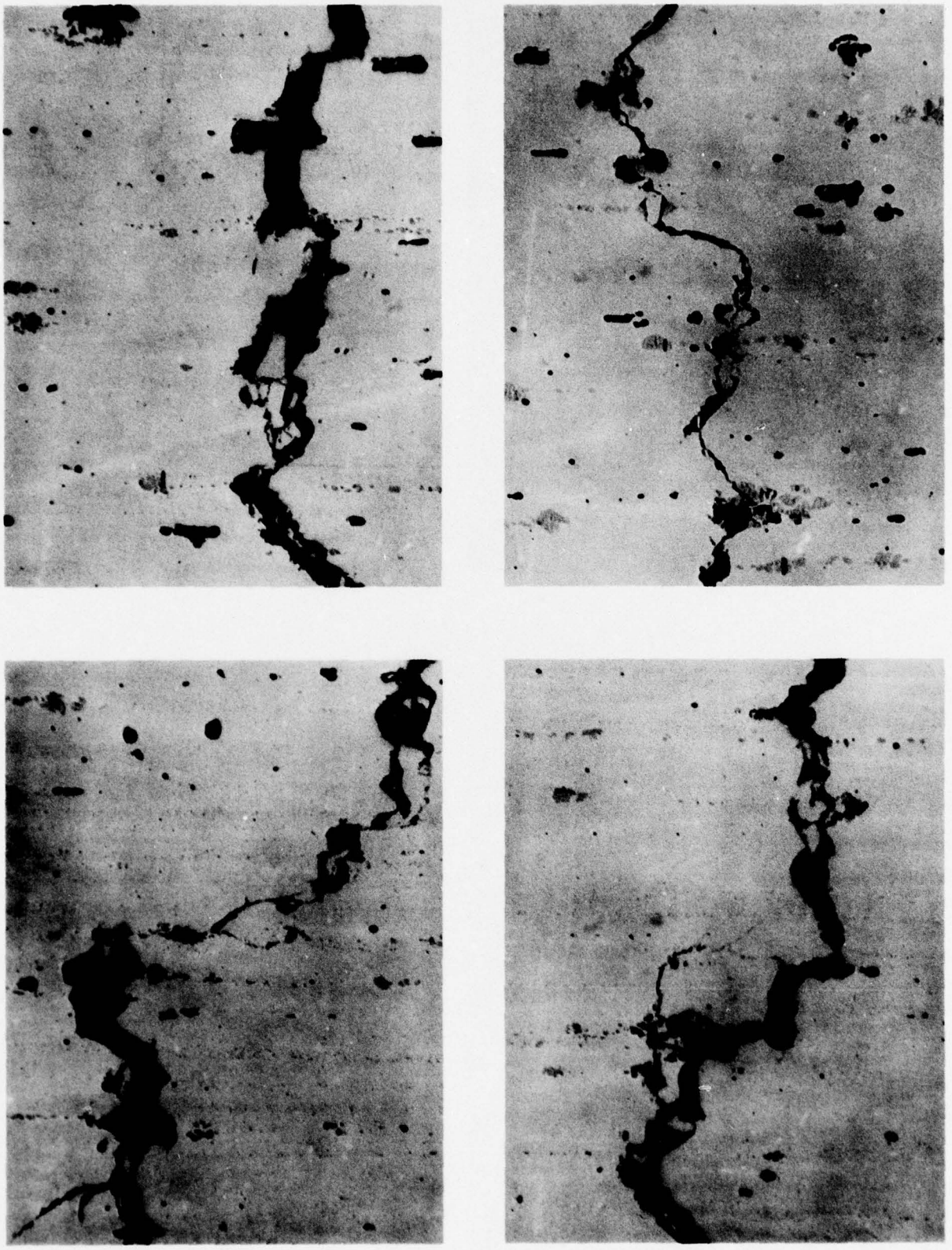

Figure 70 - Optical micrographs taken along the crack front at long crack length in the High Cu 7075-type alloy. Crack propagation direction is into the plane of the paper. 500X As-Polished

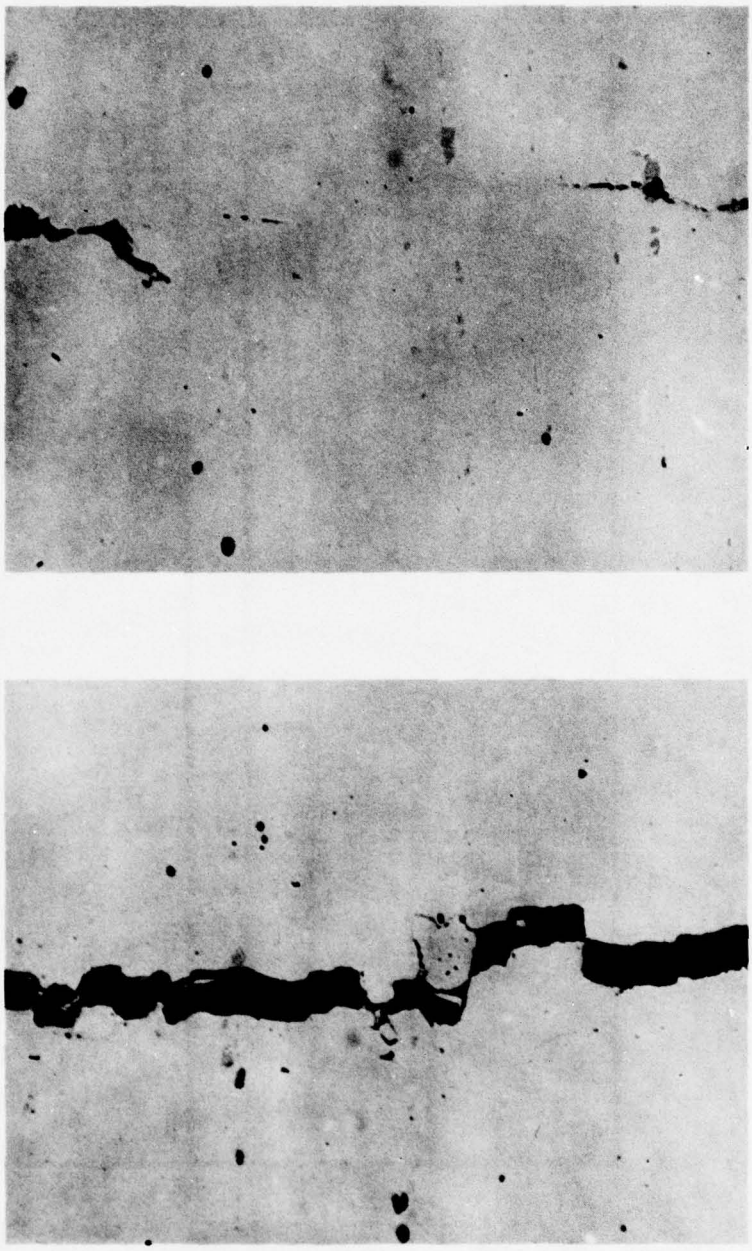

Figure 71 - Optical micrographs taken along the crack front at long crack length in the Hi Cu 7475-type alloy. Crack propagation direction is into the plane of the paper.
500X
As-Polished

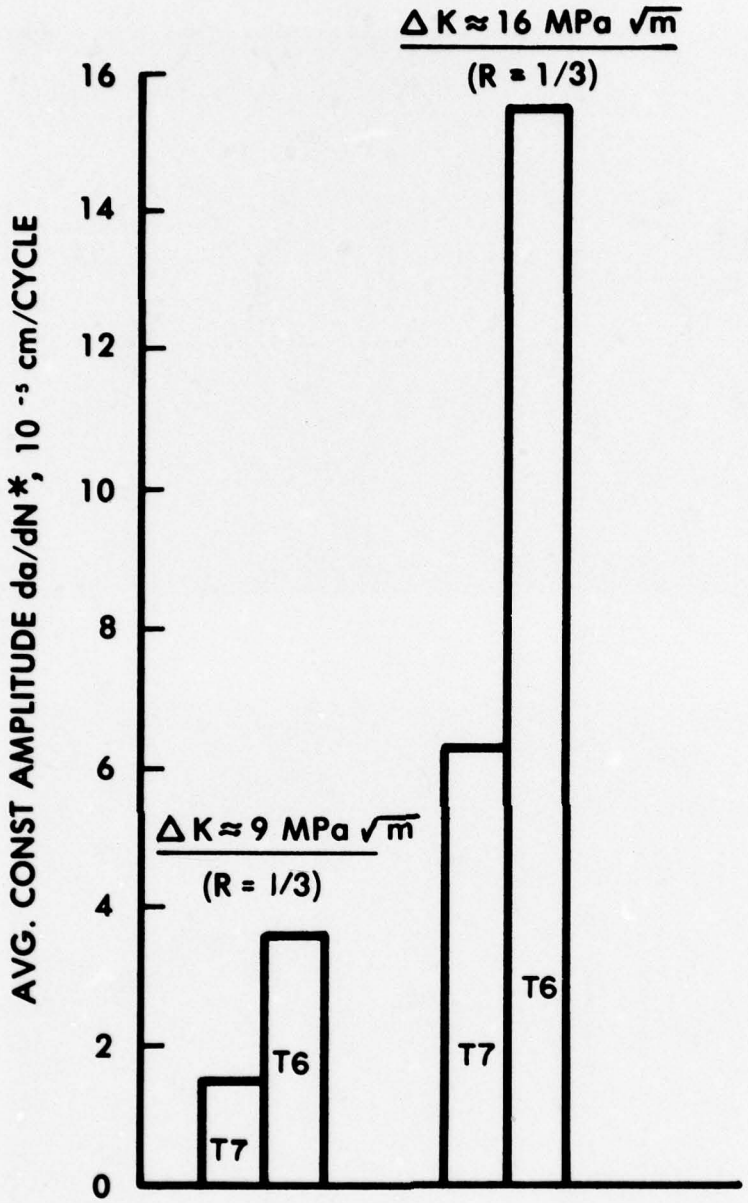

EFFECT OF TEMPER ON CONSTANT AMPLITUDE CRACK GROWTH RESISTANCE OF 7075 AND 7050 ALLOYS IN HIGH HUMIDITY AIR

(* NOTE: Computed as avg da/dN of alloys 7075 and 7050 in the same temper)

FIG. 72

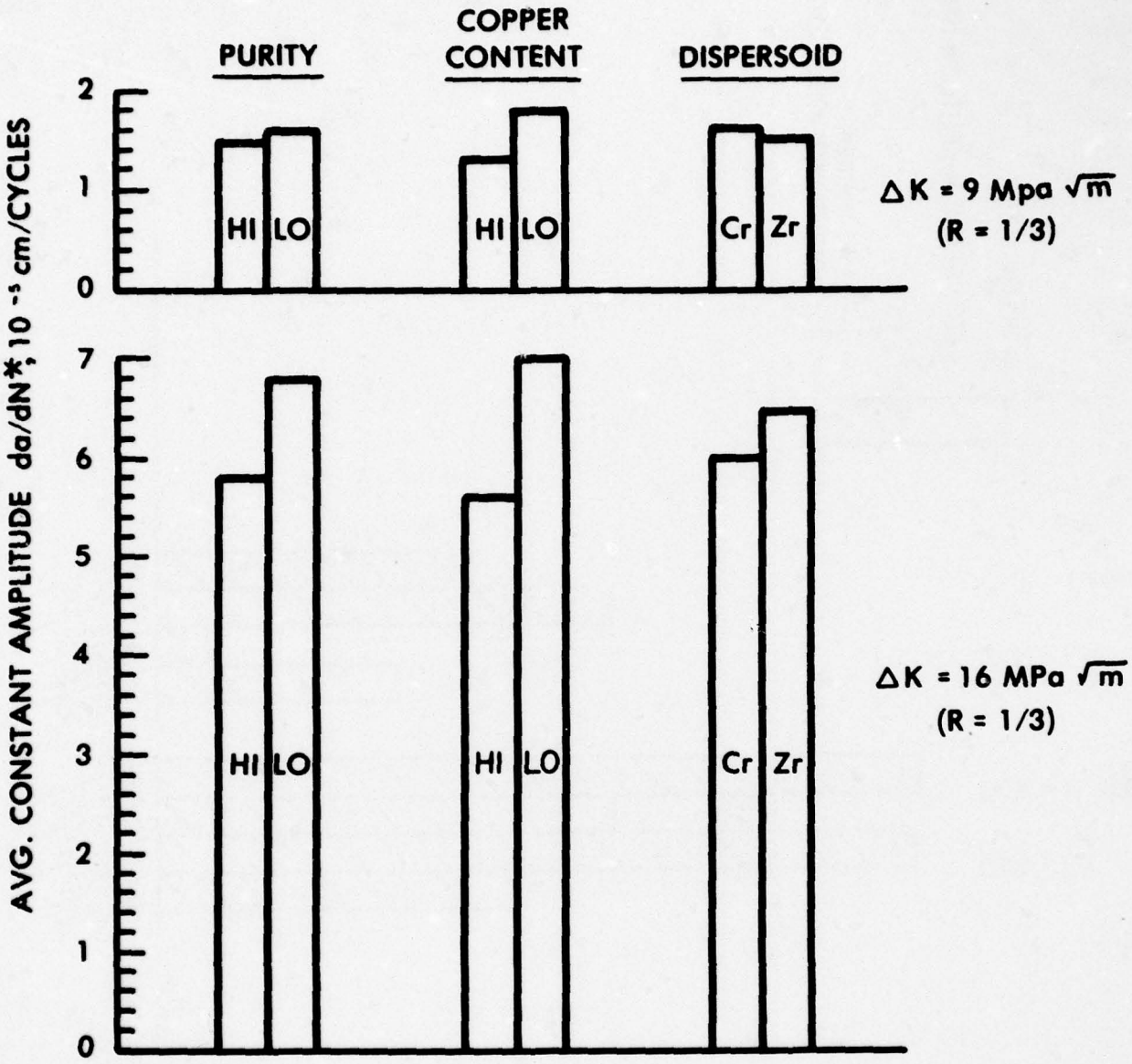

EFFECT OF PURITY, COPPER CONTENT, AND DISPERSOID ON CONSTANT AMPLITUDE CRACK GROWTH RESISTANCE OF 7XXX - T7 ALLOYS IN HIGH HUMIDITY AIR

(* NOTE : Computed as Average of Four Microstructures Containing Same Controlled Variable)

FIG. 73

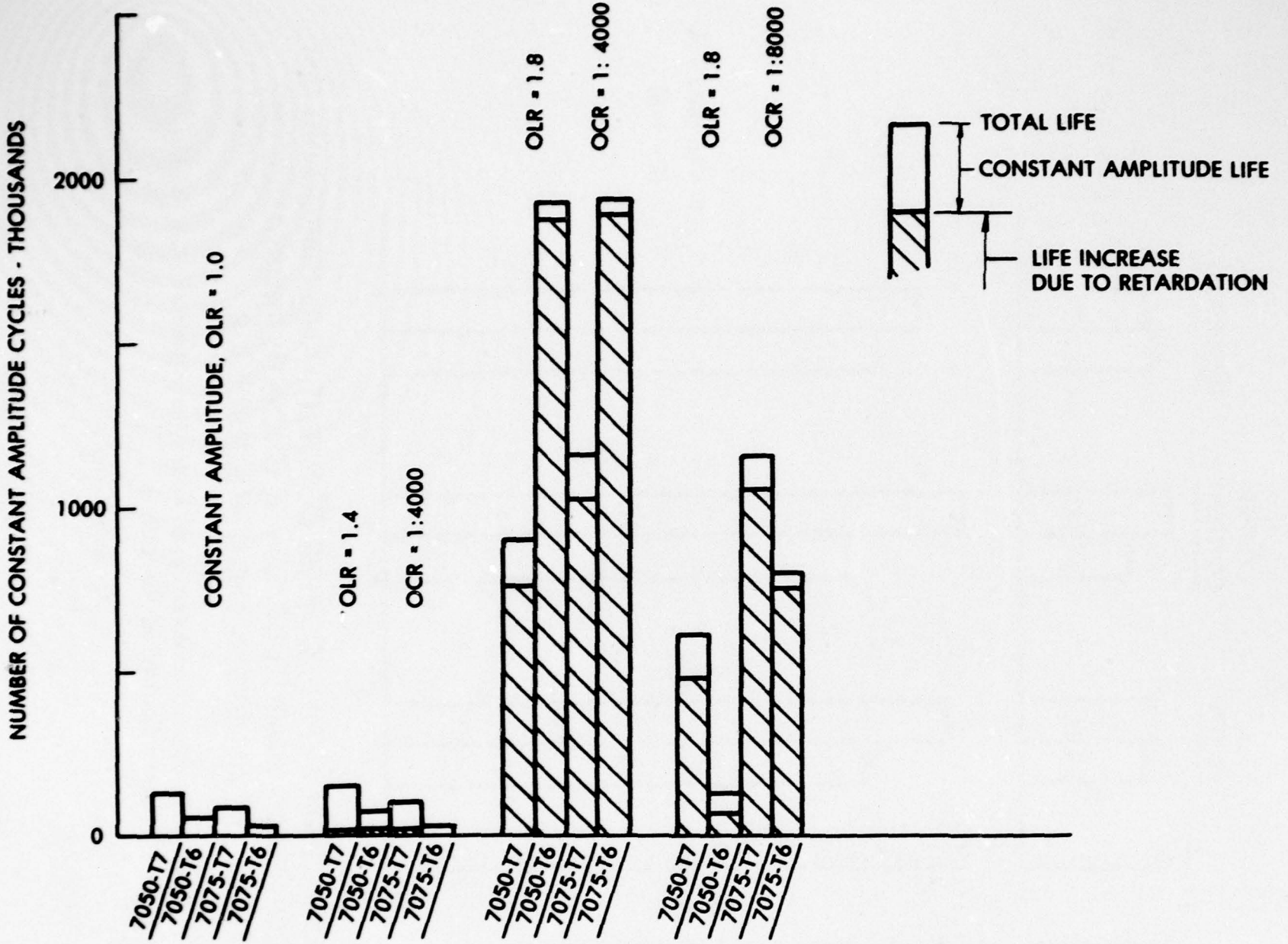

FIG. 74 RELATIVE RANKING OF FATIGUE CRACK GROWTH RESISTANCE OF 7075 AND 7050 TYPE ALLOYS UNDER CONSTANT AMPLITUDE AND PERIODIC SINGLE OVERLOAD CONDITIONS

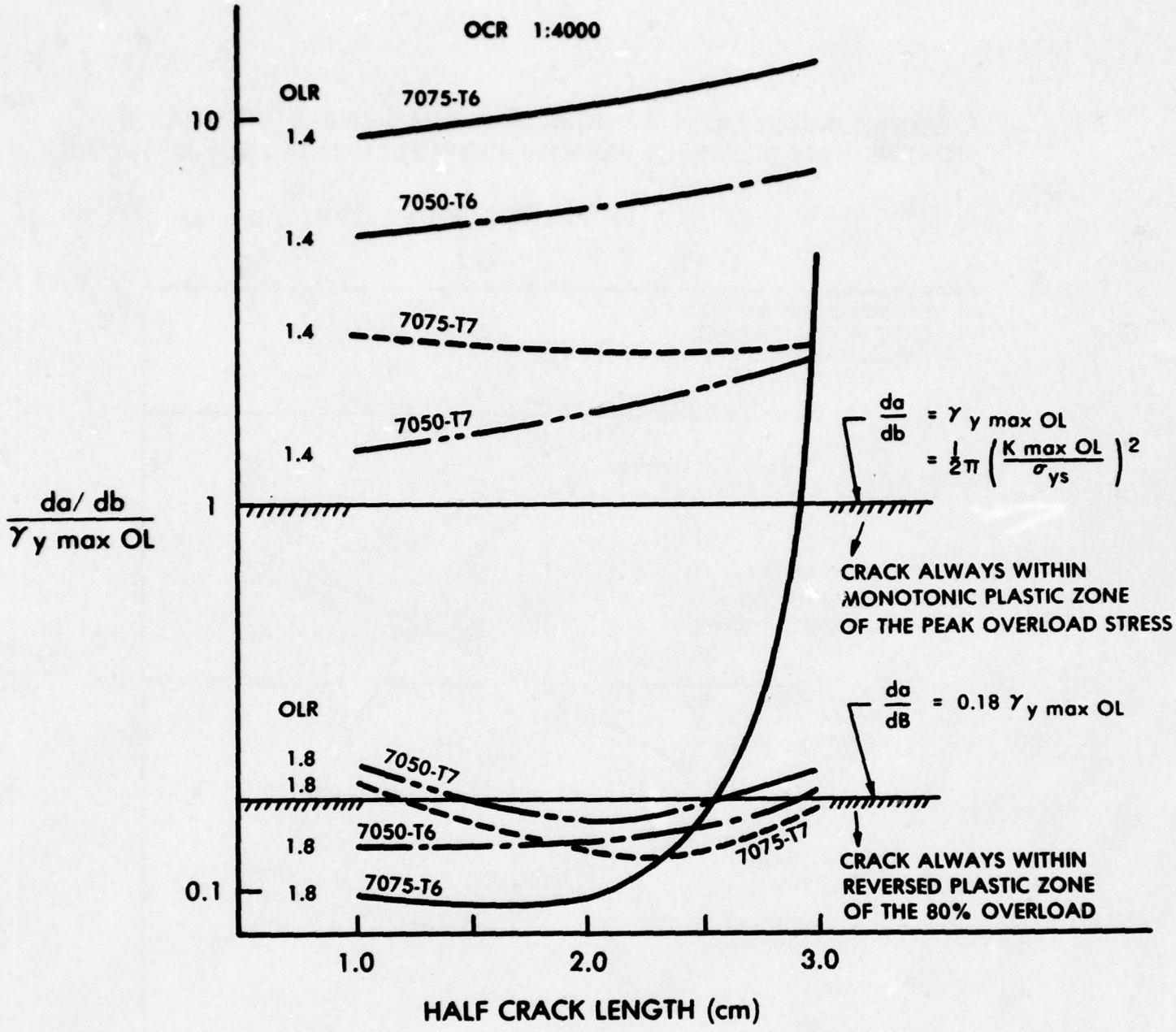

FIG. 75 CRACK GROWTH PER BLOCK RELATIVE TO PLASTIC ZONE SIZE FOR PERIODIC SINGLE OVERLOADS WITH 1:4000 OCCURRENCE RATIO

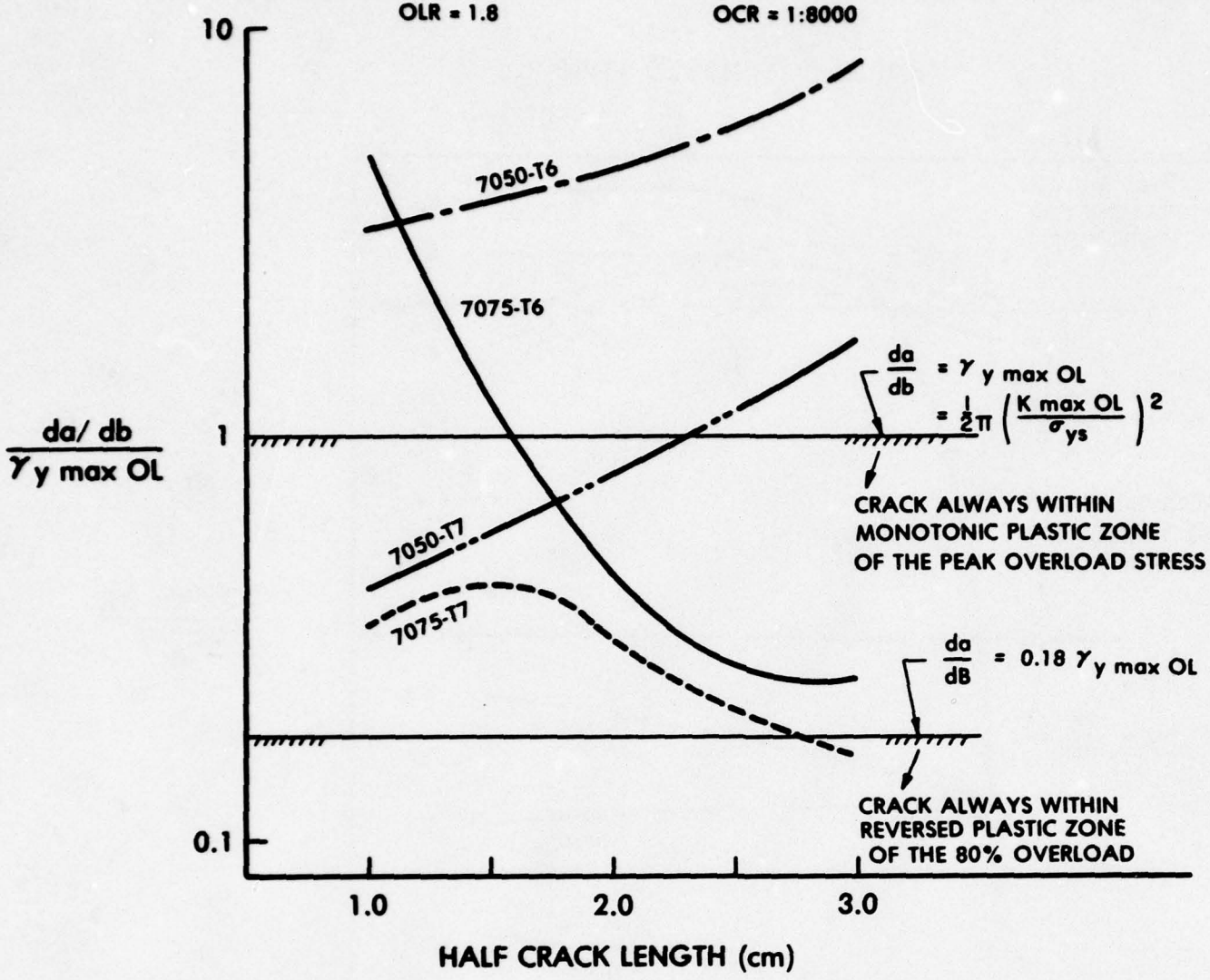

FIG. 76 CRACK GROWTH PER BLOCK RELATIVE TO PLASTIC ZONE SIZE FOR PERIODIC SINGLE OVERLOADS WITH 1:8000 OCCURRENCE RATIO

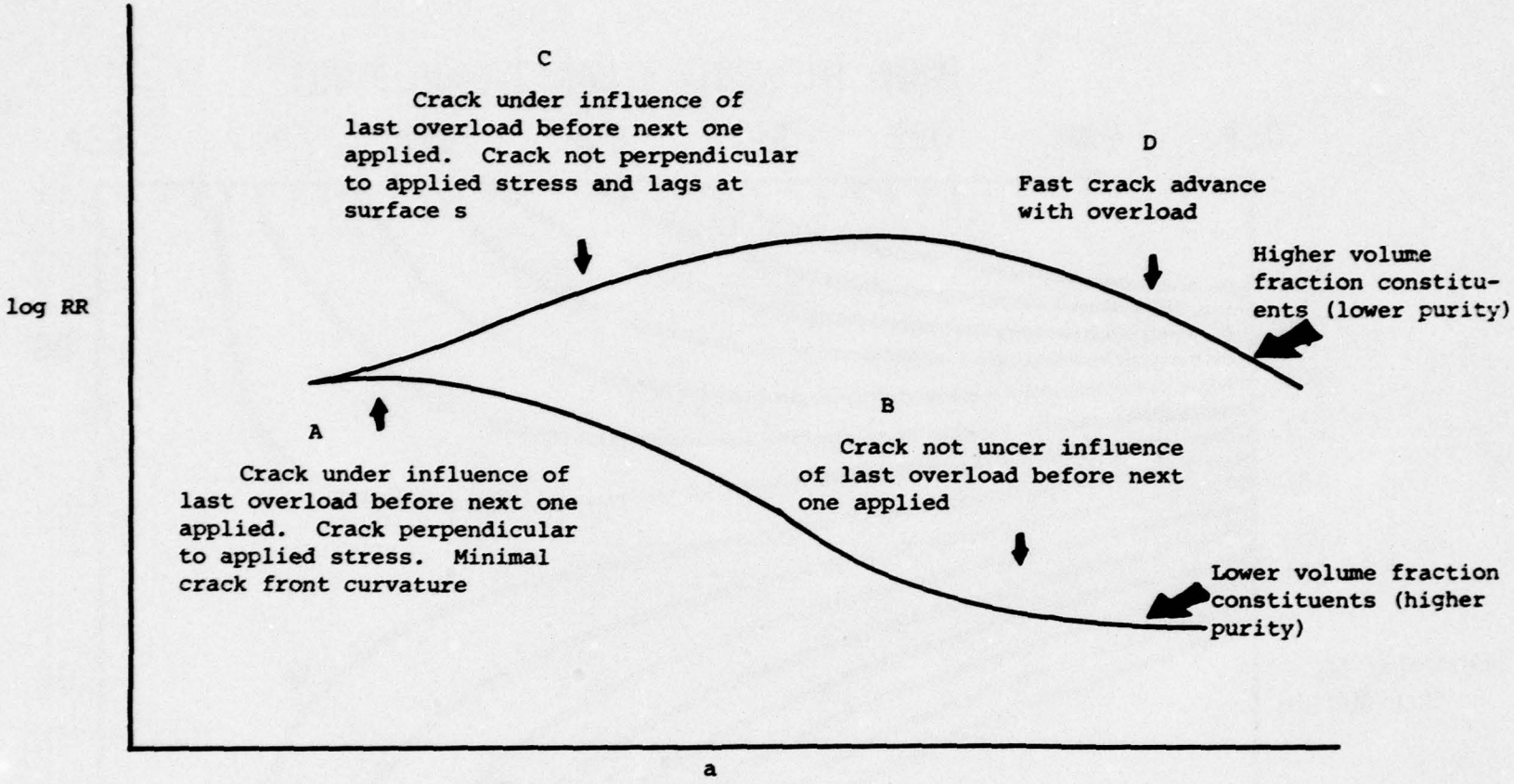

Figure 77 - Schematic log RR vs a curves.

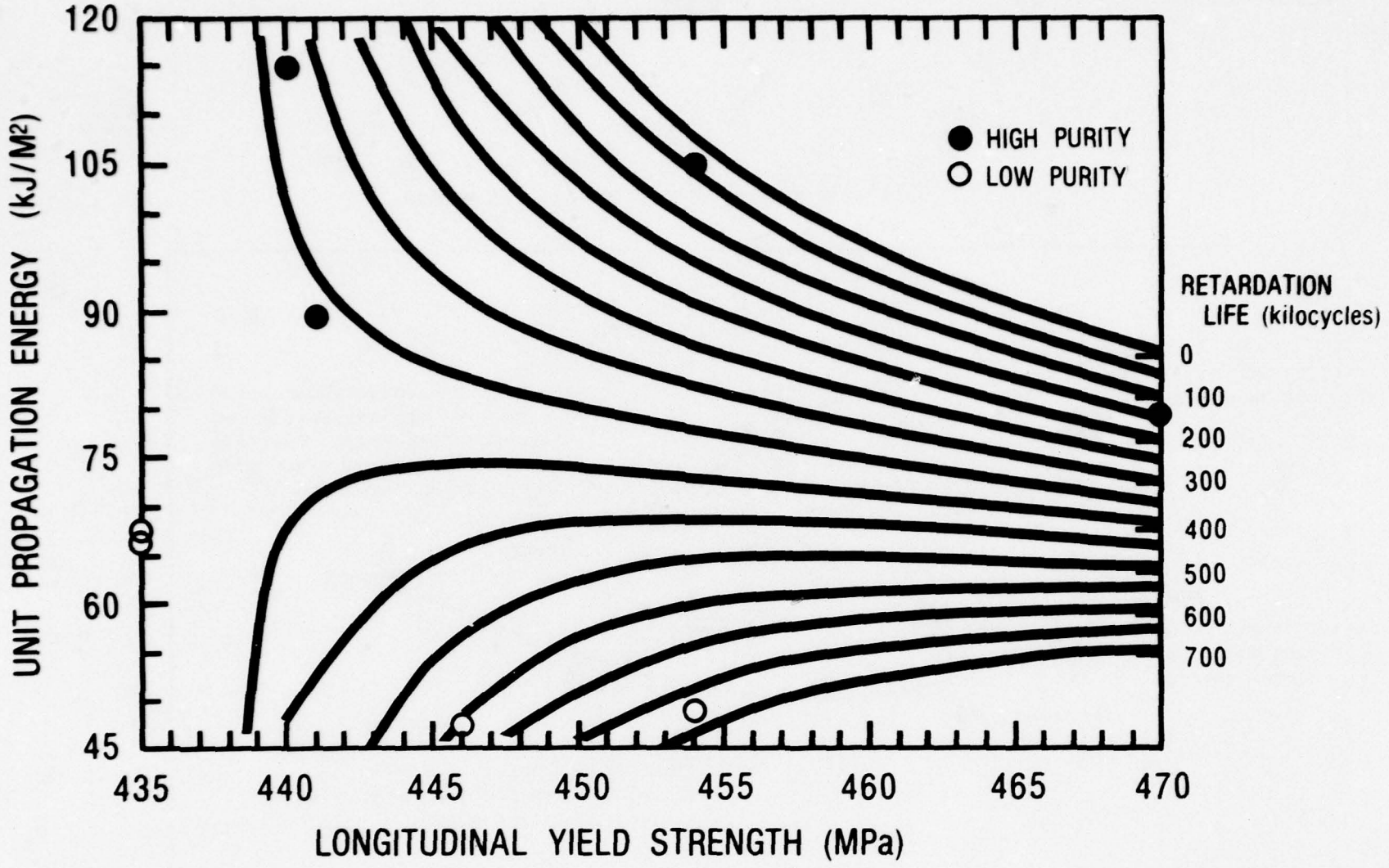

Figure 78 CONTOUR PLOT OF PREDICTED RETARDATION LIFE IN 0.25 in. 7XXX PLATE; 80 PCT. OVERLOAD EVERY 8000 CYCLES; HALF CRACK LENGTH GROWING FROM 1.2 TO 3.0 cm.

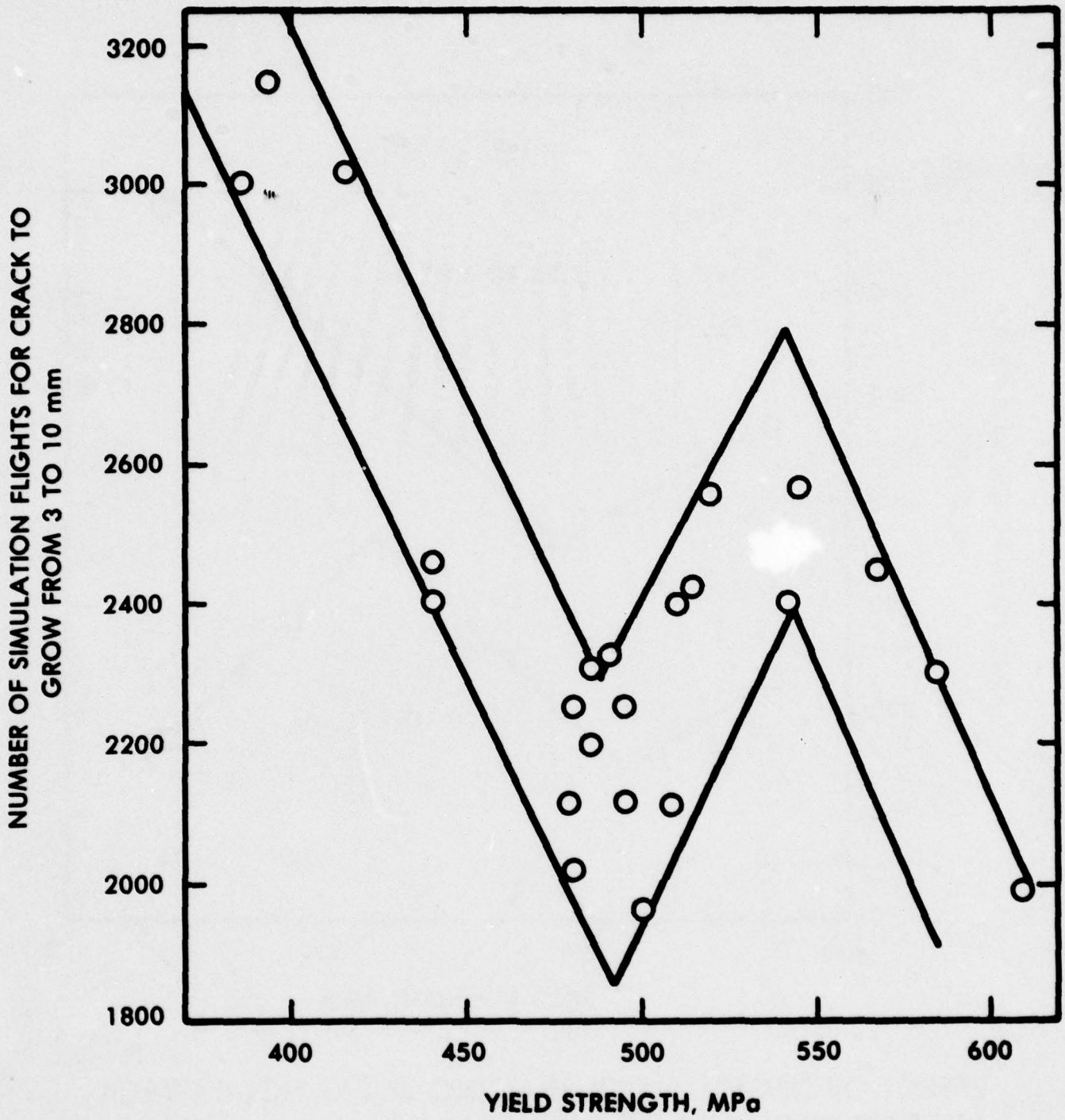

EFFECT OF YIELD STRENGTH ON FATIGUE CRACK PROPAGATION LIFE OF ALLOY 7050 FORGING UNDER FLIGHT SIMULATION LOADING. (REF. 10)

FIGURE 79

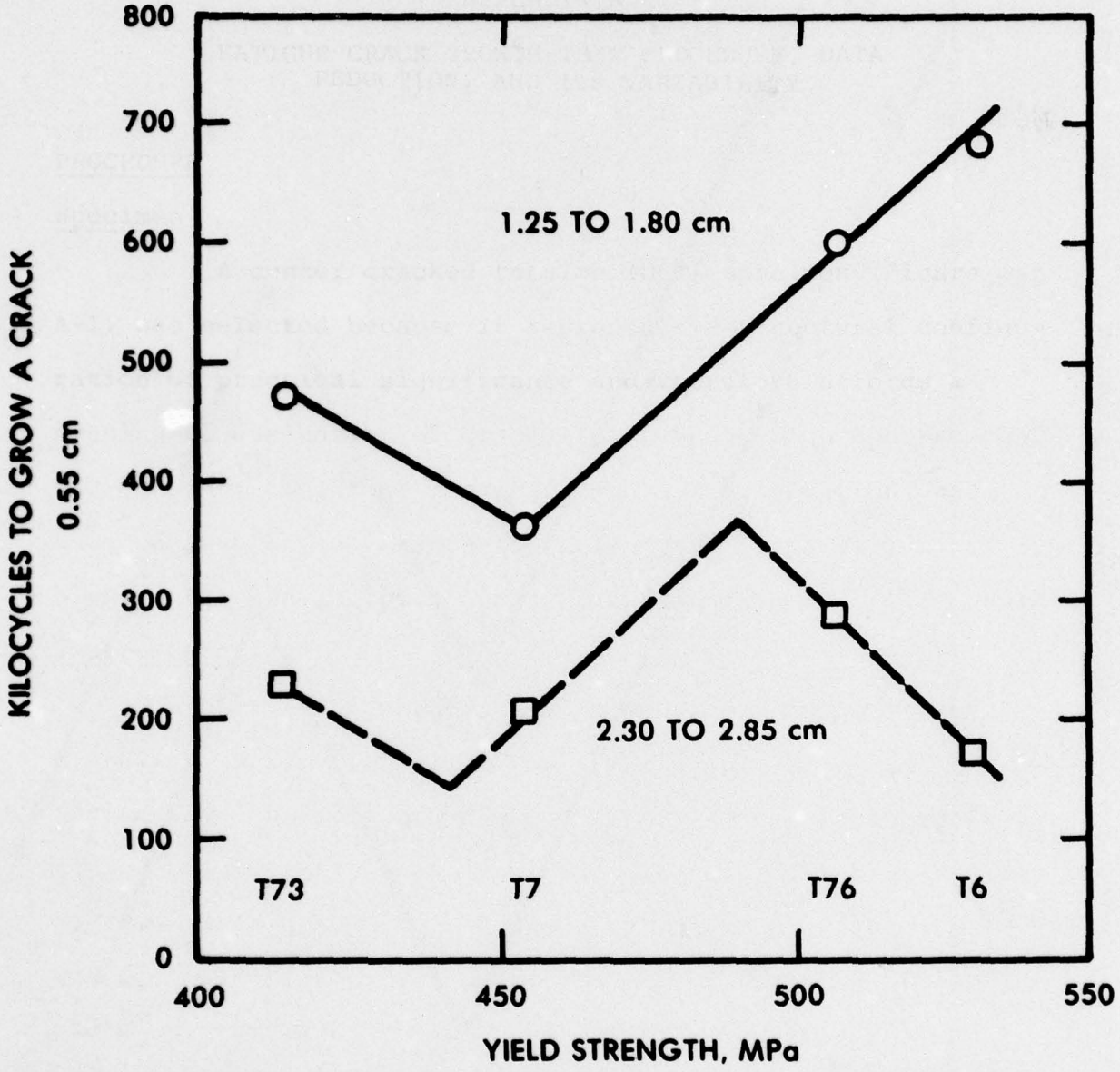

EFFECT OF DEGREE OF OVERAGING ON FATIGUE CRACK PROPAGATION LIFE OF ALLOY 7075.

1.8 OVERLOAD RATIO, 1:4000 OCCURRENCE RATIO

FIGURE 80

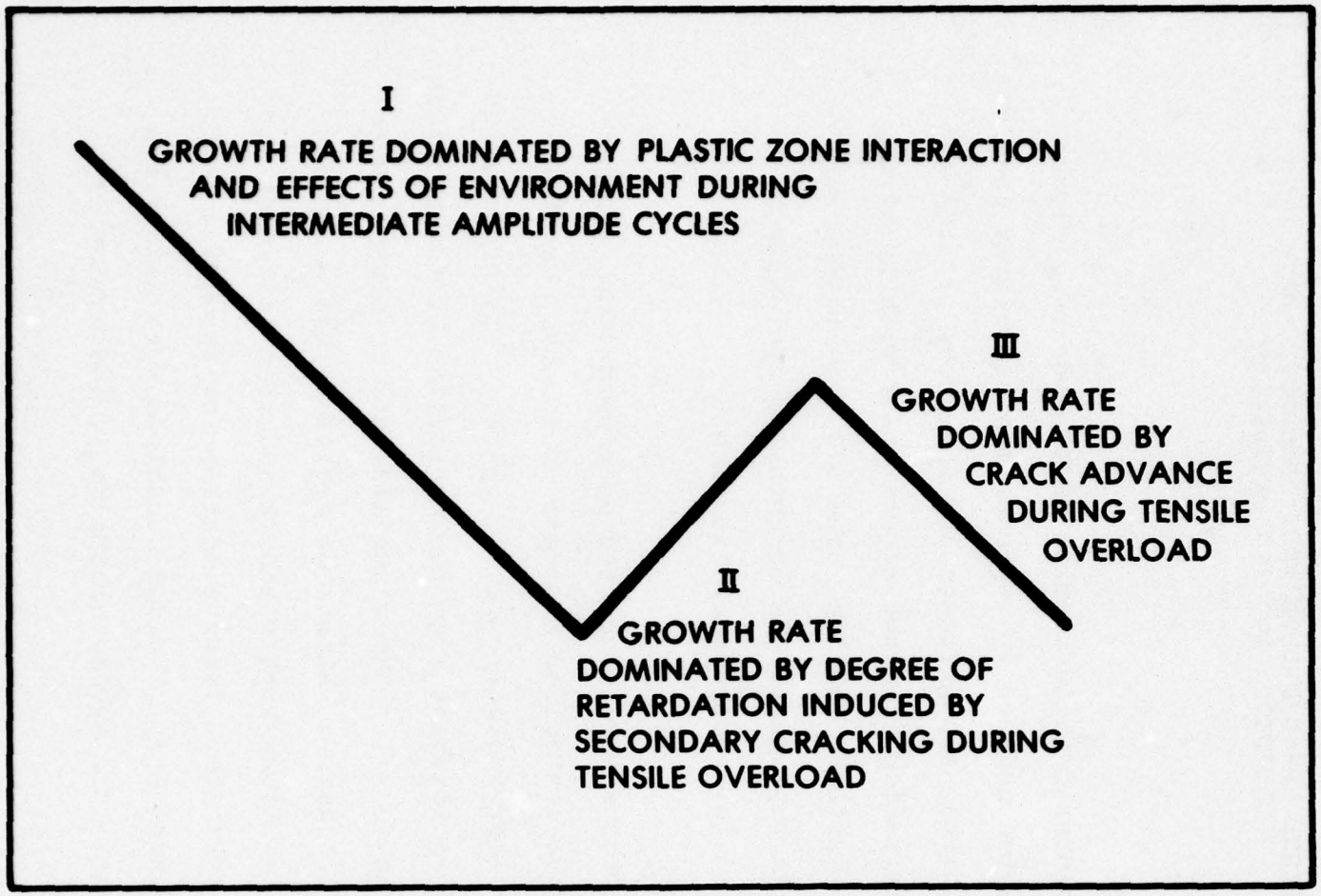

SCHEMATIC EFFECT OF YIELD STRENGTH IN PEAK AGED AND OVER AGED TEMPERS OF 7XXX ALLOYS ON FATIGUE CRACK PROPAGATION LIFE

FIGURE 31

APPENDIX A

FATIGUE CRACK GROWTH TEST PROCEDURE, DATA REDUCTION, AND ITS VARIABILITY

PROCEDURE

Specimen

A center cracked tension (CCT) specimen (Figure A-1) was selected because it represents a structural configuration of practical significance and therefore affords a meaningful evaluation of crack growth under both spectrum and constant amplitude loading. The L-T orientation was used because it represents the orientation typically most highly stressed in aerospace applications.

Instrumentation

All tests were conducted on closed loop, electro-hydraulic, servo-controlled MTS test equipment. Crack growth was monitored electronically by two crack propagation gauges bonded equidistant from the centerline of the specimen as shown in Figure A-2. The gauge elements or strands were 2.5 mm (0.1 in.) apart. Number of cycles within a cyclic block as well as block number and strand identification was monitored by teletype. Instrumentation for screening tests is shown in Figure A-3. The data obtained were half crack length (a), number of cyclic blocks (N_B), and number of cycles (N).

Periodic Single Peak Overload and Constant Amplitude

The test conditions held constant were control mode; frequency; humidity; maximum stress, stress ratio,

and intensity range for the constant amplitude portion of the test; and position of the propagation gauges. All tests were run under load control mode at a frequency of 6 Hz for baseline constant amplitude cycles and 0.2 Hz for the overload cycle.

Humid air (relative humidity 90%) at room temperature was the environment. The high humidity reduced sensitivity of crack growth to both test frequency and to small changes in moisture content [A1].

Maximum stress (σ_{max}) of 55.2 MPa (8 ksi) and constant amplitude baseline stress ratio, (R), of 1/3 were maintained during constant amplitude cycles.

Propagation gauges were located so crack growth data were obtained from 10.2 mm (0.4 in.) to 33 mm (1.3 in.) from centerline. Consequently, ΔK ranged from 7 to 16 MPa$\sqrt{m}$ (6 to 14 ksi$\sqrt{in.}$) during the test. The following factors were considered in deciding on the location of the propagation gauges:

1. Precrack interval: Sufficient precracking interval of 7.62 mm (0.3 in.) was provided to avoid any transient effects of test data. Final 2.54 mm (0.1 in.) of precracking was done under actual test spectrum and humidity level.

2. Stress intensity range: For a given gross stress and specimen geometry, maximum stress intensity (K_{max}) and constant amplitude stress intensity range (ΔK) increase with increasing crack length (Figure A-4). The gauges were

positioned such that ΔK at the start of data taking would be high enough so that test time would not be excessive and that K_{max} near the end of the test would be low enough so that fracture toughness would not greatly influence the results.

3. Nominal stress in uncracked ligament: Calculations were made to insure that the nominal stress in the uncracked ligament during overloads would not reach the static yield strength of the material during the crack growth range of interest.

Under these test conditions, crack growth rates unretarded by overloads were anticipated to lie in the linear region of typical log $\Delta a/\Delta N$ vs log ΔK curves for these alloys.

Overload ratios of 1.8 and 1.4 were employed in the initial screening tests. Based on plastic zone size calculations for an overload ratio of 1.8, an occurrence ratio of 1:4000 was initially selected. The ratio was thought to be sufficient to induce overload transients which would influence the amount of delay resulting from single peak overloads. An occurrence ratio of 1:8000 was selected for additional tests at this overload ratio. An occurrence ratio of 1:4000 was used for the tests at an overload ratio of 1.4.

Multilevel Spectrum

Service stress histories (spectra), once measured or derived, can be described as an ordered sequence of

stress events. Service spectra normally have a few identifiable stress events which repeat within a period and provide a simplified block loading tool for comparative evaluation of crack growth properties of materials. Guidelines suggested by ASTM E9.05 task group on development of reference test spectra [A2] were used in choosing the spectrum for this investigation. The spectrum is derived from load exceedence data of service spectra of fighter, commercial, and transport aircraft. The spectrum, which decays from 100 to 0% load as a straight line over four decades, was simulated by ten discrete load levels (Figure A-5).

The method of applying the loads was to make up two groups of cycles consisting of 2000 cycles. Type I group was repeated in sequence twice and Type II group was repeated three times continuously. The cycles within each group were arranged in low-high-low sequence as shown in Figure A-6. The stresses at each level are also shown. This arrangement was designed to distribute loadings uniformly throughout the spectrum and minimize any preferential effects on residual stresses.

The maximum stress of 14.4 ksi (99.3 MPa) was chosen so as to avoid excessive testing times and was determined using a flaw growth prediction model (EFFGRO) to estimate fatigue life. This maximum stress was also used in the periodic, single peak overload tests, thus facilitating comparison of test results. The minimum load of 0.288 ksi

(2.0 MPa) was chosen to maintain a small tensile load above zero. The frequency during intermediate loads was 6-7 Hz while on high overloads it was 0.5 Hz.

Raw data were plotted as half crack length, a, versus number of cyclic blocks, N_B (Figures A-7 through A-11 and A-13 through A-50).

Curve Fitting

In concept, the cyclic rate of fatigue crack propagation, da/dN, is determined as the derivative (i.e., local slope) of the crack growth curve (a vs N). However, in reality, because the crack growth curve is known only from a point-wise, experimental sampling of the crack size at finite intervals of cycling, the growth rate must be inferred from an interpolation scheme based on the discrete samples of crack growth measurements. Two general approaches exist for doing this. One approach is curve fitting wherein an analytical expression is fitted to all or part of the crack growth data by least squares regression techniques and, subsequently, differentiated to obtain the effective rate behavior. The other approach is incremental slope approximation in which a slope averaging technique is used in a local sense to define the rate behavior. In this investigation, the former approach of least squares regression technique was used.

Significant problems were encountered in attempting to utilize simple polynomial expressions to fit the experimental a vs N data. Low order polynomials were not sufficiently

pliable and higher order models introduced artifacts in the predictions. Consequently, a piece-wise cubic or spline function was chosen for curve fitting. Cubic spline fitting can be simply described as fitting a = f(N), where f(N) is a cubic polynomial segmented along the N axis and tied together at "knot" points. The important characteristics of a cubic spline are (1) it is continuous, (2) it is capable of being differentiated everywhere, and (3) its first derivative is continuous. Because of the excellent pliability of the spline function, very good fits were produced for the wide variety of curve shapes encountered in this work. Three knot points were used, two of which were fixed at the end points. The position of the one near the median N value was varied until it satisfied a least squares critierion for the predictions. This function was found to be capable of describing more than 99.2% of the variation in the experimental data when applied for prediction of an average a vs N curve using results from both sides of the specimen.

Because the curve fitting was so successful, the predictions were used for subsequent data presentation and analysis. The equations for a vs N were differentiated, and ratios of the derivatives of the constant amplitude to some of the spectrum tests were calculated.

VARIABILITY

In general, the repetition of experiments will not yield identical observations because of the intrinsic

variation introduced by the measuring devices, the materials used, the experimenter, and by the fact that it is physically impossible to repeat exactly any experimental performance. This error variance must be considered in making inferences from experimental data. The degree of confidence on inferences drawn from data increases with the number of observations. The number of tests required, however, depends on the end use of data. The intended use of crack growth data in this investigation was to discern any significant influence of metallurgical variables on fatigue crack resistance of aluminum alloys under variable amplitude loading.

The primary source of variability is the scatter encountered in the raw data (crack growth, a, vs number of cycles, N). The overall variability in fatigue crack growth rate data depends on the variability inherent in both the collection of raw data and the data processing techniques [A3]. The following analysis deals with the identification and evaluation of the variability related to the first source.

Variability in Collecton of Raw Data (a vs N)

Reproducibility of fatigue crack growth data using screening test methods may be primarily limited by: (1) surface crack length measurement resolution capability of crack propagation gauge, (2) eccentricity of gauge location from centerline of test specimen, (3) how well the surface crack represents the average crack across the thickness of specimen because of crack fron curvature, (4) load

accuracy, and (5) variability introduced by inhomogeneity in material. The first three factors affect the reproducibility of measuring crack length. The fourth affects the reproducibility of applying the stress, hence ΔK, which affects the crack growth rate and consequently cyclic life, N. The fifth affects crack growth rate, and consequently, N, for a particular crack length.

Resolution Capability of Gauge. The surface measurement resolution capability of a crack propagation gauge depends on the dimension of individual strands (0.04 mm) and the delay in detecting a crack which is underneath the strand. To assess this delay, observations were made during a spectrum test under ambient conditions. For all 20 observations, the crack tip was under the strand when the strand first indicated an open circuit. As an independent check, visual readings of crack length taken using photogrids imprinted on the specimens were compared with data taken using crack propagation gauges. These visual measurements can be made within $\pm$0.05 mm ($\pm$0.002 in.). Figures A-7 through A-11 represent the crack growth, a, vs number of cycles, N, data obtained from visual and propagation gauge measurements. It can be seen that they are in good agreement. Based on the foregoing analysis, the maximum expected error in crack detection with gauges is estimated to be about $\pm$0.1 mm.

Eccentricity of Propagation Gauge. The gauges were located at an equidistant point on either side of the

centerline of the specimens. The goal was to locate the first strand of each gauge at 10.16 mm from the centerline. All specimens were checked to determine the gauge eccentricity. An average tolerance of ±0.15 mm was maintained.

Crack Front Curvature. This phenomenon was observed to some extent in most of the fractured specimens. Because a surface crack measurement technique was used in this investigation, the difference between this measurement and average crack length through the thickness must be considered. Proposed ASTM E24.04 practice [A4] recommends that a crack curvature correction be employed when the correction results in a greater than 5% difference in calculated stress intensity at any crack length. All failed specimens which showed the highest degree of crack front curvature were measured with a ruler divided into 0.01" increments. Average crack lengths were calculated, and stress intensity was determined based on both calculated and measured crack lengths. The ratios of calculated to measured average stress intensity were within 2% so no correction was necessary.

Conclusions on Factors Affecting Variability in Measuring Crack Length. From the foregoing, it appears that crack length measurement error is almost wholly ascribable to variability in positioning the gauge and to the resolving limitation of the gauge. This error is probably no more than ±0.2 mm. Since the initial and final crack lengths were 10.2 and 33 mm, this translates to 2% error in measuring

initial crack length (a_o) and 0.6% error in measuring final crack length (a_f) in a particular test.

Load Accuracy. The load range (ΔP) and maximum load were maintained within $\pm$2%.

Combined Effects of Errors in a and P

Hilberry [A5] estimated the variability in cyclic life under constant amplitude loading for a hypothetical, structureless aluminum alloy tested over the linear portion of the log da/dN vs log ΔK curve (typical n = 3.8). He calculated the error introduced by a 2% error in measuring initial crack length, a_o, any crack length, a, and load range, ΔP, and assumed that all three measured values were statistically independent random variables with normal distributions. The error in N for various values of a/a_o for $\pm$2% error in a, a_o, and ΔP is shown in Table A-2. Since the ratio of final crack length over initial crack length, a/a_o, was 3.25, the percent error ($\pm$3 N/N%) from Table A-2 is 8.2%. Note that this error is larger for shorter cracks than for longer ones.

Material Heterogeneity. As demonstrated in the "Materials" section of this report, the materials were heterogeneous over a wide range of magnifications. Metallographic examination of the interrupted test specimens revealed that coarse constituent particles played the major role in influencing crack path and, hence, crack growth rate. Consequently, heterogeneity in the distribution of

constituents would probably contribute to test variability. Heterogeneity in distribution of constituents would be greater in the higher purity materials, so their test results are anticipated to be more variable.

Replication

An obvious measure of variability in cyclic life for different crack lengths is to run replicate tests and estimate variability from experimental results. Because conducting the large number of tests needed for such estimation is expensive, only limited reproducibility tests were run in this investigation. Triplicate test results were available up to final half crack length of 25 mm for 7075-T6 under 80% overload, 1:4000 occurrence ratio from interrupted tests. A composite curve for 7075-T6 is shown in Figure A-12. A good agreement between those curves can be observed. The final lives from triplicate tests were 438, 415, and 471 (15% range). The mean life $\bar{X}$ = 441 and the Estimate of Standard Deviation S = 28.15. The coefficient of variation $S/\bar{X}$ = 0.064 of 6.4%. Considering the same factor of three used by Hillberry, a variation of nearly 20% is predicted at a crack length of 25 mm and a/a_o ratio of = 25/10.16 = 2.46. This is over twice as large as the 8.6% error predicted by Hillberry for the same ratio of a/a_o. This difference is not unexpected because his analysis predicts the variability in cyclic life due to error in measurement of a/a_o, and ΔP only, while our reproducibility tests give overall scatter

due to other factors like variability due to material inhomogeneity. Also, duplicate tests were run on alloys 7050-T7 and 7075-T6 under 80% overload ratio and using occurrence ratios of 1:4000 and 1:8000, respectively. The cyclic lives at the final crack length for each alloy were well within 30%. Moreover, the sigmoidal shape of the crack length vs elapsed cyclic curve for alloy 7075-T6 was reproduced (Figures A-40 and A-41).

Conclusion

We can use the calculated variations to estimate our ability to detect microstructural effects on crack growth cyclic lives. Assuming that all other single observations for different structures represent the estimate of their means, and also assuming that variability for all alloys in the program does not exceed that of 7075-T6, lives are expected to fall 99.7% of the time within $\pm$30% of the indicated N. Thus, effects of microstructure which are discussed in the body of the report are those which cause differences in crack growth life in excess of 30%.

REFERENCES - APPENDIX A

A1. R. P. Wei, "Some Aspects of Environment Enhanced Fatigue Crack Growth," Engineering Fracture Mechanics, Vol 1, No. 4, April 1970.

A2. J. C. Ekvall, Correspondence, 1976 August 18 to ASTM E09.05 Task Group Development of Reference Test Spectra.

A3. Clark, W. G., Jr., and Hudak, S. J., Jr., "Variability in Fatigue Crack Growth Rate Testing," Journal of Testing and Evaluation, Vol 3, No. 6, p 454-476, 1975.

A4. ASTM E24.04, "Recommended Standard Methods of Testing and Analyzing Fatigue Crack Growth Rate Data," 1977.

A5. Hillberry, B. M., Measurement Errors in Determining Fatigue Crack Growth Propagation," unpublished notes.

TABLE A1. INFLUENCE OF THE RATIO a/a_o ON THE ERROR OF N

$\frac{a}{a_o}$	$\frac{\sigma N}{N}$	$\frac{2\sigma N\%}{N}$	$\frac{\pm 3\sigma N\%}{N}$
1.1	0.102	20.4	$\pm$30.7
1.2	0.058	11.6	$\pm$17.4
1.5	0.035	7.0	$\pm$10.4
2	0.029	5.8	$\pm$ 8.8
3	0.027	5.4	$\pm$ 8.2
5	0.027	5.4	$\pm$ 8.0

$$\left[\frac{\sigma N}{N}\right]^2 = \left[\frac{-n/2+1}{1-(a_o/a)^{-n/2+1}}\right]^2 \left[\frac{\sigma a}{a}\right]^2 + \left[\frac{-n/2+1}{(a/a_o)^{-n/2+1}-1}\right]^2 \left[\frac{\sigma a_o}{a_o}\right]^2 + (-n)^2 \left[\frac{\sigma \Delta P}{\Delta P}\right]^2 *$$

*Hillberry, B. M., "Measurement Errors in Determining Fatigue Crack Growth Propagation," unpublished notes.

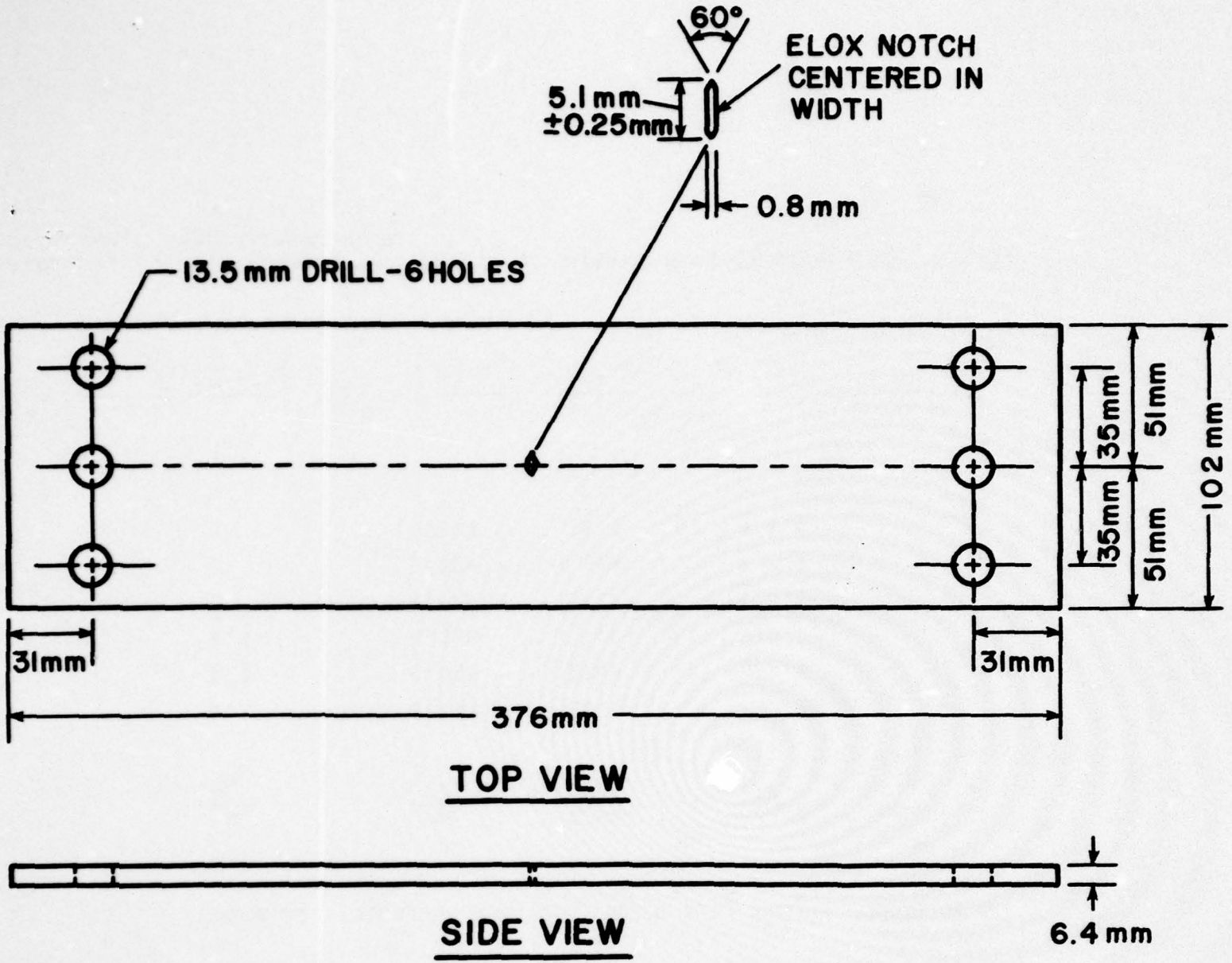

FIGURE A1 - CCT SPECIMEN GEOMETRY, L-T ORIENTATION

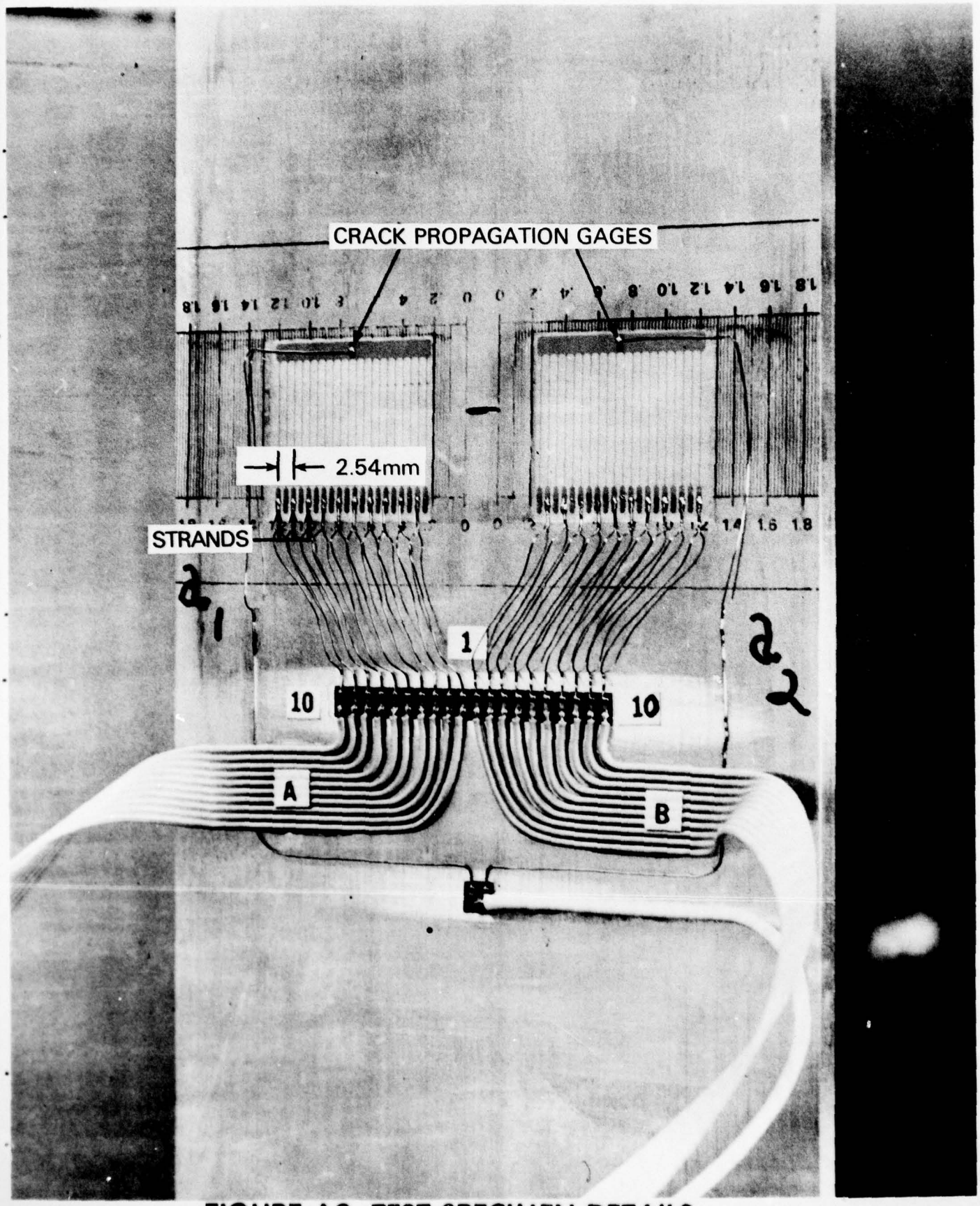

FIGURE A2 TEST SPECIMEN DETAILS

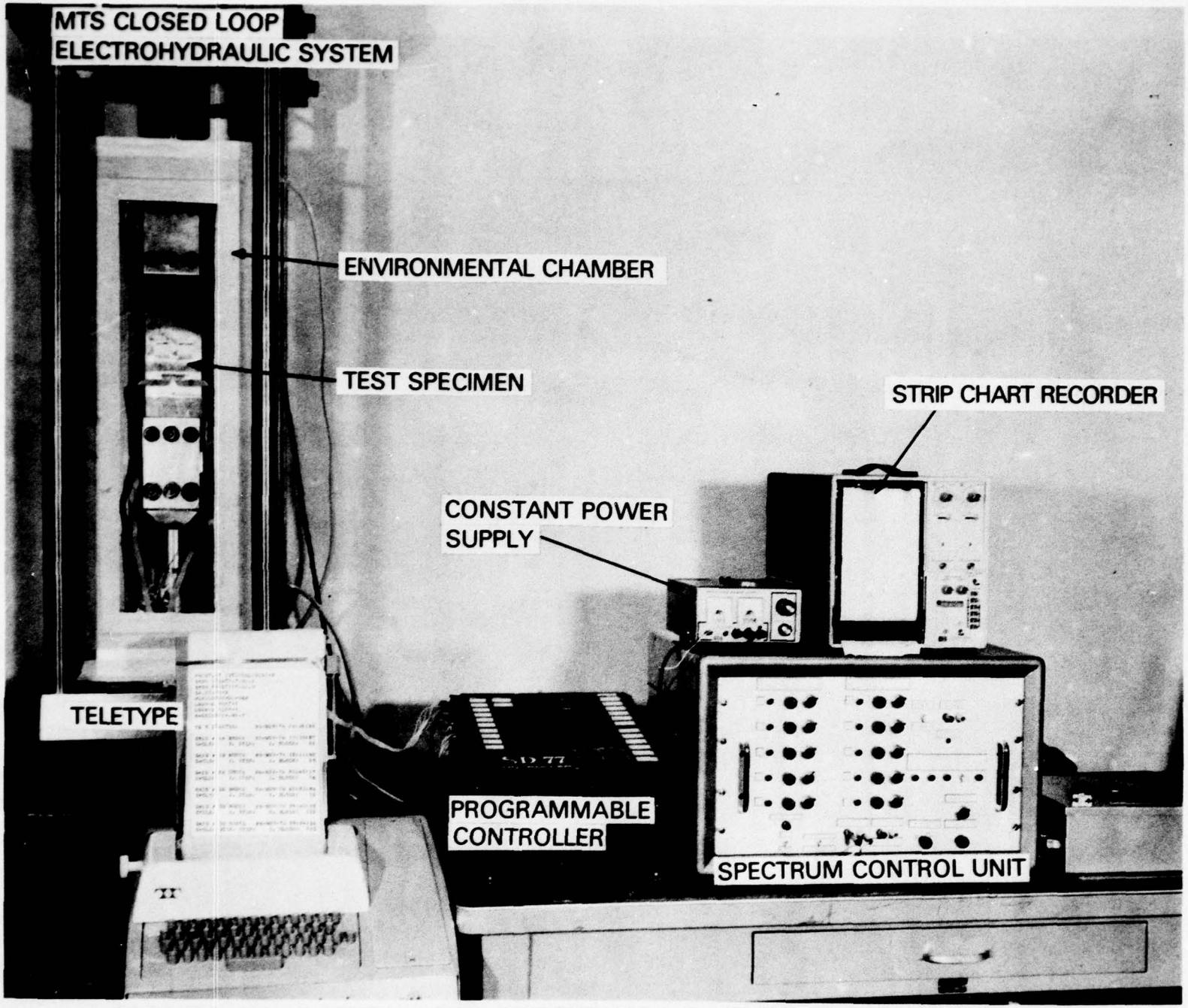

FIGURE A3 AUTOMATED SPECTRUM LOADING INSTRUMENTATION

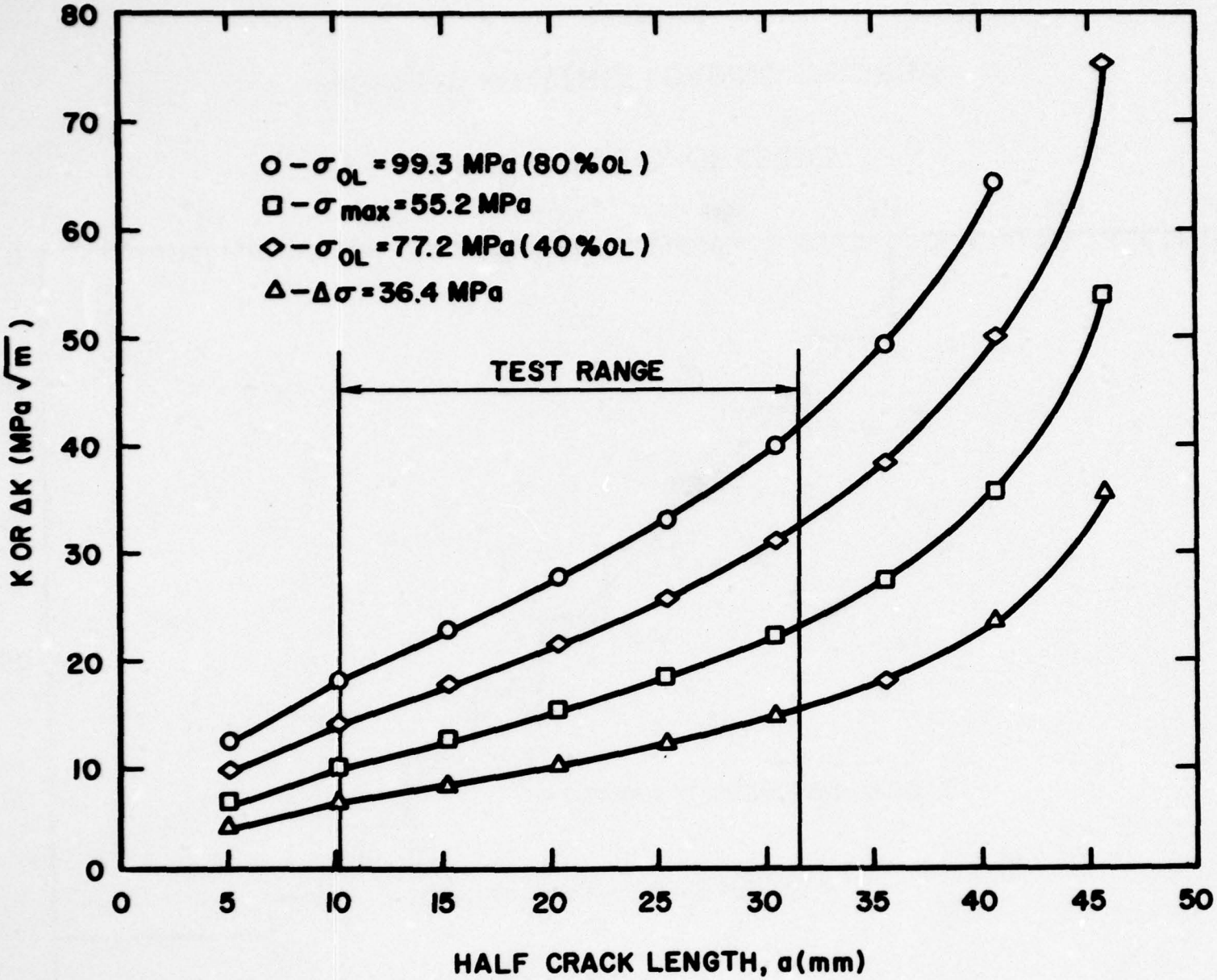

K OR ΔK VS HALF CRACK LENGTH FOR 102 mm WIDE CCT SPECIMEN

FIGURE A4

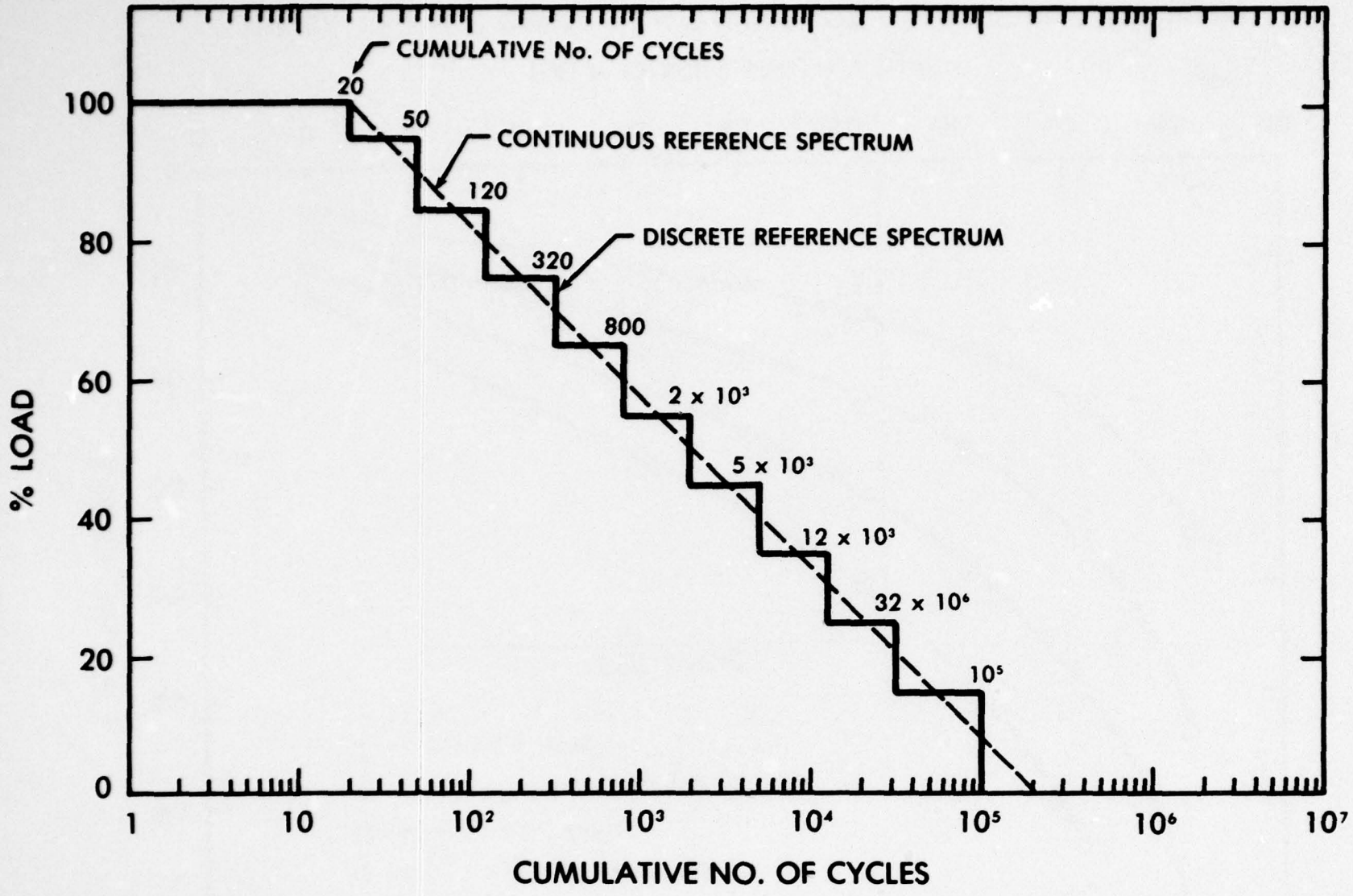

PROPOSED REFERENCE LOADING SPECTRUM

FIGURE A5

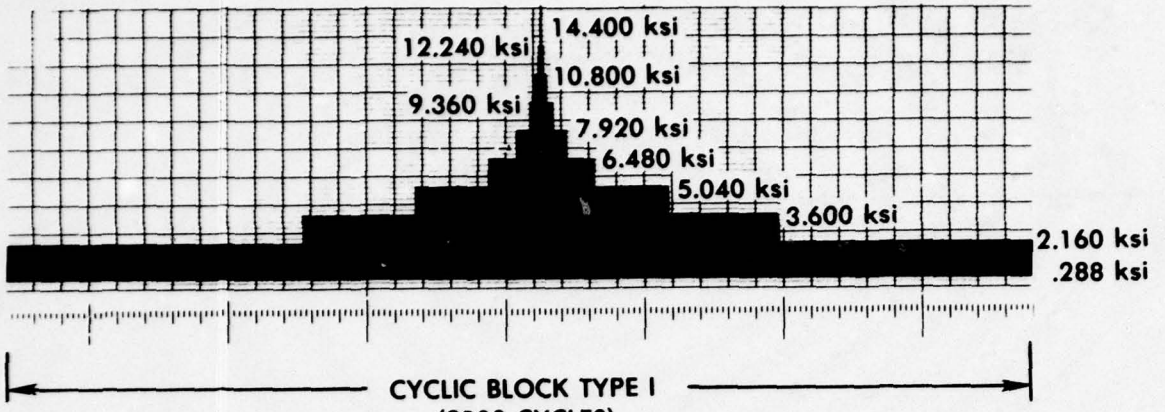

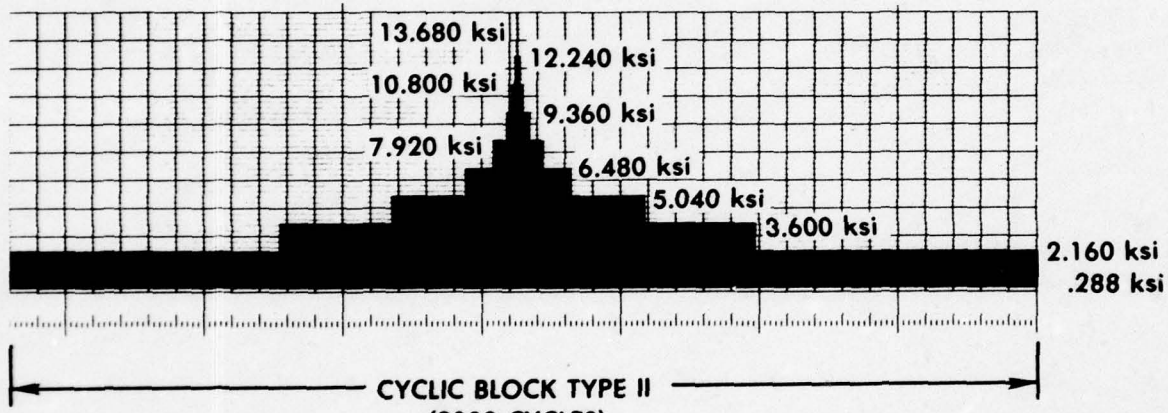

CYCLIC BLOCK TYPE I REPEATED TWICE AND TYPE II REPEATED 3 TIMES IN THAT ORDER CONTINUOUSLY.

LOW - HIGH - LOW LOADING SEQUENCE

FIGURE A6

AD-A057 129 ALUMINUM CO OF AMERICA ALCOA CENTER PA ALCOA LABS F/G 11/6
EFFECT OF MICROSTRUCTURE ON FATIGUE CRACK GROWTH OF 7XXX ALUMIN--ETC(U)
APR 78 T H SANDERS, R R SAWTELL, J T STALEY N00019-76-C-0482

UNCLASSIFIED 56-78-AF8 NL

3 OF 3
AD
A057 129

END
DATE
FILMED
9-78
DDC

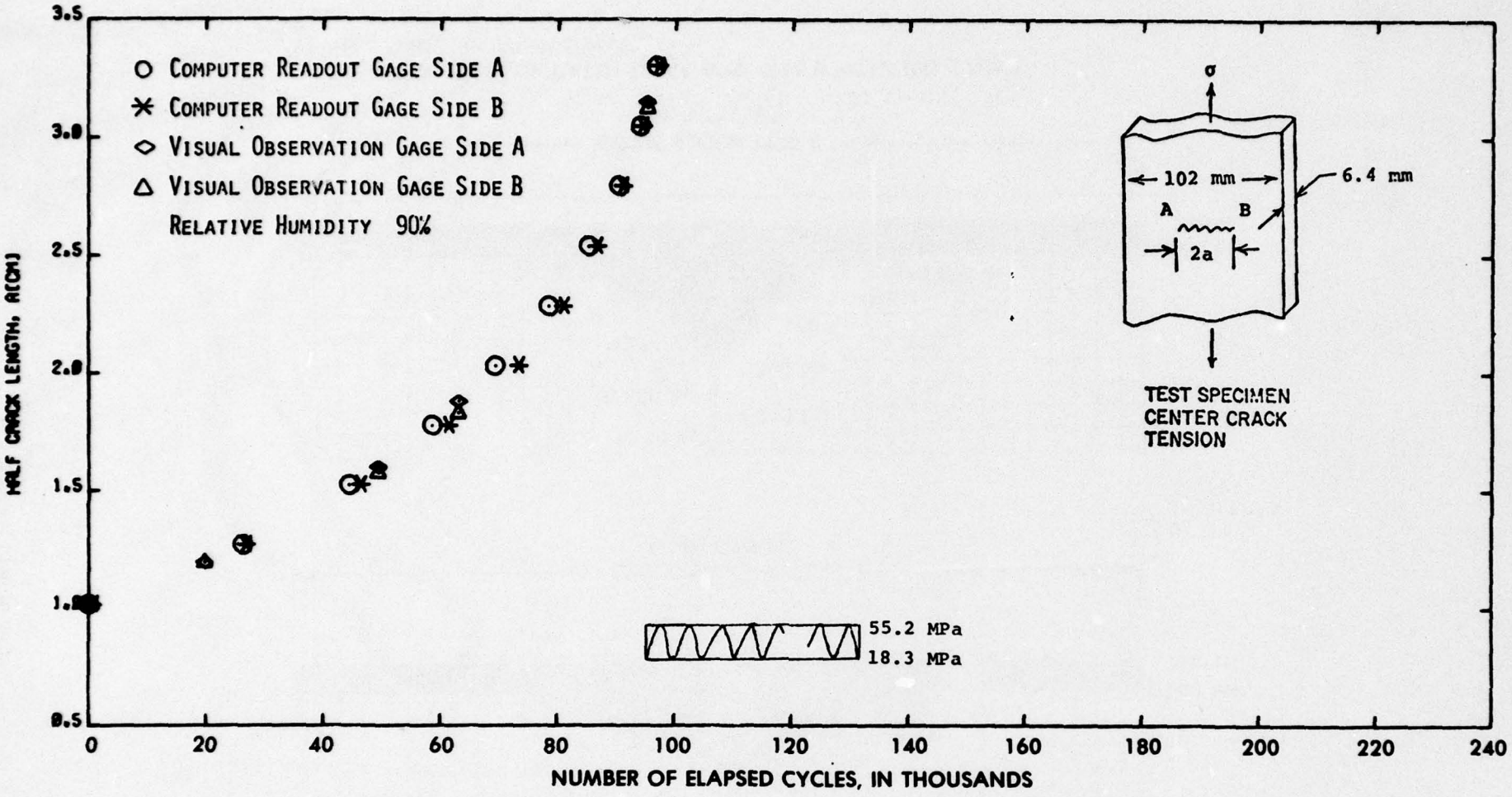

FIG. A-7 CRACK LENGTH VS. NUMBER OF ELAPSED CYCLES FOR CONSTANT AMPLITUDE TESTS OF ALLOY 7010-T7 HI PURITY

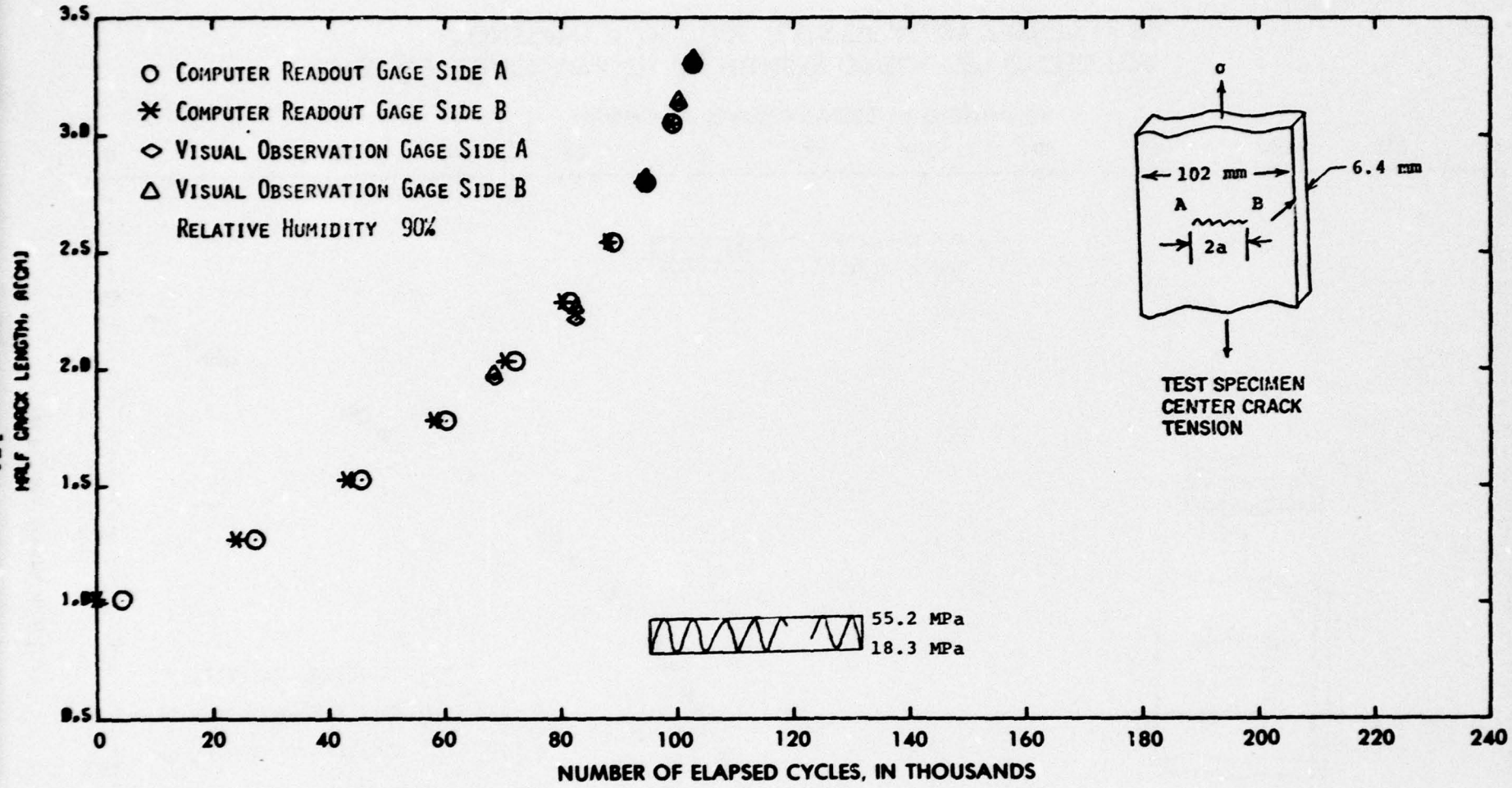

FIG. A-8 CRACK LENGTH VS. NUMBER OF ELAPSED CYCLES FOR CONSTANT AMPLITUDE TESTS OF ALLOY 7475-T7

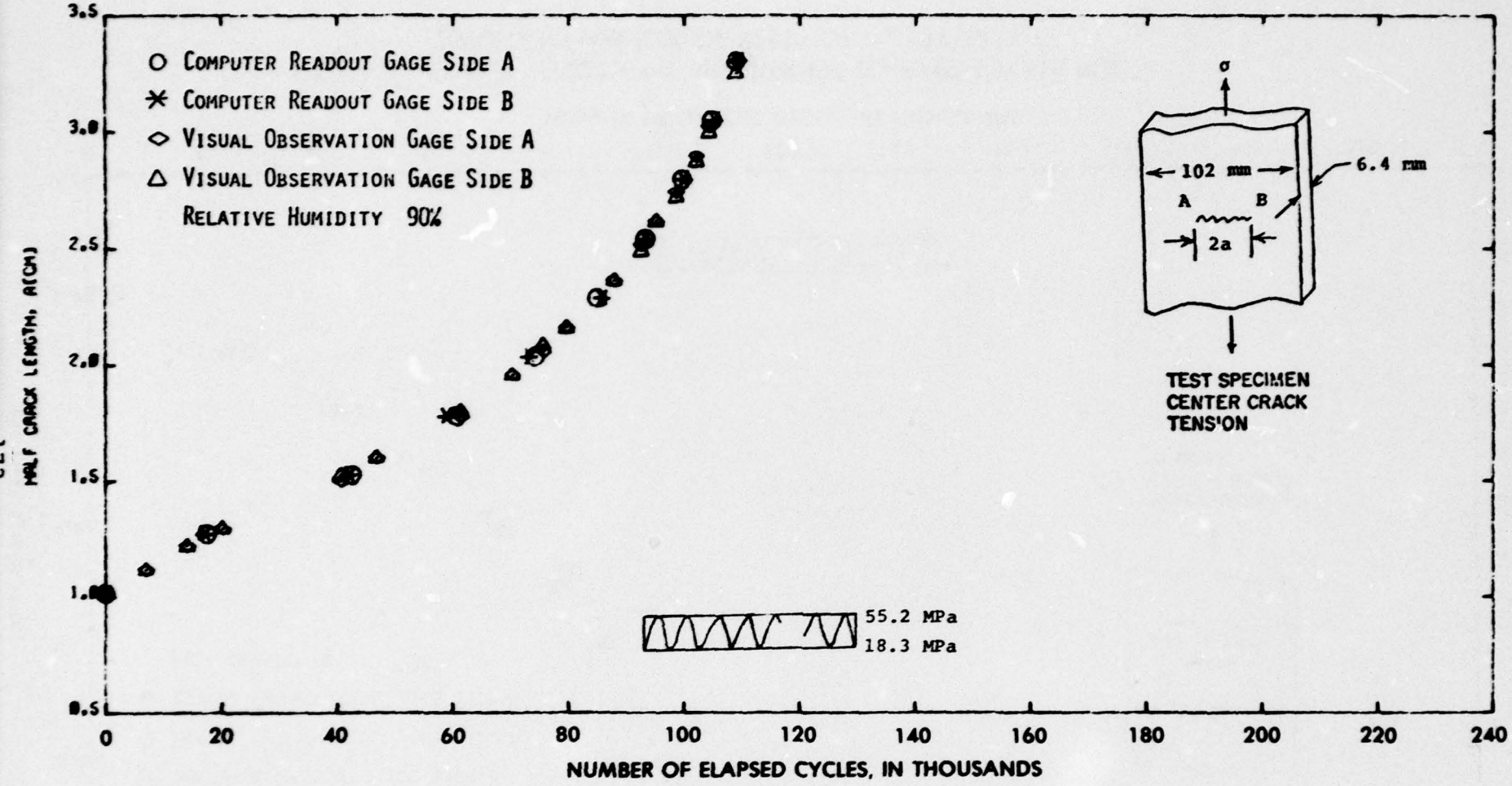

172

FIG. A-9 CRACK LENGTH VS. NUMBER OF ELAPSED CYCLES FOR CONSTANT AMPLITUDE TESTS OF ALLOY 7475-T7 HI Cu

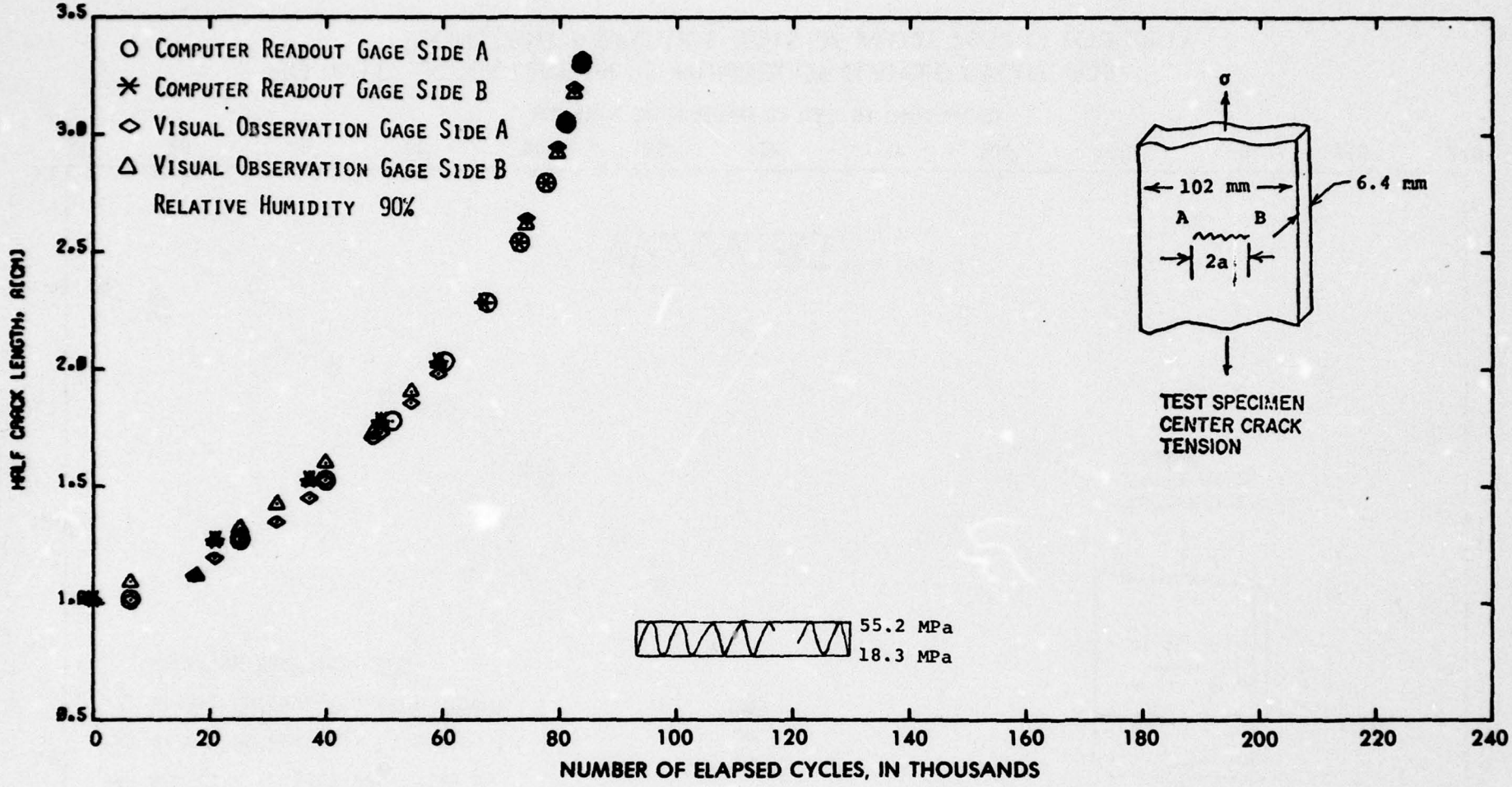

FIG. A-10 CRACK LENGTH VS. NUMBER OF ELAPSED CYCLES FOR CONSTANT AMPLITUDE TESTS OF ALLOY 7010-T7

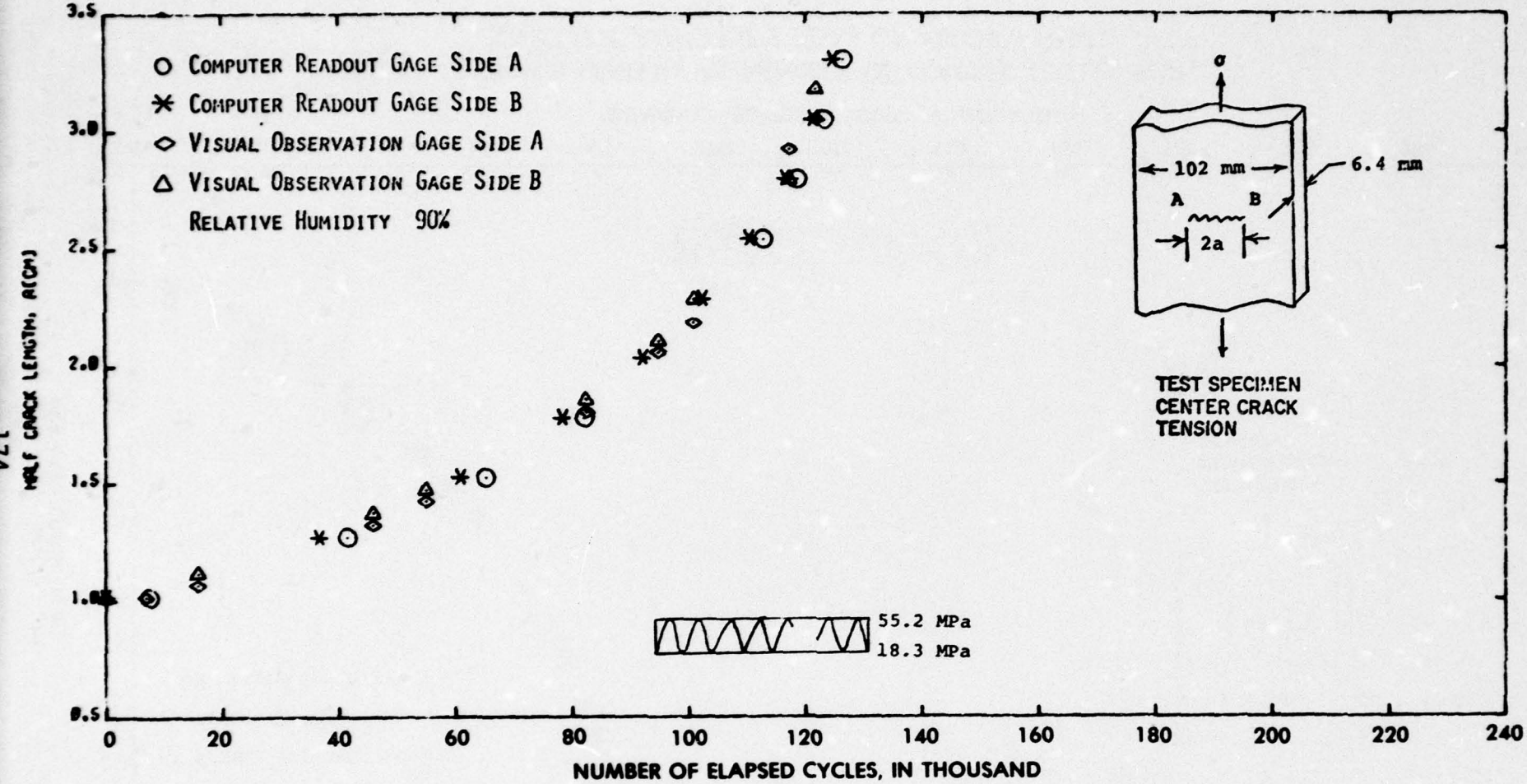

FIG. A-11 CRACK LENGTH VS. NUMBER OF ELAPSED CYCLES FOR CONSTANT AMPLITUDE TESTS OF ALLOY 7050-T7 LO PURITY

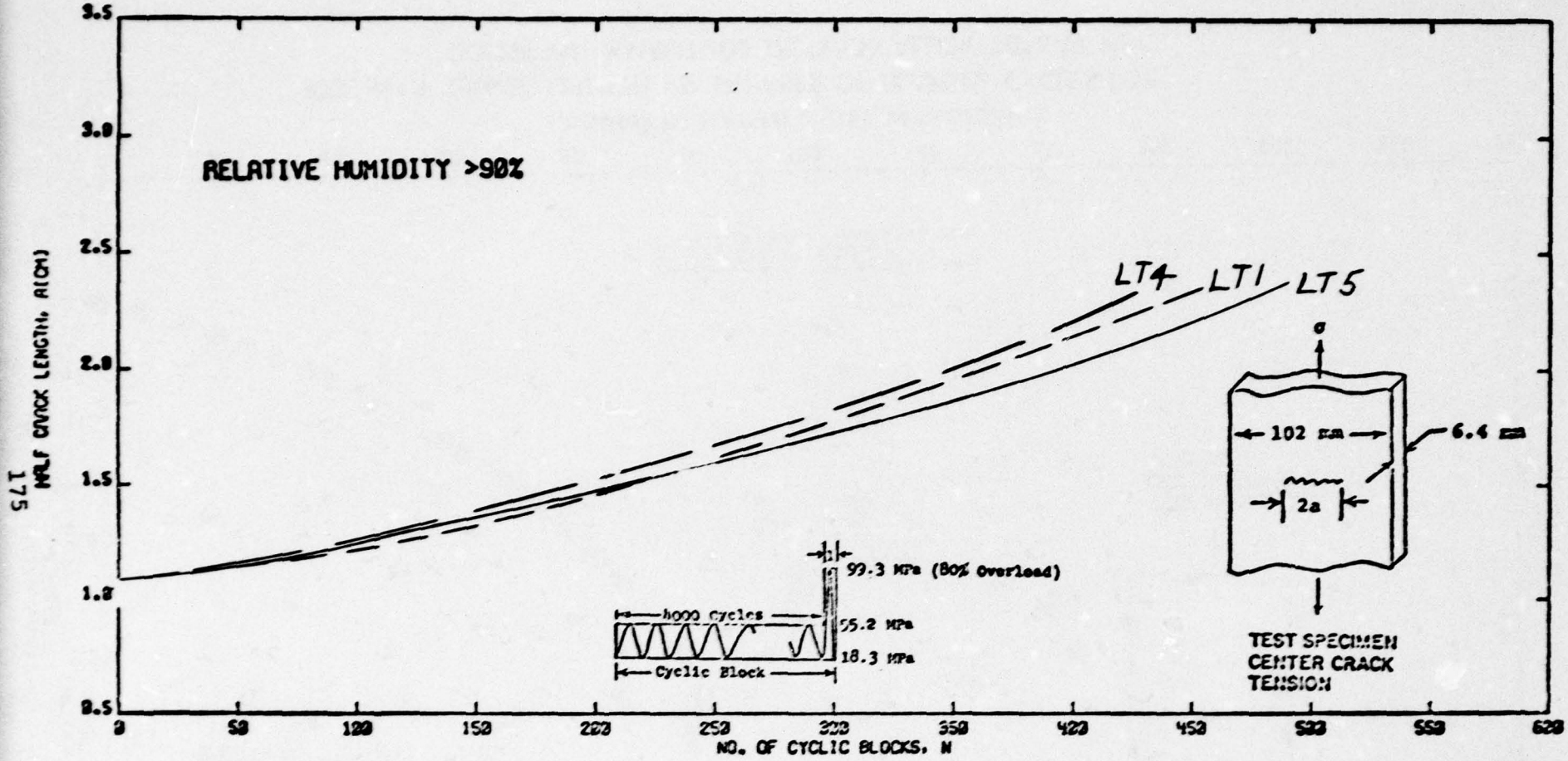

FIG. A-12 CRACK LENGTH VS. NUMBER OF ELAPSED CYCLIC BLOCKS FOR SINGLE PERIODIC OVERLOAD TESTS OF ALLOY 7075-T6

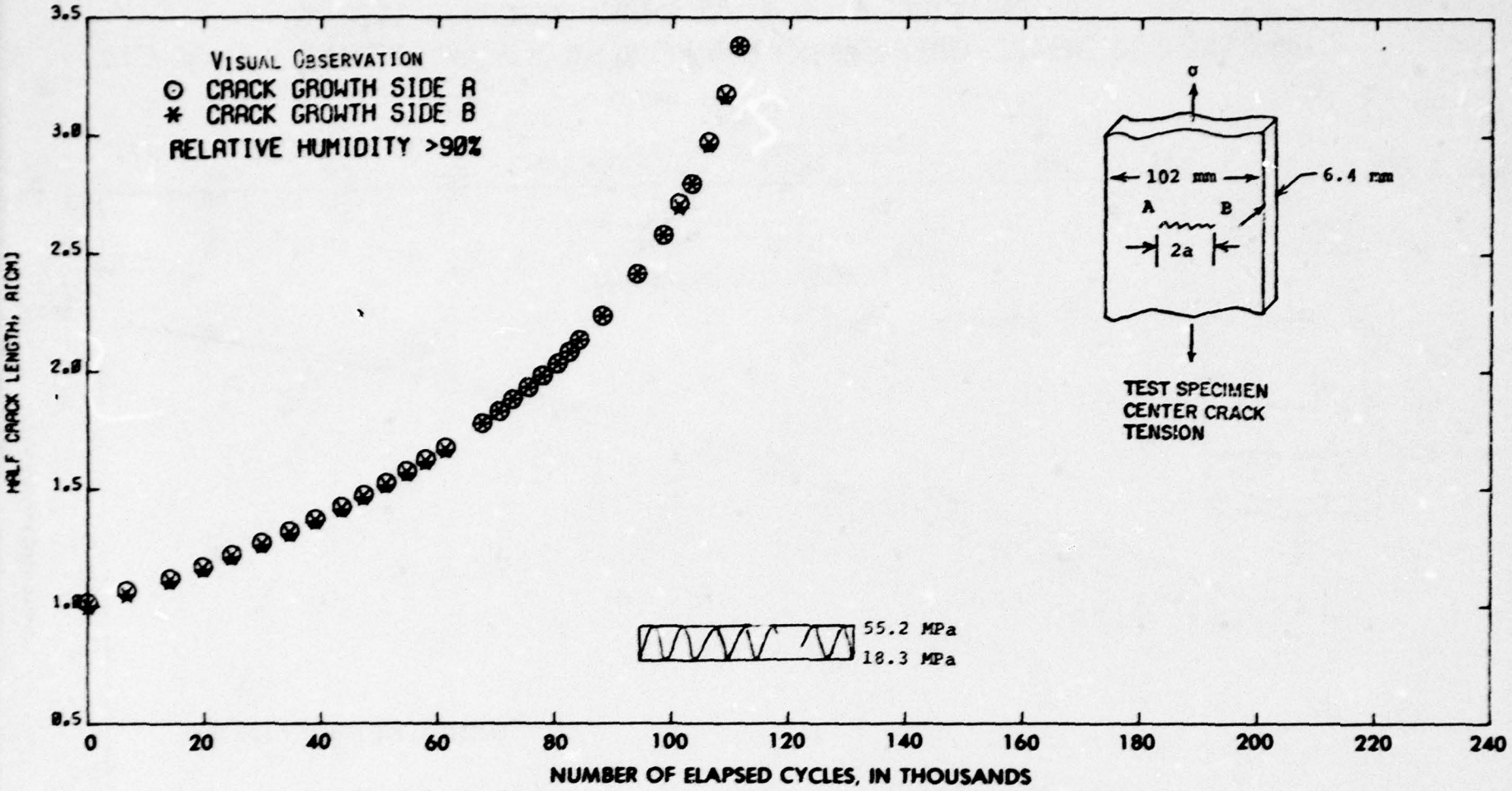

FIG. A-13 CRACK LENGTH VS. NUMBER OF ELAPSED CYCLES FOR CONSTANT AMPLITUDE TESTS OF ALLOY 7075-T7 HI Cu

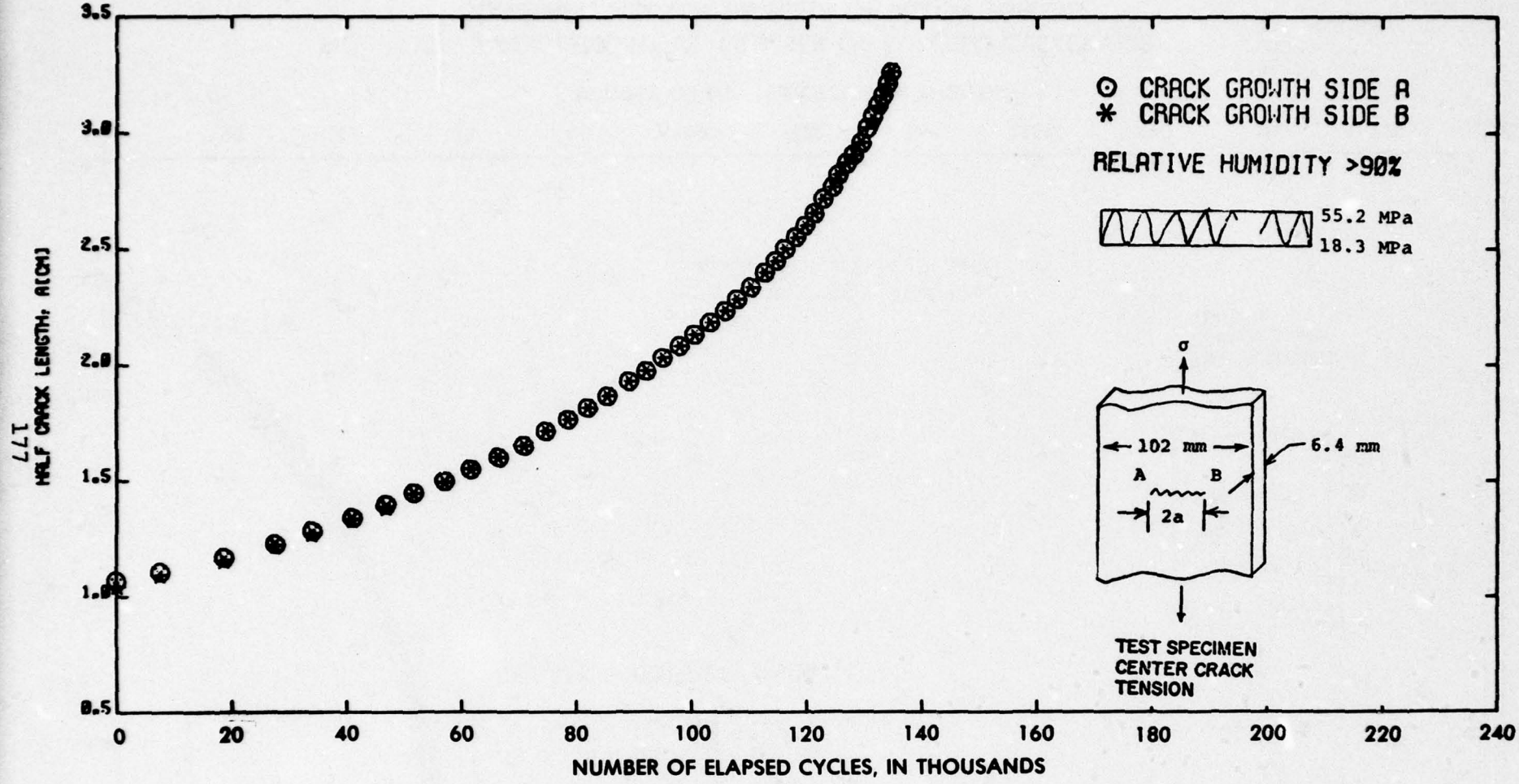

FIG. A-14 CRACK LENGTH VS. NUMBER OF ELAPSED CYCLES FOR CONSTANT AMPLITUDE TESTS OF ALLOY 7050-T7

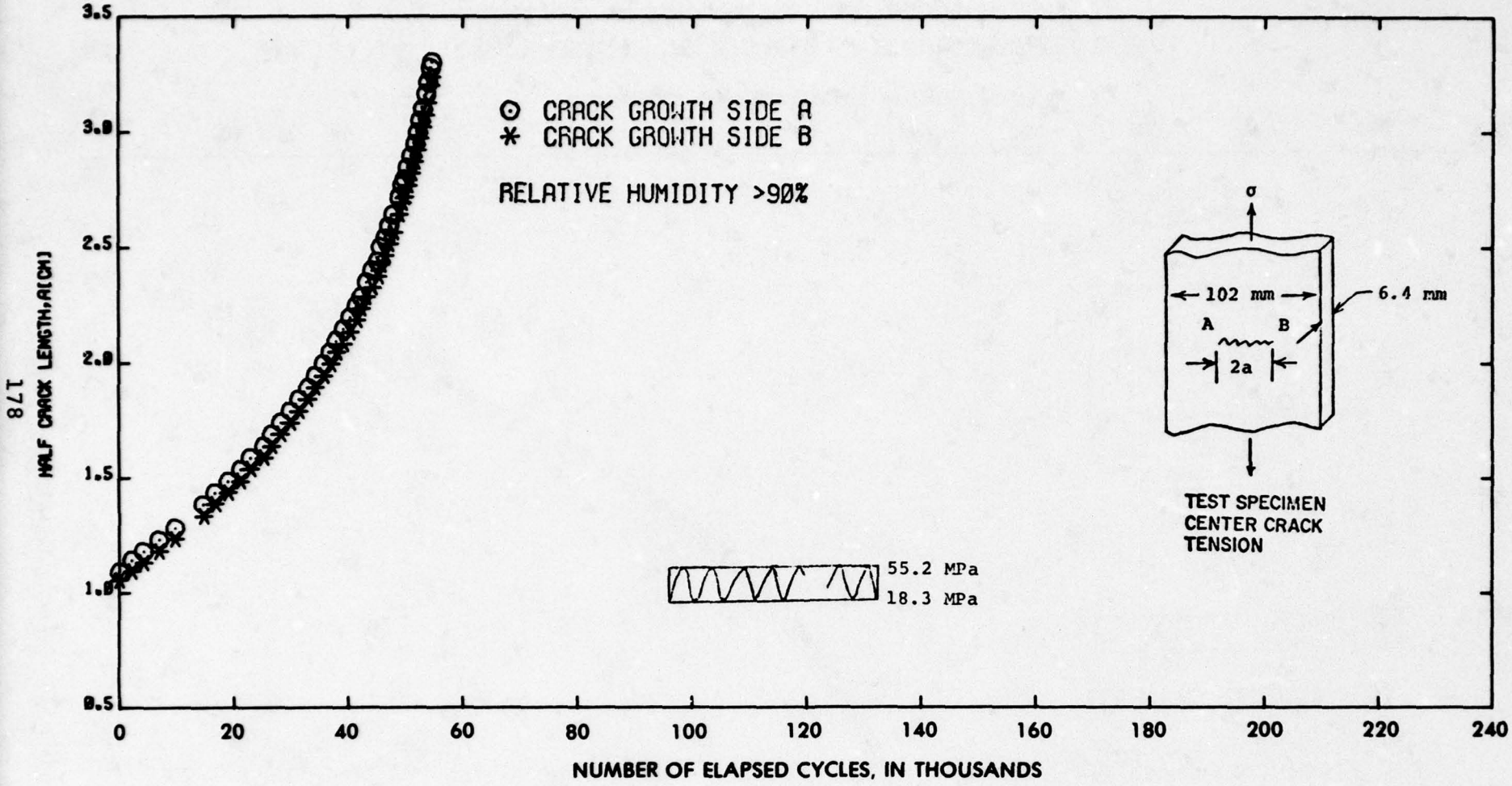

FIG. A-15 CRACK LENGTH VS. NUMBER OF ELAPSED CYCLES FOR CONSTANT AMPLITUDE TESTS OF ALLOY 7050-T6

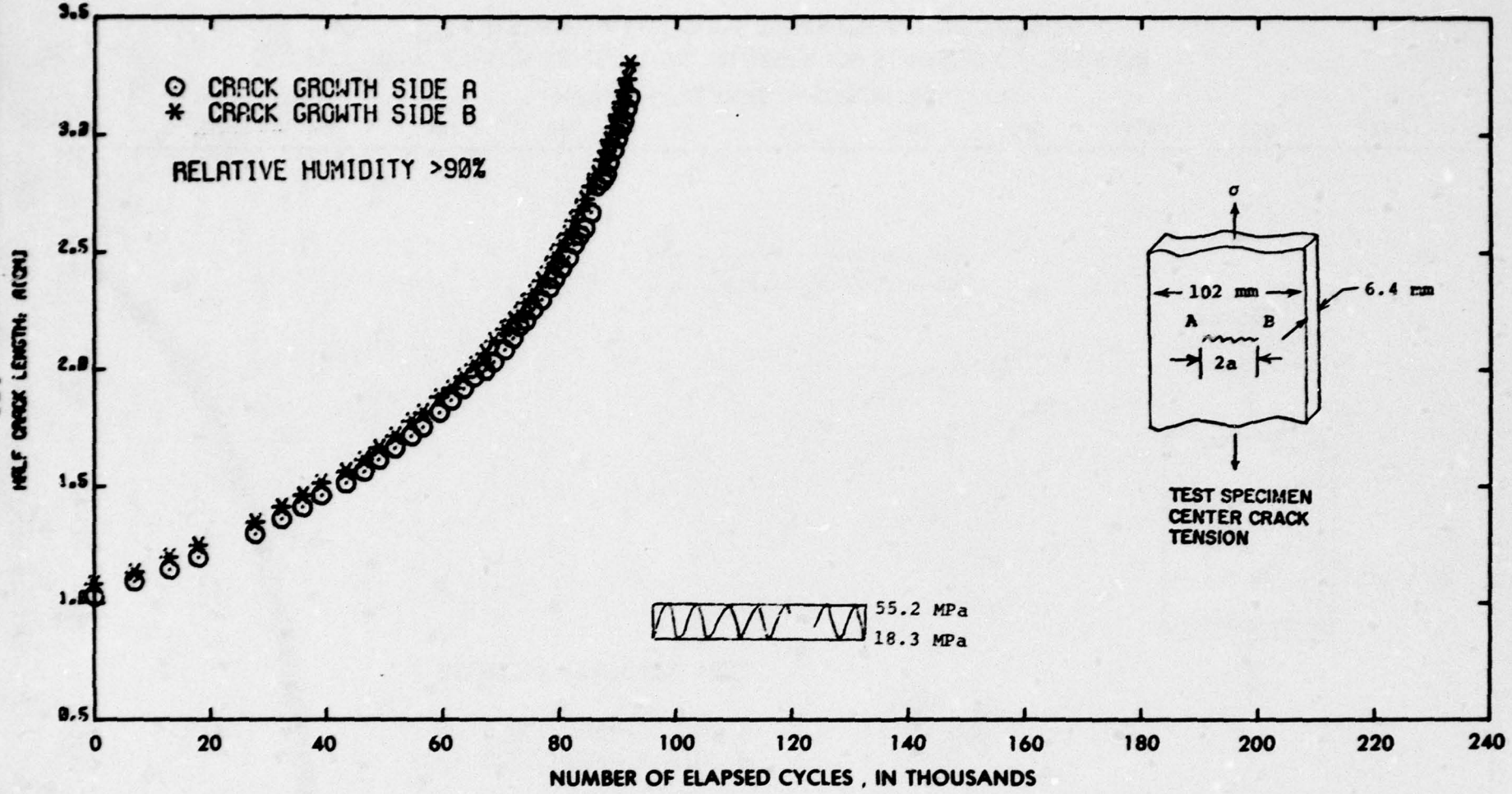

FIG. A-16 CRACK LENGTH VS. NUMBER OF ELAPSED CYCLES FOR CONSTANT AMPLITUDE TESTS OF ALLOY 7075-T7

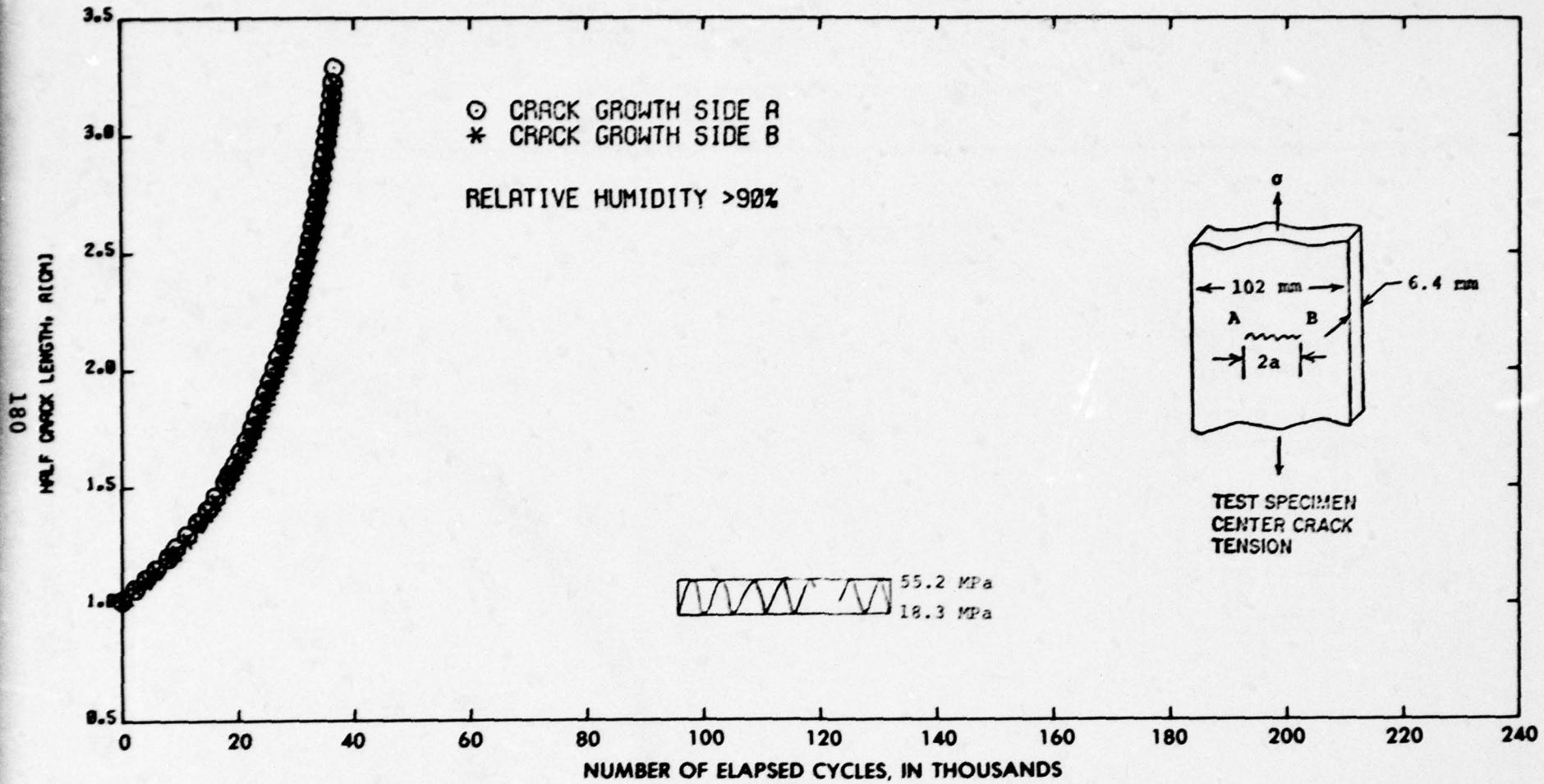

FIG. A-17 CRACK LENGTH VS. NUMBER OF ELAPSED CYCLES FOR CONSTANT AMPLITUDE TESTS OF ALLOY 7075-T6

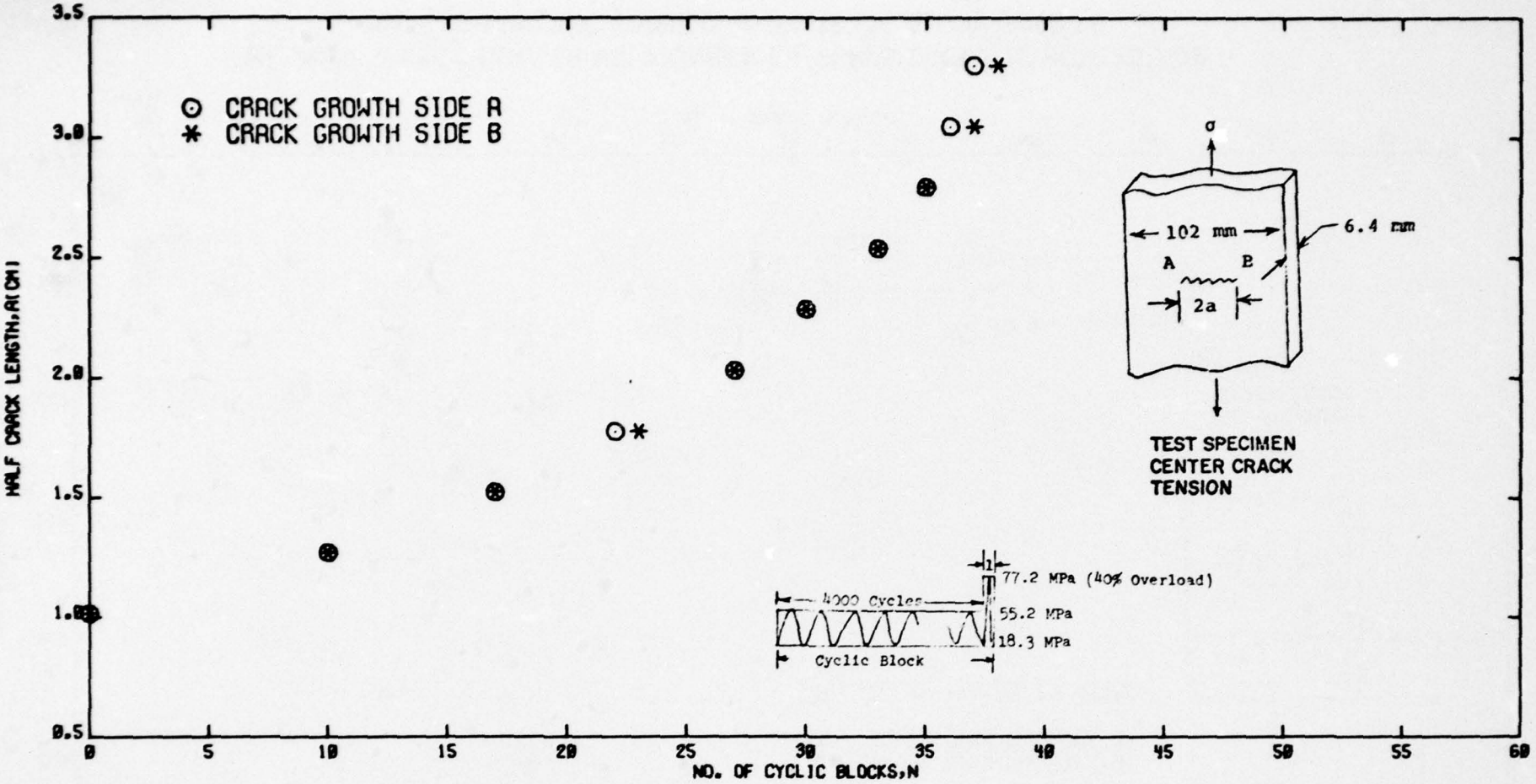

FIG. A-18 CRACK LENGTH VS. NUMBER OF ELAPSED CYCLIC BLOCKS FOR SINGLE PERIODIC OVERLOAD TESTS OF ALLOY 7050-T7

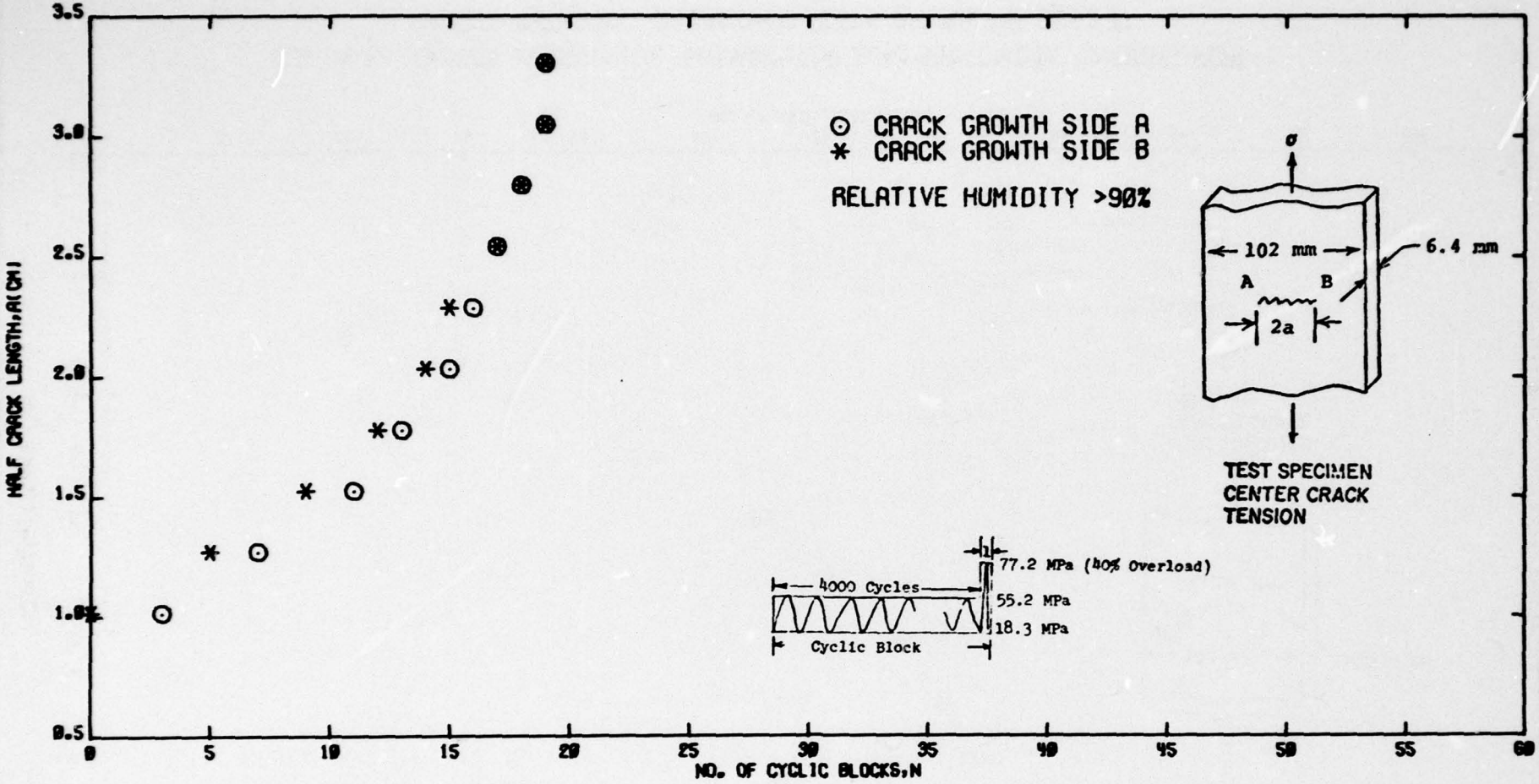

FIG. A-19 CRACK LENGTH VS. NUMBER OF ELAPSED CYCLIC BLOCKS FOR SINGLE PERIODIC OVERLOAD TESTS OF ALLOY 7050-T6

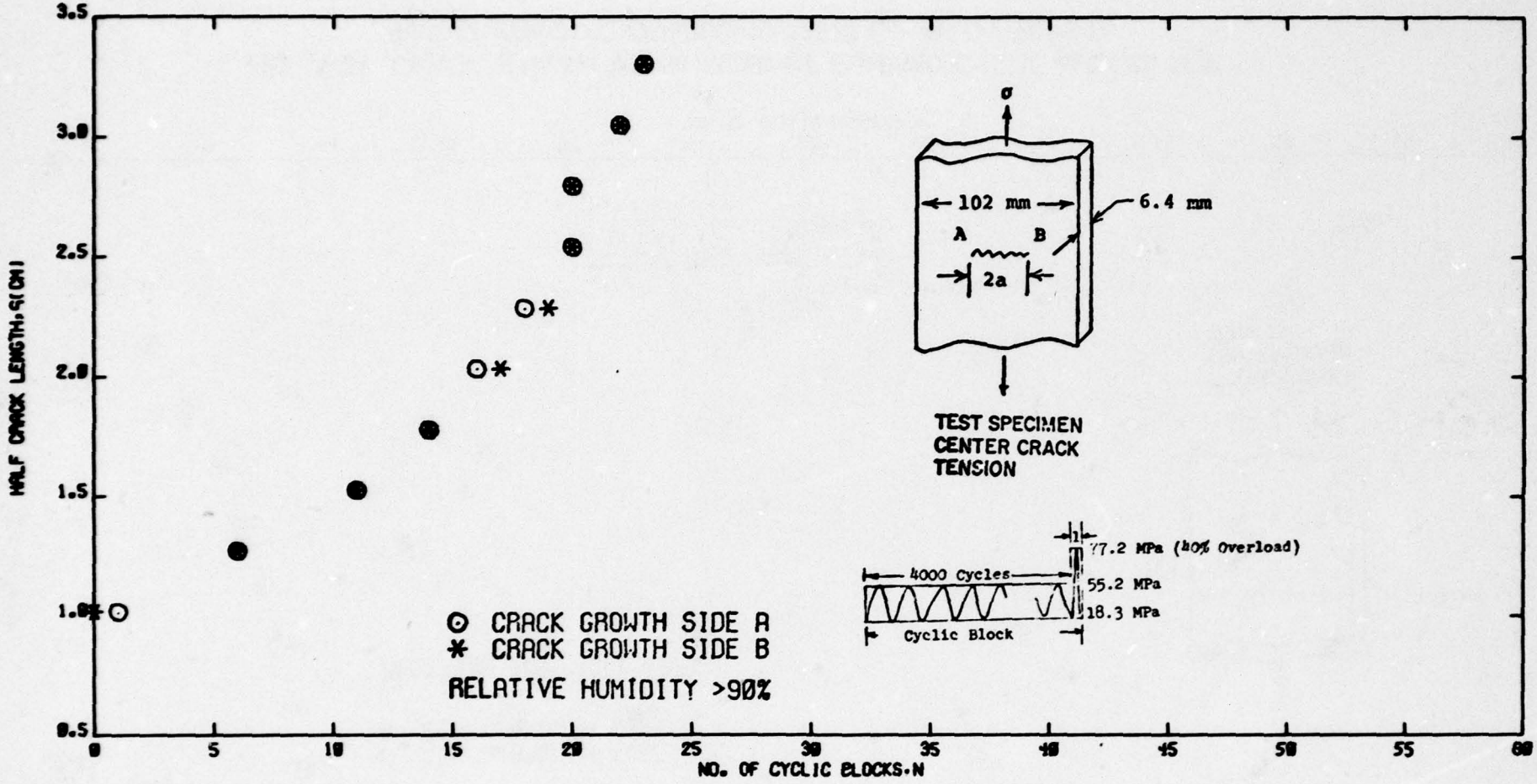

FIG. A-20 CRACK LENGTH VS. NUMBER OF ELAPSED CYCLIC BLOCKS FOR SINGLE PERIODIC OVERLOAD TESTS OF ALLOY 7075-T7

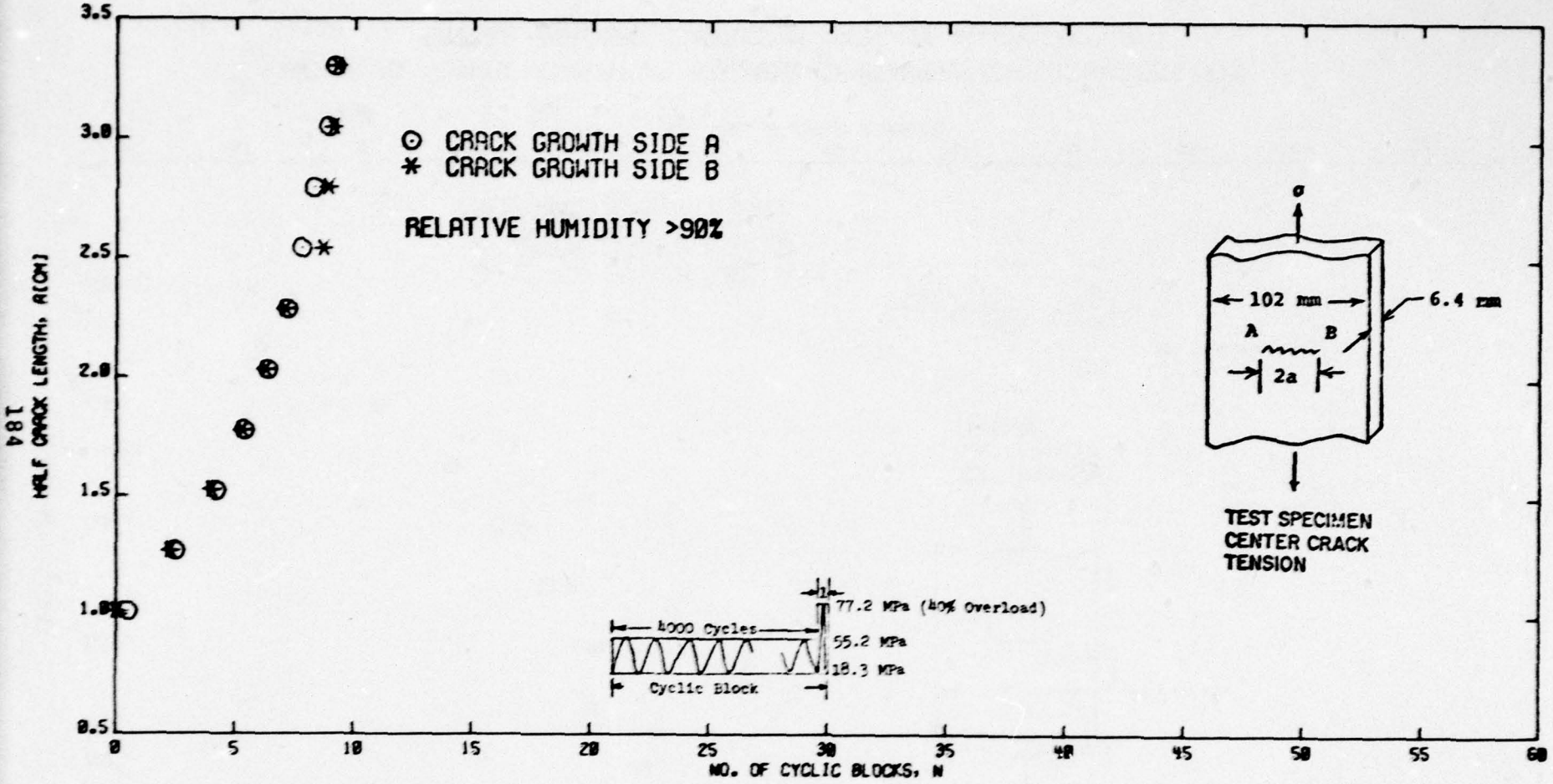

FIG. A-21 CRACK LENGTH VS. NUMBER OF ELAPSED CYCLIC BLOCKS FOR SINGLE PERIODIC OVERLOAD TESTS OF ALLOY 7075-T6

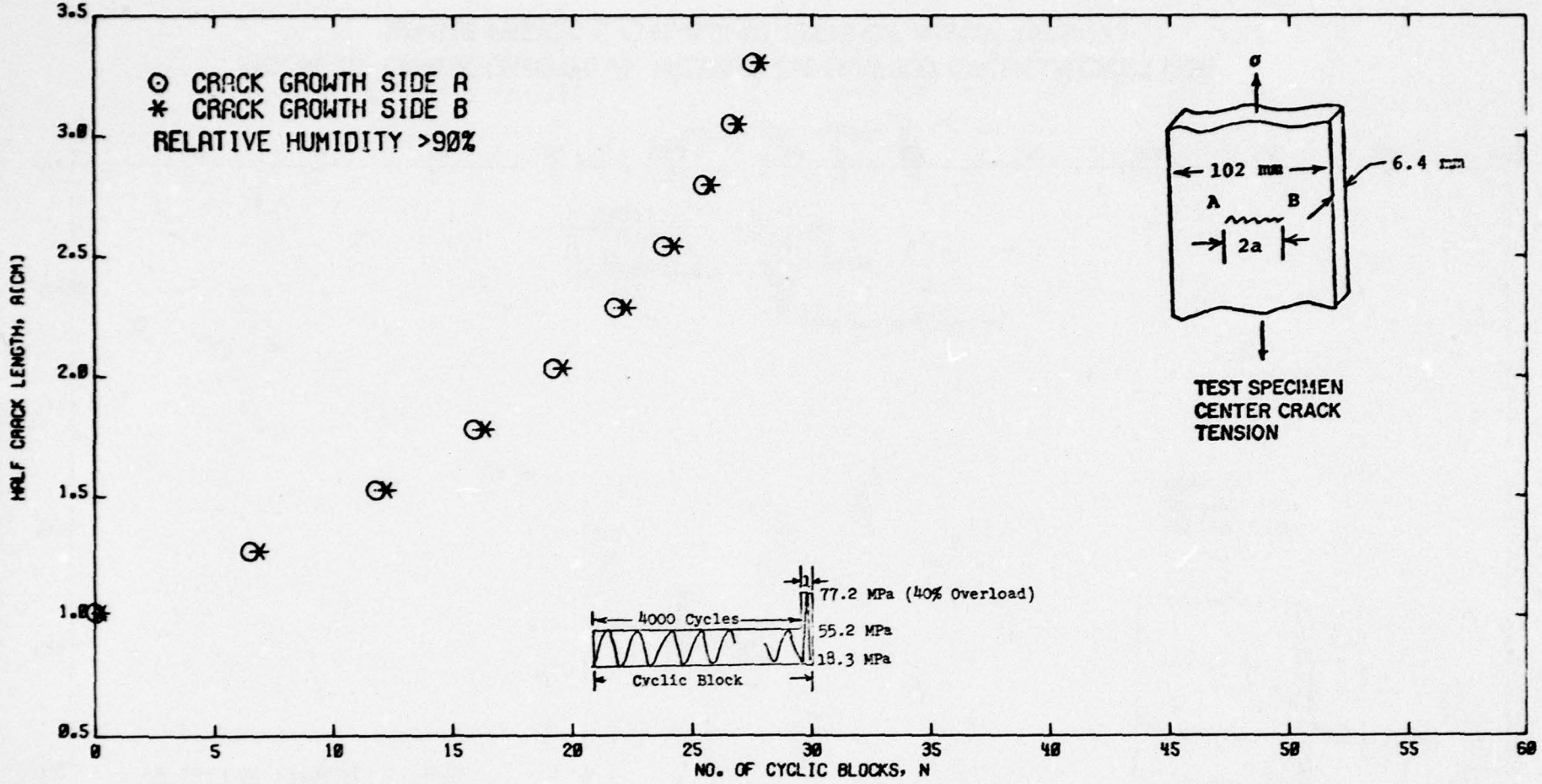

FIG. A-22 CRACK LENGTH VS. NUMBER OF ELAPSED CYCLIC BLOCKS FOR SINGLE PERIODIC OVERLOAD TESTS OF ALLOY 7075-T73

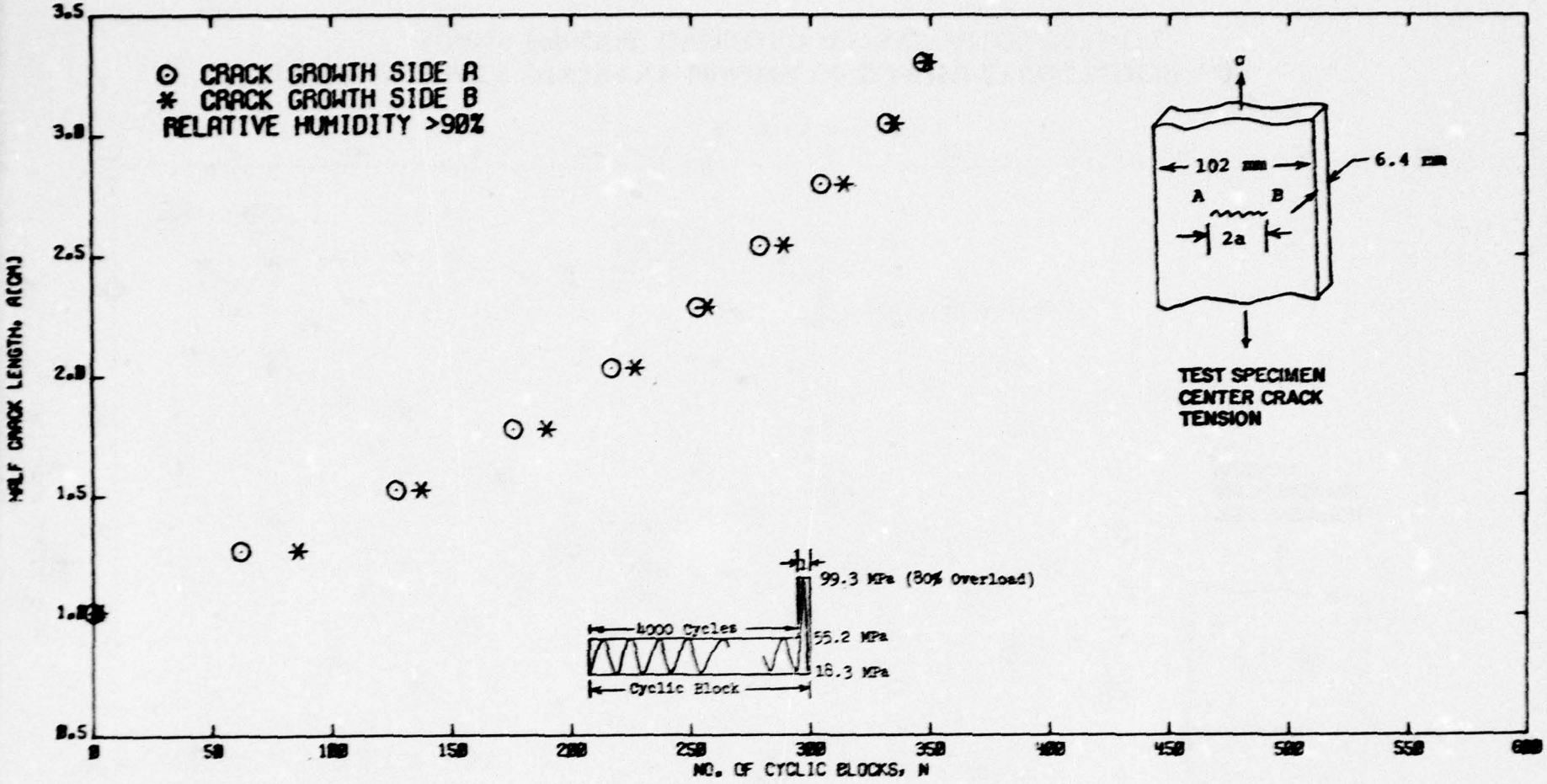

FIG. A-23 CRACK LENGTH VS. NUMBER OF ELAPSED CYCLIC BLOCKS FOR SINGLE PERIODIC OVERLOAD TESTS OF ALLOY 7075-T73

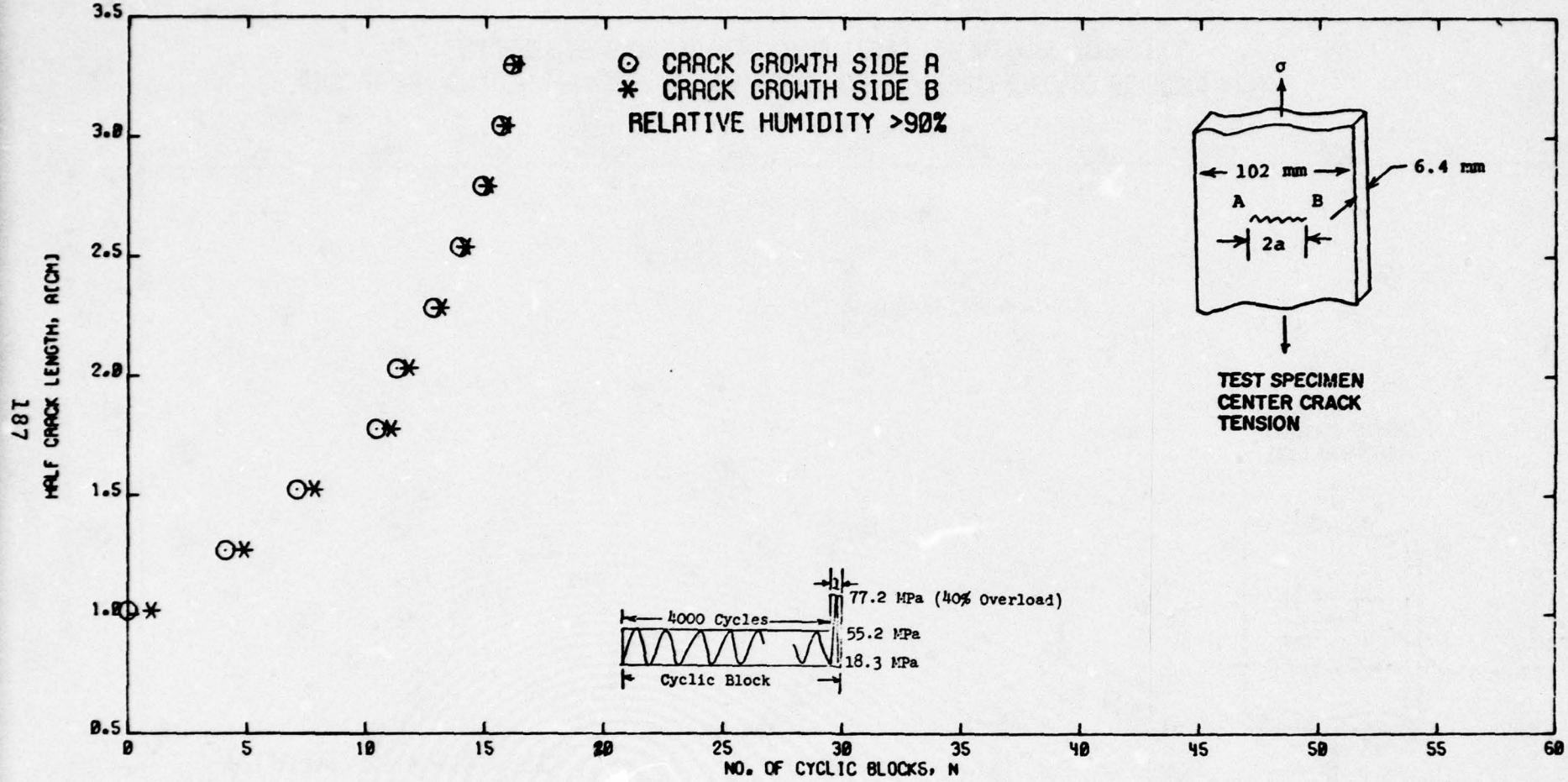

FIG. A-24 CRACK LENGTH VS. NUMBER OF ELAPSED CYCLIC BLOCKS FOR SINGLE PERIODIC OVERLOAD TESTS OF ALLOY 7075-T76

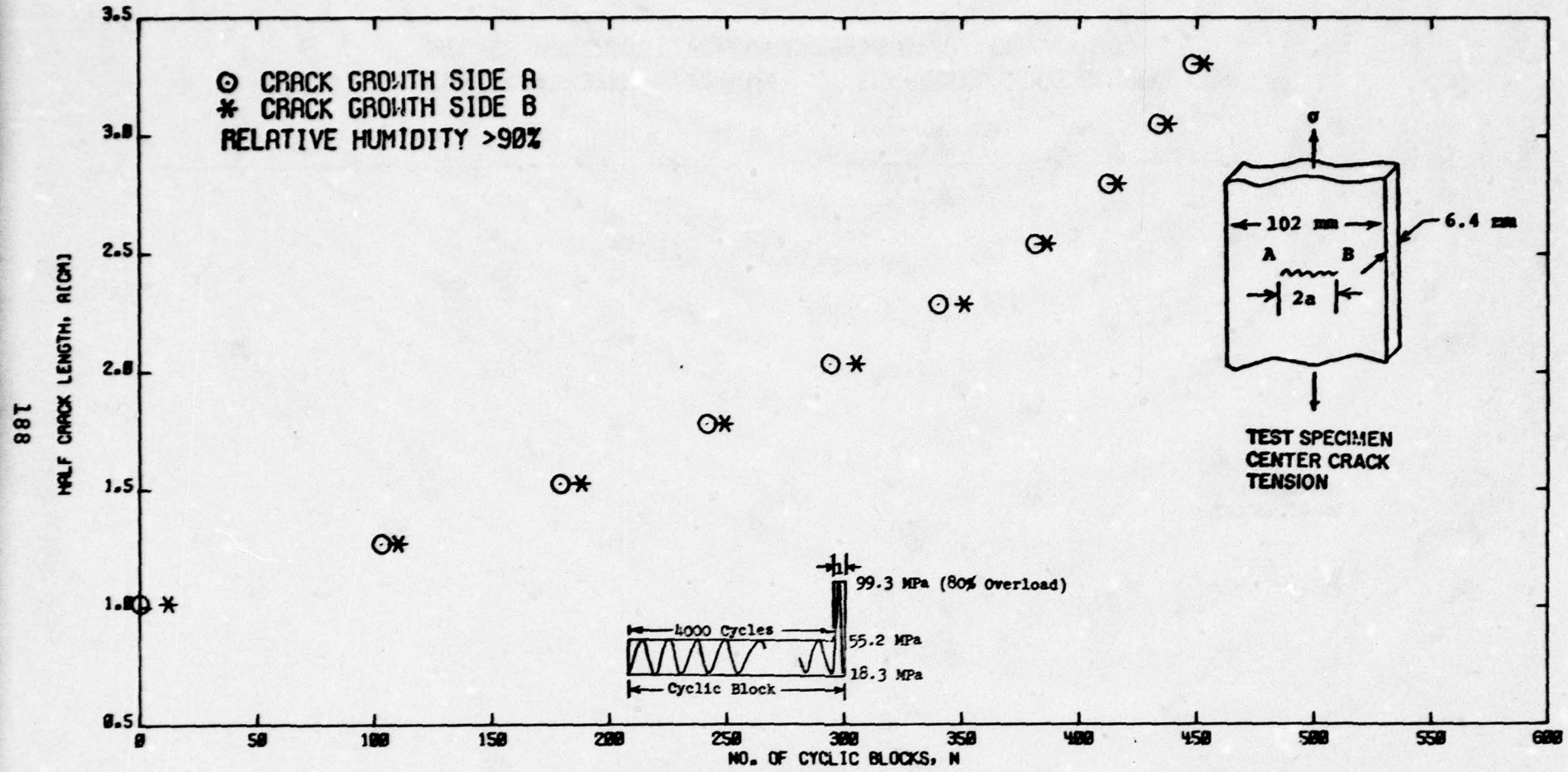

FIG. A-25 CRACK LENGTH VS. NUMBER OF ELAPSED CYCLIC BLOCKS FOR SINGLE PERIODIC OVERLOAD TESTS OF ALLOY 7075-T76

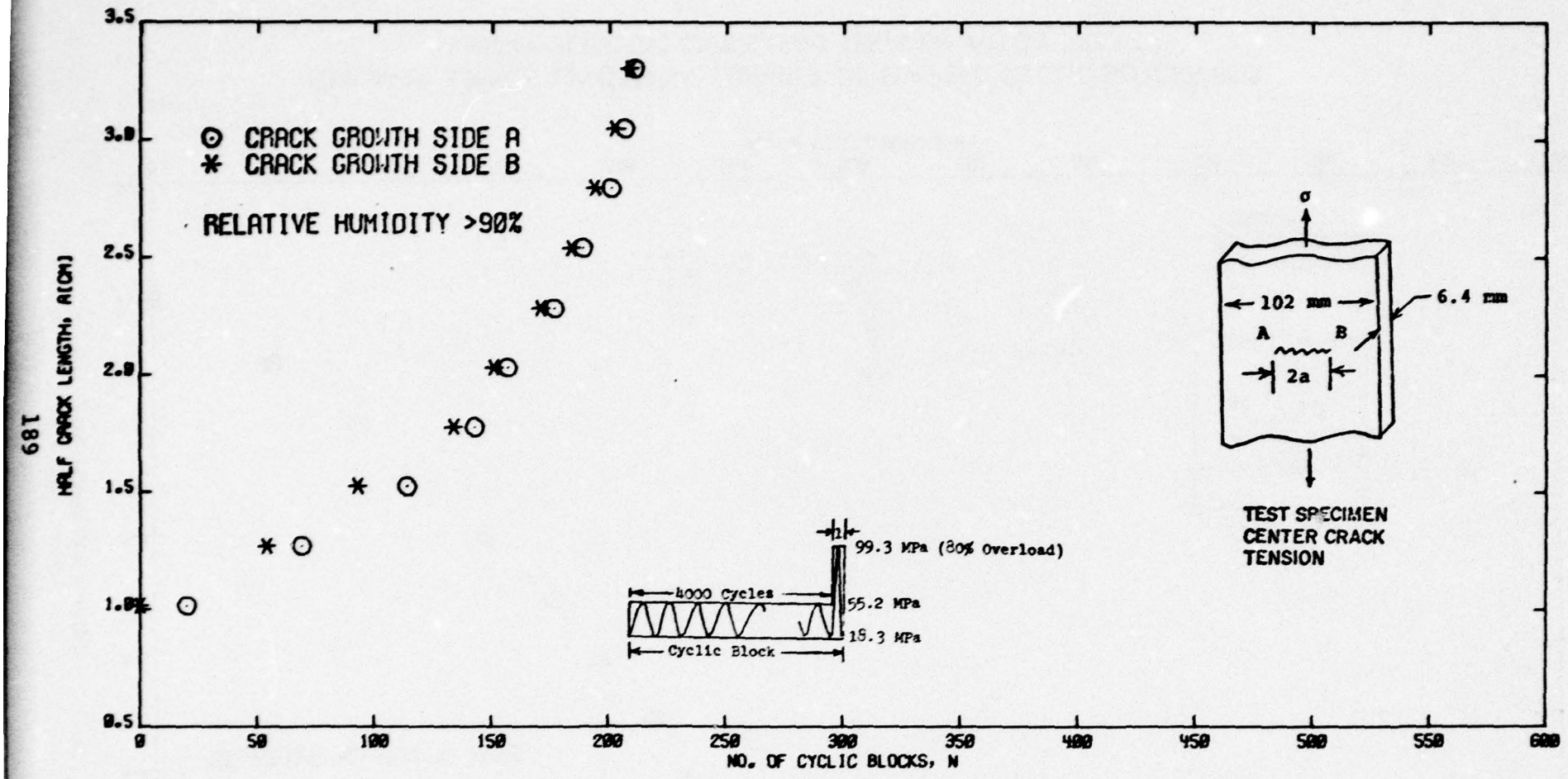

FIG. A-26 CRACK LENGTH VS. NUMBER OF ELAPSED CYCLIC BLOCKS FOR SINGLE PERIODIC OVERLOAD TESTS OF ALLOY 7050-T7

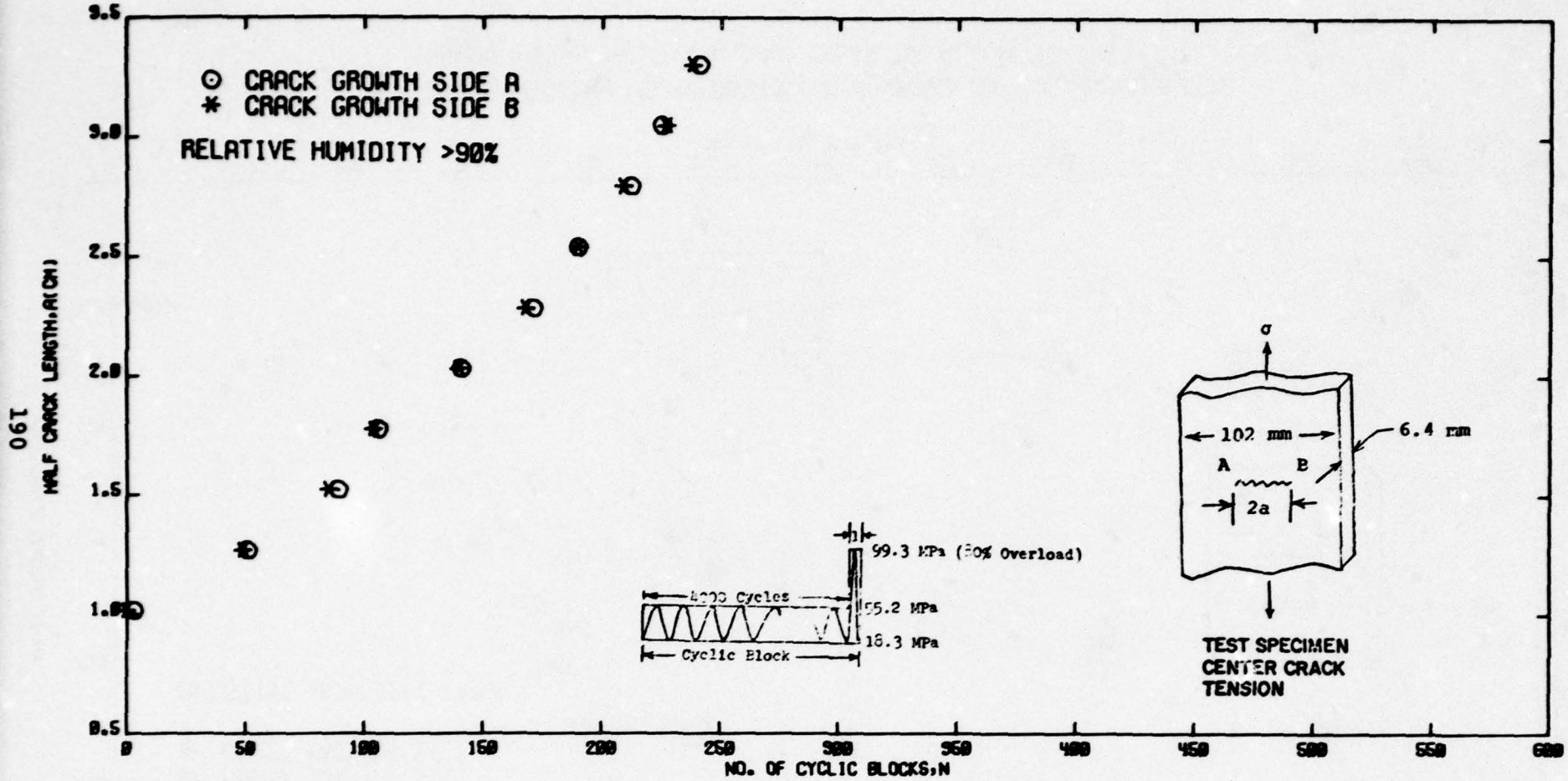

FIG. A-27 CRACK LENGTH VS. NUMBER OF ELAPSED CYCLIC BLOCKS FOR SINGLE PERIODIC OVERLOAD TESTS OF ALLOY 7050-T7

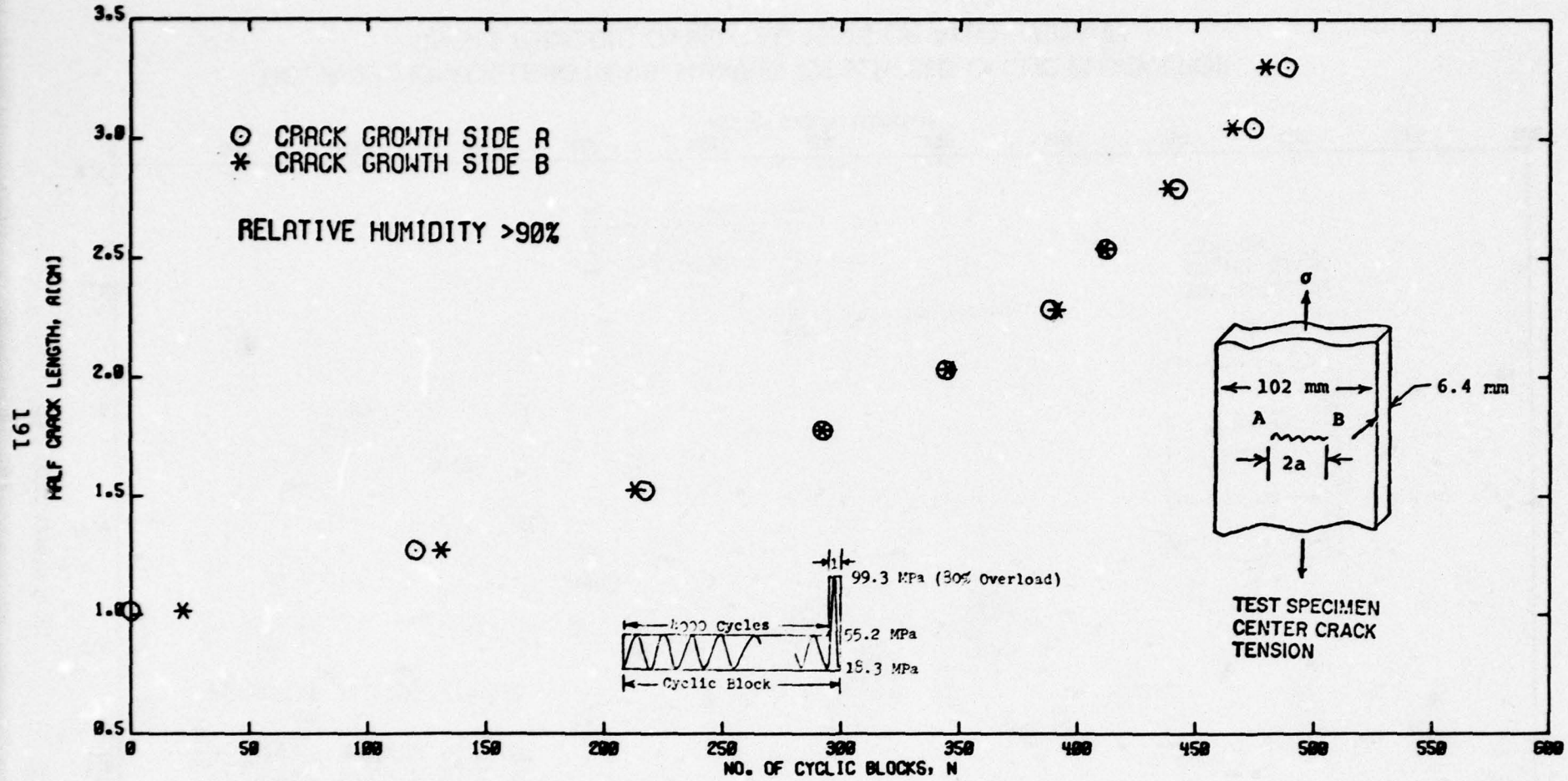

FIG. A-28 CRACK LENGTH VS. NUMBER OF ELAPSED CYCLIC BLOCKS FOR SINGLE PERIODIC OVERLOAD TESTS OF ALLOY 7050-T6

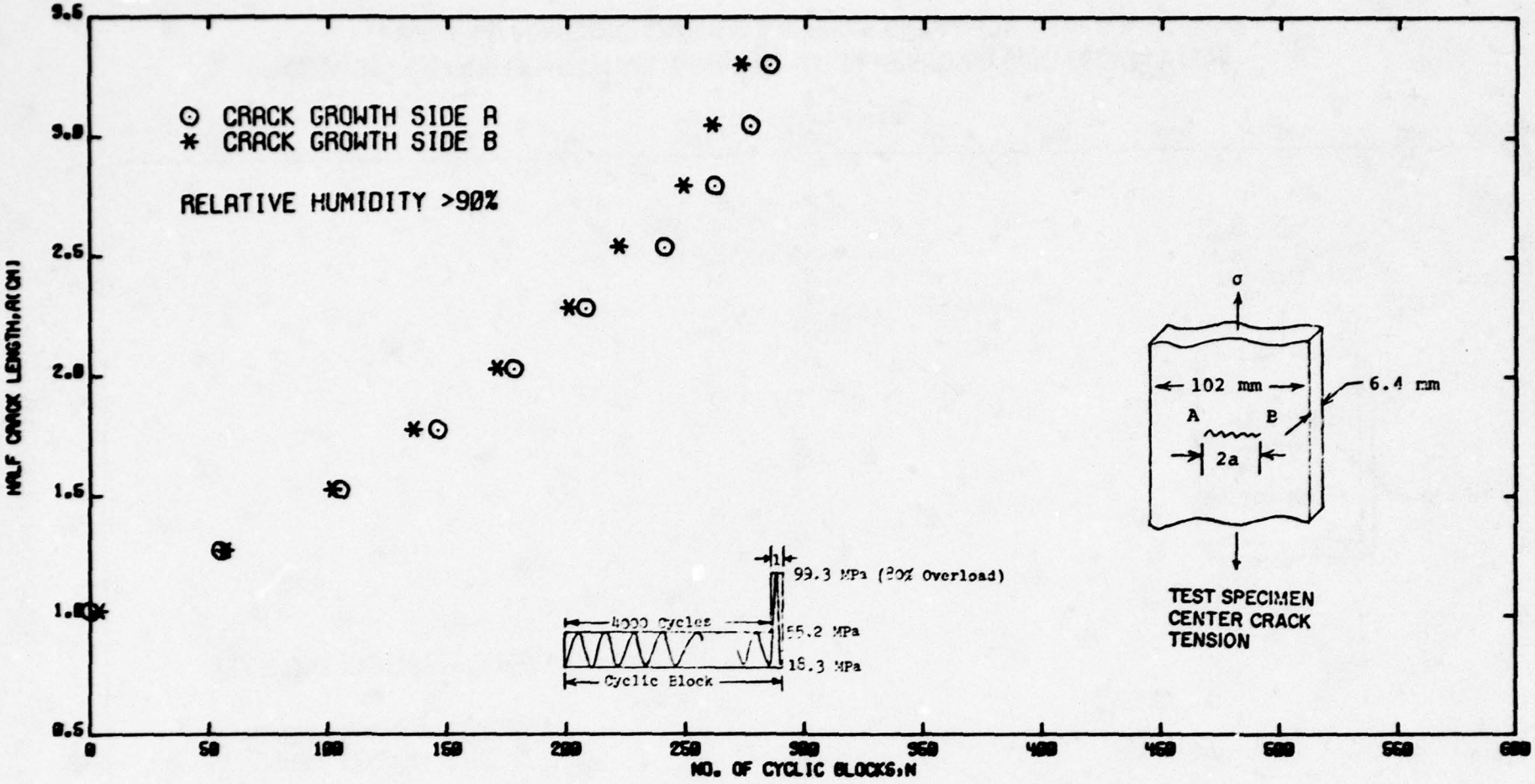

FIG. A-29 CRACK LENGTH VS. NUMBER OF ELAPSED CYCLIC BLOCKS FOR SINGLE PERIODIC OVERLOAD TESTS OF ALLOY 7075-T7

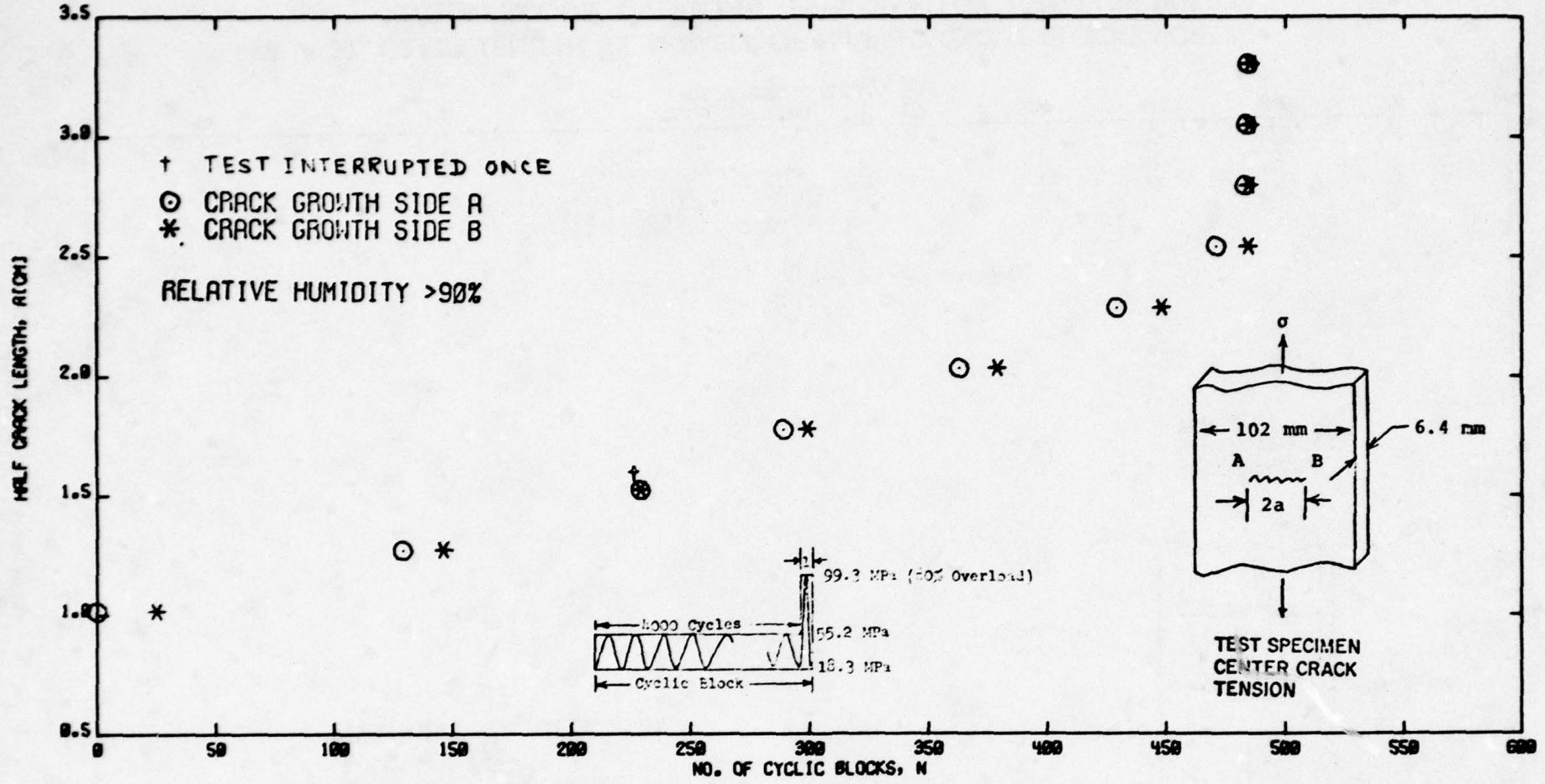

FIG. A-30 CRACK LENGTH VS. NUMBER OF ELAPSED CYCLIC BLOCKS FOR SINGLE PERIODIC TESTS OF ALLOY 7075-T6

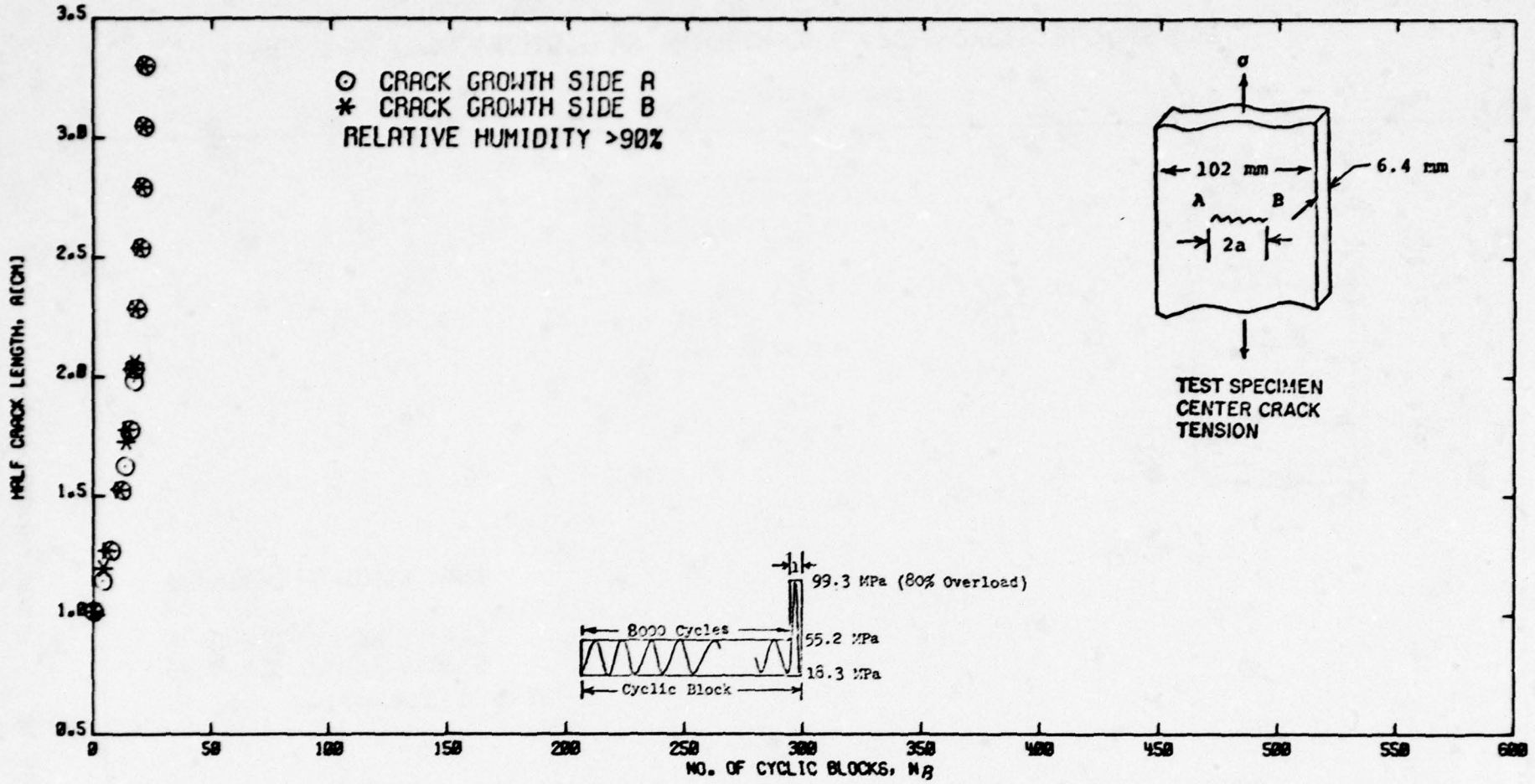

FIG. A-31 CRACK LENGTH VS. NUMBER OF ELAPSED CYCLIC BLOCKS FOR SINGLE PERIODIC OVERLOAD TESTS OF ALLOY 7010-T7 HI PURITY

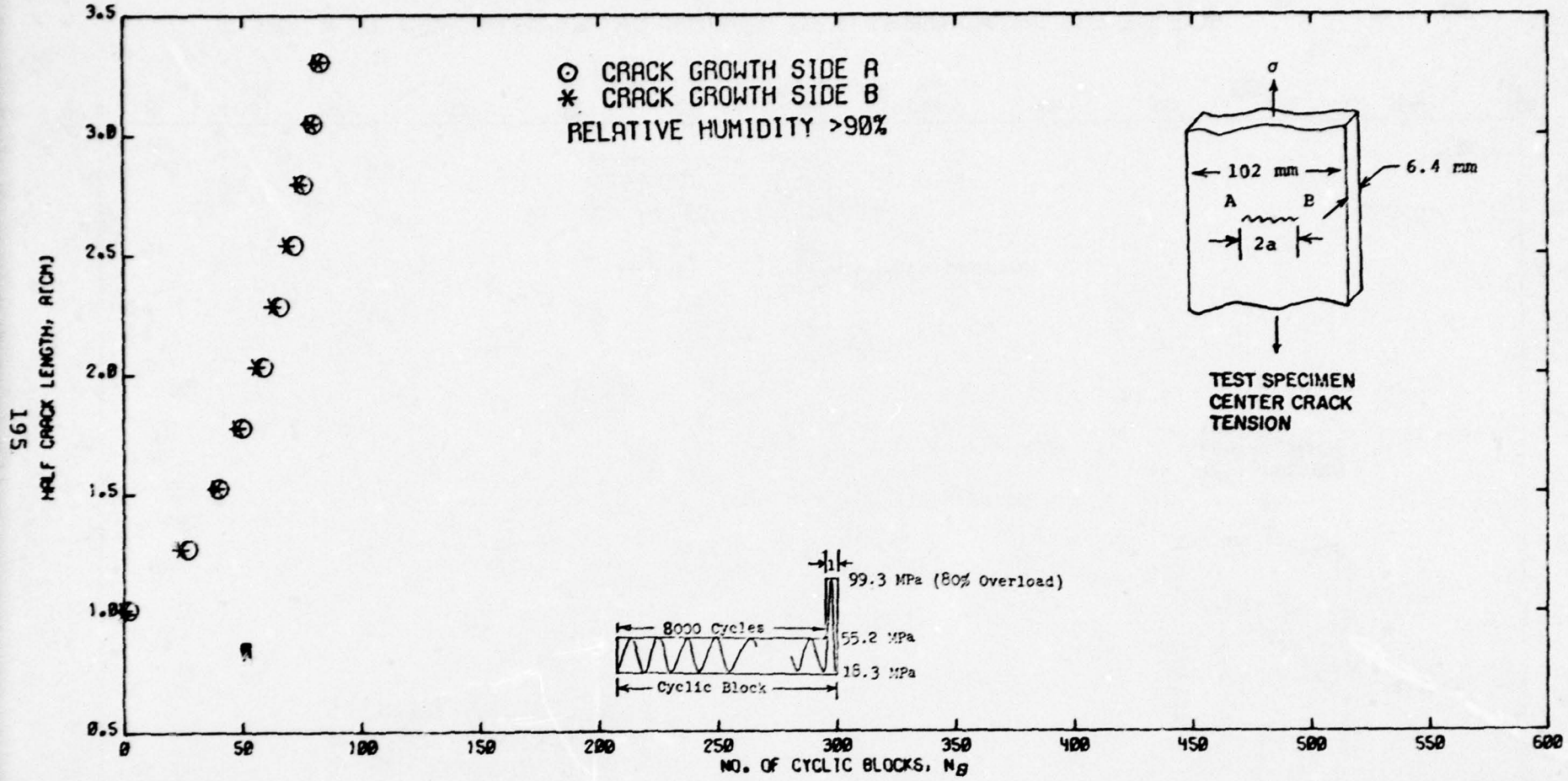

FIG. A-32 CRACK LENGTH VS. NUMBER OF ELAPSED CYCLIC BLOCKS FOR SINGLE PERIODIC OVERLOAD TESTS OF ALLOY 7475-T7

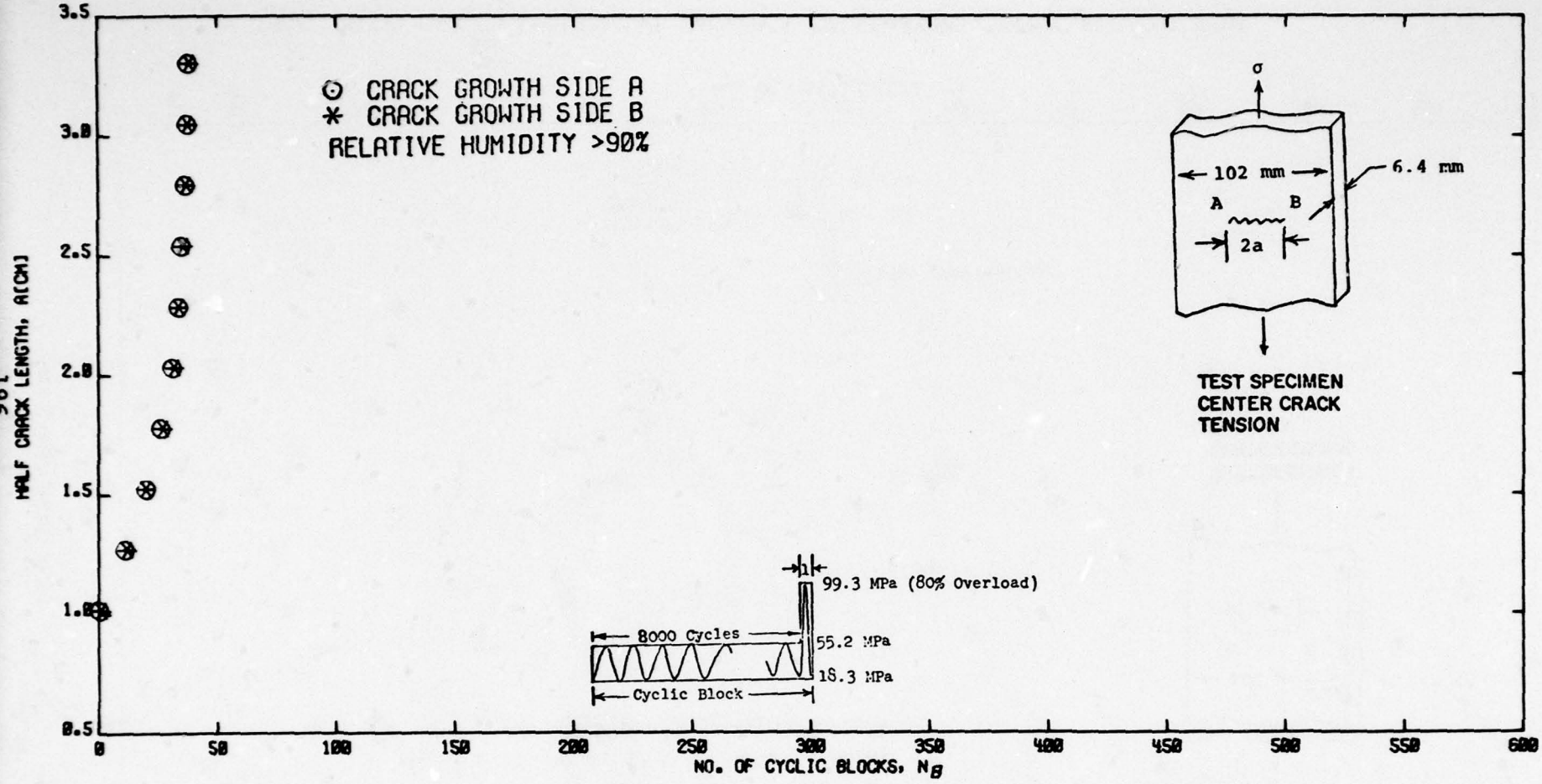

96T

FIG. A-33 CRACK LENGTH VS. NUMBER OF ELAPSED CYCLIC BLOCKS FOR SINGLE PERIODIC OVERLOAD TESTS OF ALLOY 7475-T7 HI Cu

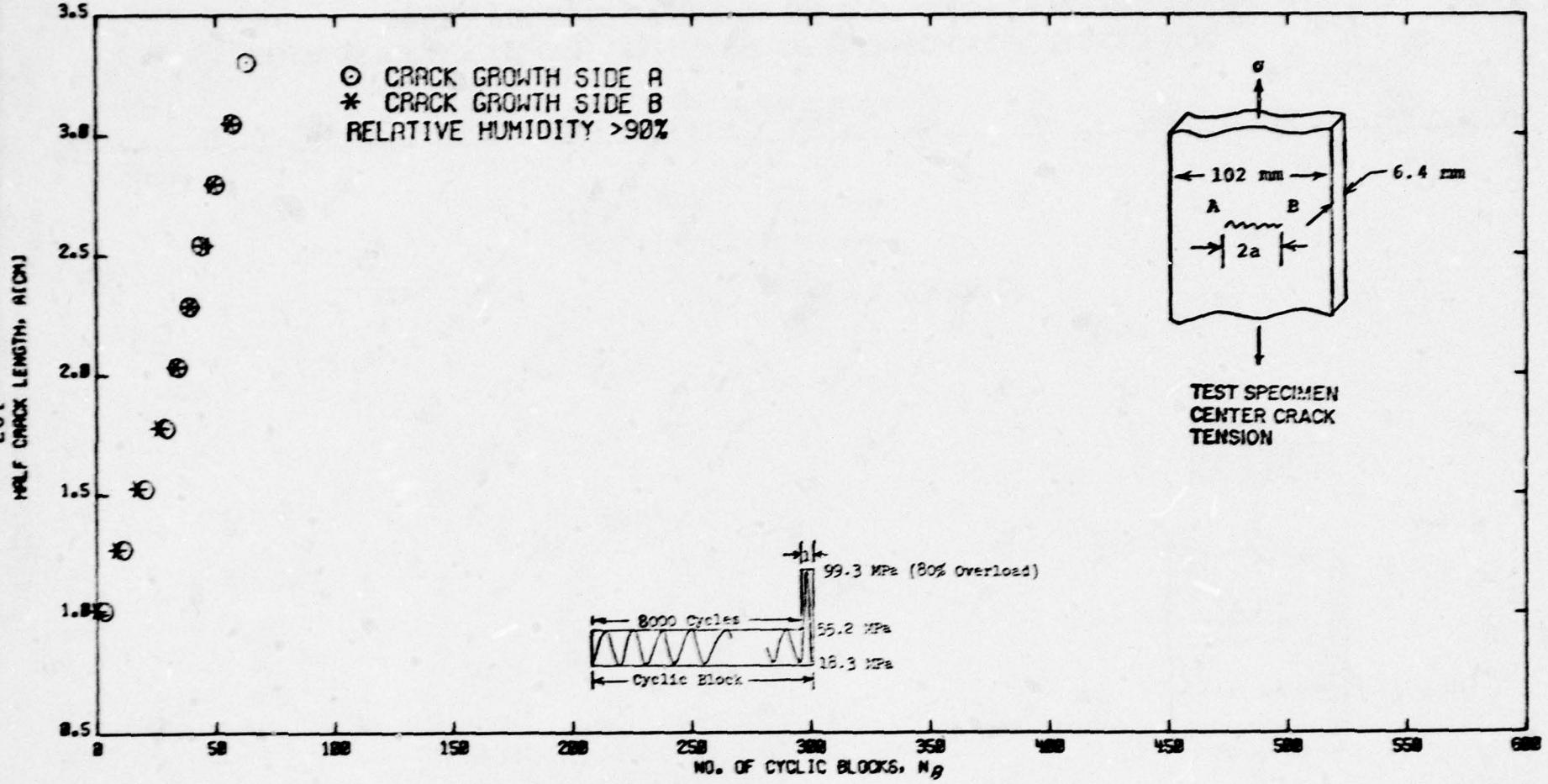

FIG. A-34 CRACK LENGTH VS. NUMBER OF ELAPSED CYCLIC BLOCKS FOR SINGLE PERIODIC OVERLOAD TESTS OF ALLOY 7010-T7

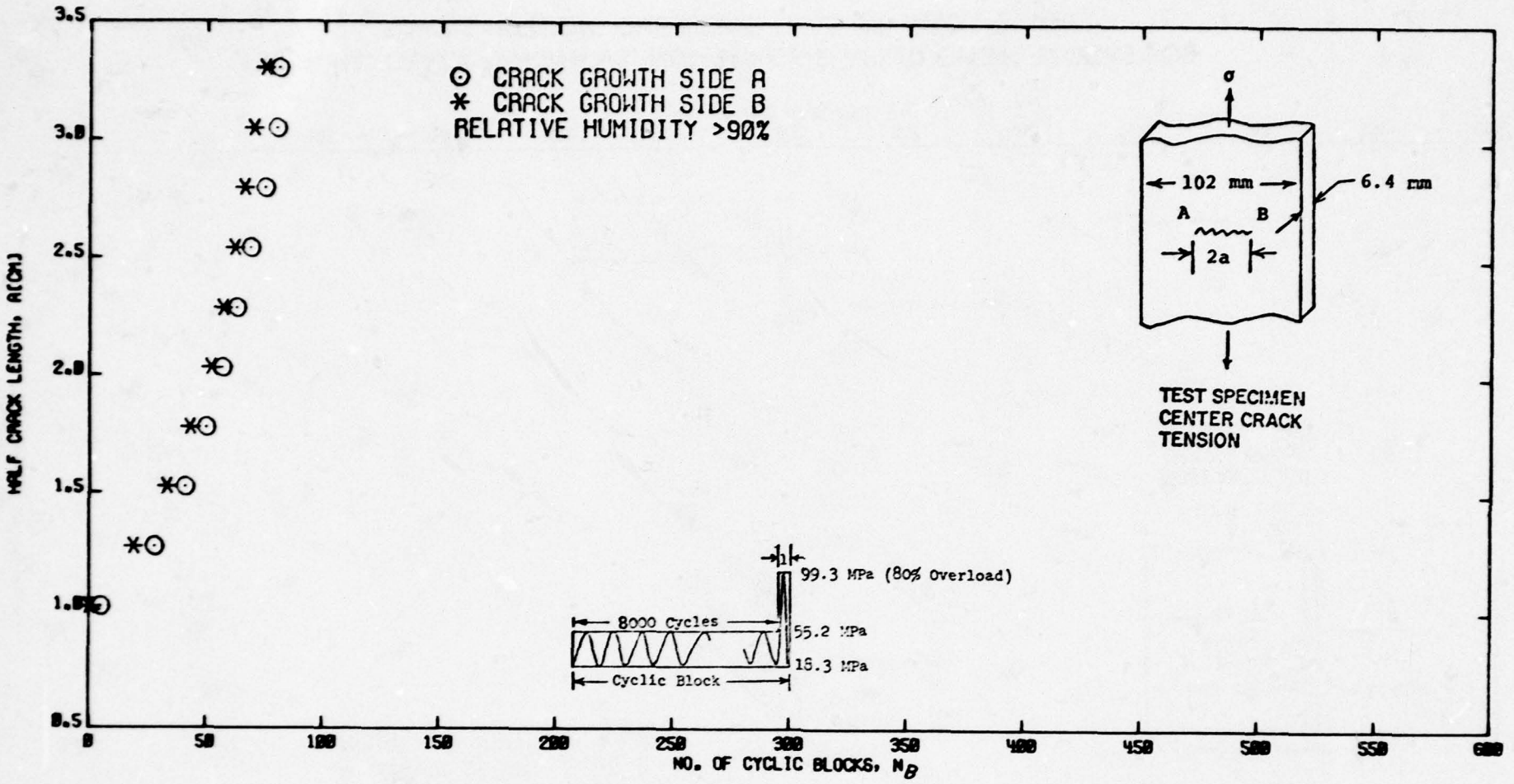

FIG. A-35 CRACK LENGTH VS. NUMBER OF ELAPSED CYCLIC BLOCKS FOR SINGLE PERIODIC OVERLOAD TESTS OF ALLOY 7050-T7 LO PURITY

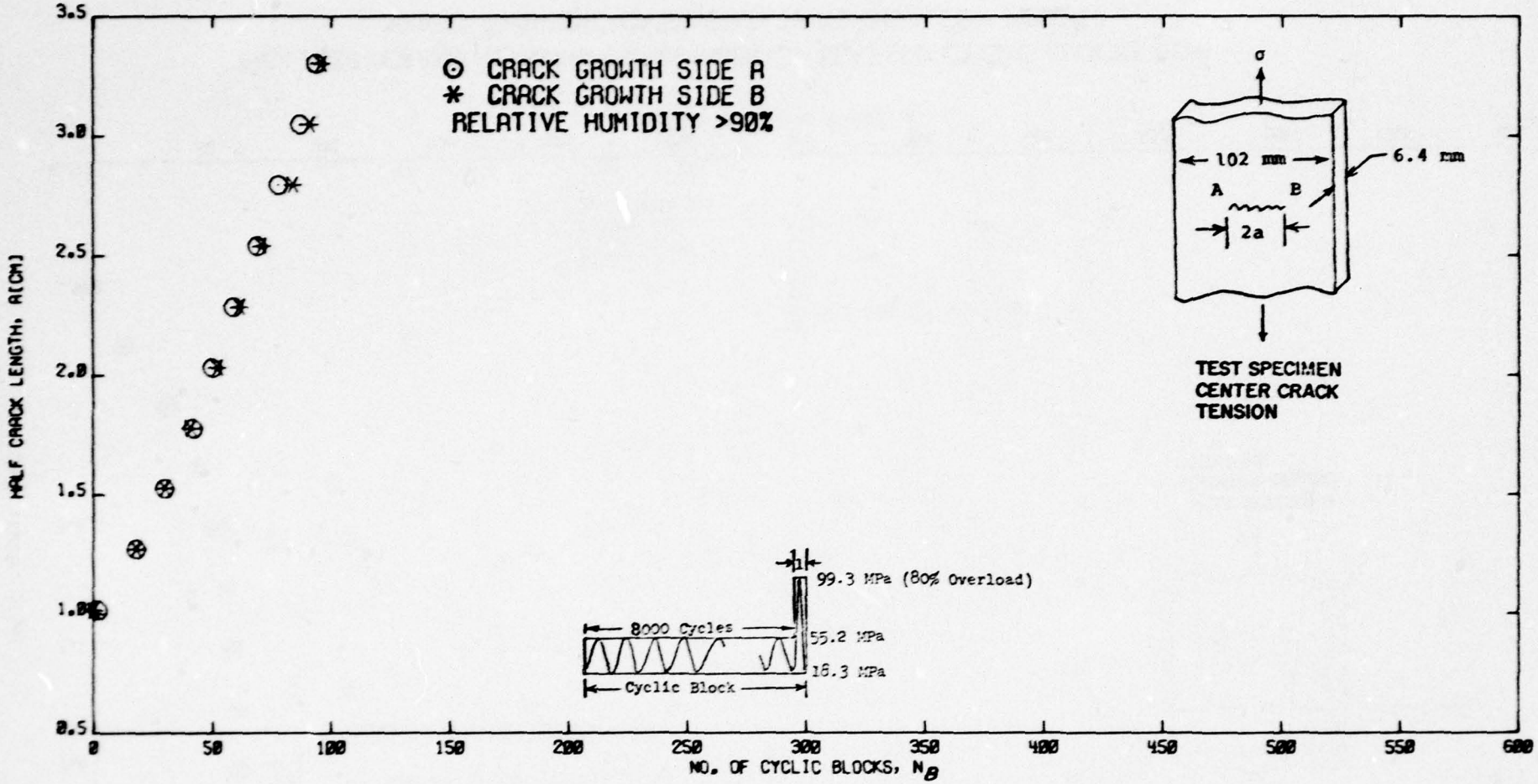

FIG. A-36 CRACK LENGTH VS. NUMBER OF ELAPSED CYCLIC BLOCKS FOR SINGLE PERIODIC OVERLOAD TESTS OF ALLOY 7075-T7 HI Cu

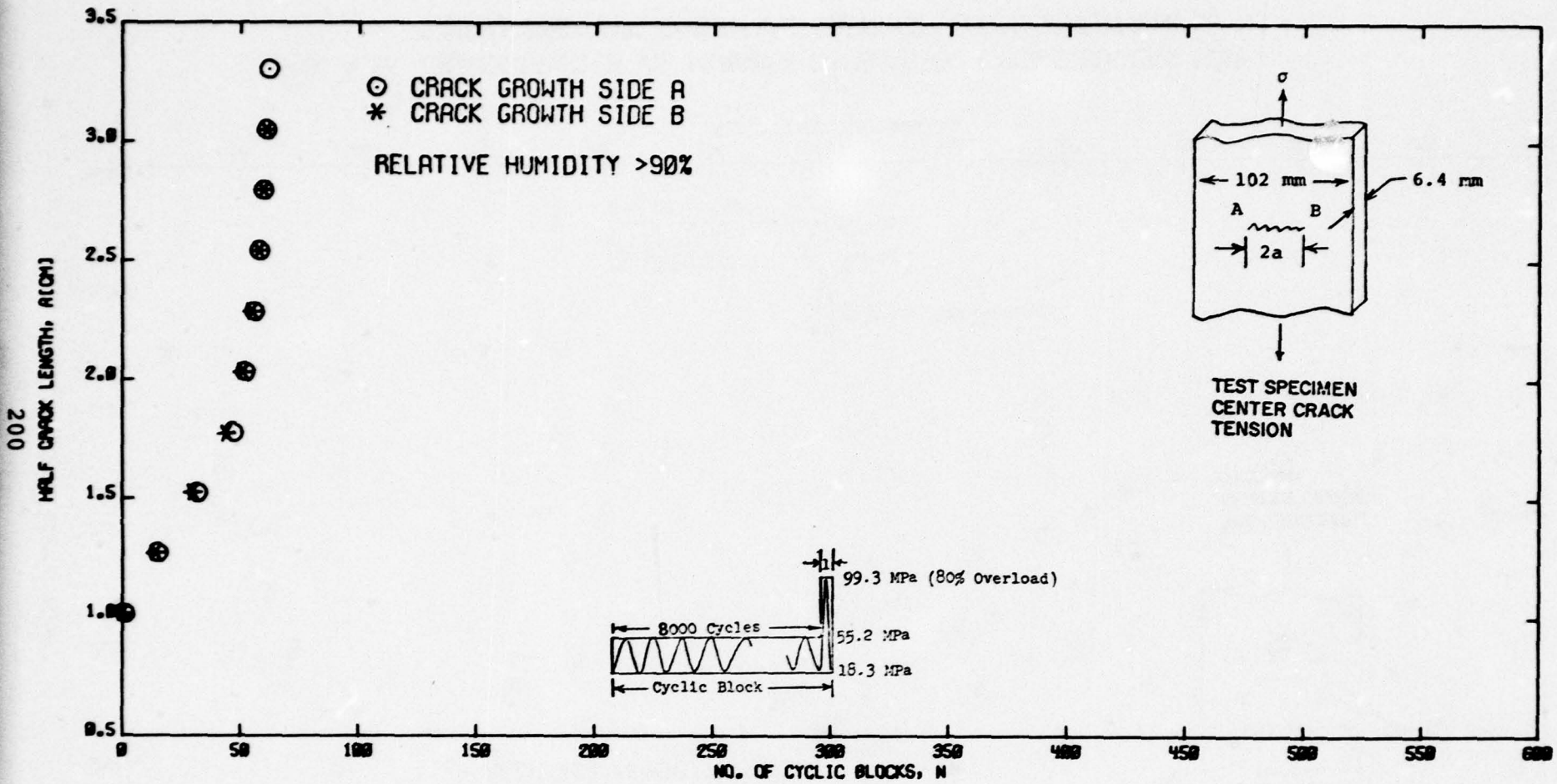

FIG. A-37 CRACK LENGTH VS. NUMBER OF ELAPSED CYCLIC BLOCKS FOR SINGLE PERIODIC OVERLOAD TESTS OF ALLOY 7050-T7

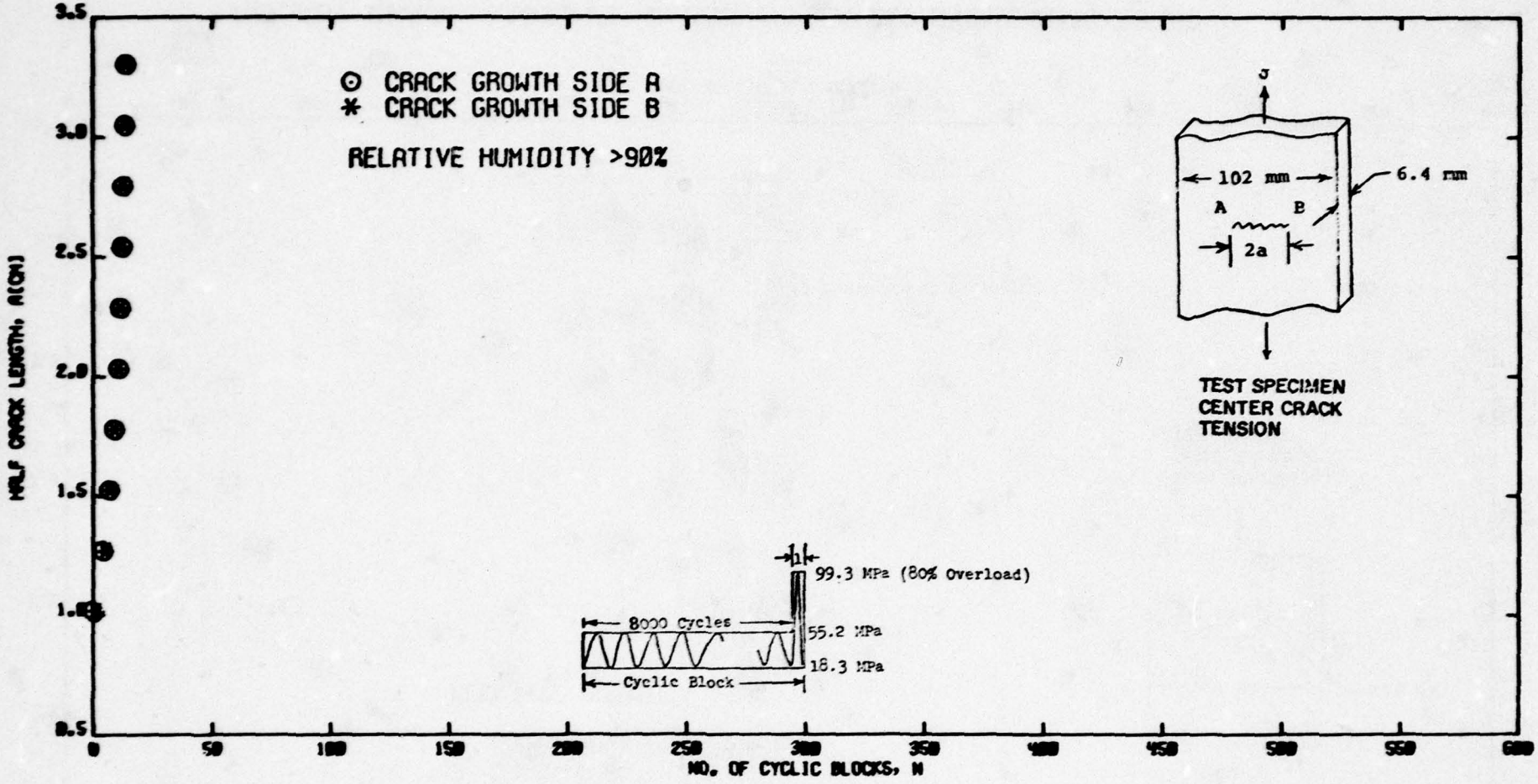

FIG. A-38 CRACK LENGTH VS. NUMBER OF ELAPSED CYCLIC BLOCKS FOR SINGLE PERIODIC OVERLOAD TESTS OF ALLOY 7050-T6

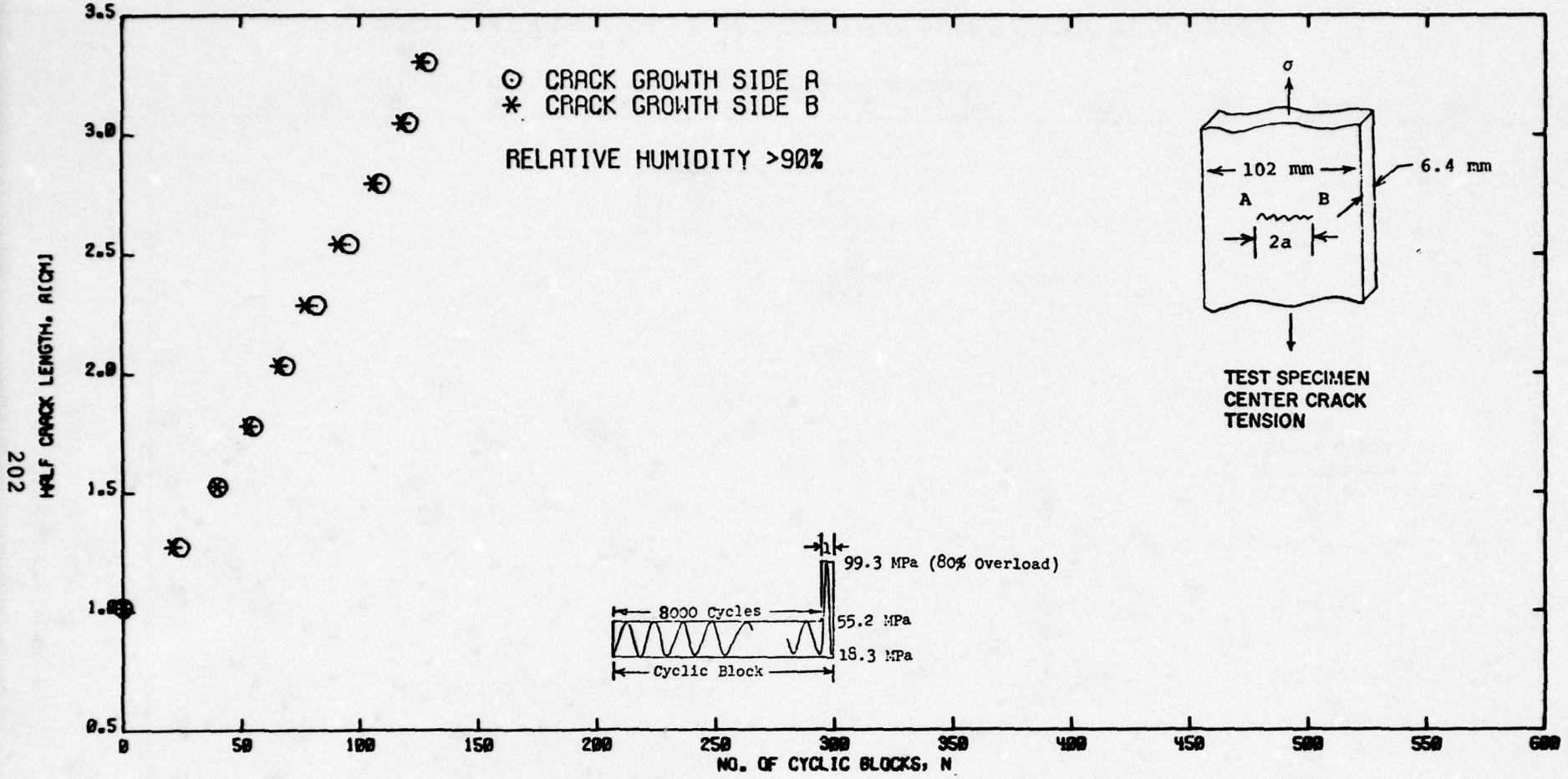

FIG. A39 CRACK LENGTH VS. NUMBER OF ELAPSED CYCLIC BLOCKS FOR SINGLE PERIODIC OVERLOAD TESTS OF ALLOY 7075-T7

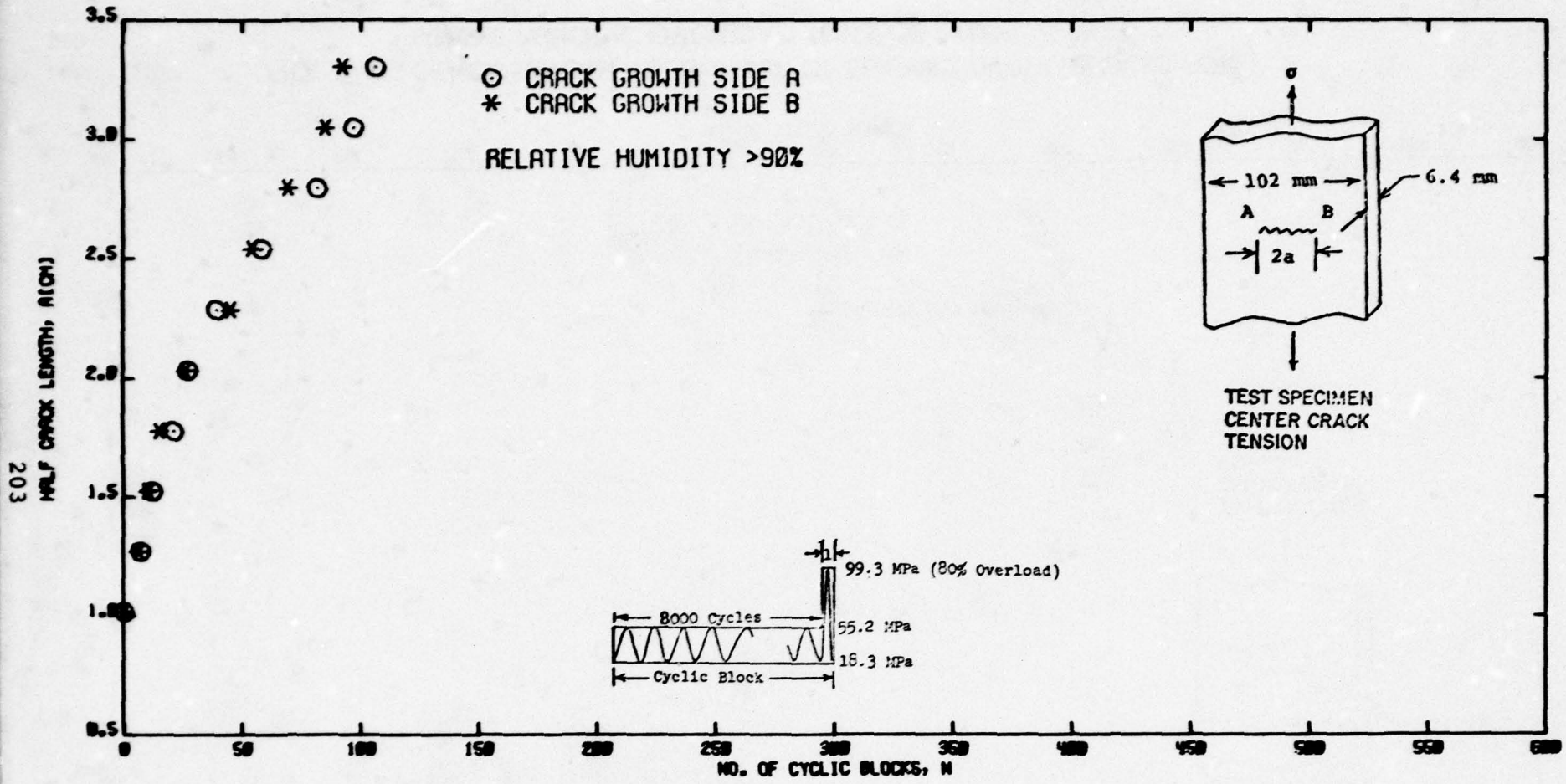

FIG. A-40 CRACK LENGTH VS. NUMBER OF ELAPSED CYCLIC BLOCKS FOR SINGLE PERIODIC OVERLOAD TESTS OF ALLOY 7075-T6

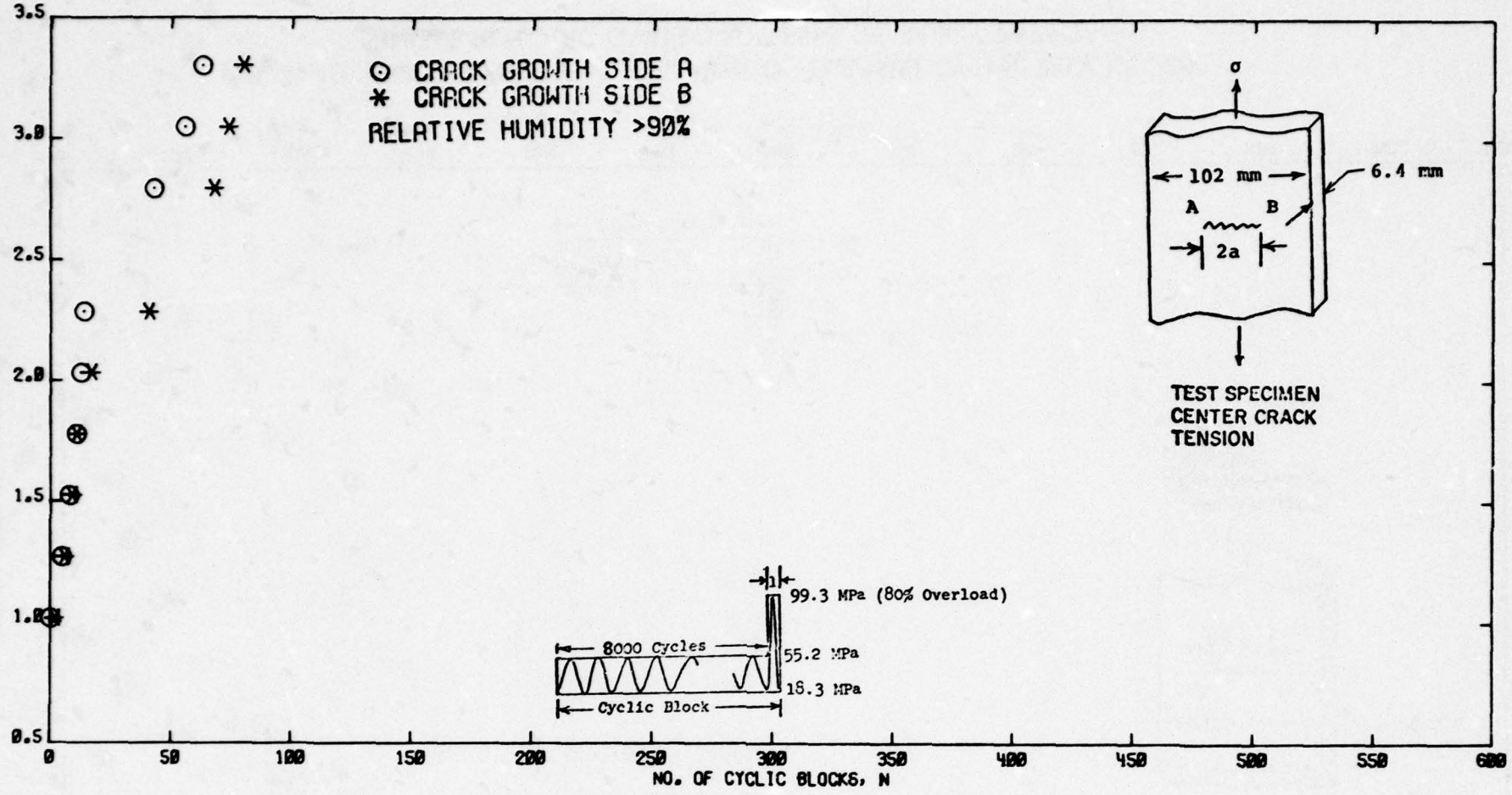

FIG. A-41 CRACK LENGTH VS. NUMBER OF ELAPSED CYCLIC BLOCKS FOR SINGLE PERIODIC OVERLOAD TESTS OF ALLOY 7075-T6

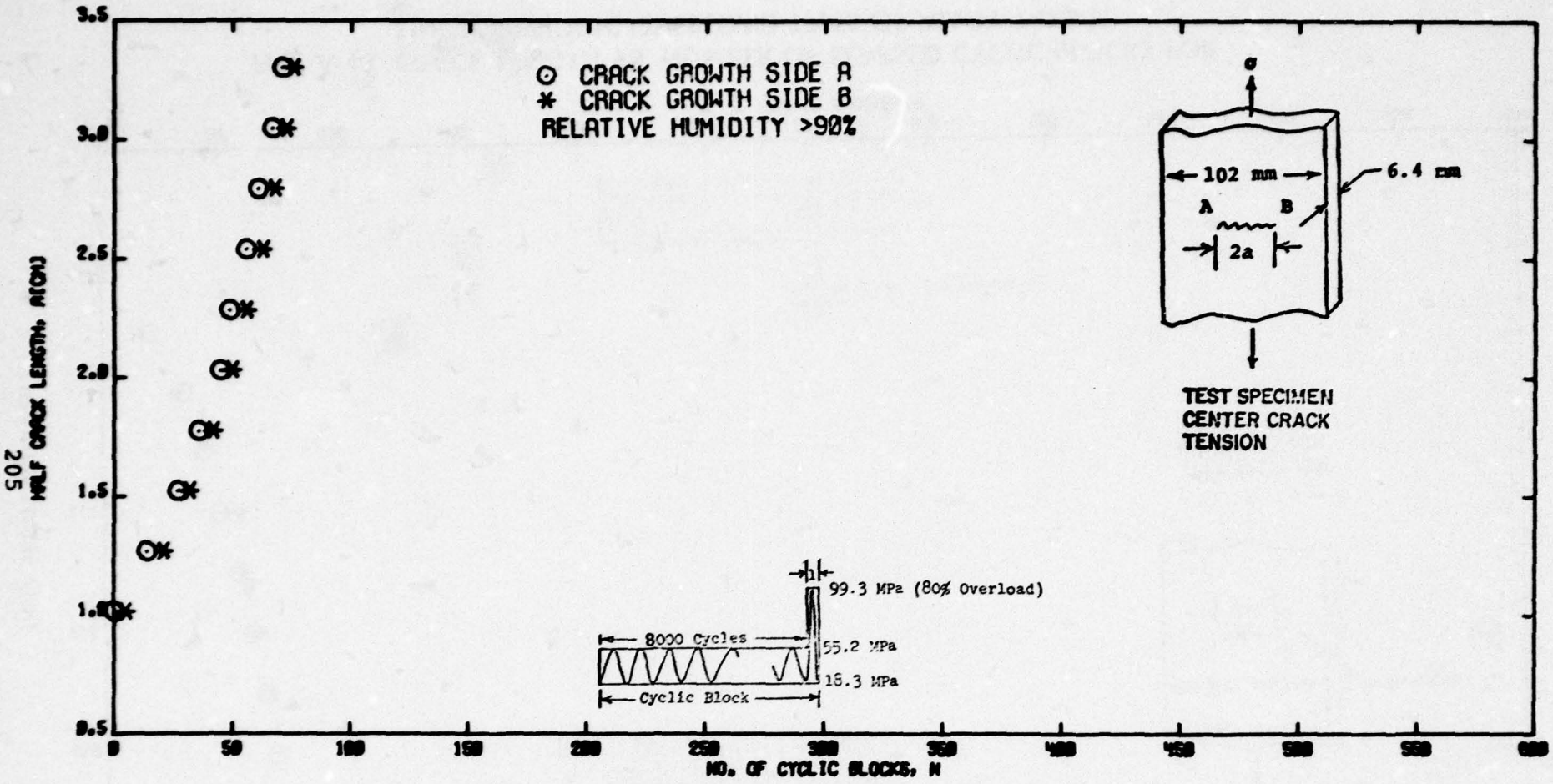

FIG. A-42 CRACK LENGTH VS. NUMBER OF ELAPSED CYCLIC BLOCKS FOR SINGLE PERIODIC OVERLOAD TESTS OF ALLOY 7475-T7

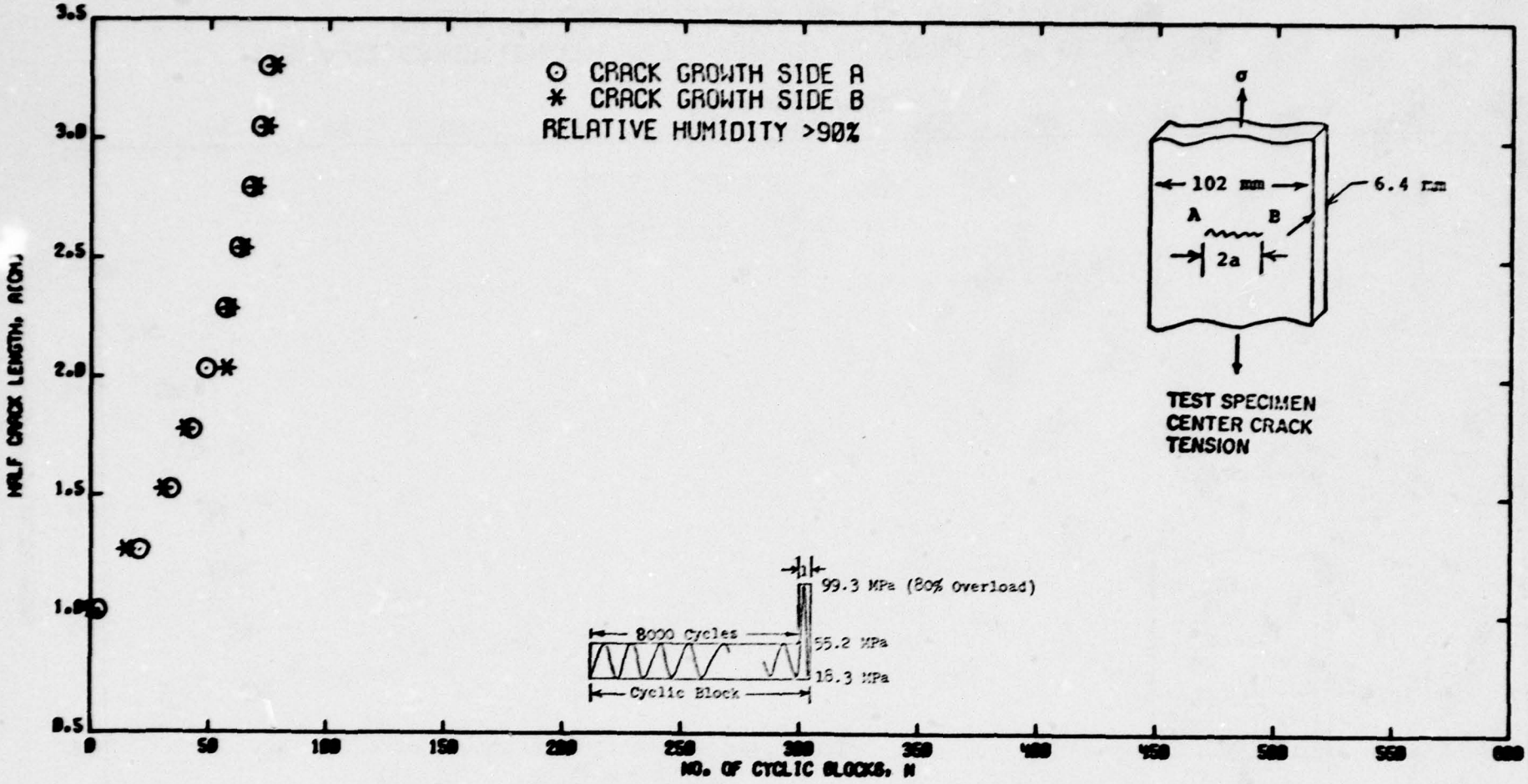

FIG. A-43 CRACK LENGTH VS. NUMBER OF ELAPSED CYCLIC BLOCKS FOR SINGLE PERIODIC OVERLOAD TESTS OF ALLOY 7475-T7

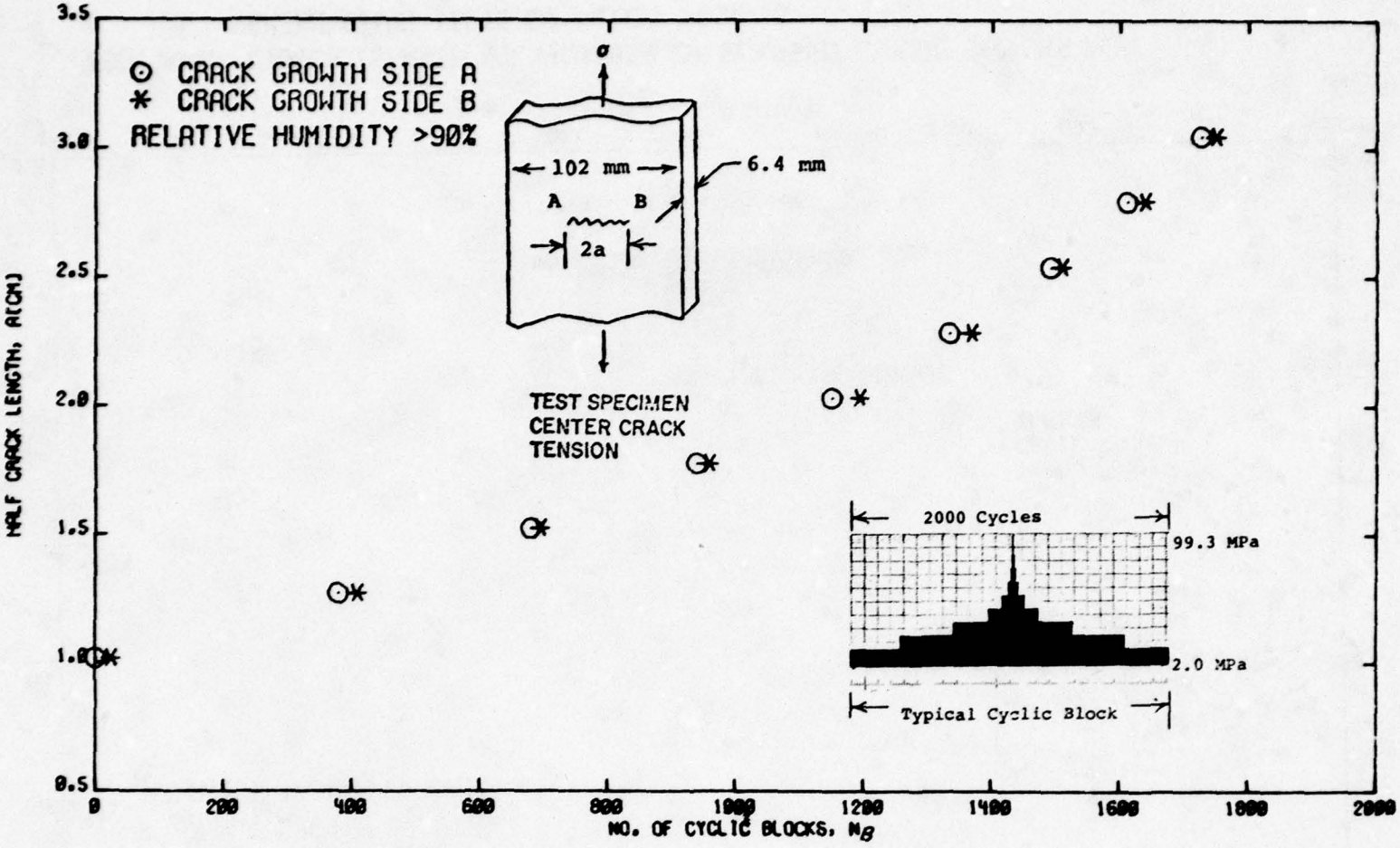

FIG. A-44 CRACK LENGTH VS. NUMBER OF ELAPSED CYCLIC BLOCKS FOR EIGHT LEVEL TESTS OF ALLOY 7050-T7

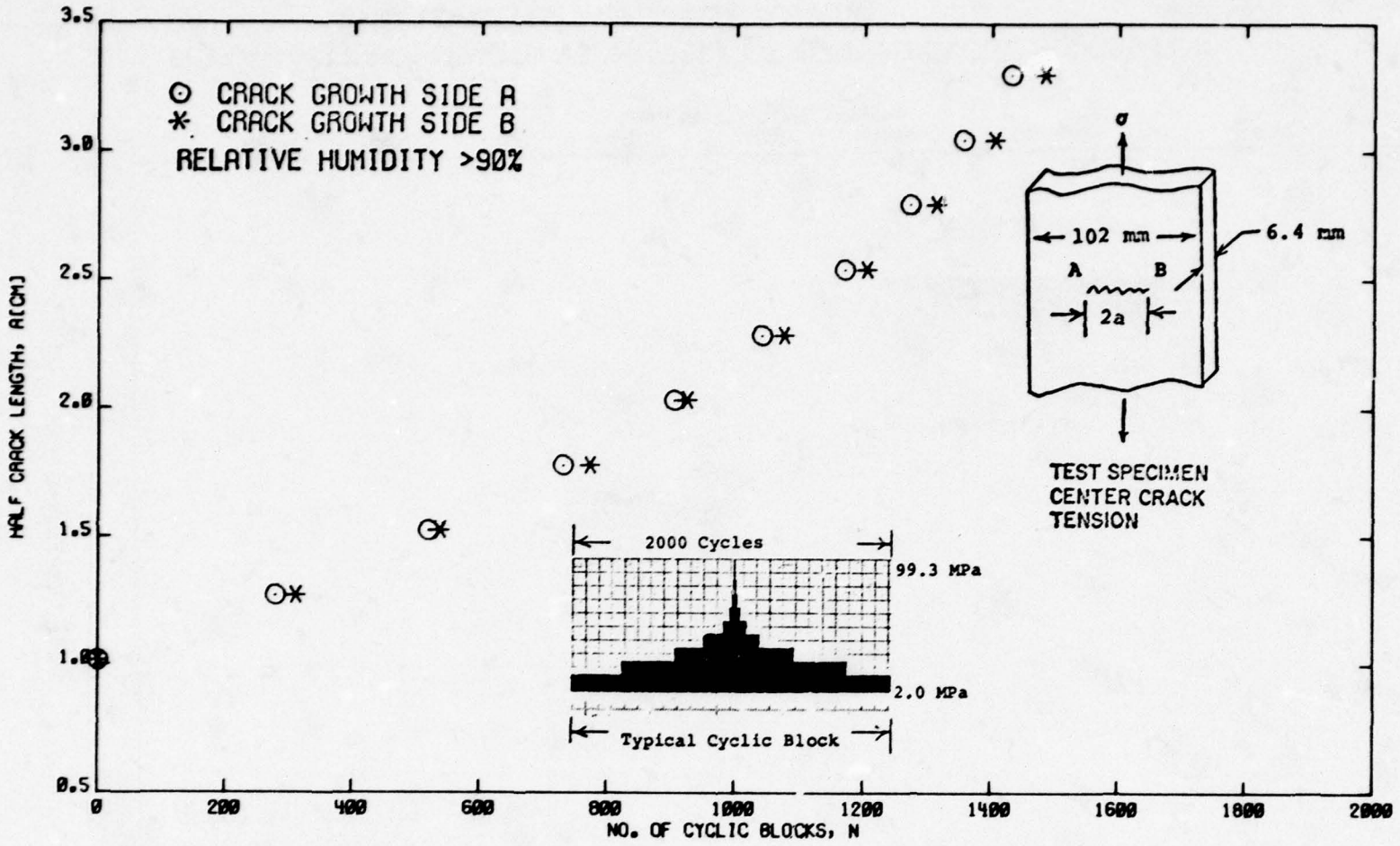

FIG. A-45 CRACK LENGTH VS. NUMBER OF ELAPSED CYCLIC BLOCKS FOR EIGHT LEVEL TESTS OF ALLOY 7050-T6

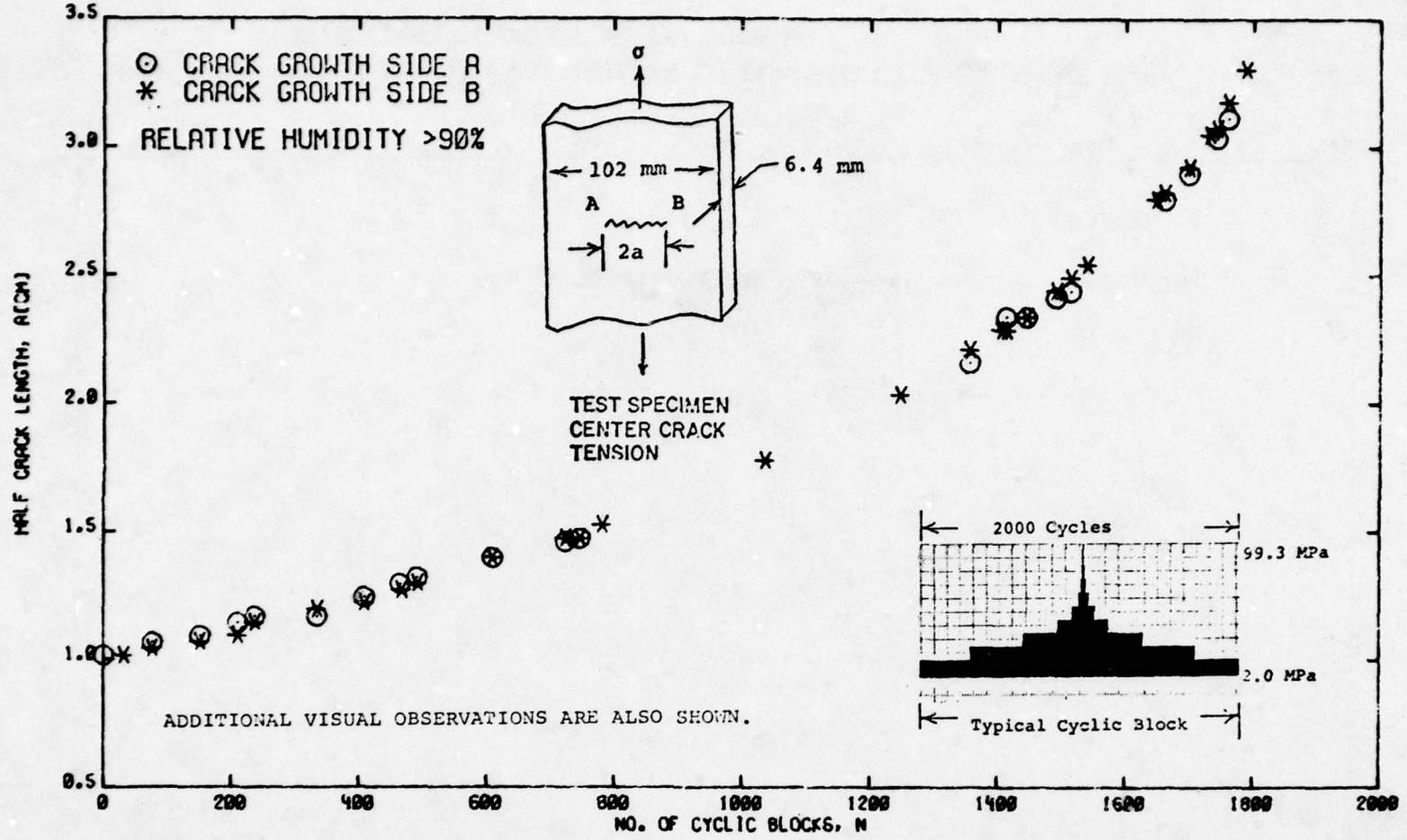

FIG. A-46 CRACK LENGTH VS. NUMBER OF ELAPSED CYCLIC BLOCKS FOR EIGHT LEVEL TESTS OF ALLOY 7075-T7

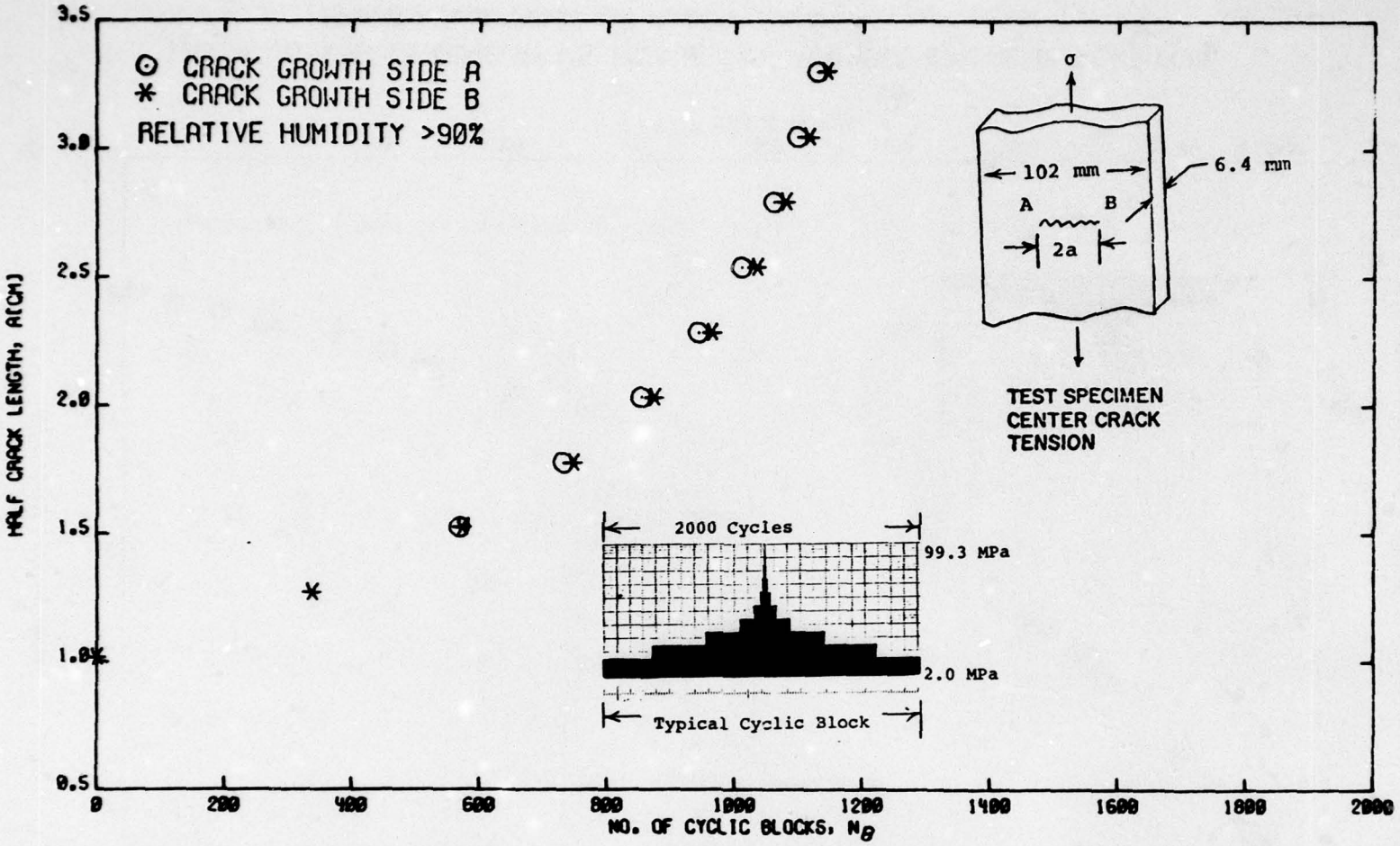

FIG. A-47 CRACK LENGTH VS. NUMBER OF ELAPSED CYCLIC BLOCKS FOR EIGHT LEVEL TESTS OF ALLOY 7075-T6

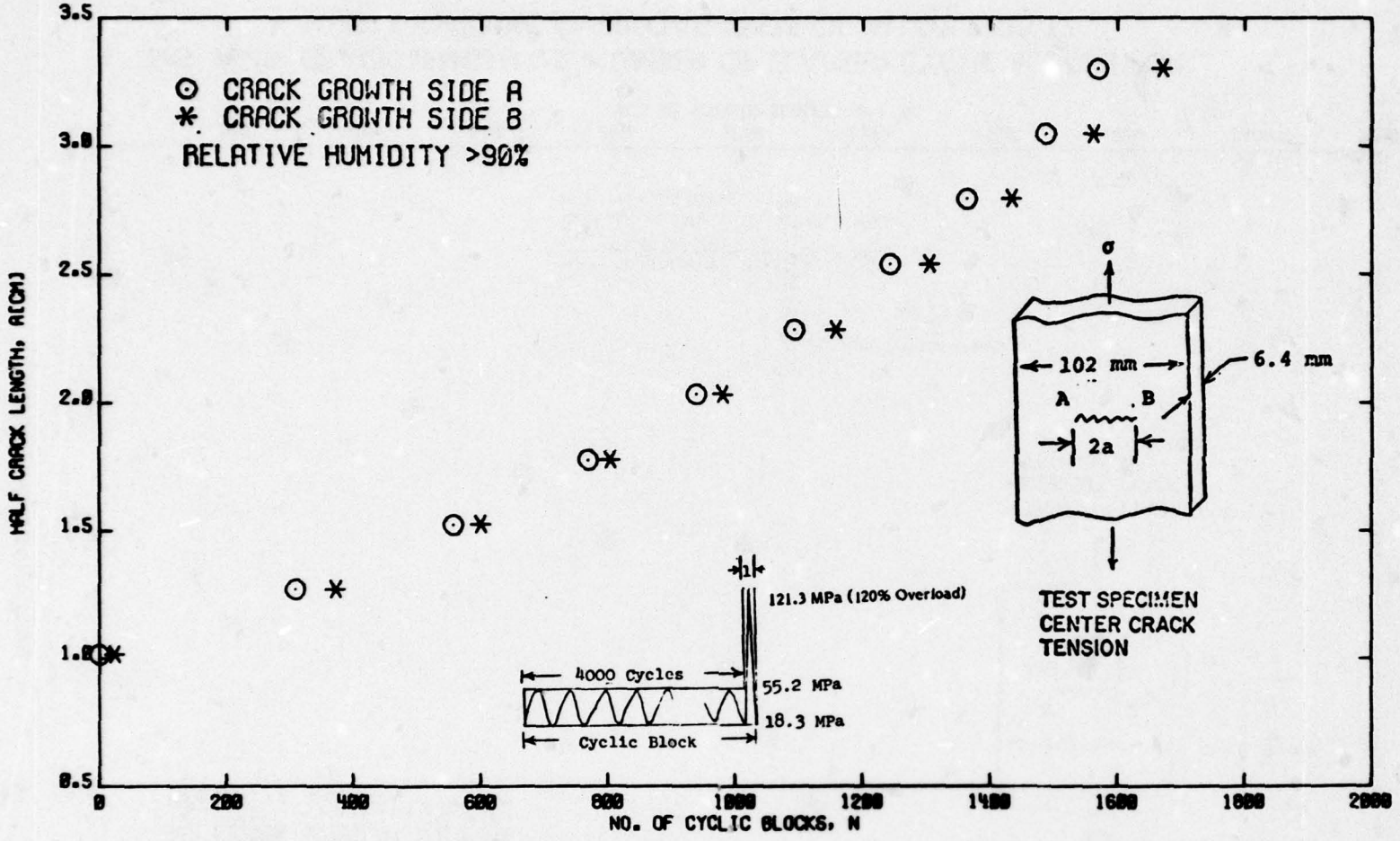

FIG. A-48 CRACK LENGTH VS. NUMBER OF ELAPSED CYCLIC BLOCKS FOR SINGLE PERIODIC OVERLOAD TESTS OF ALLOY 7050-T6

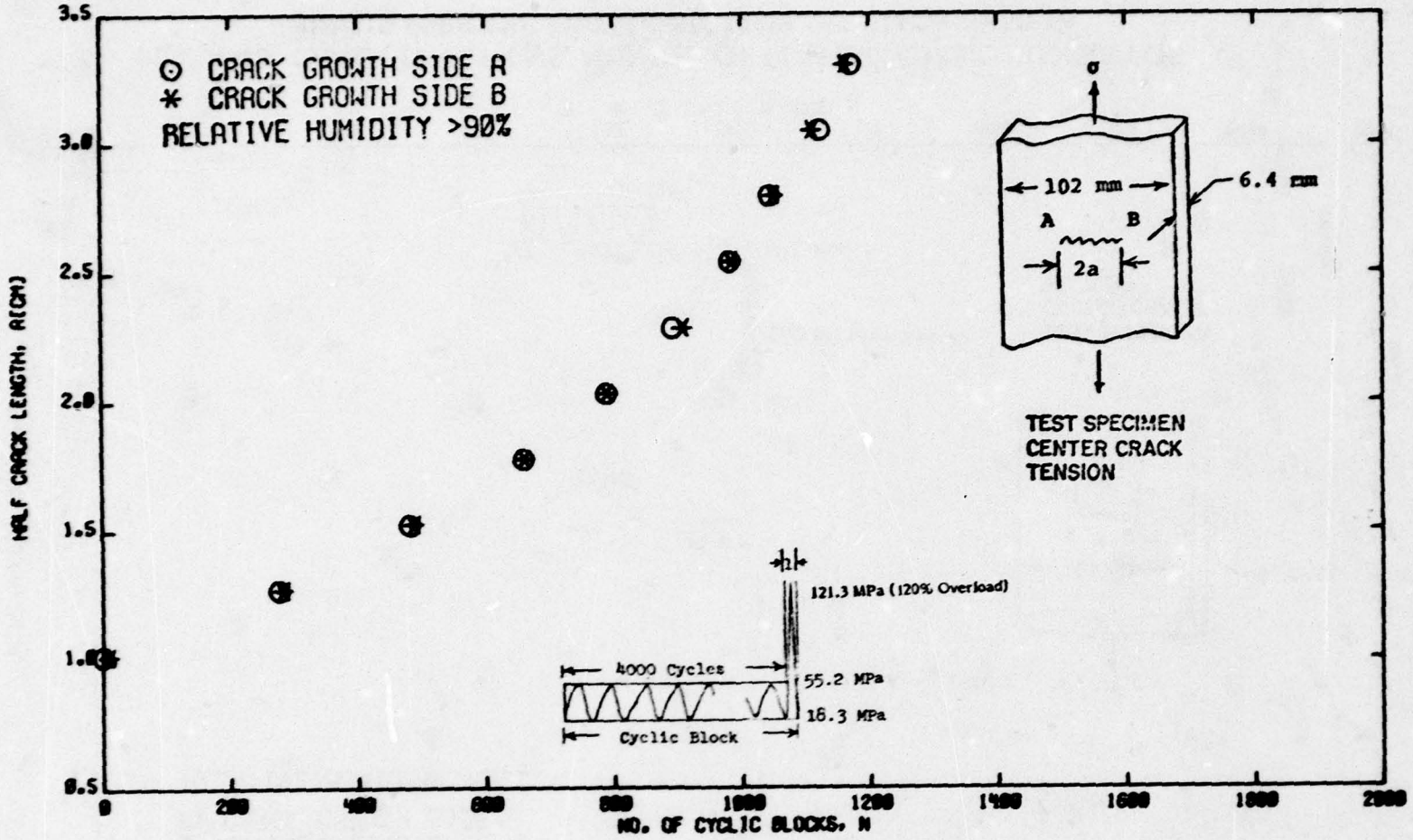

FIG. A-49 CRACK LENGTH VS. NUMBER OF ELAPSED CYCLIC BLOCKS FOR SINGLE PERIODIC OVERLOAD TESTS OF ALLOY 7075-T7

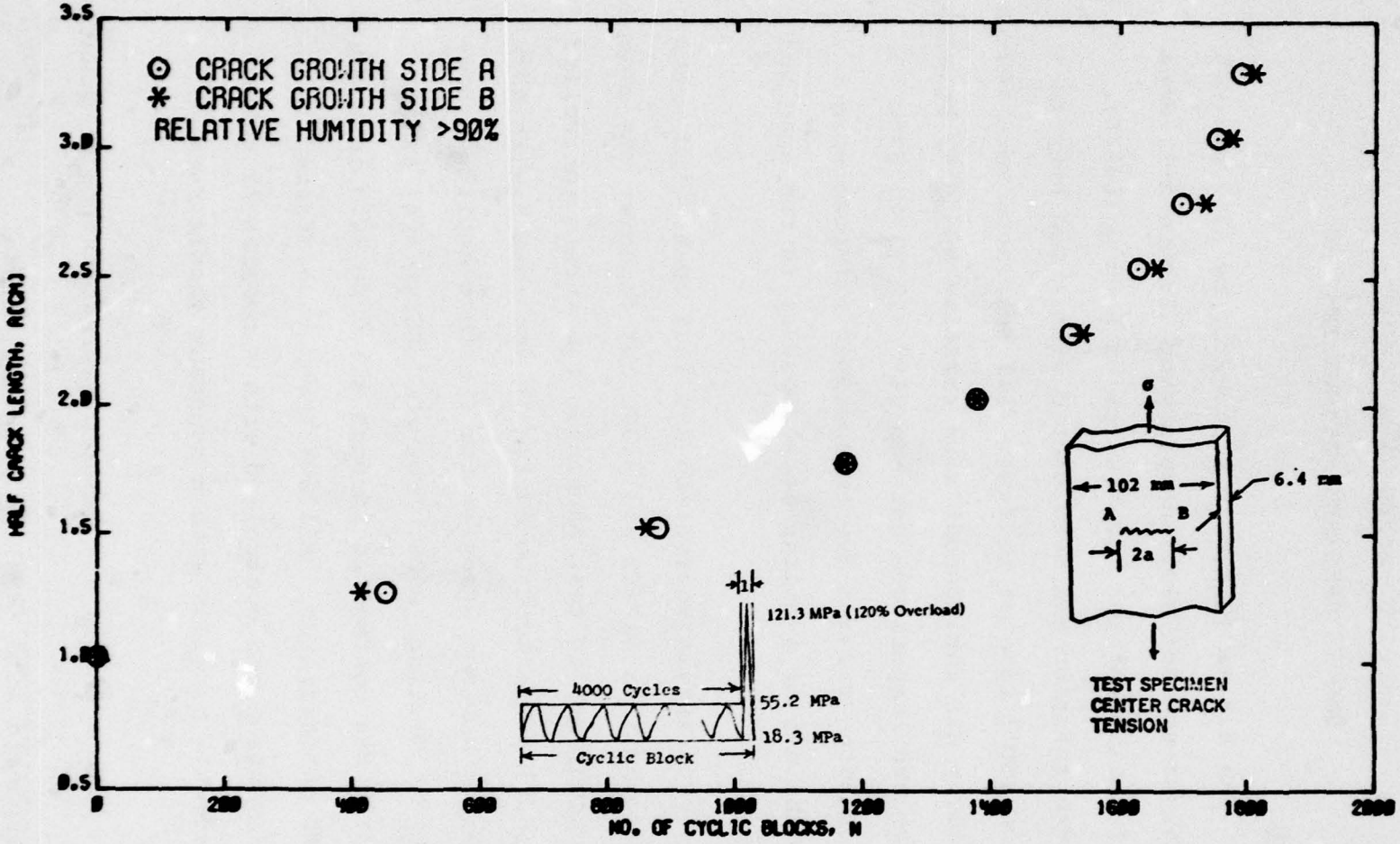

FIG. A-50 CRACK LENGTH VS. NUMBER OF ELAPSED CYCLIC BLOCKS FOR SINGLE PERIODIC OVERLOAD TESTS OF ALLOY 7075-T6

APPENDIX B

SMOOTH SPECIMEN FATIGUE TESTING

PROCEDURE

The 5.8 mm (0.230 in.) diameter by 12.7 mm (0.5 in.) straight reduced section specimens (Figure B-1) were chemically polished* for 1.5 minutes in a 85°C (185°F) temperature solution and were stored within one hour in a dessicator until time of testing. All specimens were tested in laboratory air environment with relative humidity between 40 and 60% and temperature between 24°C (75°F) to 27°C (80°F). Bending strains due to specimen gripping were minimized by use of a molten metal coupler in the specimen load train.

Both strain controlled and load controlled tests were conducted in a 44 482 N (10,000 lb) capacity MTS closed-loop electrohydraulic test machine. The strain controlled fatigue (SCF) tests were conducted in accordance with ASTM Tentative Recommended Practice for Constant Amplitude Low-Cycle Fatigue Testing, E606. For the SCF tests, axial total strain was controlled through a 7.6 mm (0.3 in.) gauge length MTS extensometer. All SCF tests were started in the tension direction and controlled with a completely reversed triangular wave function with a constant strain rate of 0.01/sec.

Figure B-2 is a schematic representation of quantities

*Orthophosphoric Acid (85%) 94 parts by volume.
Nitric Acid (concentrated) (70%) 6 parts by volume.

associated with a generalized stress-strain hysteresis loop and relative contributions of components of elastic plus plastic strain to the strain-life relationship. From the strain-life relationship, long life fatigue resistance is seen to be governed by the elastic strains while short life is governed by the plastic strains.

In this investigation, hysteresis loops were acquired directly by a DEC System PDP/11 digital computer at logarithmic increments with load and strain peaks acquired through an electronic interface at shorter intervals. Analysis of each hysteresis loop to determine elastic, plastic, and total strain amplitudes as well as stress amplitude was conducted on a DEC System 10 digital computer. Plastic strain amplitude was defined as one-half the hysteresis loop width at zero stress.

Specimen failure ($2N_f$) in the strain controlled tests was defined for this investigation as the number of reversals required to develop a crack large enough to cause a decrease in load carrying capacity greater than the magnitude of the possible error in stress measurement (6.9 MPa or 1 ksi). For a test with a fracture life less than 2000 reversals, the stress amplitude would drop 1 ksi within 20 reversals; for fracture lives between 2000 and 20,000 reversals, the drop would occur within 200 reversals. Strain was not monitored during load controlled tests due to concern of possibly initiating cracks at extensometer knife

edges. However, the difference in the number of cycles between crack initiation and fracture has been shown to be low under load control in the long life range [B1]. Consequently, specimen failure for the load control tests was defined as the number of reversals to cause specimen fracture.

Results were analyzed as either plastic or total strain stress amplitudes vs number of reversals to failure ($2N_f$). The plot of plastic strain amplitude vs $2N_f$ is a graphical representation of the empirical Coffin-Manson relationship. Mathematically, this relationship is of the form:

$$\frac{\Delta\varepsilon_p}{2} = \varepsilon'_f(2N_f)^c,$$

and when plotted as:

$$\log\frac{\Delta\varepsilon_p}{2} = \log(\varepsilon'_f) + c\,\log(2N_f),$$

results in a linear relationship where:

$\Delta\varepsilon_p$ = plastic strain amplitude,

ε'_f = fatigue ductility coefficient,

c = fatigue ductility exponent,

$2N_f$ = reversals to failure.

Cyclic stress-strain curves were obtained using the multiple specimen technique [B1].

RESULTS AND DISCUSSIONS

The strain control fatigue (SCF) parameters determined on the different tempers of 7075 and 7050 used in this program are summarized in Table B1, and the long-life cyclic stress tests are summarized in Table B2.

The SCF results were similar to data presented elsewhere on similar high-strength 7XXX alloys. Factors which increased tensile ductility (overaging and higher purity) increased SCF performance. Multiple slope behavior in the Coffin-Manson plot occurred and, as discussed elsewhere [B2, B3], this departure from single slope behavior has been interpreted on the basis of strain localization during cyclic straining. Figure B-3 is a representative Coffin-Manson plot of 7050-T7 illustrating the dual slope behavior. In general, overaging tended to shift the position of the break in the curve to longer lives, and for equivalent yield strengths, 7050 tended to perform slightly better than 7075 during strain cycling.

Figure B-4 contains stress amplitude response curves for two strain levels of 7050-T7. As with 7050-T6 and the four tempers of 7075, the materials tended to be cyclically stable.

The cyclic stress tests tended to support numerous observations concerning the effect of static yield strength on the cyclic life during load control. Materials with higher yield strengths tend to have longer cyclic lives.

Plotting total strain amplitude vs initiation life for 7075 and 7050 alloys illustrates the crossover trend in the strength-ductility-fatigue relationship (Figure B-5). In general, long life is favored by increasing strength, while short life is favored by increasing ductility as measured by percent elongation. According to these results, alloy 7050-T6 performed best at low strains while alloy 7050-T7 performed best at high strains. The crossover behavior pattern observed in Figure B-5 emphasizes the dependence of the particular material application when rating alloy fatigue resistance. That is, ranking alloy performance for a particular application requires identification of the most damaging cycles in the component fatigue spectrum for appropriate consideration of trade-offs with other properties.

REFERENCES - APPENDIX B

B1. Handbook of Fatigue Testing, ASTM STP 566, ASTM, October 1974, p 44.

B2. Sandor, Bela I., Fundamentals of Cyclic Stress and Strain, University of Wisconsin Press, Madison, Wisconsin, 1972.

B3. Sanders, T. H. and Starke, E. A., Met. Trans., Vol 70, September 1976, p 1407.

B4. Sanders, T. H., Mauney, D. A., and Staley, J. T., Fundamental Aspects of Structural Alloy Design, Plenum Press, N.Y., p 487

TABLE B1. SCF DATA FOR 7075 AND 7050

Alloy Type and Temper	S. No.	Stress Amplitude, $\Delta\sigma/2$ MPa	Stress Amplitude, $\Delta\sigma/2$ ksi	Total Strain Amplitude, $\Delta\varepsilon/2$	Elastic Strain Amplitude, $\Delta\varepsilon_e/2$	Plastic Strain Amplitude, $\Delta\varepsilon_p/2$	Fatigue Life, Reversals, 2N	Fatigue Ductility Coefficient, ε'_{f1}	Fatigue Ductility Coefficient, ε'_{f2}	Fatigue Ductility Exponent, c_1	Fatigue Ductility Exponent, c_2
7075-T6	454550-9	494	71.6	0.0071	0.0070	0.0001	5024				
		525	76.1	0.0077	0.0074	0.0003	1806				
		584	84.7	0.0155	0.0085	0.0070	202	0.2121	4905	-0.6761	-2.17
		629	91.2	0.0205	0.0095	0.0110	58				
7075-T7	454549	421	61.0	0.0063	0.0059	0.0004	3412				
		422	61.2	0.0061	0.0059	0.0002	5414				
		429	62.2	0.0072	0.0062	0.0010	2618	0.2700	22073	-0.6431	-2.17
		478	69.4	0.0154	0.0072	0.0082	260				
		507	73.6	0.0204	0.0075	0.0130	98				
7075-T76	438642-1	469	68.1	0.0068	0.0066	0.0002	2814				
		475	68.9	0.0071	0.0068	0.0003	3022				
		488	70.8	0.0092	0.0072	0.0019	1206	0.1924	9283	-0.6068	-2.17
		528	76.5	0.0153	0.0084	0.0069	240				
		559	81.1	0.0204	0.0083	0.0121	96				
7075-T73	438642-2	389	56.4	0.0058	0.0055	0.0003	5428				
		398	57.7	0.0064	0.0057	0.0007	3212				
		399	57.9	0.0071	0.0058	0.0013	3018				
		420	60.9	0.0103	0.0062	0.0041	992	0.3051	32896	-0.6106	-2.17
		444	64.5	0.0154	0.0068	0.0085	420				
		466	67.6	0.0204	0.0072	0.0132	172				
7050-T6	454544-3	495	71.8	0.0071	0.0070	0.0001	4218				
		501	72.6	0.0071	0.0070	0.0001	3202				
		545	79.1	0.0076	0.0074	0.0002	4802				
		569	82.5	0.0087	0.0080	0.0007	2388	0.2544	15797	-0.7090	-2.17
		585	84.9	0.0101	0.0082	0.0019	1094				
		616	89.4	0.0155	0.0090	0.0065	406				
		649	94.1	0.0205	0.0092	0.0113	58				
7050-T7	454543	421	61.0	0.0064	0.0061	0.0003	5418				
		421	61.1	0.0064	0.0060	0.0004	5006				
		433	62.8	0.0071	0.0060	0.0011	2208	0.5305	29492	-0.7228	-2.17
		481	69.7	0.0154	0.0072	0.0082	300				
		485	70.4	0.0204	0.0072	0.0132	178				

TABLE B2. STRESS CONTROLLED, SMOOTH SPECIMEN FATIGUE

Alloy Type and Temper	S. No.	Stress Amplitude, $\Delta\sigma/2$ MPa	Stress Amplitude, $\Delta\sigma/2$ ksi	Reversals to Failure, $2N_f$	Yield Strength, σ_{YS} 2% offset MPa	Yield Strength, σ_{YS} 2% offset ksi
7075-T6	454550	212	30.7	4,317,000	530	76.9
70750T76	438642-1	204	29.6	4,316,000	507	73.5
7075-T7	454549	211	30.6	300,400	505	73.2
7075-T73	438642-2	213	30.9	259,800	417	60.5
7050-T6	454544	212	30.7	12,169,800	612	88.7
7050-T7	454543	219		203,800	511	74.1

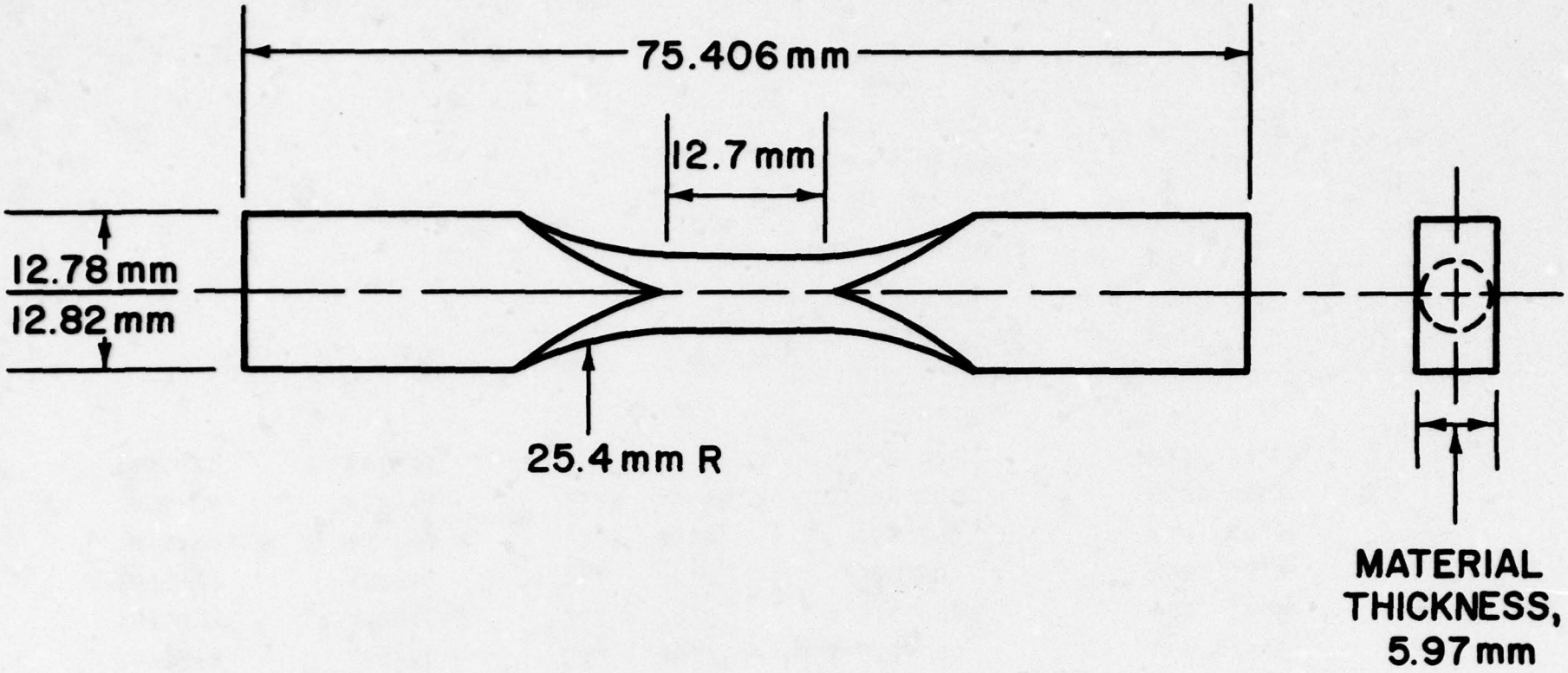

FIG. B-1 AXIAL STRAIN CONTROL FATIGUE SPECIMEN FOR 5.97 mm THICK SHEET

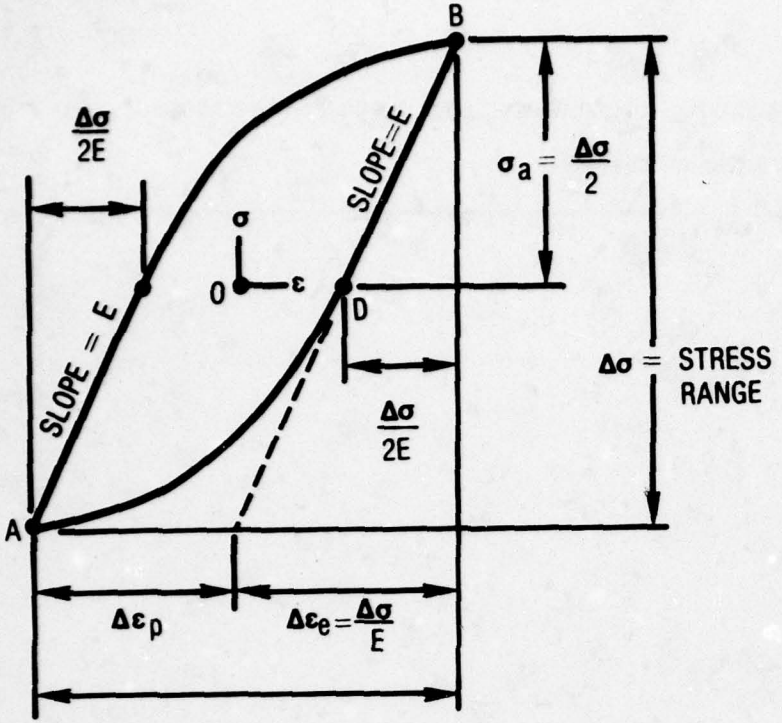

$\Delta\varepsilon_t$ = TOTAL STRAIN RANGE = $\varepsilon_e + \varepsilon_p$

(a) CYCLE DEPENDENT MATERIAL RESPONSE DURING STRAIN CONTROL FATIGUE TEST

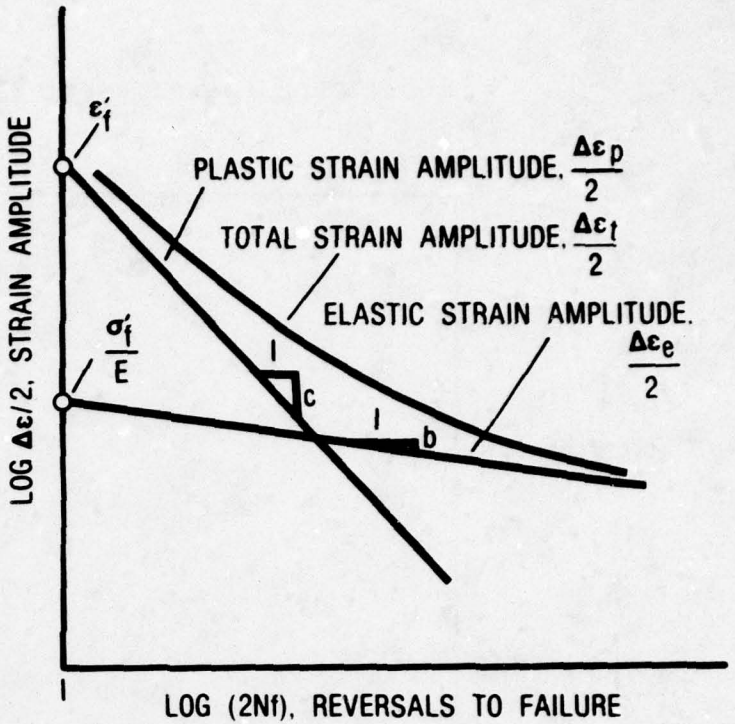

$$\frac{\Delta\varepsilon_t}{2} = \frac{\Delta\varepsilon_e}{2} + \frac{\Delta\varepsilon_p}{2}$$

$$= \frac{\sigma'_f}{E}(2Nf)^b + \varepsilon'_f (2Nf)^c$$

WHERE: σ'_f = FATIGUE STRENGTH DUCTILITY COEFFICIENT
ε'_f = FATIGUE DUCTILITY COEFFICIENT
b = FATIGUE STRENGTH EXPONENT
c = FATIGUE DUCTILITY EXPONENT

(b) LIFE AS A FUNCTION OF ELASTIC, PLASTIC AND TOTAL STRAIN AMPLITUDE

FIG. B-2 STRAIN CONTROL APPROACH TO FATIGUE

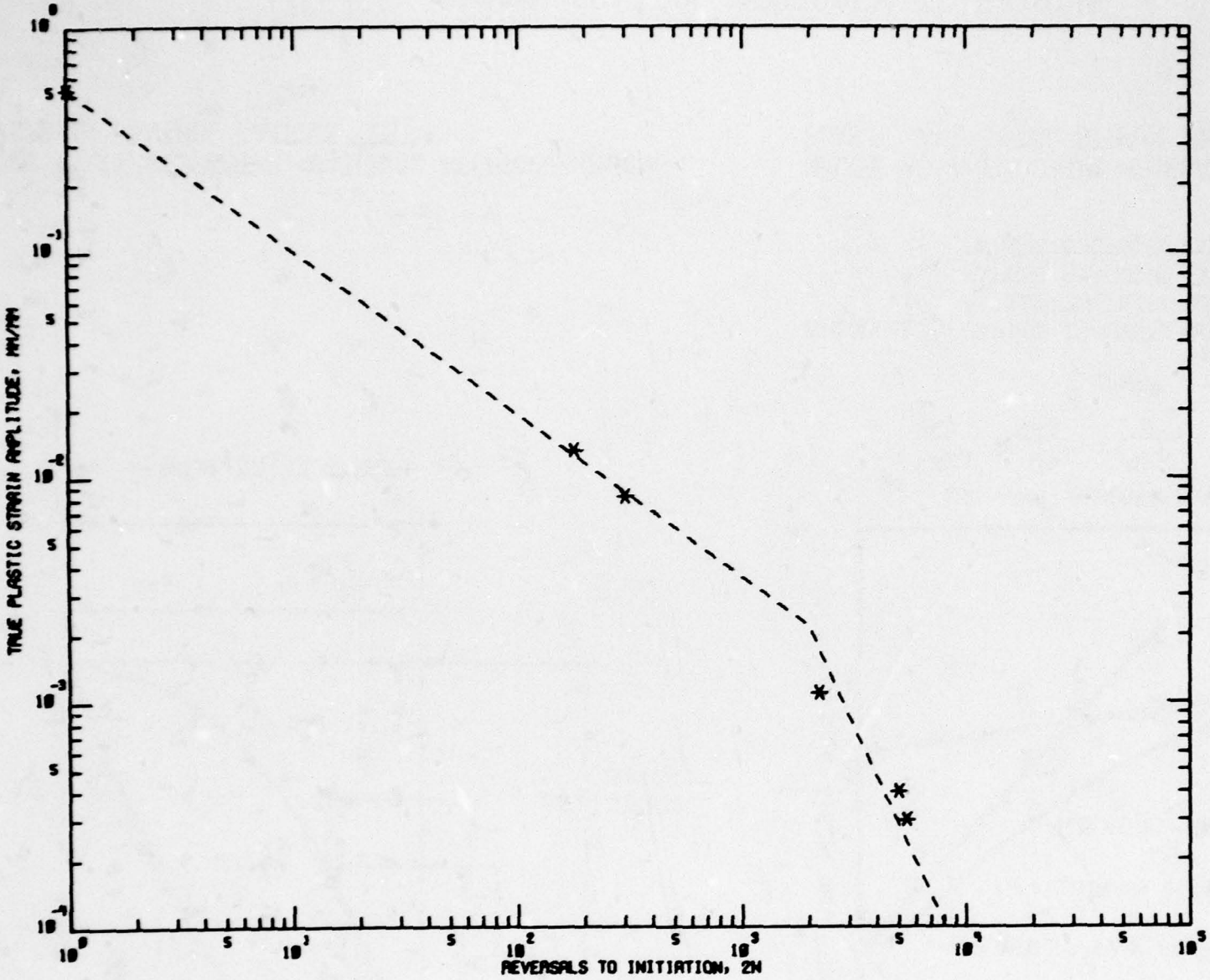

Fig. B-3 - Representative Coffin-Manson Plot of 7050-T7 Illustrating Dual Slope Behavior.

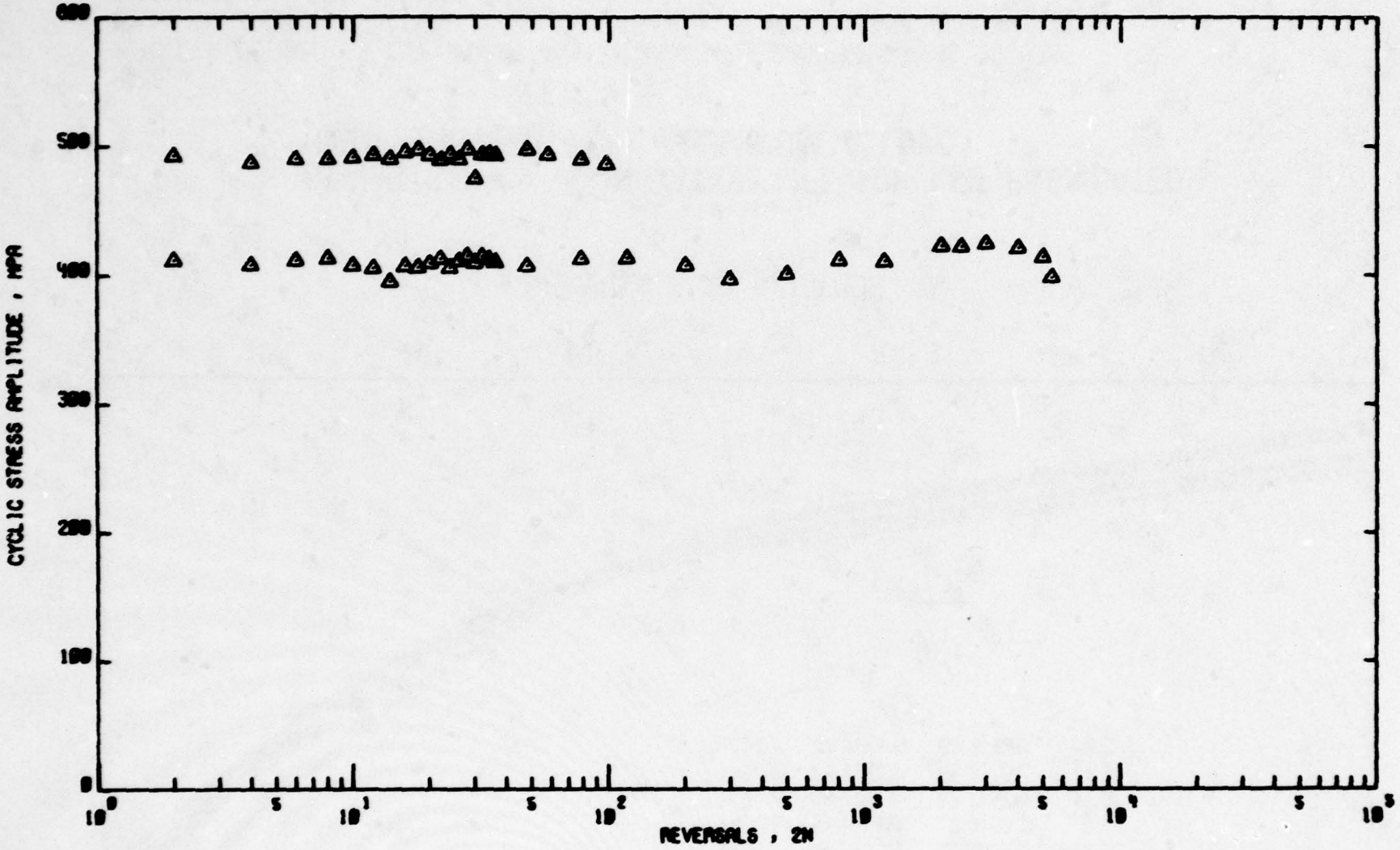

Fig. B-4 - Stress Amplitude vs Life for Two Strain Levels of 7050-T7.

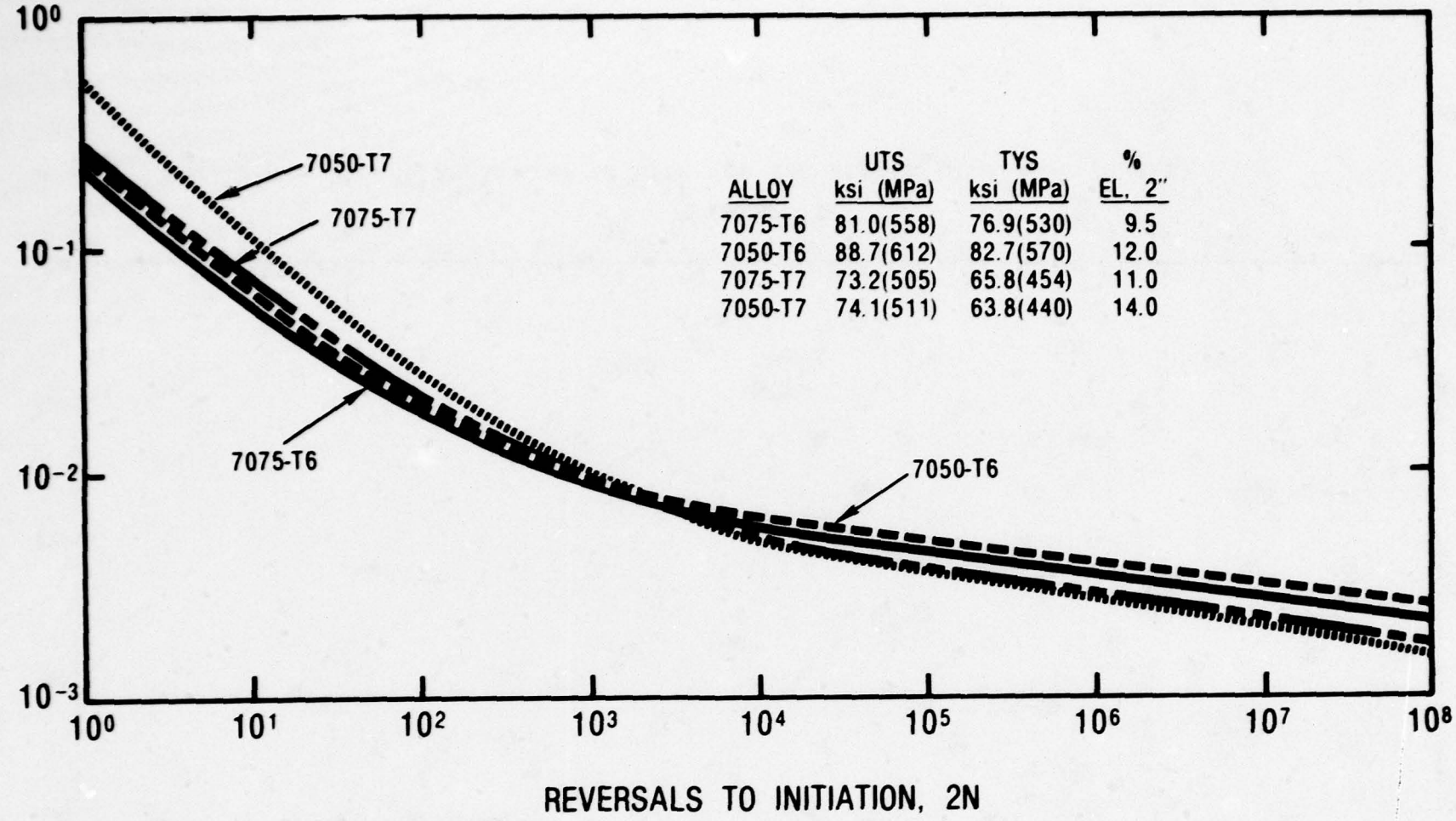

FIG. B-5 CYCLIC STRAIN vs INITIATION LIFE FOR LAB FABRICATED HIGH STRENGTH 7XXX ALUMINUM ALLOYS

NOTE:
INITIATION DEFINED AS LIFE WHERE A 1 ksi (6.9 MPa) DROP IN STRESS OCCURS IN 10 CYCLES FOR FRACTURE LIVES LESS THAN 1000 CYCLES, AND IN 100 CYCLES FOR FRACTURE LIVES GREATER THAN 1000 CYCLES

APPENDIX C

COMPARISON OF EXPERIMENTAL AND PREDICTED CYCLIC CRACK GROWTH LIVES BY FLAW GROWTH PREDICTION MODEL (EFFGRO)

Several load interaction models have been proposed which embrace fracture mechanics concepts to predict flaw growth under variable amplitude loading. Though limitations are recognized in current modeling approaches, these methods have achieved moderate success in predicting flaw growth under complex load histories. Moreover, these predictive methods offer considerable potential to handle rationally the interactions produced by variable load history with complex structural configurations by computer programmable procedures.

The program, EFFGRO, is essentially a specialized integration routine. An initial crack length is given, and da/dn (which is a function of crack length, a, and the loadings) is integrated to yield the relationship between a and cyclic life, N, for a given load spectrum. In addition to constant amplitude crack growth rate information, the program uses yield strength, σ_Y; critical stress intensity, K_{Ic}; and geometric parameters as input. The program predicts crack propagation based on G. Vroman's crack growth method [Ref. 14, main text]. The method utilizes the fact that small changes in crack length have a minimal effect on the crack growth rate and, therefore, is able to calculate crack propagation histories efficiently. Crack growth may be analyzed

with or without attempting to consider the effects of retardation due to overloads. The analysis is ended when maximum stress intensity approaches the critical stress intensity (K_c) and instability occurs. The program replaces all negative minimum stresses by zero and all maximum stresses less than 1 by 1 psi (7 MPa).

The flaw growth prediction model uses a modified version of Forman's equation:

$$\frac{da}{dn} = \frac{c(\Delta K_{eff})^n}{(1-R)K_F - \Delta K_{eff}},$$

to calculate fatigue crack propagation rates. Two values each of c and n are used which correspond to appropriate high and low ranges of ΔK_{eff}. A single value of K_F is used for both ranges. Note that the conventional ΔK has been replaced by ΔK_{eff}. ΔK_{eff} is calculated from ΔK and previous crack growth history. ΔK_{eff} accounts for the effect of previous high loads on the retardation of crack growth from plastic zone considerations. The output contains crack length at the end of each cyclic block.

Table C-1 gives "EFFGRO" predictions for alloys 7050 and 7075 in two tempers, T6 and T7. Four loading conditions are evaluated for each alloy and temper combination. Also shown in this table are experimental values for these cases. Comparison of these values leads to the following observations:

1. "EFFGRO" predictions were conservative for all cases.

2. For 40% periodic overloads (no appreciable overloads), the predictions for all alloys were nearly within factor of two.
3. EFFGRO predictions for eight level spectra were within factor of two for all cases except for 7075-T6 alloy.
4. For 80% periodic overloads, the predictions were consistently poor and off by more than an order of magnitude in some cases.

TABLE C1. COMPARISON OF EXPERIMENTAL AND PREDICTED CYCLIC CRACK GROWTH LIVES BY FLAW GROWTH PREDICTION MODEL (EFFGRO) [Ref. 14]

Alloy Type and Temper	OLR	OCR	Cycles/BK	Experimental Cyclic Life (Blocks) N_B 10·2 to 33 mm	Predicted Cyclic Life (Blocks) N_B 10·2 to 33 mm
7050-T6	1·4	1:4000	4001	19	16
	1·8	1:4000	4001	484	17
	1·8	1:8000	8001	16	9
	8-level	--	2000	1516	660
7050-T7	1·4	1:4000	4001	38	35
	1·8	1:4000	4001	225	46
	1·8	1:8000	8001	77	19
	8-level	--	2000	1725	1585
7075-T6	1·4	1:4000	4001	8	9
	1·8	1:4000	4001	485	10
	1·8	1:8000	8001	100	5
	8-level	--	2000	1143	275
7075-T7	1·4	1:4000	4001	28	23
	1·8	1:4000	4001	279	30
	1·8	1:8000	8001	145	13
	8-level	--	2000	1833	880

DISTRIBUTION LIST

(6 + balance)
Mr. E. S. Balmuth
AIR-52031G
Naval Air Systems Command
Washington, DC 20361

Commander
Naval Air Development Center (Code 306)
Warminster, PA 18974

Naval Sea Systems Command (Code 035)
Department of the Navy
Washington, DC 20360

Naval Ships Research &
Development Center
Code 2812
Annapolis, MD 21402

Naval Ships Research &
Development Center
Washington, DC 20007
Attn: Mr. Abner R. Willner
Chief of Metals Research

Commander
Naval Surface Weapons Center
Metallurgy Division
White Oak, Silver Spring, MD 20910

Director
Naval Research Laboratory
Code 6380
Washington, DC 20390

Director
Naval Research Laboratory
Code 6490
Washington, DC 20390

Director
Naval Research Laboratory
Code 8430
Washington, DC 20390

Office of Naval Research
The Metallurgy Program
Code 471
Arlington, VA 22217

Dr. T. R. McNelley
Dept. of Mechanical Engineering
(Code 59)
Naval Postgraduate School
Monterey, CA 93940

Wright-Patterson Air Force Base
Dayton, OH 45433
Attn: W. Griffith, AFML/LLS

Wright-Patterson Air Force Base
Dayton, OH 45433
Attn: N. Klarquist, AFML/LTM

Wright-Patterson Air Force Base
Dayton, OH 45433
Attn: AFML/MXA

Wright-Patterson Air Force Base
Dayton, OH 45433
Attn: H. Koenigsberg, FTD/PDIT

DCASMA Pittsburgh
1610-S Federal Building
1000 Liberty Avenue
Pittsburgh, PA 15222
Attn: K. Madden

Army Materials & Mechanics
Research Center
Watertown, MA 02172
Attn: Dr. A. Gorum

Wright-Patterson Air Force Base
Dayton, OH 45433
Attn: AFML/LLN

Commanding Officer
Office of Army Research
Box CM, Duke Station
Durham, NC 27706

U.S. Army Armament R&D Command
(ARRADCOM)
Dover, NJ 07801
Attn: Dr. J. Waldman
DRDAR-SCM-P, Bldg 3409

National Aeronautics & Space
Administration
(Code RWM)
600 Independence Ave., S.W.
Washington, DC 20546

National Aeronautics & Space
Administration
Langley Research Center
Materials Div., Langley Station
Hampton, VA 23365
Attn: Mr. H. F. Hardrath
STOP 188M

National Aeronautics & Space
Administration
George C. Marshall Space Flight
Center
Huntsville, AL 35812
Attn: Mr. J. G. Williamson
S&E-ASTN-MMC

National Academy of Sciences
Materials Advisory Board
Washington, DC 20418
Attn: Dr. J. Lane

U.S. Energy Research & Development
Administration
Savannah River Operations Office
P.O. Box A
Aiken, SC 29801
Attn: N. J. Donahue
Reactor Materials

Director
National Bureau of Standards
Washington, DC 20234
Attn: Dr. E. Passaglia

Battelle Memorial Institute
505 King Avenue
Columbus, OH 43201
Attn: Stephen A. Rubin, Mgr.
Information Operations

IIT Research Institute
Metals Research Department
10 West 35th Street
Chicago, Illinois 60616
Attn: Dr. N. Parikh

General Dynamics Convair Div.
P.O. Box 80847
San Diego, CA 92138
Attn: Jack Christian, Code 643-10

Kaman Aerospace Corporation
Old Windsor Road
Bloomfield, CT 06001
Attn: Mr. M. L. White

Rockwell International
Columbus Division
Columbus, OH 43216
Attn: P. Maynard, Dept. 75
Group 521

Rockwell International
Rocketdyne Division
Canoga Park, CA 91305
Attn: Dr. Al Jacobs
Group Scientist
Materials Branch

Rockwell International
Los Angeles Division
International Airport
Los Angeles, CA 90009
Attn: Gary Keller
Materials Applications

Lockheed Palo Alto Research
Laboratories
Materials Science Laboratory
3251 Hanover Street
Palo Alto, CA 94303
Attn: Dr. D. Webster
Bldg. 201 Org. 52-31

Lockheed California Company
P.O. Box 551
Burbank, CA 91503
Attn: Mr. J. M. VanOrden
Dept. 74-71
Bldg. 221, Plt. 2

Lockheed-Georgia Company
Marietta, GA 30061
Attn: E. Bateh

Lockheed Missile & Space Corp.
Box 504
Sunnyvale, CA 94088
Attn: Mr. G. P. Pinkerton
Bldg. 154, Dept 8122

Douglas Aircraft Company
3855 Lakewood Blvd
Long Beach, CA 90808
Attn: Mr. Fred Mehe, C1-250

Sikorsky Aircraft
Div. of United Technologies, Inc.
Stratford, CT 06497
Attn: Materials Dept.

Grumman Aerospace Corp.
Plant 12
Bethpage, NY 11714
Attn: R. Heitzmann

Bell Helicopter Co.
A Textron Division
P.O. Box 482
Fort Worth, TX 76101
Attn: M. A. Green

United Technology Center
P.O. Box 358
Sunnyvale, CA 94088
Attn: George Kreici

Hughes Helicopters
Division Summa Corporation
Centinela & Teale Sts
Culver City, CA 90230
Attn: T. Matsuda

Norman A. Nielson
Engineering Technology Laboratories
E. I. Dupont de Nemours
Wilmington, DE 19898

Massachusetts Institute of Technology
Dept of Metallurgy & Materials Science
Cambridge, MA 02139
Attn: Dr. N. J. Grant

Dr. J. Williams
Dept. of Metallurgy & Materials Science
Carnegie-Mellon University
Pittsburgh, PA 15213

The Franklin Institute Research
Laboratories
Twentieth & Parkway
Philadelphia, PA 19103
Attn: Technical Director

Whittaker Corporation
Nuclear Metals Division
West Concord, MA 01718

Dept of Metallurgical Engineering
Drexel University
32nd & Chestnut Streets
Philadelphia, PA 19104

Martin Marietta Aluminum
Attn: Mr. Paul E. Anderson (M/C 5401)
19200 South Western Avenue
Torrance, CA 90509

Mr. W. Spurr
The Boeing Company
12842 72nd Ave., N.E.
Kirkland, WA 98033

Dr. John A. Sehey
Dept. of Materials Engineering
University of Illinois at
Chicago Circle
Box 4348
Chicago, IL 60680

Dr. Otto Buck
Rockwell International
P.O. Box 1082
1027 Camino Dos Rios
Thousand Oaks, CA 91360

Pratt & Whitney Aircraft Group
Div. of United Technologies
Florida Research & Development Ctr.
P.O. Box 2691
West Palm Beach, FL 33402

Martin Marietta Corporation
P.O. Box 5837
Orlando, FL 32805
Attn: Dr. Richard C. Hall
Mail Point 275

Dr. D. L. Davidson
Southwest Research Institute
8500 Culebra Road
P.O. Drawer 28510
San Antonio, TX 78284

Boeing-Vertol Company
Boeing Center
P.O. Box 16858
Philadelphia, PA 19142
Attn: Mr. J. M. Clark

The Boeing Company
Commercial Airplane
ORG. 6-8733, MS77-18
P.O. Box 3707
Seattle, WA 98124
Attn: Cecil E. Parsons

Northrop Corporation
Aircraft Division
Dept. 3771-62
3901 West Broadway
Hawthorne, CA 90250
Attn: Mr. Allen Freedman

Vought Corporation
P.O. Box 5907
Dallas, TX 75222
Attn: Mr. A. Hohman

McDonnell Aircraft Co
P.O. Box 516
St. Louis, MO 63166
Attn: Mr. H. Turner
Materials & Processes Dev.
General Engineering Div.

Grumman Aerospace Corp
Research Dept
Bethpage, NY 11714
Attn: Dr. G. Geschwind

Detroit Diesel Allison Division
General Motors Corporation
Materials Laboratories
Indianapolis, IN 46206

General Electric Company
Aircraft Engine Group
Materials & Processes Technology Labs
Evendale, OH 45215

Dr. Charles Gilmore
Tompkins Hall
George Washington University
Washington, DC 20006

Mr. Michael Hyatt
The Boeing Company
P.O. Box 707
Seattle WA 98124

General Electric Co.
Corporate Research & Development
Bldg. 36-441
Schenectady, NY 12345
Attn: Dr. J. H. Westbrook, Mgr
Materials Information Services

General Electric Company
Corporate Research & Development
P.O. Box 8
Schenectady, NY 12301
Attn: Dr. D. Wood

Westinghouse Electric Company
Materials & Processing Laboratories
Beulah Road
Pittsburgh, Pa 15235
Attn: Don E. Harrison

Dr. D. B. Williams
Dept. of Metallurgy & Materials Science
Whitaker Lab - #5
Lehigh University
Bethlehem, PA 18015

General Dynamics Corp
Convair Aerospace Division
Fort Worth Operation
P.O. Box 748
Fort Worth, TX 76101
Attn: Tom Coyle

Dr. D. Matlock
Dept. of Metallurgical Engineering
Hill Hall
Colorado School of Mines
Golden, CO 80401

Brush Wellman, Inc
17876 St. Clair Avenue
Cleveland, OH 44110
Attn: Mr. Bryce King

Mr. H. S. Rubenstein
6803 Lemon Rd
McLean, VA 22101

General Electric
Missile & Space Division
Materials Science Section
P.O. Box 8555
Philadelphia, PA 91901

Kawecki Berylco Industries
Attn: Mr. C. B. Criner
P.O. Box 1462
Reading, PA 19603

ERDA Division of Reactor Development & Technology
Washington, DC 20545
Attn: Mr. J. M. Simmons, Chief
Metallurgy Section

Dr. F. N. Mandigo
Olin Metals Research Laboratories
91 Shelton Avenue
New Haven, CT 06515

Kaiser Aluminum & Chemical Corp
Aluminum Division Research Center for Technology
P.O. Box 870
Pleasonton, CA 94566
Attn: T. R. Pritchett

Reynolds Metals Company
Metallurgical Research Division
4th & Canal Sts
Richmond, VA 23219
Attn: Dr. J. H. Dedrick

Dr. E. A. Starke, Jr.
School of Chemical Engineering & Metallurgy
Georgia Institute of Technology
Atlanta, GA 30332

General Electric Co
1000 Western Ave
Lynn, MA 01910
Attn: Mr. John Shai

United Technologies Research Labs
East Hartford, CT 06108
Attn: Mr. Roy Fanti

Autonetics Division of Rockwell International
P.O. Box 4173
Anaheim, CA 92803
Attn: Mr. A. G. Gross, Jr.
Dept. 522-92

Dr. J. W. Edington
Dept of Mechanical & Aerospace Engineering
University of Delaware
Newark, DE 19711

Dr. R. Balluffi, Chairman
Dept of Materials Science & Engineering
Bard Hall
Cornell University
Ithaca, NY 14853

Dr. D. J. Duquette
Materials Engineering Dept
RPI
Troy, NY 12181

Dr. M. Fine
Northwestern University
Dept. of Materials Sciences
Evanston, IL 60201

Dr. C. Laird
Dept of Metallurgy & Materials Science
University of Pennsylvania
Philadelphia, PA 19174

Dr. B. Jarkowski
Tuskegee Research Institute
Tuskegee, AL 36088

Mr. Charles Gure
Wyman-Gordon Company
Worcester Street
North Grafton, MA 01536

Dr. H. Marcus
Dept. of Mechanical Engineering
University of Texas
Austin, TX 78712

Dr. A. J. McEvily
Dept. of Metallurgy
University of Connecticut
Storrs, CT 06268

Dr. R. Pelloux
Dept. of Metallurgy
MIT
Cambridge, MA 02100

FINAL REPORT ONLY:

Commander
Naval Air Systems Command
Air-954 (2 copies)
Washington, DC 20361

(12 copies)
Defense Documentation Center
Cameron Station
Alexandria, VA 22314
VIA: Commander
Naval Air Systems Command
Code AIR-954
Washington, DC 20361

AFOSR-NE, Bldg. 410
Bolling AFB
Washington, DC 20332
Attn: Dr. A. H. Rosenstein

Dr. W. C. Setzer, Director
Metallurgy & Surface Technology
Consolidated Aluminum Corp
P.O. Box 14448
St. Louis, MO 63178